Journal of
Mechanics of
Materials and Structures

See inside back cover or http://www.jomms.org for submission guidelines.

COMPOSITE MODELING FOR THE EFFECTIVE ELASTIC PROPERTIES OF SEMICRYSTALLINE POLYMERS

SAID AHZI, NADIA BAHLOULI, AHMED MAKRADI AND SALIM BELOUETTAR

It is established that upper and lower bounds predict results far apart from each other for the effective elastic properties of semicrystalline polymers such as polyethylene. This is manly due to the high anisotropy of the elastic properties of the crystals. Composite modeling has been used to predict intermediate results between the bounds. Here, we show the details of composite modeling based on a two phase inclusion (crystalline lamella and amorphous domain) as the local representative element of a semicrystalline polymer. Three approaches, two composite bounds, and a composite self-consistent model, are used to compute the overall elastic properties. Details of the development of these approaches are given in this paper. We find good agreement between results from these approaches and experimental results for polyethylene.

1. Introduction

Under a nondistorted state, semicrystalline polymer morphology is often presented in the shape of spherulites. Each spherulite is composed of crystalline plates arranged radially and separated by an amorphous domain. The macroscopic mechanical behavior of the spherulitic polymer is assumed to be isotropic. When the material is distorted, the spherulitic morphology disappears, leading to an oriented morphology with privileged directions. This arrangement contributes to the increase in global elastic anisotropy. We note that the elastic stiffness in the chain direction of the crystalline lamellae is very high. This local anisotropy appears at a macroscopic scale in the case of oriented polymers.

One of the current and very important challenges for cost-effective design of new advanced polymers and polymer matrix composites hinges upon the use of advanced computational methods and novel micromechanical models that bridge the gap between different material length scales. Here we consider simplified homogenization techniques based on continuum mechanics where the molecular architecture and molecular weight are not explicitly accounted for. However, their effects are somehow included in the values chosen for the homogenized local properties and in the volume fractions of the phases.

For the general case of predicting the effective properties of heterogeneous media, such as the two phase composites, there exist several theories that are used as averaging schemes. For instance, the asymptotic method proposed by [Berlyand and Kozlov 1992; Berlyand and Promislow 1995] can be used to predict the asymptotic behavior of the effective elastic properties of a two phase composite material as the ratio δ of the moduli for the soft (matrix) and hard (inclusion) phases tends to zero ($\delta \to 0$). This asymptotic method has been used to design both isotropic and orthotropic composite materials with particular elastic properties. Among other widely used theories are the Hashin–Shtrikman bounds

Keywords: effective elastic properties, crystalline polymers, homogenization, micromechanics, composite averaging schemes.

[1963], the Mori–Tanaka approach [Mori and Tanaka 1973; Benveniste 1987], the Ponte Castaneda–Willis approach [1995], the double inclusion theory [Hori and Nemat-Nasser 1993; Hu and Weng 2000; Aboutajeddine and Neale 2005] and the statistical approach [Lin and Garmestani 2000; Jefferson et al. 2005]. Specific application of these approaches to semicrystalline polymers is yet to be done to compare results for these materials. While this is an important task, it is out of the scope of the present work, in which we discuss simpler methods.

To calculate the mechanical properties of semicrystalline polymers, Takayanagi et al. [1966] considered the two polymer phases as oriented crystalline blocks alternating with an amorphous phase. This simple model was used to predict the tensile moduli parallel and perpendicular to the draw direction. Another model, proposed by Barham and Arridge [1977], considers the composite nature of the semicrystalline polymer. These two models are used and discussed in [Ward 1985]. Wang [1973] proposed a composite model based on the self-consistent approach of [Hill 1964; 1965; Hermans 1967]. To predict the elastic constant for transcrystalline polyethylene using Hertman's formulation, [Wang 1973] considered transcrystalline polyethylene as crystalline fibers embedded in an isotropic amorphous matrix.

Ahzi et al. [1995] showed that the classical upper and lower bounds result in estimates far apart from each other for elastic isotropic polyethylene (PE), and that the results of [Wang 1973] for transcrystalline PE are very close to those predicted by the classical upper bound. They also suggested the use of two-phase composite inclusion-based modeling to develop intermediate estimates of the elastic properties of semicrystalline polymer. However, some of the details of the intermediate modeling approach were not given in [Ahzi et al. 1995].

Molecular weight is not explicitly accounted for in our present proposed approach. It is well established that small-strain tensile deformation properties, such as Young's modulus, yield stress, and yield strain are directly related to percent crystallinity, independently of molecular weight; [Jordens et al. 2000]. However for low and medium density, Nakayama et al. [1991] and Capaccio et al. [1976] have shown that the crystallinity decreases with increasing molecular weight of PE. This is the case for PE processed following the standard procedure based on slow cooling from the melt, according to this last reference. For instance, the thickness of the amorphous domains is directly related to the square root of molecular weight [Flory 1969]. Under these conditions the crystalline PE has an orthorhombic structure, but when PE is processed under high pressure, a hexagonal crystalline phase is obtained [de Langen et al. 2000]. In the present work we consider PE obtained by slow cooling, where the crystalline phase can be considered as entirely orthorhombic [Addiego et al. 2006]. In our approach, the percent of crystallinity is imposed and therefore the corresponding molecular weight is implicitly accounted for. For other processing procedures where the link between crystallinity and molecular weight may not be so simple, our approach should be modified. This can be done by introducing the molecular weight effect directly in the expression of the local properties. Averaging will therefore account for the effect of molecular weight. However, this point is out of the scope of the current paper.

The present work is based on the composite model of [Ahzi et al. 1995], where the following hypotheses are considered: the elementary representative volume of a semicrystalline polymer is considered as a two-phase composite inclusion representing a crystalline plate and the neighboring amorphous domain. These composite inclusions can be modeled as an extended sandwich with an infinite planar interface (Figure 1). We give the details of the development of three composite models: composite upper bound,
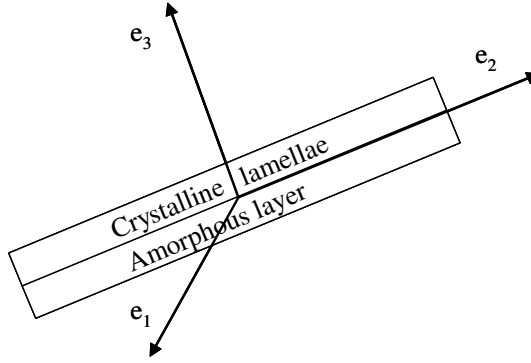
Figure 1. Two-phase composite inclusion.

composite lower bound and composite self-consistent model. To illustrate the result of these intermediate models, we applied them to predict the elastic properties of spherulitic polyethylene. We also compare these results to experimental ones from the literature. These comparisons show that the developed intermediate models give good bounding of experimental results for different crystallinities.

2. Local elastic properties

The elastic constants of the crystals of polyethylene (PE) used in this work are computed in [Zehnder et al. 1996] using atomistic simulations. These elastic constants are expressed in the orthonormal axis of the orthorhombic unit cell of PE crystals as follows:

$$C^c = \begin{bmatrix} 8.50 & 5.00 & 4.50 & 0.00 & 0.00 & 0.00 \\ 5.00 & 9.00 & 6.40 & 0.00 & 0.00 & 0.00 \\ 4.50 & 6.40 & 250.00 & 0.00 & 0.00 & 0.00 \\ 0.00 & 0.00 & 0.00 & 2.80 & 0.00 & 0.00 \\ 0.00 & 0.00 & 0.00 & 0.00 & 1.70 & 0.00 \\ 0.00 & 0.00 & 0.00 & 0.00 & 0.00 & 3.40 \end{bmatrix} \text{GPa,}$$

$$S^c = (C^c)^{-1} = \begin{bmatrix} 0.17 & -0.09 & -0.0006 & 0.00 & 0.00 & 0.00 \\ -0.09 & 0.16 & -0.0025 & 0.00 & 0.00 & 0.00 \\ -0.0006 & -0.0025 & 0.004 & 0.00 & 0.00 & 0.00 \\ 0.00 & 0.00 & 0.00 & 0.35 & 0.00 & 0.00 \\ 0.00 & 0.00 & 0.00 & 0.00 & 0.58 & 0.00 \\ 0.00 & 0.00 & 0.00 & 0.00 & 0.00 & 0.29 \end{bmatrix} \text{GPa}^{-1}.$$

For the amorphous phase, since polyethylene (PE) is rubbery at room temperature, atomistic simulations cannot be used to compute the elastic properties. However, Gray and McCrum [1969] reported a Poisson ratio $v = 0.49$ and a shear modulus $G^a = 0.1$ GPa for polyethylene. The shear modulus appears to be two orders of magnitude higher than what one would expect for the rubbery phase of PE. This is due to the fact that the measured value is influenced by the presence of the crystalline phase. In the applications shown in this work, we will keep $v = 0.49$ and shear modulus $G^a = 0.1$ GPa. As one would
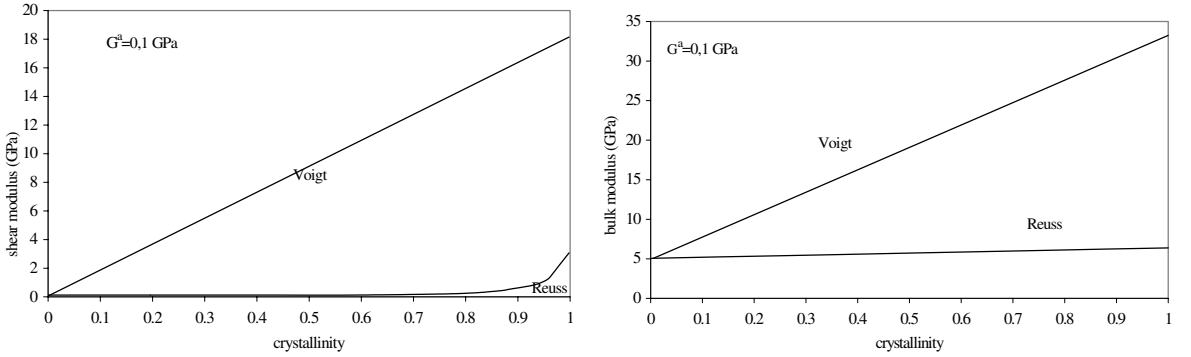
Figure 2. Classical bounds for the shear modulus (left) and bulk modulus (right) for isotropic PE.

expect, the amorphous domains in semicrystalline polymers will not have the same properties as the corresponding bulk material.

3. Classical upper and lower bounds (Voigt and Reuss)

For a semicrystalline polymer with a volume fraction f_a of the amorphous phase, the classical bounds, Voigt (upper bound) and Reuss (lower bound), can be used to compute the effective (average) elastic properties. The Voigt model assumes the uniformity of strain in the material which leads to the expression

$$\boldsymbol{C}^{\text{eff}} = \left\langle f_a \boldsymbol{C}^a + (1 - f_a) \boldsymbol{C}^c \right\rangle \tag{1}$$

for the effective stiffness tensor. The Reuss model assumes uniformity of the stress which yields the expression

$$\boldsymbol{S}^{\text{eff}} = \left\langle f_a \boldsymbol{S}^a + (1 - f_a) \boldsymbol{S}^c \right\rangle \tag{2}$$

for the effective compliance tensor. Here, $\langle \cdot \rangle$ represents the volume average over the aggregate. These classical bounds were implemented in [Ahzi et al. 1995] to predict the effective elastic properties of polyethylene with isotropic distribution of the crystalline lamellae, which represent a spherulitic morphology of polyethylene. The analytical integration procedure for isotropic distribution is outlined in Appendix A. The predicted effective isotropic properties are shown in Figure 2, which depicts the evolution of the shear and bulk moduli as functions of the crystallinity of PE. These results show a very large gap between the predictions of the Voigt and the Reuss models for increasing values of crystallinity. This gap is due to the high anisotropy of the crystalline phase and the fact that these classical models account for the composite nature of semicrystalline polymers, such as PE, only through the volume fraction of the two phases. The wide gap between the two model predictions makes it difficult to consider the classical bounds for accurate predictions of the elastic properties of semicrystalline polymers. Polyethylenes usually have crystallinities ranging from 0.3 to 0.8 and for this range the gap between the curves is too wide to make an estimate of the actual values of the macroscopic elastic properties. As seen in the next section, the development of new composite bounds ensures that the gap between these new bounds is drastically reduced compared to the classical bounds, and hence more accurate predictions of the elastic properties can be made.

4. Proposed composite modelling

Composite inclusion model. The morphology of semicrystalline polymers may be thought of as an assemblage of two-phase inclusions. Each inclusion consists of a crystalline lamella and an adjacent amorphous layer as shown in Figure 1 (see also [Ahzi et al. 1990; Ahzi et al. 1995] and [Lee et al. 1993]). The inclusions are of high aspect ratio and are modeled as infinitely extended planar structures with planar interface between the crystalline and the amorphous phase. Lamellar twist is neglected and linear elasticity is assumed for each individual phase as well as for the composite inclusion and the matrix. Let σ^c, σ^a, and σ^I be the Cauchy stress tensors of the crystalline phase, amorphous phase and the inclusion respectively and let ε^c, ε^a and ε^I be the corresponding infinitesimal elastic strain tensors. The constitutive relation for each phase as well as for the composite inclusion may be written as follows:

Crystalline lamella.

$$\sigma^c = C^c \varepsilon^c \qquad \text{or} \qquad \varepsilon^c = S^c \sigma^c, \tag{3}$$

Crystalline lamella.

$$\sigma^a = C^a \varepsilon^a \qquad \text{or} \qquad \varepsilon^a = S^a \sigma^a, \tag{4}$$

Crystalline lamella.

$$\sigma^I = C^I \varepsilon^I \qquad \text{or} \qquad \varepsilon^I = S^I \sigma^I. \tag{5}$$

Here C^c, C^a, nad C^I represent the fourth order stiffness tensors for the crystalline lamella, the amorphous domain and the composite inclusion respectively, and S^c, S^a, S^I are the corresponding compliance tensors (the inverses of the stiffness tensors). The inclusion stress and strain may be obtained by the volume average of the constituent's stress and strain fields

$$\sigma^I = f_a \sigma^a + (1 - f_a) \sigma^c, \tag{6}$$

and

$$\varepsilon^I = f_a \varepsilon^a + (1 - f_a) \varepsilon^c, \tag{7}$$

where f_a is the volume fraction of the amorphous phase, assumed to be the same for all inclusions.

Interface compatibility and equilibrium. Let us first define the vector form of the stress and strain tensors. These tensors can be expressed as

$$\sigma \equiv \left(\sigma_{11}, \sigma_{22}, \sigma_{33}, \sigma_{23}, \sigma_{13}, \sigma_{12} \right)^T \equiv \left(\sigma_1, \sigma_2, \sigma_3, \sigma_4, \sigma_5, \sigma_6 \right)^T, \tag{8}$$

and

$$\varepsilon \equiv \left(\varepsilon_{11}, \varepsilon_{22}, \varepsilon_{33}, \varepsilon_{23}, \varepsilon_{13}, \varepsilon_{12} \right)^T \equiv \left(\varepsilon_1, \varepsilon_2, \varepsilon_3, \varepsilon_4, \varepsilon_5, \varepsilon_6 \right)^T, \tag{9}$$

where the superscript T designates the transpose.

The interface between the crystalline and the amorphous phase of each inclusion requires the enforcement of the compatibility and equilibrium conditions. Considering an orthonormal basis (e_1, e_2, e_3) with e_3 normal to the interface and (e_1, e_2) in the plane of the interface, we can then write the strain compatibility at the interface as

$$\varepsilon_\alpha^c = \varepsilon_\alpha^a = \varepsilon_\alpha^I. \tag{10}$$

Here α takes the values 1, 2 and 6. This means that the in-plane strains are continuous across the interface. The stress equilibrium conditions ensure interface traction equilibrium. These conditions are represented by

$$\sigma_\beta^c = \sigma_\beta^a = \sigma_\beta^I. \tag{11}$$

Here β takes the value 3, 4 and 5.

Now the problem is to determine the expressions for $\boldsymbol{C}^I$ and $\boldsymbol{S}^I$ from the stiffness and compliance tensors of the individual phases. From Equations (3), (4), and (5) we note that, to get the expression for the inclusion stiffness and compliance tensors, we need to express $\boldsymbol{\sigma}^a$ and $\boldsymbol{\sigma}^c$ in terms of $\boldsymbol{\sigma}^I$, and $\boldsymbol{\varepsilon}^a$ and $\boldsymbol{\varepsilon}^c$ in terms of $\boldsymbol{\varepsilon}^I$. From the above linear relations, we show (see Appendix B) that the phase stress and strain tensors are linearly related to the inclusion stress and strain tensors, respectively. These relations are given by

$$\boldsymbol{\sigma}^a = \boldsymbol{R}^a \boldsymbol{\sigma}^I, \qquad \text{and} \qquad \boldsymbol{\sigma}^c = \boldsymbol{R}^c \boldsymbol{\sigma}^I \tag{12}$$

$$\boldsymbol{\varepsilon}^a = \boldsymbol{Q}^a \boldsymbol{\varepsilon}^I \qquad \text{and} \qquad \boldsymbol{\varepsilon}^c = \boldsymbol{Q}^c \boldsymbol{\varepsilon}^I. \tag{13}$$

The fourth order tensors $\boldsymbol{Q}^a$, $\boldsymbol{Q}^c$, $\boldsymbol{R}^a$ and $\boldsymbol{R}^c$ depend on the elastic moduli of the phases. These mapping tensors are termed phase concentration tensors and the analytical determination of their expressions are given in Appendix B.

Inclusion elastic constants. Introducing the constitutive relations given by (3), (4) and (5) in Equation (6) we obtain

$$\boldsymbol{C}^I \boldsymbol{\varepsilon}^I = f_a \boldsymbol{C}^a \boldsymbol{\varepsilon}^a + (1 - f_a) \boldsymbol{C}^c \boldsymbol{\varepsilon}^c, \tag{14}$$

and the use of (12) in (13) leads to

$$\boldsymbol{C}^I \boldsymbol{\varepsilon}^I = \left[f_a \boldsymbol{C}^a \boldsymbol{Q}^a + (1 - f_a) \boldsymbol{C}^c \boldsymbol{Q}^c \right] \boldsymbol{\varepsilon}^I. \tag{15}$$

Thus, the inclusion stiffness tensor is obtained as

$$\boldsymbol{C}^I = f_a \boldsymbol{C}^a \boldsymbol{Q}^a + (1 - f_a) \boldsymbol{C}^c \boldsymbol{Q}^c. \tag{16}$$

Similarly, introducing the constitutive relations (3), (4), and (5) in (7) we obtain

$$\boldsymbol{S}^I \boldsymbol{\sigma}^I = f_a \boldsymbol{S}^a \boldsymbol{\sigma}^a + (1 - f_a) \boldsymbol{S}^c \boldsymbol{\sigma}^c. \tag{17}$$

If the relations of (12) are used in (17), we obtain

$$\boldsymbol{S}^I \boldsymbol{\sigma}^I = \left[f_a \boldsymbol{S}^a \boldsymbol{R}^a + (1 - f_a) \boldsymbol{S}^c \boldsymbol{R}^c \right] \boldsymbol{\sigma}^I. \tag{18}$$

Thus, the inclusion compliance tensor is obtained as

$$\boldsymbol{S}^I = f_a \boldsymbol{S}^a \boldsymbol{R}^a + (1 - f_a) \boldsymbol{S}^c \boldsymbol{R}^c. \tag{19}$$

We note that the expression (19) for the composite inclusion elastic constants is dual to Equation (16): $\boldsymbol{C}^I = (\boldsymbol{S}^I)^{-1}$. However, Voigt-type inclusion-averaging, $\boldsymbol{C}^I_{\text{Voigt}}$, is obtained by setting $\boldsymbol{Q}^a$ and $\boldsymbol{Q}^c$ to identity in relation (16). Reuss-type inclusion averaging, $\boldsymbol{S}^I_{\text{Reuss}}$, is also obtained by setting $\boldsymbol{R}^a$ and $\boldsymbol{R}^c$ to identity in relation (19).
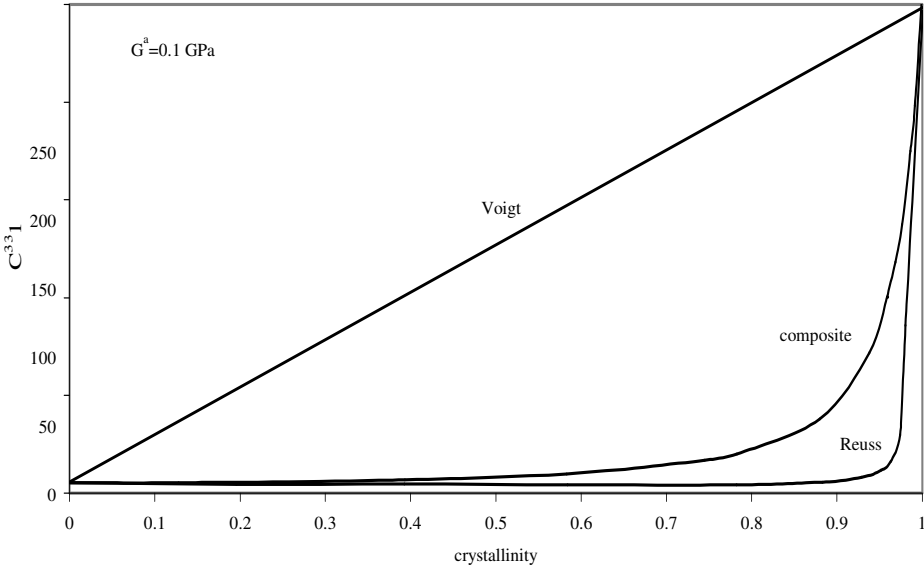
Figure 3. Inclusion stiffness C^I_{33} component.

The stiffness matrix $\boldsymbol{C}^I$ is an important indicator regarding the elastic constants of bulk crystalline polymers such as polyethylene. If we assume the chain direction of the crystalline lamella to be parallel to the inclusion interface normal ($\boldsymbol{e}_3$), the C^I_{33} element of the inclusion stiffness matrix reflects the variation of local elastic stiffness with crystallinity. Figure 3 shows the variation of this stiffness component as function of crystallinity for the three local averaging schemes discussed above: $\boldsymbol{C}^I{}_{\text{Composite}}$, $\boldsymbol{C}^I{}_{\text{Voigt}}$, and $\boldsymbol{C}^I{}_{\text{Reuss}} = (\boldsymbol{S}^I{}_{\text{Reuss}})^{-1}$.

Composite averaging schemes. The overall (effective) elastic properties of an aggregate consisting of N inclusions is obtained by averaging the local elastic properties. We consider an aggregate of volume V subjected to a remote macroscopic stress tensor $\bar{\boldsymbol{\sigma}}$ and to the corresponding macroscopic elastic strain tensor $\bar{\boldsymbol{\varepsilon}}$. Considering the overall behavior to be linear elastic, Hooke's law is then given by

$$\bar{\boldsymbol{\sigma}} = \boldsymbol{C}^{\text{eff}}\bar{\boldsymbol{\varepsilon}} \qquad \text{or} \qquad \bar{\boldsymbol{\varepsilon}} = \boldsymbol{S}^{\text{eff}}\bar{\boldsymbol{\sigma}}, \tag{20}$$

where $\boldsymbol{C}^{\text{eff}}$ and $\boldsymbol{S}^{\text{eff}}$ are the effective stiffness and compliance tensors of the aggregate, respectively. The consistency condition dictates that the average of the local stresses and strains should equal the macroscopic ones, that is

$$\bar{\boldsymbol{\sigma}} = \langle \boldsymbol{\sigma}^I \rangle \equiv \frac{1}{V} \int \boldsymbol{\sigma}^I dV, \tag{21}$$

and

$$\bar{\boldsymbol{\varepsilon}} = \langle \varepsilon^I \rangle \equiv \frac{1}{V} \int \varepsilon^I dV. \tag{22}$$

To obtain an expression for the effective elastic constants as a function of the local ones, we need to apply an interaction law which consists of a relationship between the macroscopic stress (or strain) tensors. This will depend upon the type of averaging scheme chosen.

Composite lower bound. The lower bound estimate assumes stress uniformity within the aggregate. To extend this model to our composite approach, we assume the composite-inclusion stress to be uniform, and the macroscopic stress $\bar{\sigma}$ to be

$$\sigma^I = \bar{\sigma}. \tag{23}$$

Note that the stress in each phase σ^a and σ^c are not necessarily equal to $\bar{\sigma}$. Substituting (23) in (5) we obtain

$$\varepsilon^I = S^I \bar{\sigma}. \tag{24}$$

Taking the volume average of this relation leads to

$$\langle \varepsilon^I \rangle = \langle S^I \rangle \bar{\sigma}. \tag{25}$$

By imposing the global condition (22), and the second equation of (20) we obtain the following expression for the effective compliance tensor:

$$S^{\text{eff}} = \langle S^I \rangle. \tag{26}$$

Using the expression (19), the composite lower bound averaging expression (27) can be written as

$$S^{\text{eff}} = \langle S^I \rangle = \langle f_a S^a R^a + (1 - f_a) S^c R^c \rangle. \tag{27}$$

We note that relation (27) reduces to the Reuss estimate given by (2) if the phase concentration tensors R reduce to identity. The effective stiffness tensor is then obtained by inverting the effective compliance tensor:

$$C^{\text{eff}} = (S^{\text{eff}})^{-1}. \tag{28}$$

Composite upper bound. For the composite upper bound estimate, we assume strain uniformity in the aggregate. That is, each composite inclusion is subjected to the same macroscopic strain $\bar{\varepsilon}$

$$\varepsilon^I = \bar{\varepsilon}, \tag{29}$$

which allows ε^a and ε^c to deviate from $\bar{\varepsilon}$. Substituting (29) in the first part of (5) and taking the volume average of the resulting relation we obtain

$$\langle \sigma^I \rangle = \langle C^I \rangle \bar{\varepsilon}. \tag{30}$$

Using the global equilibrium condition (21) and comparing to the first part of (20) we obtain the composite upper bound expression for the effective elastic stiffness tensor

$$C^{\text{eff}} = \langle C^I \rangle. \tag{31}$$

Using (16), relation (33) becomes

$$C^{\text{eff}} = \langle C^I \rangle = \langle f_a C^a Q^a + (1 - f_a) C^c Q^c \rangle. \tag{32}$$

Here again, we note that relation (32) reduces to the Voigt estimate given by (1) if the phase concentration tensors Q reduce to identity The effective compliance tensor for the composite upper bound is then obtained by inverting the effective stiffness tensor, as

$$S^{\text{eff}} = (C^{\text{eff}})^{-1}. \tag{33}$$

Self-consistent estimate. In our proposed composite bounds, partial local compatibility and equilibrium are satisfied. This is due to the composite inclusion interface conditions given by (10) and (11). To develop a composite self-consistent scheme, we propose to use the two-phase composite inclusion as the local representative element with an elliptical shape, and embedded in infinite homogeneous equivalent medium. To derive the self-consistent interaction law, we use the integral equation method for which details are given in Appendix C. This treatment is analogous to the work of [Zeller and Dederichs 1973], where the Green function method is used to define the integral equation linking local velocity gradient to the macroscopic one. The interaction law obtained by this scheme, in terms of the inclusion versus the macroscopic strain (or stress) tensors, can be expressed by one of the two following dual expressions (see Appendix C):

$$\boldsymbol{\varepsilon}^I = \boldsymbol{B}^I \langle \boldsymbol{B}^I \rangle^{-1} \bar{\boldsymbol{\varepsilon}} \qquad \text{or} \qquad \boldsymbol{\sigma}^I = \boldsymbol{A}^I \bar{\boldsymbol{\sigma}}. \tag{34}$$

Here the fourth order strain-concentration tensor, $\boldsymbol{B}^I$, and the stress-concentration tensor $\boldsymbol{A}^I$ depend on the effective elastic constants, the inclusion elastic constants, and the shape of the inclusion. Because of the normalization procedure used in the development of the self-consistent scheme (see (Appendix C), the consistency conditions (21) and (22) are trivially satisfied by the interaction law (34).

If we insert (34) in the first equation of (5) we obtain

$$\boldsymbol{\sigma}^I = \boldsymbol{C}^I \boldsymbol{B}^I \langle \boldsymbol{B}^I \rangle^{-1} \bar{\boldsymbol{\varepsilon}}. \tag{35}$$

Taking the volume average of (35) and making use of (21), then comparing the final expression with the first equation of (20) leads to the following composite self-consistent expression of the effective stiffness tensor

$$\boldsymbol{C}^{\text{eff}} = \langle \boldsymbol{C}^I \boldsymbol{B}^I \rangle \langle \boldsymbol{B}^I \rangle^{-1}. \tag{36}$$

If we use (16), the above expression becomes

$$\boldsymbol{C}^{\text{eff}} = \langle [f_a \boldsymbol{Q}^a \boldsymbol{C}^a + (1 - f_a) \boldsymbol{Q}^c \boldsymbol{C}^c] \boldsymbol{B}^I \rangle \langle \boldsymbol{B}^I \rangle^{-1}. \tag{37}$$

The self-consistent estimate of the effective compliance tensor can be obtained by inverting the stiffness tensor given by (37). Or, if we use the interaction law given by the second equation of (34) and reasoning similar to that given above, a dual expression to (37) can be obtained as

$$\boldsymbol{S}^{\text{eff}} = \langle (f_a \boldsymbol{R}^a \boldsymbol{S}^a + (1 - f_a) \boldsymbol{R}^c \boldsymbol{S}^c) \boldsymbol{A}^I \rangle. \tag{38}$$

5. Results and discussion

Predicted results for isotropic polyethylene. To illustrate differences between model predictions, we first evaluate the single inclusion elastic constant C_{33}^I as a function of crystallinity. For this, the crystal elastic constants of the polyethylene are computed by [Zehnder et al. 1996] using atomistic simulations (see Section 1), while those for the amorphous phase are calculated using a shear modulus $G^a = 0.1$ GPa. In Figure 3, the values of C_{33}^I have been plotted against crystallinity for the Voigt model (Equation (16), with $\boldsymbol{Q}^a = \boldsymbol{Q}^c = \boldsymbol{I}$), Reuss model (as in Equation (19), with $\boldsymbol{R}^a = \boldsymbol{R}^c = \boldsymbol{I}$), and composite inclusion model (Equation (16)). The nature of the curves reflects that the C_{33}^I elastic constant for the Voigt model increases almost linearly as a function of the crystallinity, compared to the composite inclusion and Reuss models. These predicted results show moderate variation of the elastic constant C_{33}^I with the crystallinity for the composite inclusion and Reuss models except for polyethylene with high crystallinity.

Comparisons between models. The predicted results for the effective shear and bulk moduli as a function of crystallinity of isotropic polyethylene are reported in Figure 4. We notice that the gap between the composite inclusion bounds is drastically reduced relative to the classical bounds except for high concentration of the crystalline phase. In fact, the composite inclusion bounds demonstrate dependence of the stiffness of the crystalline and amorphous phases by enforcement of interface compatibility and equilibrium conditions, which result in reduction of the stiffness of the composite inclusion in the chain direction. In contrast, the classical Voigt and Reuss models assume that the crystalline and amorphous phases deform independently. The imposed uniform strain and high stiffness of the crystals in the chain directions are responsible for over-prediction of the elastic properties by the classical Voigt model.

Regarding self-consistent representation based on the composite inclusion-model, the predicted results fall between the composite bounds. At low crystallinity, the self-consistent curves show a closer response
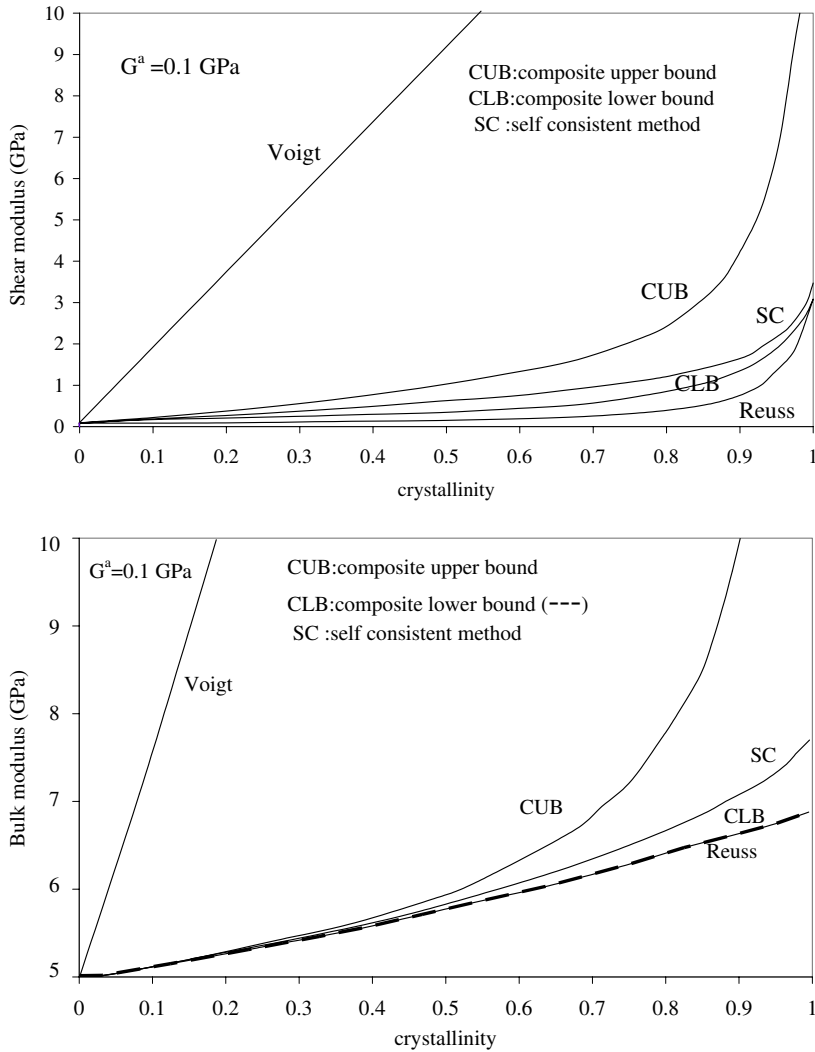
Figure 4. Shear modulus (top) and bulk modulus (bottom) for polyethelyne.

to the composite inclusion lower bound. This behavior is moderately inverted as crystallinity increases but remains in general closer to the composite inclusion lower bound.

Shape effect for the composite self-consistent model. Since the self-consistent approach accounts for inclusion shape effects, in the shear and bulk moduli are reported in Figure 5 for isotropic polyethylene with different inclusion shapes: spherical ($a/c = b/c = 1$), penny-shaped ($a/c = b/c = 5$), and oblate ($a/c = 5$, $b/c = 10$). It can be seen that the predicted elastic properties are very similar for both the penny-shaped and oblate-shaped inclusions. Both the penny and oblate shapes can be used as good inclusion shape approximations of the lamellar structure of polyethylene.

Comparison with experimental results. Davidse et al. [1962] have determined the Young's modulus by measuring the sound velocity, ν, and density, ρ, of various polyethylene samples. The Young's modulus
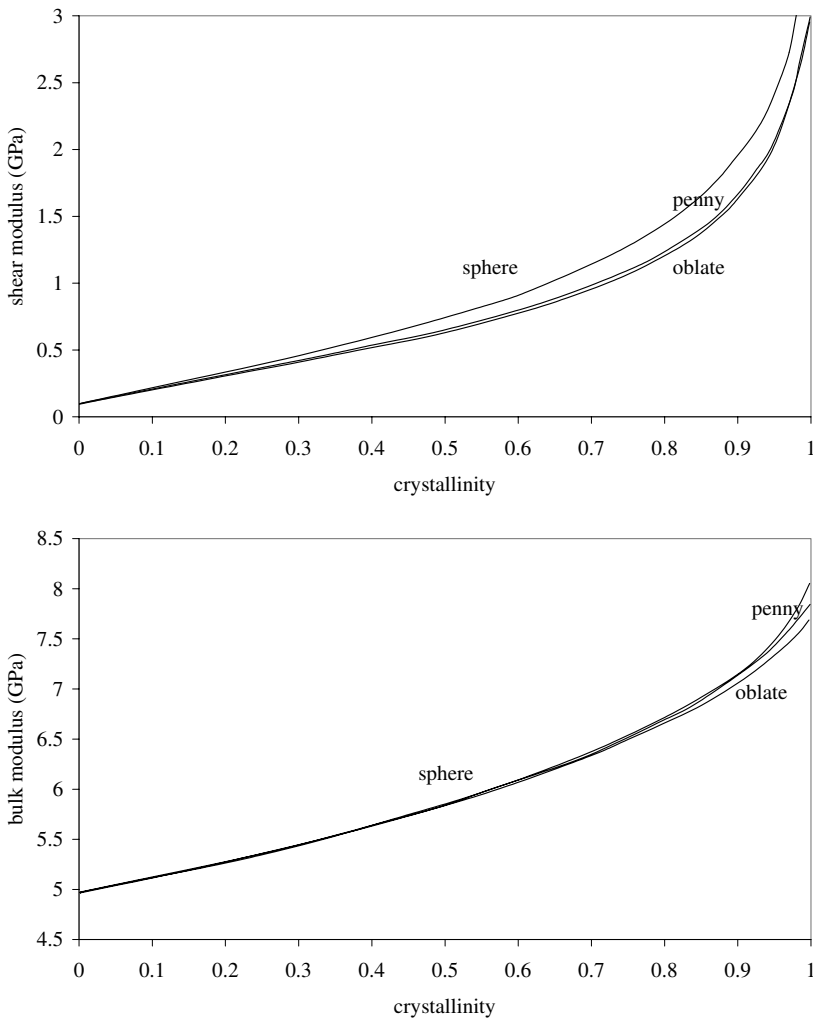
Figure 5. Shear modulus (top) and bulk modulus (bottom) for different inclusion shapes by the self-consistent model.

is related to the sound velocity as

$$E = v^2 \rho. \tag{39}$$

According to [Janzen 1992a; 1992b; 1997], the experimental results of Davidse et al. [1962] cannot be uncritically accepted because their measurements are about three times greater than those obtained from bending and tensile tests. Though this difference was attributed to larger deformations in the bending and tensile tests, the anomaly needs to looked into with a deeper perspective.

[Janzen 1992b] has compared values of the Young's modulus of polyethylene obtained from ultrasound techniques with those obtained from static compression tests. The ultrasound experimental data are from [Hartmann and Jarzynski 1974], while static compression results are taken from [Lagakos et al. 1986].

Experimental data from [Janzen 1992b] and [Davidse et al. 1962] are compared to our predicted results in Figure 6 for the Young's and shear moduli. These results show that the experimental results lie within the composite inclusion bounds.
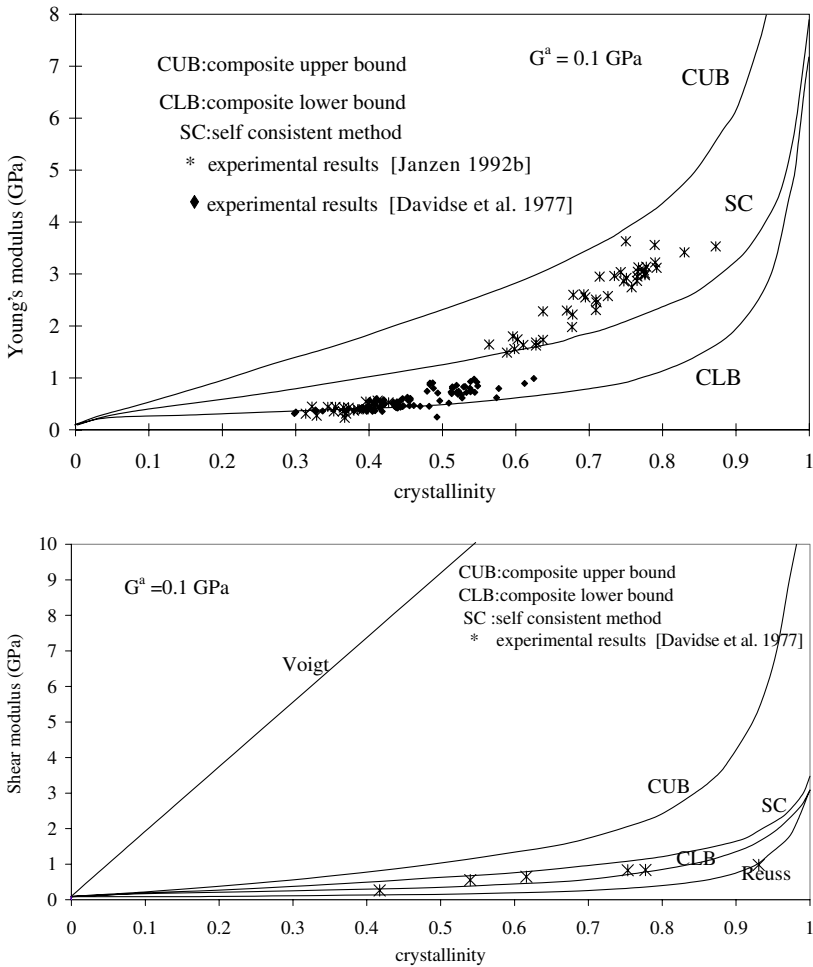
Figure 6. Predicted Young's modulus (left) and shear modulus (right) compared to experimental results of [Janzen 1992b; Davidse et al. 1962].

Conclusion

An averaging scheme for a semicrystalline polymeric material is developed to predict the evolution of the elastic properties function of the crystalline phase volume fraction. The proposed scheme is formulated so as to enforce the local equilibrium and compatibility conditions, which are violated partially by Voigt and Reuss estimates. The classical Voigt and Reuss averaging schemes, where the presence of both crystalline and amorphous phases is represented only by their relative volume fractions, results in far-apart estimates of the effective elastic properties, particularly for the high volume fraction of the crystalline phase. To develop new bounds, the problem of two-phase composite inclusion is considered, where the crystalline and amorphous domains of such a homogenized inclusion are subject to piecewise constant strains and stresses. The satisfaction of interface compatibility and traction equilibrium results in a softer inclusion stiffness, particularly in the crystallographic chain direction. Composite bounds, as well as a self-consistent averaging scheme are used to predict elastic properties of isotropic polyethylene. The composite approach resulted in much narrower difference between the new composite bounds compared to the classical ones. Comparison of predictions of the composite inclusion models with experimental data shows good agreement. We are working on other homogenization approaches for these materials.

An important shortcoming of the proposed modeling is related to the effects of molecular weight and molecular architecture that are ignored. Molecular weight is certainly an important factor that needs to be addressed. In our model, molecular weight is included in a very simple implicit way through the crystallinity and through the chosen values for the local properties. A way to extend the proposed model to include the effect of molecular weight would be to express the crystallinity and local properties as function of the molecular weight. In the modeling proposed here the effect of molecular architecture (that is, linear versus branched chains) cannot be accounted for in an explicit way since the local properties (inputs) are rather homogenized over a local volume. Only molecular simulations can directly account for the effect of molecular architecture. Thus, one way of resolving this would be to combine our modeling with molecular simulations. The latter can be used to compute the local properties as function of molecular architecture then use the results as input for our modeling. We note that for the crystalline phase, the input we used (the elastic properties of the crystalline phase), are those based on atomistic simulations. Here again, the atomistic simulations were conducted on a small volume, which represents only a fraction of the crystalline lamella. In our approach, we have simplified the problem by assuming that these atomistically computed properties are homogeneous within the entire crystalline lamella. Without these simplifying assumptions, no homogenization technique can be developed based on continuum mechanics.

Appendix A. Isotropic distribution

This appendix develops the inclusion average of the stiffness (or compliance), in the case of isotropic distribution of the aggregate such as in spherulitic morphology. If we consider θ, ϕ and Φ to be the Euler angles between the local coordinate system of inclusion and the global coordinate system, we can write the inclusion average of the stiffness (or compliance) as

$$\langle C^I_{ijkl} \rangle = \int_0^{2\pi} \int_0^{2\pi} \int_0^{\pi} a_{ii'}, a_{jj'}, a_{kk'}, a_{ll'}, C^I_{i'j'k'l'} \Phi \sin\theta \, d\theta \, d\phi \, d\psi, \tag{A1}$$

where $\Phi = 1/(8\pi^2)$ and the transform matrix components $a_{ij'}$ are given by

$a_{11'} = \cos\psi\cos\theta\cos\phi - \sin\psi\sin\phi,$ $a_{21'} = \cos\psi\cos\theta\sin\phi + \sin\psi\cos\phi,$ $a_{31'} = -\cos\psi\sin\theta,$

$a_{12'} = -\cos\psi\sin\phi - \sin\psi\cos\theta\cos\phi,$ $a_{22'} = -\sin\psi\cos\theta\sin\phi + \cos\psi\cos\phi,$ $a_{32'} = \sin\psi\sin\theta,$

$a_{13'} = \sin\theta\cos\phi,$ $a_{23'} = \sin\theta\sin\phi,$ $a_{33'} = \cos\theta.$

Carrying out this integration we get the following nonzero components of the symmetric effective stiffness tensor:

$$
\begin{aligned}
C^{\mathrm{eff}} &= \langle C^I \rangle, \\
C^{\mathrm{eff}}_{11} = C^{\mathrm{eff}}_{22} = C^{\mathrm{eff}}_{33} &= \tfrac{1}{15}\big(3(C^I_{11} + C^I_{22} + C^I_{33}) + 2(C^I_{12} + C^I_{13} + C^I_{23}) + 4(C^I_{44} + C^I_{55} + C^I_{66})\big), \\
C^{\mathrm{eff}}_{12} = C^{\mathrm{eff}}_{23} = C^{\mathrm{eff}}_{13} &= \tfrac{1}{15}\big((C^I_{11} + C^I_{22} + C^I_{33}) + 4(C^I_{12} + C^I_{13} + C^I_{23}) - 2(C^I_{44} + C^I_{55} + C^I_{66})\big), \\
C^{\mathrm{eff}}_{21} = C^{\mathrm{eff}}_{31} = C^{\mathrm{eff}}_{32} &= C^{\mathrm{eff}}_{12} \\
C^{\mathrm{eff}}_{44} = C^{\mathrm{eff}}_{55} = C^{\mathrm{eff}}_{66} &= \tfrac{1}{15}\big((C^I_{11} + C^I_{22} + C^I_{33}) - (C^I_{12} + C^I_{13} + C^I_{23}) + 3(C^I_{44} + C^I_{55} + C^I_{66})\big).
\end{aligned}
\tag{A2}
$$

Appendix B. Determination of phase concentration tensors

The phase concentration tensors relate the stress and strain of the phases to the inclusion stress as shown by Equations (10)–(13). We first determine the expression for the tensors $\boldsymbol{Q}^c$ and $\boldsymbol{Q}^a$. In this appendix, the Greek subscripts α and α' take the values 1, 2 and 6, and β and β' take the values 3, 4 and 5. The non-Greek subscripts take all integer values from 1 to 6.

Determination of $\boldsymbol{Q}^c$. The second relation in (13) may be written in component form as

$$
\varepsilon^c_i = Q^c_{ij}\varepsilon^I_j,
\tag{B1}
$$

where the index i and j both range from 1 to 6. For the index $\alpha = 1, 2,$ and 6 we can write this equation as

$$
\varepsilon^c_\alpha = Q^c_{\alpha j}\varepsilon^I_j.
\tag{B2}
$$

Using the compatibility condition as given by (9) we can write (B2) as

$$
\varepsilon^I_\alpha = Q^c_{\alpha j}\varepsilon^I_j.
\tag{B3}
$$

Now, when $j = \alpha$, $Q^c_{\alpha j}$ should be equal to identity and when $j \neq \alpha$, $Q^c_{\alpha j}$ should be zero, that is,

$$
Q^c_{\alpha j} = \delta_{\alpha j},
\tag{B4}
$$

where δ is the Kronecker delta symbol.

To determine the other components of $\boldsymbol{Q}^c$, that is, $Q_{\beta j}$, with $\beta = 3, 4, 5$ we need to consider the equilibrium condition $\sigma^c_\beta = \sigma^a_\beta$ represented by Equation (9). Inserting Hooke's law into this equation we obtain

$$
C^c_{\beta j}\varepsilon^c_j = C^a_{\beta j}\varepsilon^a_j.
\tag{B5}
$$

Equation (5) may be rewritten as

$$
\varepsilon^a_j = \frac{1}{f_a}\varepsilon^I_j - \frac{1-f_a}{f_a}\varepsilon^c_j.
\tag{B6}
$$

Substituting this in (B5) we obtain

$$\left(C_{\beta j}^c + \frac{1-f_a}{f_a} C_{\beta j}^a\right) \varepsilon_j^c = \frac{1}{f_a} C_{\beta j}^a \varepsilon_j^I. \tag{B7}$$

This equation can be split into components represented by indices α and β as

$$\left(C_{\beta\beta'}^c + \frac{1-f_a}{f_a} C_{\beta\beta'}^a\right) \varepsilon_{\beta'}^c + \left(C_{\beta\alpha}^c + \frac{1-f_a}{f_a} C_{\beta\alpha}^a\right) \varepsilon_\alpha^c = \frac{1}{f_a} C_{\beta j}^a \varepsilon_j^I, \tag{B8}$$

where β' takes the value 3, 4 and 5. Using the compatibility condition $\varepsilon_\alpha^c = \varepsilon_\alpha^I$ as given Equation (8), we obtain

$$\left(C_{\beta\beta'}^c + \frac{1-f_a}{f_a} C_{\beta\beta'}^a\right) \varepsilon_{\beta'}^c = \frac{1}{f_a} C_{\beta j}^a \varepsilon_j^I - \left(C_{\beta\alpha}^c + \frac{1-f_a}{f_a} C_{\beta\alpha}^a\right) \delta_{\alpha j} \varepsilon_j^I. \tag{B9}$$

This equation may be written in a more convenient form as

$$H_{\beta\beta'} \varepsilon_{\beta'}^c = K_{\beta j} \varepsilon_j^I, \tag{B10}$$

where

$$H_{\beta\beta'} = C_{\beta\beta'}^c + \frac{1-f_a}{f_a} C_{\beta\beta'}^a \tag{B11}$$

and

$$K_{\beta j} = \frac{1}{f_a} C_{\beta j}^a - \left(C_{\beta\alpha}^c + \frac{1-f_a}{f_a} C_{\beta\alpha}^a\right) \delta_{\alpha j}. \tag{B12}$$

From (B10) we get

$$\varepsilon_{\beta'}^c = H_{\beta\beta'}^{-1} K_{\beta j} \varepsilon_j^I. \tag{B13}$$

Comparing with (B1) we deduce

$$Q_{\beta j}^c = H_{\beta\beta'}^{-1} K_{\beta' j}. \tag{B14}$$

Finally, (B4) and (B14) define the tensor $\boldsymbol{Q}^c$ completely.

Determination of $\boldsymbol{Q}^a$. Equation (13) in indicial notation may be written as

$$\varepsilon_i^a = Q_{ij}^a \varepsilon_j^I \tag{B15}$$

again continuity condition (9) implies

$$Q_{\alpha j}^a = \delta_{\alpha j}. \tag{B16}$$

The other components of $Q_{\alpha j}^a$ ie. $Q_{\beta j}^a$ are obtained as follows. Substituting (B1) in (7) we obtain

$$\varepsilon_\beta^I = f_a \varepsilon_\beta^a + (1-f_a) Q_{\beta j}^c \varepsilon_j^I \tag{B17}$$

or

$$\varepsilon_\beta^a = \frac{1}{f_a} \left(\delta_{\beta j} + (1-f_a) Q_{\beta j}^c\right) \varepsilon_j^I; \tag{B18}$$

comparing this with (B15) we obtain

$$Q_{\beta j}^a = \frac{1}{f_a} \left(\delta_{\beta j} + (1-f_a) Q_{\beta j}^c\right). \tag{B19}$$

Therefore, (B16) and (B19) define the tensor $\boldsymbol{Q}^a$ completely. We now determine the phase concentration tensors $\boldsymbol{R}^c$ and $\boldsymbol{R}^a$.

Determination of $\boldsymbol{R}^c$. The second relation in (12) in indicial notation may be written as

$$\sigma_i^c = R_{ij}^c \sigma_i^I. \tag{B20}$$

For $\beta = 3, 4$, and 5 we can write

$$\sigma_\beta^c = R_{\beta j}^c \sigma_j^I. \tag{B21}$$

Using the equilibrium condition (11) leads to

$$R_{\beta j}^a = \delta_{\beta j}. \tag{B22}$$

The remaining components of $\boldsymbol{R}^a$ are determined by considering the compatibility conditions. Introducing Hooke's law into the compatibility equation $\varepsilon_\alpha^c = \varepsilon_\alpha^a$ as given by (10) we obtain

$$S_{\alpha j}^c \sigma_j^c = S_{\alpha j}^a \sigma_j^a. \tag{B23}$$

From (6) and (B23) we obtain

$$\left(S_{\alpha j}^c + \frac{1 - f_a}{f_a} S_{\alpha j}^a\right)\sigma_j^c = \frac{1}{f_a} S_{\alpha j}^a \sigma_j^I. \tag{B24}$$

Splitting this equation into components given by the indices α and β we obtain

$$\left(S_{\alpha\alpha'}^c + \frac{1 - f_a}{f_a} S_{\alpha\alpha'}^a\right)\sigma_{\alpha'}^c + \left(S_{\alpha\beta}^c + \frac{1 - f_a}{f_a} S_{\alpha\beta}^a\right)\sigma_\beta^c = \frac{1}{f_a} S_{\alpha j}^a \sigma_j^I, \tag{B25}$$

where α' takes the value 1, 2 and 6. Using the equilibrium relation $\sigma_\beta^c = \sigma_\beta^I$ as given by (11) we obtain

$$\left(S_{\alpha\alpha'}^c + \frac{1 - f_a}{f_a} S_{\alpha\alpha'}^a\right)\sigma_{\alpha'}^c = \frac{1}{f_a} S_{\alpha j}^a \sigma_j^I - \left(S_{\alpha\beta}^c + \frac{1 - f_a}{f_a} S_{\alpha\beta}^a\right)\delta_{\beta j}\sigma_j^I. \tag{B26}$$

This equation may be written in a more convenient form as

$$L_{\alpha\alpha'}\sigma_{\alpha'}^c = M_{\alpha j}\sigma_j^I, \tag{B27}$$

where

$$L_{\alpha\alpha'} = S_{\alpha\alpha'}^c + \frac{1 - f_a}{f_a} S_{\alpha\alpha'}^a, \tag{B28}$$

and

$$M_{\alpha j} = \frac{1}{f_a} S_{\alpha j}^a - \left(S_{\alpha\beta}^c + \frac{1 - f_a}{f_a} S_{\alpha\beta}^a\right)\delta_{\beta j}. \tag{B29}$$

Thus

$$\sigma_{\alpha'}^c = L_{\alpha\alpha'}^{-1} M_{\alpha j}\sigma_j^I. \tag{B30}$$

Comparing this with Equation (B20) gives

$$R_{\alpha j}^c = L_{\alpha\alpha'}^{-1} M_{\alpha' j}. \tag{B31}$$

Therefore, (B22) and (B31) define the tensor $\boldsymbol{R}^c$.

Determination of R^a. The first relation in (12) in indicial notation may be written as

$$\sigma_i^a = R_{ij}^a \sigma_j^I. \tag{B32}$$

The equilibrium condition (11) implies

$$R_{\beta j}^a = \delta_{\beta j}. \tag{B33}$$

The other components of R_{ij}^a, that is, $R_{\beta j}^a$ are obtained as follows. Substituting (B32) in (6) we obtain

$$\sigma_\beta^I = f_a \sigma_\beta^a + (1 - f_a) R_{\beta j}^c \sigma_j^I, \tag{B34}$$

or

$$\sigma_\beta^a = \frac{1}{f_a} \big(\delta_{\beta j} - (1 - f_a) R_{\beta j}^c \big) \sigma_j^I. \tag{B35}$$

Comparing this with (B32) we obtain

$$R_{\beta j}^a = \frac{1}{f_a} \big(\delta_{\beta j} - (1 - f_a) R_{\beta j}^c \big). \tag{B36}$$

Equations (B33) and (B36) define the tensor $\boldsymbol{R}^a$ completely.

Appendix C. Self-consistent model

In this appendix we develop the self consistent approach applied to semicrystalline polymers. This approach is based on the self-consistent scheme developed in [Zeller and Dederichs 1973] for the elastic properties of polycrystals. Here, we assume small elastic deformations, and that the components of the strain field, ε_{ij}, are defined as the symmetric part of the displacement gradient:

$$\varepsilon_{ij} = \tfrac{1}{2}(u_{i,j} + u_{j,i}) \tag{C1}$$

with

$$u_{i,j} = \frac{\partial u_i}{\partial r_j}, \tag{C2}$$

where the u_i are the components of the displacement vector and the r_j the components of the spatial position vector $\boldsymbol{r}$.

In an elastic material, the stress field is in general dependent on the spatial position $\boldsymbol{r}$, and is related to the strain field ε_{ij} through a local Hooke's law

$$\sigma_{ij} = C_{ijkl}\varepsilon_{kl} \equiv C_{ijkl} u_{k,l}. \tag{C3}$$

The elastic constants are statistically fluctuating quantities which can be decomposed into a sum of a constant part, C_{ijkl}^0, and a fluctuating part, $\tilde{C}_{ijkl}(r)$

$$C_{ijkl} = C_{ijkl}^0 + \tilde{C}_{ijkl}. \tag{C4}$$

The macroscopic homogeneous material is subject to a stress field $\bar{\sigma}_{ij}$, and a corresponding strain field $\bar{\varepsilon}_{ij}$. The elastic constants C_{ijkl}^0 used in the decomposition can be taken as equal to those of the homogeneous equivalent medium, as

$$C_{ijkl}^0 = C_{ijkl}^{\text{eff}}. \tag{C5}$$

The problem consists of finding a solution for the local strain or stress fields as a function of the macroscopic fields. We start by writing the equilibrium

$$\sigma_{ij,j} = C^{\text{eff}}_{ijkl} u_{k,lj} + (\tilde{C}_{ijkl} u_{k,l})_{,j} = 0. \tag{C6}$$

The solution of the Navier equation given by (C6), for given surface displacements $\bar{u}^*_i$, can be written as

$$u_i(\boldsymbol{r}) = \bar{u}^*_i(\boldsymbol{r}) + \int_V G_{ik}(\boldsymbol{r}, \boldsymbol{r}') \big[\tilde{C}_{klmn}(\boldsymbol{r}') u_{m,n}(\boldsymbol{r}')\big]_{,l'} d\boldsymbol{r}', \tag{C7}$$

where V is the volume of the entire aggregate and $G_{kl}(\boldsymbol{r}, \boldsymbol{r}')$ are the components of a Green tensor which satisfies the equilibrium relation

$$C^{\text{eff}}_{ijkl} G_{km,lj}(\boldsymbol{r}, \boldsymbol{r}') + \delta_{im} \delta(\boldsymbol{r} - \boldsymbol{r}') = 0. \tag{C8}$$

It is convenient to assume an infinite medium. This assumption implies the following properties:

$$G_{ij}(\boldsymbol{r}, \boldsymbol{r}') = G_{ij}(\boldsymbol{r} - \boldsymbol{r}') \tag{C9}$$

$$G_{ij,l'} = -G_{ij,l}. \tag{C10}$$

Note that indexes with a prime symbol are relative to $\boldsymbol{r}'$.

By partial integration and subsequent differentiation of (C7) we obtain an integral equation for the local strain tensor

$$\varepsilon_{ij}(\boldsymbol{r}) = \bar{\varepsilon}^*_{ij} + \int_V g_{ijkl}(\boldsymbol{r}, \boldsymbol{r}') \tilde{C}_{klmn}(\boldsymbol{r}') \, \varepsilon_{mn}(\boldsymbol{r}') d^3\boldsymbol{r}', \tag{C11}$$

where

$$g_{ijkl} = \tfrac{1}{4}(G_{ik,jl} + G_{jk,il} + G_{il,jk} + G_{jl,ik}). \tag{C12}$$

We are now looking for an approximate solution of the integral equation (C11). For this, we make use of the Eshelby's solution and proof [1957] of the uniformity of the strain field within an ellipsoidal inclusion embedded in a linear matrix. Our material is represented by N inclusions, and the strain of each of them can be taken as

$$\varepsilon^I_{ij} = \frac{1}{V_I} \int_{V_I} \varepsilon_{ij}(\boldsymbol{r}) d^3\boldsymbol{r}, \tag{C13}$$

where V_I is the volume of the inclusion I. Since the strain is uniform within each inclusion, we have

$$\varepsilon_{ij}(\boldsymbol{r}) = \sum_{I=1}^N \varepsilon^I_{ij} \Delta_I(\boldsymbol{r}), \qquad C_{ijkl}(\boldsymbol{r}) = \sum_{I=1}^N C^I_{ijkl} \Delta_I(\boldsymbol{r}), \qquad \tilde{C}_{ijkl}(\boldsymbol{r}) = \sum_{I=1}^N \tilde{C}^I_{ijkl} \Delta_I(\boldsymbol{r}). \tag{C14}$$

Here, Δ_I is the characteristic function of the inclusion I. It has unit value if $\boldsymbol{r}$ falls within V_I and zero value if not.

If we insert (C13) and (C14) into (C11) and neglect the inclusion-inclusion interaction terms [Molinari et al. 1987], the integral equation (C11) is then approximated by

$$\varepsilon^I_{ij} = \bar{\varepsilon}^{*I}_{ij} + \Gamma_{ijkl} \tilde{C}^I_{klmn} \varepsilon^I_{mn}. \tag{C15}$$

The matrix-inclusion interaction tensor Γ is given by

$$\Gamma_{ijkl} = \frac{1}{V_I} \int_{V_I} \int_{V_I} g_{ijkl} d^3\boldsymbol{r} d^3\boldsymbol{r}'. \tag{C16}$$

Note that the Eshelby tensor is defined as $E_{ijkl} = -\Gamma_{ijmn} C_{mnkl}^{\text{eff}}$.

Finally, a rearrangement of (C15) leads to

$$\varepsilon_{ij}^I = B_{ijkl}^I \bar{\varepsilon}_{kl}^*, \tag{C17}$$

with

$$B_{ijkl}^I = \left[I_{ijkl} - \Gamma_{ijmn} \tilde{C}_{mnkl}^I \right]^{-1}. \tag{C18}$$

At this point, the macroscopic strain $\bar{\boldsymbol{\varepsilon}}^*$ is not specified. The consistency condition requires that the average of local (inclusion) strains should equal the macroscopically imposed strain. If all inclusions of the aggregate have parallel principal axes, this condition is easily met, which also implies that $\bar{\varepsilon}^*$ is exactly the macroscopically imposed strain. However, if the principal axes of the inclusions are not parallel, the consistency condition needs to be enforced using a normalization procedure. For this, we denote by $\bar{\boldsymbol{\varepsilon}}$ the macroscopically imposed strain and assume the relation

$$\bar{\boldsymbol{\varepsilon}}^* = \boldsymbol{K}\bar{\varepsilon}, \tag{C19}$$

where the fourth order tensor K is uniform. If we insert (C19) into (C17) we obtain

$$\langle \boldsymbol{\varepsilon}^I \rangle = \langle \boldsymbol{B}^I \rangle \boldsymbol{K}\bar{\varepsilon}. \tag{C20}$$

Therefore, the consistency condition leads to

$$\boldsymbol{K} = \langle \boldsymbol{B}^I \rangle^{-1}. \tag{C21}$$

The final expression of the interaction law (C17) is given by

$$\boldsymbol{\varepsilon}^I = \boldsymbol{B}^I \langle \boldsymbol{B}^I \rangle^{-1} \bar{\boldsymbol{\varepsilon}}. \tag{C22}$$

Now, if we insert Hooke's law into (C17), a dual interaction law that expresses the inclusion stress $\boldsymbol{\sigma}^I$ as a function of the macroscopic one, $\bar{\sigma}$ can be obtained as

$$\sigma_{ij}^I = A_{ijkl}^I \bar{\sigma}_{kl}, \tag{C23}$$

with

$$A^I = C^I B^I \langle B^I \rangle^{-1} (C^{\text{eff}})^{-1}. \tag{C24}$$

By averaging Equations (C23) and using the estimate given by (36) with relation (C24), one can easily show that $\langle \boldsymbol{A}^I \rangle = \boldsymbol{I}$.

To compute the interaction tensor $\boldsymbol{\Gamma}$ we use the Fourier transform method. Details of the computations may be found in [Ghahremani 1977] and [Gavazzi and Lagoudas 1990].

References

[Aboutajeddine and Neale 2005] A. Aboutajeddine and K. W. Neale, "The double-inclusion model: a new formulation and new estimates", *Mech. Mater.* **37**:2–3 (2005), 331–341.

[Addiego et al. 2006] F. Addiego, A. Dahoun, C. G'Sell, and J. M. Hiver, "Characterization of volume strain at large deformation under uniaxial tension in high-density polyethylene", *Polymer* **47**:12 (2006), 4387–4399.

[Ahzi et al. 1990] S. Ahzi, D. M. Parks, and A. S. Argon, "Modeling of plastic deformation and evolution of anisotropy in semi-crystalline polymers", pp. 287–292 in *Computer modeling and simulation of manufacturing processes: presented at the Winter Annual Meeting of the ASME* (Dallas, TX), edited by B. Singh, ASME, New York, 1990.

[Ahzi et al. 1995] S. Ahzi, D. Parks, and A. Argon, "Estimates of the overall elastic properties in semi-crystalline polymers", pp. 31–44 in *Current research in the thermo-mechanics of polymers in the rubbery-glassy range* (Los Angeles), edited by M. Negahban, Applied Materials Division **203**, ASME, New York, 1995.

[Barham and Arridge 1977] P. J. Barham and R. G. C. Arridge, "Fiber composite model of highly oriented polyethylene", *J. Polym. Sci. B Polym. Phys.* **15**:7 (1977), 1177–1188.

[Benveniste 1987] Y. Benveniste, "A new approach to the application of Mori–Tanaka's theory in composite materials", *Mech. Mater.* **6**:2 (1987), 147–157.

[Berlyand and Kozlov 1992] L. V. Berlyand and S. M. Kozlov, "Asymptotics of the homogenized moduli for the elastic chessboard composite", *Arch. Ration. Mech. An.* **118**:2 (1992), 95–112.

[Berlyand and Promislow 1995] L. V. Berlyand and K. Promislow, "Effective elastic moduli of soft medium with hard polygonal inclusions and external behavior of effective Poisson's ratio", *J. Elasticity* **40**:1 (1995), 45–73.

[Capaccio et al. 1976] G. Capaccio, T. A. Crompton, and I. M. Ward, "The drawing behavior of linear polyethylene, I: Rate of drawing as a function of polymer molecular weight and initial thermal treatment", *J. Polym. Sci. B Polym. Phys.* **14**:9 (1976), 1641–1658.

[Davidse et al. 1962] P. D. Davidse, H. I. Waterman, and J. B. Westerdijk, "Sound velocity and Young's modulus in polyethylene", *J. Polym. Sci.* **59** (1962), 389–400.

[Eshelby 1957] J. D. Eshelby, "The determination of the elastic field of an ellipsoidal inclusion, and related problems", *Proc. R. Soc. A* **241**:1226 (1957), 376–396.

[Flory 1969] P. J. Flory, *Statistical mechanics of chain molecules*, Oxford University Press, New York, 1969.

[Gavazzi and Lagoudas 1990] A. C. Gavazzi and D. C. Lagoudas, "On the numerical evaluation of the Eshelby's tensor and its application to elastoplastic fibrous composites", *Comput. Mech.* **7**:1 (1990), 13–19.

[Ghahremani 1977] F. Ghahremani, "Numerical evaluation of the stresses and strains in ellipsoidal inclusions in an anisotropic elastic material", *Mech. Res. Commun.* **4**:2 (1977), 89–91.

[Gray and McCrum 1969] R. W. Gray and N. G. McCrum, "Origin of the γ relaxations in polyethylene and polytetrafluoroethylene", *J. Polym. Sci.* **7**:8 (1969), 1329–1355.

[Hartmann and Jarzynski 1974] B. Hartmann and J. Jarzynski, "Immersion apparatus for ultrasonic measurements in polymers", *J. Acoust. Soc. Am.* **56**:5 (1974), 1469–1477.

[Hashin and Shtrikman 1963] Z. Hashin and S. Shtrikman, "A variational approach to the theory of the elastic behaviour of multiphase materials", *J. Mech. Phys. Solids* **11**:2 (1963), 127–140.

[Hermans 1967] J. J. Hermans, "The elastic properties of fiber-reinforced materials when the fibers are aligned", *P. K. Ned. Akad. Wetensc.* **B70** (1967), 1–9.

[Hill 1964] R. Hill, "Theory of mechanical properties of fibre-strengthened materials, I: Elastic behaviour", *J. Mech. Phys. Solids* **12**:4 (1964), 199–212.

[Hill 1965] R. Hill, "Theory of mechanical properties of fibre-strengthened materials, III: Self-consistent model", *J. Mech. Phys. Solids* **13**:4 (1965), 189–198.

[Hori and Nemat-Nasser 1993] M. Hori and S. Nemat-Nasser, "Double-inclusion and overall moduli of multi-phase composites", *Mech. Mater.* **14**:3 (1993), 189–206.

[Hu and Weng 2000] G. K. Hu and G. J. Weng, "The connections between the double-inclusion model and the Ponte Castaneda–Willis, Mori–Tanaka, and Kluster–Toksoz models", *Mech. Mater.* **32**:8 (2000), 495–503.

[Janzen 1992a] J. Janzen, "Crystalline elastic constants and macroscopic moduli of isotropic semi-crystalline polyethylene", *Polym. Eng. Sci.* **32**:17 (1992), 1255–1260.

[Janzen 1992b] J. Janzen, "Elastic moduli of semi-crystalline polyethylene compared with theoretical micromechanical models for composites", *Polym. Eng. Sci.* **32**:17 (1992), 1242–1254.

[Janzen 1997] J. Janzen, "Further refinement of the self-consistent model for the dependence of polyethylene elastic constants upon density", Paper presented at the ACS "Advances in Polyolefins" workshop (Napa Valley, CA), 1997.

[Jefferson et al. 2005] G. Jefferson, H. Garmestani, R. Tannenbaum, A. Gokhale, and E. Tadd, "Two-point probability distribution function analysis of co-polymer nano-composites", *Int. J. Plast.* **21**:1 (2005), 185–198.

[Jordens et al. 2000] K. Jordens, G. L. Wiles, J. Janzen, D. C. Rohlfing, and M. B. Welch, "The influence of molecular weight and thermal history on the thermal, rheological, and mechanical properties of metallocene catalyzed linear polyethylenes", *Polymer* **41**:19 (2000), 7175–7192.

[Lagakos et al. 1986] N. Lagakos, J. Jarzynski, J. B. Cole, and J. A. Bucaro, "Frequency and temperature dependence of elastic moduli of polymers", *J. Appl. Phys.* **59**:12 (1986), 4017–4031.

[de Langen et al. 2000] M. de Langen, H. Luigjes, and K. O. Prins, "High pressure NMR study of chain dynamics in orthorhombic phase of polyethylene", *Polymer* **41**:3 (2000), 1183–1191.

[Lee et al. 1993] B. J. Lee, D. M. Parks, and S. Ahzi, "Micromechanical modeling of large plastic deformation and texture evolution in semi-crystalline polymers", *J. Mech. Phys. Solids* **41**:10 (1993), 1651–1687.

[Lin and Garmestani 2000] S. Lin and H. Garmestani, "Statistical continuum mechanics analysis of an elastic two-isotropic-phase composite material", *Compos. B Eng.* **31**:1 (2000), 39–46.

[Molinari et al. 1987] A. Molinari, G. Canova, and S. Ahzi, "A self-consistent approach of the large deformation polycristal viscoplasticity", *Acta Metall.* **35**:12 (1987), 2983–2994.

[Mori and Tanaka 1973] T. Mori and K. Tanaka, "Average stress in matrix and average elastic energy of materials with misfitting inclusions", *Acta Metall.* **21**:5 (1973), 571–574.

[Nakayama et al. 1991] K. Nakayama, A. Furumiya, T. Okamoto, K. Yagi, A. Kaito, C. R. Choe, L. Wu, G. Zhang, L. Xiu, D. Liu, T. Masuda, and A. Nakajima, "Structure and mechanical propreties of ultra-high molecular weight polyethylene deformed near melting temperature", *Pure Appl. Chem.* **63** (1991), 1793–1804.

[Ponte Castaneda and Willis 1995] P. Ponte Castaneda and J. R. Willis, "The effect of spatial distribution on the effective behaviour of composite materials and cracked media", *J. Mech. Phys. Solids* **43**:12 (1995), 1919–1951.

[Takayanagi et al. 1966] M. Takayanagi, K. Imada, and T. Kajiyama, "Mechanical properties and fine structure of drawn polymers", *J. Polym. Sci. C Pol. Sym.* **15** (1966), 263–281.

[Wang 1973] T. T. Wang, "Morphology and mechanical properties of crystalline polymers, I: Transcrystalline polyethylene", *J. Appl. Phys.* **44**:5 (1973), 2218–2224.

[Ward 1985] I. M. Ward, *Mechanical properties of solid polymers*, Wiley, New York, 1985.

[Zehnder et al. 1996] M. M. Zehnder, A. A. Gusev, and U. W. Suter, "Predicting and understanding the elastic properties of polymers using atomistic simulation", *Rev. I. Fr. Petrol.* **51** (1996), 131–137.

[Zeller and Dederichs 1973] R. Zeller and P. H. Dederichs, "Elastic constants of polycrystals: basic research", *Phys. Status Solidi B* **55** (1973), 831–842.

SAID AHZI: ahzi@imfs.u-strasbg.fr
University Louis Pasteur, Institute of Fluid and Solid Mechanics, UMR 7507, 2 Rue Boussingault, 67000 Strasbourg, France

NADIA BAHLOULI: bahlouli@imsf.u-strasbg.fr
University Louis Pasteur, Institute of Fluid and Solid Mechanics, UMR 7507, 2 Rue Boussingault, 67000 Strasbourg, France

AHMED MAKRADI: makradi@imfs.u-strasbg.fr
University Louis Pasteur, Institute of Fluid and Solid Mechanics, UMR 7507, 2 Rue Boussingault, 67000 Strasbourg, France

SALIM BELOUETTAR: salim.belouettar
LTI, Research Center Henry Tudor, 70 Rue de Luxembourg, L-4221 Esch-sur-Alzette, Luxembourg

DISLOCATION INTERACTING WITH COLLINEAR RIGID LINES IN PIEZOELECTRIC MEDIA

BINGJIN CHEN, DONGWEI SHU AND ZHONGMIN XIAO

The electro-elastic interaction between a piezoelectric dislocation and collinear rigid lines embedded in a piezoelectric medium is studied in the framework of linear elastic theory. The rigid lines are considered, respectively, as dielectrics or conductors. We present a general solution of the problem based on the extended Stroh's formalism. Explicit expressions of the field intensity factors are obtained for the special case of a single rigid line. The image force acting on the piezoelectric dislocation due to the presence of a single rigid line is calculated by using the generalized Peach-Koehler formula. Numerical examples show the shielding effects of field intensity factors and image force on the dislocation. The solution we present can be served as a Green's function for investigating the micro-crack initiation mechanism at the tip of a rigid line.

1. Introduction

Piezoelectric materials are widely used in devices such as sensors and actuators. When subjected to mechanical and electric loads, these piezoelectric materials can fail prematurely due to defects arising in the manufacturing process. It is therefore important to study how defects such as dislocations and inclusions disturb the field variables, and how stress concentration arises as a result of defects. When a flat inclusion is much harder than the matrix, it is reasonable to consider it as a rigid line. There are numerous contributions to the literature on electro-elastic coupling characteristics of piezoelectric composite materials. To name a few, Pak [1992a] studied the anti-plane problem of a piezoelectric circular inclusion; Meguid and Zhong [1997] provided a general solution for the elliptical inhomogeneity problem in piezoelectric material under anti-plane shear and an in-plane electric field; Kattis et al. [1998] investigated the electro-elastic interaction effects of a piezoelectric screw dislocation with circular inclusion in piezoelectric material; Deng and Meguid [1998; 1999] considered the interaction between the piezoelectric elliptical inhomogeneity and a screw dislocation located inside inhomogeneity and outside inhomogeneity respectively under anti-plane shear and an in-plane electric field. More recently, Huang and Kuang [2001] evaluated the generalized electro-mechanical force for dislocation located inside, outside and on the interface of elliptical inhomogeneity in an infinite piezoelectric medium.

For rigid line problems in piezoelectric media, Liang et al. [1995] derived an exact general solution for an infinite piezoelectric medium with a rigid line and a crack. Shi [1997] investigated the collinear rigid lines under anti-plane deformation and in-plane electric field in piezoelectric media. Deng and Meguid [1998] addressed the plane problem of an interfacial rigid line between dissimilar piezoelectric materials. Gao and Fan [2000] investigated the generalized plane problem of piezoelectric media with collinear rigid lines under the loads at infinity. Chen et al. [2002] studied the problem of a screw dislocation

---

Keywords: rigid lines, dislocation, piezoelectric, field intensity factors, force on dislocation.

near a semi-infinite rigid line in a piezoelectric solid. More recently, Liu and Fang [2003] dealt with the interaction problem of a piezoelectric screw dislocation with circular interfacial rigid lines.

In the present work, we address the plane problem of a dislocation interacting with collinear rigid lines in piezoelectric media. Following this brief introduction, in Section 2 we outline the basic theory of the Stroh formalism. In Section 3 we state the problem to be investigated. We solve the problem of dielectric lines in Section 4 and that of conducting lines in Section 5. We present numerical examplesin Section 6, and concluding remarks in Section 7.

2. The Stroh formalism

In fixed rectangular coordinates x_i ($i = 1, 2, 3$), the basic equations for linear piezoelectric materials at constant temperature can be written as

$$\sigma_{ij,j} = 0, \tag{2–1}$$

$$D_{i,i} = 0, \tag{2–2}$$

$$\gamma_{ij} = \tfrac{1}{2}(u_{i,j} + u_{j,i}), \tag{2–3}$$

$$E_i = -\phi_{,i}, \tag{2–4}$$

$$\sigma_{ij} = c_{ijkl}\gamma_{kl} - e_{kij}E_k, \tag{2–5}$$

$$D_i = e_{ikl}\gamma_{kl} + \varepsilon_{ik}E_k, \tag{2–6}$$

where σ_{ij}, γ_{ij}, u_i, D_i, E_i, ϕ are stress, strain, mechanical displacement, electric displacement, electric field and electric potential, respectively. c_{ijkl}, e_{kij} and ε_{ij} are the corresponding elastic, piezoelectric and dielectric constants, respectively, which satisfy the symmetric relations

$$c_{ijkl} = c_{klij} = c_{ijlk} = c_{jikl}, \qquad e_{kij} = e_{kji}, \qquad \varepsilon_{ik} = \varepsilon_{ki}, \tag{2–7}$$

where $i, j, k, l = 1, 2, 3$, repeated Latin indices mean summation, and a comma stands for partial differentiation.

Substitution of (2–3) and (2–4) into (2–5) and (2–6) yields

$$\sigma_{ij} = c_{ijkl}u_{k,l} + e_{kij}\phi_{,k}, \tag{2–8}$$

$$D_i = e_{ikl}u_{k,l} - \varepsilon_{ik}\phi_{,k}. \tag{2–9}$$

Furthermore, substituting (2–8) and (2–9) into (2–1) and (2–2) results in

$$(c_{ijkl}u_k + e_{lij}\phi)_{,li} = 0, \tag{2–10}$$

$$(e_{ikl}u_k - \varepsilon_{il}\phi)_{,li} = 0. \tag{2–11}$$

Here we only address a generalized two-dimensional deformation problem in the (x_1, x_2) plane. Therefore all the variables are constant along the x_3 axis. For such two-dimensional deformations where the physical quantities only depend on the coordinates x_1 and x_2, the general displacement solution to the above equations is

$$\boldsymbol{u} = \left\{u_1\ u_2\ u_3\ u_4\right\}^T = \boldsymbol{a}f(z), \quad z = x_1 + px_2, \tag{2–12}$$

or

$$u_k = a_k f(z), \quad k = 1, 2, 3, 4, \tag{2–13}$$

where $u_4 = \phi$ is the electric displacement, p and a are constants to be determined, and $f(z)$ is an arbitrary function of z. Substituting (2–12) into (2–10) and (2–11) yields

$$\left(c_{1jk1} + p(c_{2jk1} + c_{1jk2}) + p^2 c_{2jk2}\right)a_k + \left(e_{1j1} + p(e_{1j2} + e_{2j1}) + p^2 e_{2j2}\right)a_4 = 0, \tag{2–14}$$

$$\left(e_{1k1} + p(e_{1k2} + e_{2k1}) + p^2 e_{2k2}\right)a_k - \left(\varepsilon_{11} + p(\varepsilon_{12} + \varepsilon_{21}) + p^2 \varepsilon_{22}\right)a_4 = 0, \tag{2–15}$$

where $k = 1, 2, 3$. In view of (2–7), these equations can be rewritten as

$$\left(\boldsymbol{Q} + p(\boldsymbol{R} + \boldsymbol{R}^T) + p^2 \boldsymbol{T}\right)\boldsymbol{a} = 0, \tag{2–16}$$

where

$$Q_{ik} = c_{i1k1}, \qquad R_{ik} = c_{i1k2}, \qquad T_{ik} = c_{i2k2}. \tag{2–17}$$

The stresses and electric displacements can be expressed as

$$\sigma_{ij} = \left((c_{ijk1} + pc_{ijk2})a_k + (e_{1ji} + pe_{2ji})a_4\right)f'(z), \tag{2–18}$$
$$D_i = \left((e_{ik1} + pe_{ik2})a_k - (\varepsilon_{1i} + p\varepsilon_{2i})a_4\right)f'(z), \tag{2–19}$$

or

$$\{\sigma_{2j}, D_2\}^T = (\boldsymbol{R}^T + p\boldsymbol{T})\boldsymbol{a} f'(z), \qquad \{\sigma_{1j}, D_1\}^T = (\boldsymbol{Q} + p\boldsymbol{R})\boldsymbol{a} f'(z). \tag{2–20}$$

Defining

$$\boldsymbol{b} = (\boldsymbol{R}^T + p\boldsymbol{T})\boldsymbol{a}, \tag{2–21}$$

and comparing it with (2–16), we get

$$\boldsymbol{b} = (\boldsymbol{R}^T + p\boldsymbol{T})\boldsymbol{a} = -\frac{1}{p}(\boldsymbol{Q} + p\boldsymbol{R})\boldsymbol{a}. \tag{2–22}$$

By introducing the additional solution

$$\boldsymbol{\Phi} = \boldsymbol{b} f(z), \tag{2–23}$$

then (2–20) can be expressed as

$$\{\sigma_{2j}, D_2\}^T = \boldsymbol{\Phi}_{,1}, \qquad \{\sigma_{1j}, D_1\}^T = -\boldsymbol{\Phi}_{,2}. \tag{2–24}$$

The eigenvalue problem (2–16) gives four pairs of complex conjugates and corresponding vectors. p_α ($\alpha = 1, 2, 3, 4$) as the eigenvalues with positive imaginary part, and $\boldsymbol{a}_\alpha$ and $\boldsymbol{b}_\alpha$ as the associated vectors, we can write

$$p_{\alpha+4} = \bar{p}_\alpha, \qquad \boldsymbol{a}_{\alpha+4} = \bar{\boldsymbol{a}}_\alpha, \qquad \boldsymbol{b}_{\alpha+4} = \bar{\boldsymbol{b}}_\alpha, \tag{2–25}$$

where the over-bar denotes the complex conjugate. Assuming that p_α are distinct, the general solution can be written as

$$u = \sum_{\alpha=1}^{4} \left(a_\alpha f_\alpha(z_\alpha) + \bar{a}_\alpha f_{\alpha+4}(\bar{z}_\alpha) \right), \tag{2–26}$$

$$\Phi = \sum_{\alpha=1}^{4} \left(b_\alpha f_\alpha(z_\alpha) + \bar{b}_\alpha f_{\alpha+4}(\bar{z}_\alpha) \right), \tag{2–27}$$

where $z_\alpha = x_1 + p_\alpha x_2$ and f_l ($l = 1, 2, 3, 4, 5, 6, 7, 8$) are arbitrary functions to be determined according to the boundary conditions. In many applications they could be assumed to have the same function form

$$f_\alpha(z_\alpha) = q_\alpha f(z_\alpha), \qquad f_{\alpha+4}(\bar{z}_\alpha) = \bar{q}_\alpha \bar{f}(\bar{z}_\alpha), \tag{2–28}$$

where q_α are constants to be determined, and $\bar{f}(\bar{z}_\alpha)$ is the conjugate complex of $f(z_\alpha)$. Defining two 4×4 complex matrices

$$A = \begin{bmatrix} a_1 & a_2 & a_3 & a_4 \end{bmatrix}, \tag{2–29}$$

$$B = \begin{bmatrix} b_1 & b_2 & b_3 & b_4 \end{bmatrix}, \tag{2–30}$$

Equations (2–26) and (2–27) can be written as

$$u = Af(z) + \overline{Af}(\bar{z}), \tag{2–31}$$

$$\Phi = Bf(z) + \overline{Bf}(\bar{z}), \tag{2–32}$$

where

$$f(z) = \langle f(z_\alpha) \rangle q, \tag{2–33}$$

with

$$\langle f(z_\alpha) \rangle = \mathrm{diag}\left[f(z_1), f(z_2), f(z_3), f(z_4) \right], \tag{2–34}$$

$$q = \{q_1, q_2, q_3, q_4\}^T. \tag{2–35}$$

With the help of (2–22), the eigenvalue problem (2–16) can be expressed in a standard form as

$$\begin{bmatrix} -T^{-1}R^T & T^{-1} \\ RT^{-1}R^T - Q & -RT^{-1} \end{bmatrix} \begin{bmatrix} a \\ b \end{bmatrix} = p \begin{bmatrix} a \\ b \end{bmatrix}, \tag{2–36}$$

The A and B expressed in (2–29) and (2–30) satisfy the normalized orthogonality relation

$$\begin{bmatrix} B^T & A^T \\ \bar{B}^T & \bar{A}^T \end{bmatrix} \begin{bmatrix} A & \bar{A} \\ B & \bar{B} \end{bmatrix} = \begin{bmatrix} I & 0 \\ 0 & I \end{bmatrix}, \tag{2–37}$$

from which three real 4×4 matrices can be defined

$$S = i(2AB^T - I), \qquad H = 2iAA^T, \qquad L = -2iBB^T, \tag{2–38}$$

where, I is the 4×4 identity matrix and $i = \sqrt{-1}$. It is easy to show that

$$HL - SS = LH - S^T S^T = I, \qquad LS + S^T T = SH + HS^T = 0. \tag{2–39}$$

For a dislocation $d = [d_1, d_2, d_3, d_4]$ located at z_d in an infinite homogenous material, the vector q and the functions $f(z_\alpha)$ in (2–33) can be written as

$$q = \frac{1}{2\pi i} B^T d, \qquad f(z_\alpha) = \ln(z_\alpha - z_{d\alpha}). \tag{2–40}$$

Differentiating (2–31) and (2–32) with x_1, we obtain

$$u_{,1} = AF(z) + \overline{A}\overline{F}(\bar{z}), \tag{2–41}$$

$$\Phi_{,1} = BF(z) + \overline{B}\overline{F}(\bar{z}) = iMAF(z) - i\overline{MA}\overline{F}(\bar{z}), \tag{2–42}$$

where

$$F(z) = df(z)/dz, \tag{2–43}$$

$$M = -iBA^{-1} = H^{-1} + iH^{-1}S. \tag{2–44}$$

3. Statement of the problem

The physical problem to be investigated is shown in Figure 1. A charged dislocation $d = [d_1, d_2, d_3, d_4]$ is located at the point $z_d(r_d, \theta_d)$ near some rigid lines L_r ($r = 1, 2, \ldots, N$) embedded in an infinite piezoelectric medium. The rigid lines are assumed to be collinearly located along the x_1-axis of a Cartesian coordinate system $x_1 x_2 x_3$. The dislocation is assumed to be straight and infinitely long in the x_3-direction, suffering a finite discontinuity in the displacement and electric potential across the slip plane. Assume that the deformations of the solid depend on x_1 and x_2 only.

The mechanical boundary conditions at any rigid line surface are

$$u_j(t)^+ = u_j(t)^- = u_{j0} + w_r x_1 \delta_{j2}, \quad j = 1, 2, 3, \ t \in L_r, \tag{3–1}$$

where the superscript "+" and "−" refer, respectively, to the upper and lower rigid line surfaces, u_{j0} are displacements of the inclusions, w_r is the counterclockwise rotation with respect to the x_3 axis, and δ_{j2} is the Kronecker coefficient.
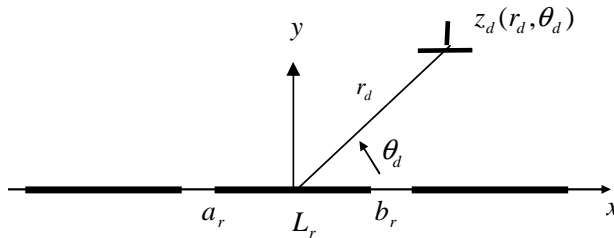
Figure 1. A piezoelectric screw dislocation near collinear rigid line inclusions.

The electric boundary conditions at any rigid line surface are

$$E_1(t)^+ = E_1(t)^-, \quad t \in L_r \tag{3–2a}$$

$$D_2(t)^+ = D_2(t)^-, \quad t \in L_r, \tag{3–2b}$$

for the dielectric rigid lines, and

$$u_4(t)^+ = u_4(t)^- = u_{40}, \quad t \in L_r \tag{3–3}$$

for the conducting rigid lines, where u_{40} is a constant.

By using the perturbation technique, the complex potential vectors for the current problem can be expressed as

$$\boldsymbol{F}(z) = \boldsymbol{F}_0(z) + \boldsymbol{F}_1(z), \tag{3–4}$$

where $\boldsymbol{F}_0(z)$ is associated with the unperturbed field that is related to the solutions of an infinite homogeneous medium without the inclusions and is holomorphic in the entire domain except at z_d. $\boldsymbol{F}_0(z)$ can be expressed as

$$\boldsymbol{F}_0(z) = \frac{1}{2\pi i} \Big\langle \frac{1}{z_\alpha - z_{d\alpha}} \Big\rangle \boldsymbol{B}^T \boldsymbol{d}. \tag{3–5}$$

The function $\boldsymbol{F}_1(z)$ corresponds to the perturbed field due to the introducing of the rigid lines and is holomorphic in the entire domain excluded the rigid lines. It is an unknown function to be determined according to the boundary conditions of the rigid lines.

4. Interaction of a dislocation with rigid dielectric lines

4.1. *Determination of the complex potential function.* In this case, the boundary conditions (3–1) and (3–2) apply. Conditions (3–1) and (3–2) can be rewritten as

$$u'_j(t)^+ = u'_j(t)^- = w_r \delta_{j2}, \qquad E_1(t)^+ = E_1(t)^-, \quad j = 1, 2, 3, \ t \in L_r, \tag{4–1}$$

$$D_2(t)^+ = D_2(t)^-, \quad t \in L_r, \tag{4–2}$$

where the prime denotes differentiation with respect to x_1. Using (2–41) and (3–4), condition (4–1) becomes

$$\boldsymbol{A}\boldsymbol{F}(t)^+ + \overline{\boldsymbol{A}\boldsymbol{F}}(t)^- = \boldsymbol{h}_0, \quad t \in L \tag{4–3}$$

$$\boldsymbol{A}\boldsymbol{F}(t)^- + \overline{\boldsymbol{A}\boldsymbol{F}}(t)^+ = \boldsymbol{h}_0, \quad t \in L \tag{4–4}$$

which leads to

$$[\boldsymbol{A}\boldsymbol{F}(t) - \overline{\boldsymbol{A}\boldsymbol{F}}(t)]^+ - [\,\boldsymbol{A}\boldsymbol{F}(t) - \overline{\boldsymbol{A}\boldsymbol{F}}(t)]^- = 0, \quad t \in L, \tag{4–5}$$

$$[\boldsymbol{A}\boldsymbol{F}(t) + \overline{\boldsymbol{A}\boldsymbol{F}}(t)]^+ + [\boldsymbol{A}\boldsymbol{F}(t) + \overline{\boldsymbol{A}\boldsymbol{F}}(t)]^- = 2\boldsymbol{h}_0, \quad t \in L, \tag{4–6}$$

where $\boldsymbol{h}_0(t) = (0, w_r, 0, -E_1(t))^T$, and $E_1(t)$ the unknown function that indicates the boundary value of

$E_1(z)$ on the inclusion faces [Gao and Fan 2000]. The substitution of (3–4) into (4–5) and (4–6) yields

$$[\boldsymbol{A}\boldsymbol{F}_1(t) - \overline{\boldsymbol{A}\boldsymbol{F}}_1(t)]^+ - [\boldsymbol{A}\boldsymbol{F}_1(t) - \overline{\boldsymbol{A}\boldsymbol{F}}_1(t)]^- = 0, \quad t \in L \tag{4–7}$$

$$[\boldsymbol{A}\boldsymbol{F}_1(t) + \overline{\boldsymbol{A}\boldsymbol{F}}_1(t)]^+ + [\boldsymbol{A}\boldsymbol{F}_1(t) + \overline{\boldsymbol{A}\boldsymbol{F}}_1(t)]^- = 2[\boldsymbol{h}_0(t) + \boldsymbol{h}(t)], \quad t \in L, \tag{4–8}$$

where

$$\boldsymbol{h}(t) = -\frac{\boldsymbol{A}}{2\pi i}\left\langle \frac{1}{t - z_{d\alpha}}\right\rangle \boldsymbol{B}^T \boldsymbol{d} + \frac{\bar{\boldsymbol{A}}}{2\pi i}\left\langle \frac{1}{t - \bar{z}_{d\alpha}}\right\rangle \bar{\boldsymbol{B}}^T \boldsymbol{d}. \tag{4–9}$$

Based on the theory of [Muskhelishvili 1975] and the assumption that $\boldsymbol{F}_1(z)$ vanishes at infinity, the solution of boundary problems (4–7) and (4–8) can be obtained as

$$\boldsymbol{A}\boldsymbol{F}_1(z) - \overline{\boldsymbol{A}\boldsymbol{F}}_1(z) = 0, \tag{4–10}$$

$$\boldsymbol{A}\boldsymbol{F}_1(z) + \overline{\boldsymbol{A}\boldsymbol{F}}_1(z) = \boldsymbol{h}_0(z) + 2[\boldsymbol{Z}(z) + X_0(z)\boldsymbol{P}(z)], \tag{4–11}$$

where

$$X_0(z) = \prod_{j=1}^{N}(z - a_j)^{-\frac{1}{2}}(z - b_j)^{-\frac{1}{2}}, \tag{4–12}$$

$$\boldsymbol{Z}(z) = \frac{X_0(z)}{2\pi i}\int_L \frac{\boldsymbol{h}(t)dt}{X_0^+(t)(t - z)}, \tag{4–13}$$

$$\boldsymbol{P}(z) = \boldsymbol{c}_N z^N + \boldsymbol{c}_{N-1}z^{N-1} + \cdots + \boldsymbol{c}_0. \tag{4–14}$$

Incorporating Equations (4–10) and (4–11) results in

$$\boldsymbol{A}\boldsymbol{F}_1(z) = \frac{\boldsymbol{h}_0(z)}{2} + \boldsymbol{Z}(z) + X_0(z)\boldsymbol{P}(z). \tag{4–15}$$

Taking the limit $z \to \infty$ in (4–15), and noting that $\boldsymbol{F}_1(\infty) = 0$, and $E_1(\infty) = 0$, the constant $\boldsymbol{c}_N$ can be obtained as

$$\boldsymbol{c}_N = (0, -w_r/2, 0, 0)^T. \tag{4–16}$$

The other constants, that is, the vector $\boldsymbol{c}_{N-1}, \ldots, \boldsymbol{c}_0$ and $w_N, \ldots, w_1$ can be determined by single-value displacement, the irrotationality of electric fields and the force equilibrium conditions. With reference to (2–42), these conditions can be written as

$$\oint_\Lambda \boldsymbol{A}\boldsymbol{F}_1(z)dz = 0, \qquad \hat{\boldsymbol{H}}_2 \oint_\Lambda \boldsymbol{A}\boldsymbol{F}_1(z)z dz = 0, \tag{4–17}$$

where Λ is the closed path around each inclusion, and $\hat{\boldsymbol{H}}_2$ is the second low of the real 4×4 matrix $\hat{\boldsymbol{H}} = \boldsymbol{H}^{-1}$. The complex potential is therefore obtained if the function $E_1(z)$ is known.

To obtain $E_1(z)$, we introduce the condition (4–2). Using (2–42), (4–2) can be rewritten as

$$i\boldsymbol{M}_4\boldsymbol{A}\boldsymbol{F}_1^+(t) - i\bar{\boldsymbol{M}}_4\overline{\boldsymbol{A}\boldsymbol{F}_1^-}(t) = i\boldsymbol{M}_4\boldsymbol{A}\boldsymbol{F}_1^-(t) - i\bar{\boldsymbol{M}}_4\overline{\boldsymbol{A}\boldsymbol{F}_1^+}(t), \tag{4–18}$$

where the vector $\boldsymbol{M}_4$ is the fourth low of the matrix $\boldsymbol{M}$ as expressed in (2–44). From [Muskhelishvili 1975] we know that the solution of the Equation (4–18) is

$$\hat{\boldsymbol{H}}_4\boldsymbol{A}\boldsymbol{F}_1(z) = 0, \tag{4–19}$$
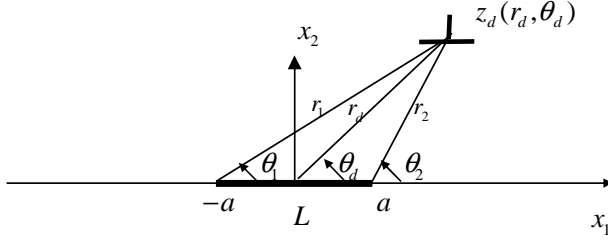
Figure 2. A piezoelectric screw dislocation near a rigid line inclusion.

where $\hat{\boldsymbol{H}}_4 = (\hat{H}_{41}, \hat{H}_{42}, \hat{H}_{43}, \hat{H}_{44})^T$ is the fourth low of the real 4×4 matrix $\hat{\boldsymbol{H}}$. Inserting (4–15) into (4–19) yields

$$E_1(z) = \frac{\hat{H}_{43}}{\hat{H}_{44}} w_r + \frac{2\hat{\boldsymbol{H}}_4}{\hat{H}_{44}} [\boldsymbol{Z}(z) + X_0(z)\boldsymbol{P}(z)]. \tag{4–20}$$

The complex potentials for the problem are thus determined. After $\boldsymbol{F}(z)$ has been obtained, we can calculate the stress and the electrical displacement fields. Thus, we can derive the field intensity factors and the force on the dislocation.

As an example, consider a single rigid line as shown in Figure 2. We can then simplify Equations (4–12) to (4–14) as

$$X_0(z) = (z^2 - a^2)^{-\frac{1}{2}}, \tag{4–21}$$

$$\boldsymbol{P}(z) = \boldsymbol{c}_1 z + \boldsymbol{c}_0, \tag{4–22}$$

$$\boldsymbol{Z}(z) = \frac{\bar{\boldsymbol{A}}}{4\pi i} \left\langle \frac{1}{z_\alpha - \bar{z}_{d\alpha}} - \frac{\sqrt{\bar{z}_{d\alpha}^2 - a^2}}{\sqrt{z_\alpha^2 - a^2}(z_\alpha - \bar{z}_{d\alpha})} - \frac{1}{\sqrt{z_\alpha^2 - a^2}} \right\rangle \bar{\boldsymbol{B}}^T \boldsymbol{d}$$

$$- \frac{\boldsymbol{A}}{4\pi i} \left\langle \frac{1}{z_\alpha - z_{d\alpha}} - \frac{\sqrt{z_{d\alpha}^2 - a^2}}{\sqrt{z_\alpha^2 - a^2}(z_\alpha - z_{d\alpha})} - \frac{1}{\sqrt{z_\alpha^2 - a^2}} \right\rangle \boldsymbol{B}^T \boldsymbol{d}. \tag{4–23}$$

Substituting (4–15), together with (4–21), (4–22) and (4–23) into (4–17) yields

$$\boldsymbol{c}_0 = \boldsymbol{0}, \qquad \hat{\boldsymbol{H}}_2 \boldsymbol{c}_1 = \boldsymbol{0}. \tag{4–24}$$

Then, substituting (4–16) into (4–24) yields

$$\boldsymbol{c}_0 = \boldsymbol{0}, \qquad \boldsymbol{c}_1 = 0, \qquad w_r = 0, \tag{4–25}$$

The complex potentials are thus written as

$$\boldsymbol{A}\boldsymbol{F}_1(z) = (\boldsymbol{I} - \boldsymbol{Y})\boldsymbol{Z}(z), \tag{4–26}$$

where I is the 4×4 identity matrix, and

$$Y = \begin{bmatrix} 0 & 0 & 0 & 0 \\ 0 & 0 & 0 & 0 \\ 0 & 0 & 0 & 0 \\ \hat{H}_{41}/\hat{H}_{44} & \hat{H}_{42}/\hat{H}_{44} & \hat{H}_{43}/\hat{H}_{44} & 1 \end{bmatrix}. \tag{4-27}$$

When the material is purely elastic, the solution reduces to that of [Fan and Keer 1993].

4.2. *Field intensity factors.* Using (2–24), the field intensity factors at the right rigid line tip can be defined as

$$K = \{K_{II}, K_I, K_{II}, K_D\}^T = \lim_{x_1 \to a} \sqrt{2\pi(x_1 - a)}\, \mathbf{\Phi}_{,1}(x_1), \tag{4-28}$$

where

$$\mathbf{\Phi}_{,1}(x_1) = 2\operatorname{Re} i\, \boldsymbol{M}\boldsymbol{A}\boldsymbol{F}_1(x_1) = -2\boldsymbol{H}^{-1}\boldsymbol{S}(\boldsymbol{I} - \boldsymbol{Y})\operatorname{Re} \boldsymbol{Z}(x_1). \tag{4-29}$$

Substituting (4–23) into (4–29) yields

$$\mathbf{\Phi}_{,1}(x_1) = \frac{\boldsymbol{H}^{-1}\boldsymbol{S}(\boldsymbol{I} - \boldsymbol{Y})}{\pi\sqrt{x_1^2 - a^2}} \left(\operatorname{Im} \boldsymbol{A} \left\langle \frac{\sqrt{x_1^2 - a^2} - \sqrt{z_{d\alpha}^2 - a^2}}{x_1 - z_{d\alpha}} - 1 \right\rangle \boldsymbol{B}^T \boldsymbol{d} \right). \tag{4-30}$$

The field intensity factors are thus obtained as

$$K = \frac{\boldsymbol{H}^{-1}\boldsymbol{S}(\boldsymbol{I} - \boldsymbol{Y})}{\sqrt{\pi a}} \left(\operatorname{Im} \boldsymbol{A} \left\langle \sqrt{\frac{z_{d\alpha} + a}{z_{d\alpha} - a}} - 1 \right\rangle \boldsymbol{B}^T \boldsymbol{d} \right). \tag{4-31}$$

When the dislocation lies along the real axis $z_d = (x_d, 0)$, (4–15) reduces to

$$K = -\frac{\boldsymbol{H}^{-1}\boldsymbol{S}(\boldsymbol{I} - \boldsymbol{Y})\boldsymbol{S}\boldsymbol{d}}{2\sqrt{\pi a}} \left(\sqrt{\frac{x_d + a}{x_d - a}} - 1 \right). \tag{4-32}$$

4.3. *Force on dislocation.* To analyze the possible balance position of a dislocation, it is of interest to compute the image force acting on the dislocation due to the presence of the rigid lines. The image force per unit length is defined as the negative gradient of the interaction energy with respect to the position of the dislocation. The image force [Pak 1990] can be written as

$$F_{x_1} = d_1\sigma_{21}^1 + d_2\sigma_{22}^1 + d_3\sigma_{23}^1 + d_4 D_2^1 = \boldsymbol{d}^T \mathbf{\Phi}_{,1}^1, \tag{4-33}$$

$$F_{x_2} = -\left(d_1\sigma_{11}^1 + d_2\sigma_{12}^1 + d_3\sigma_{13}^1 + d_4 D_1^1\right) = \boldsymbol{d}^T \mathbf{\Phi}_{,2}^1, \tag{4-34}$$

where $\mathbf{\Phi}^1$ is associated with the perturbed field calculated from $\boldsymbol{F}_1(z)$ with $z_\alpha \to z_{d\alpha}$, that is,

$$\boldsymbol{F}_1(z_{d\alpha}) = \frac{1}{2\pi i}\left[\boldsymbol{A}^{-1}(\boldsymbol{I} - \boldsymbol{Y})\bar{\boldsymbol{A}}\langle G_1\rangle \bar{\boldsymbol{B}}^T + \boldsymbol{A}^{-1}(\boldsymbol{I} - \boldsymbol{Y})\boldsymbol{A}\langle G_2\rangle \boldsymbol{B}^T\right]\boldsymbol{d}, \tag{4-35}$$

with

$$G_1(z_{d\alpha}) = \frac{\sqrt{z_{d\alpha}^2 - a^2} - \sqrt{\bar{z}_{d\alpha}^2 - a^2} - (z_{d\alpha} - \bar{z}_{d\alpha})}{2(z_{d\alpha} - \bar{z}_{d\alpha})\sqrt{z_{d\alpha}^2 - a^2}},$$

$$(4\text{--}36)$$

$$G_2(z_{d\alpha}) = -\frac{z_{d\alpha} - \sqrt{z_{d\alpha}^2 - a^2}}{2(z_{d\alpha}^2 - a^2)}.$$

As a result, we obtain

$$\boldsymbol{\Phi}_{,1}^1(z_{d\alpha}) = \frac{1}{\pi} \operatorname{Im} \left(\boldsymbol{B} \boldsymbol{A}^{-1}(\boldsymbol{I} - \boldsymbol{Y})\bar{\boldsymbol{A}}\langle G_1\rangle \bar{\boldsymbol{B}}^T + \boldsymbol{B}\boldsymbol{A}^{-1}(\boldsymbol{I} - \boldsymbol{Y})\boldsymbol{A}\langle G_2\rangle \boldsymbol{B}^T \right)\boldsymbol{d}, \tag{4--37}$$

$$\boldsymbol{\Phi}_{,2}^1(z_{d\alpha}) = \frac{1}{\pi} \operatorname{Im} \left(\boldsymbol{B} \boldsymbol{A}^{-1}(\boldsymbol{I} - \boldsymbol{Y})\bar{\boldsymbol{A}}\langle p_\alpha G_1\rangle \bar{\boldsymbol{B}}^T + \boldsymbol{B}\boldsymbol{A}^{-1}(\boldsymbol{I} - \boldsymbol{Y})\boldsymbol{A}\langle p_\alpha G_2\rangle \boldsymbol{B}^T \right)\boldsymbol{d}. \tag{4--38}$$

When the dislocation lies on the x_1-axis, that is, $z_{ad} = x_{1d} = x_d$, we can simplify the expressions (4–37) and (4–38) as

$$\boldsymbol{\Phi}_{,1}^1(x_d) = -g(x_d)\boldsymbol{H}^{-1}\boldsymbol{S}(\boldsymbol{I} - \boldsymbol{Y})\boldsymbol{S}\boldsymbol{d}, \tag{4--39}$$

$$\boldsymbol{\Phi}_{,2}^1(x_d) = g(x_d) \operatorname{Im} \left(\boldsymbol{B}\boldsymbol{A}^{-1}(\boldsymbol{I} - \boldsymbol{Y})\left(\bar{\boldsymbol{A}}\langle p_\alpha\rangle \bar{\boldsymbol{B}}^T - \boldsymbol{A}\langle p_\alpha\rangle \boldsymbol{B}^T\right)\right)\boldsymbol{d}, \tag{4--40}$$

where

$$g(x_d) = \frac{1}{2\pi} \frac{x_d - \sqrt{x_d^2 - a^2}}{x_d^2 - a^2}. \tag{4--41}$$

5. Interaction of a dislocation with rigid conducting lines

5.1. *Determination of the complex potential function.* In the case of rigid conducting lines, the boundary conditions (3–1) and (3–3) apply. Conditions (3–1) and (3–3) can be rewritten as

$$u_j'(t)^+ = u_j'(t)^- = w_r\delta_{j2}, \quad j = 1, 2, 3, \ t \in L_r \tag{5--1}$$

$$u_4'(t)^+ = u_4'(t)^- = 0, \quad t \in L_r, \tag{5--2}$$

where the prime denotes differentiation with respect to with x_1. With reference to (2–41) and (3–4), conditions (5–1) and (5–2) arrive at

$$\boldsymbol{A}\boldsymbol{F}(t)^+ + \overline{\boldsymbol{A}\boldsymbol{F}}(t)^- = \boldsymbol{h}_0, \quad t \in L, \tag{5--3}$$

$$\boldsymbol{A}\boldsymbol{F}(t)^- + \overline{\boldsymbol{A}\boldsymbol{F}}(t)^+ = \boldsymbol{h}_0, \quad t \in L, \tag{5--4}$$

which lead to

$$\left[\boldsymbol{A}\boldsymbol{F}(t) - \overline{\boldsymbol{A}\boldsymbol{F}}(t)\right]^+ - \left[\boldsymbol{A}\boldsymbol{F}(t) - \overline{\boldsymbol{A}\boldsymbol{F}}(t)\right]^- = 0, \quad t \in L, \tag{5--5}$$

$$\left[\boldsymbol{A}\boldsymbol{F}(t) + \overline{\boldsymbol{A}\boldsymbol{F}}(t)\right]^+ + \left[\boldsymbol{A}\boldsymbol{F}(t) + \overline{\boldsymbol{A}\boldsymbol{F}}(t)\right]^- = 2\boldsymbol{h}_0, \quad t \in L, \tag{5--6}$$

where $\boldsymbol{h}_0 = (0, w_r, 0, 0)^T$. Substituting (3–4) into (5–5) and (5–6) yields

$$\left[\boldsymbol{A}\boldsymbol{F}_1(t) - \overline{\boldsymbol{A}}\overline{\boldsymbol{F}}_1(t)\right]^+ - \left[\boldsymbol{A}\boldsymbol{F}_1(t) - \overline{\boldsymbol{A}}\overline{\boldsymbol{F}}_1(t)\right]^- = 0, \quad t \in L, \tag{5–7}$$

$$\left[\boldsymbol{A}\boldsymbol{F}_1(t) + \overline{\boldsymbol{A}}\overline{\boldsymbol{F}}_1(t)\right]^+ + \left[\boldsymbol{A}\boldsymbol{F}_1(t) + \overline{\boldsymbol{A}}\overline{\boldsymbol{F}}_1(t)\right]^- = 2[\boldsymbol{h}_0 + \boldsymbol{h}(t)], \quad t \in L, \tag{5–8}$$

where $\boldsymbol{h}(t)$ is as defined in (4–9). This problem is a special case of the case solved in the previous section. The solution can be obtained from the previous solution by setting $\boldsymbol{Y} = \boldsymbol{0}$. For a single rigid conducting line as shown in Figure 2, the complex potential corresponding to the perturbed field is

$$\boldsymbol{A}\boldsymbol{F}_1(z) = \boldsymbol{Z}(z), \tag{5–9}$$

where $\boldsymbol{Z}(z)$ is as in (4–23).

5.2. *Field intensity factors.* The field intensity factors at the right inclusion tip can be defined as

$$\boldsymbol{K} = \frac{\boldsymbol{H}^{-1}\boldsymbol{S}}{\sqrt{\pi a}}\left(\operatorname{Im}\boldsymbol{A}\left\langle\sqrt{\frac{z_{d\alpha} + a}{z_{d\alpha} - a}} - 1\right\rangle\boldsymbol{B}^T\boldsymbol{d}\right). \tag{5–10}$$

When the dislocation lies along the real axis $z_d = (x_d, 0)$, Equation (5–15) reduces to

$$\boldsymbol{K} = -\frac{\boldsymbol{H}^{-1}\boldsymbol{S}^2\boldsymbol{d}}{2\sqrt{\pi a}}\left(\sqrt{\frac{x_d + a}{x_d - a}} - 1\right). \tag{5–11}$$

5.3. *Force on dislocation.* The image force on dislocation can be written as

$$F_{x_1} = \boldsymbol{d}^T\boldsymbol{\Phi}^1_{,1}(z_{d\alpha}), \tag{5–12}$$

$$F_{x_2} = \boldsymbol{d}^T\boldsymbol{\Phi}^1_{,2}(z_{d\alpha}), \tag{5–13}$$

where

$$\boldsymbol{\Phi}^1_{,1}(z_{d\alpha}) = \frac{1}{\pi}\operatorname{Im}\left[\boldsymbol{B}\boldsymbol{A}^{-1}\overline{\boldsymbol{A}}\langle G_1\rangle\overline{\boldsymbol{B}}^T + \boldsymbol{B}\langle G_2\rangle\boldsymbol{B}^T\right]\boldsymbol{d}, \tag{5–14}$$

$$\boldsymbol{\Phi}^1_{,2}(z_{d\alpha}) = \frac{1}{\pi}\operatorname{Im}\left[\boldsymbol{B}\boldsymbol{A}^{-1}\overline{\boldsymbol{A}}\langle p_\alpha G_1\rangle\overline{\boldsymbol{B}}^T + \boldsymbol{B}\langle p_\alpha G_2\rangle\boldsymbol{B}^T\right]\boldsymbol{d}. \tag{5–15}$$

$G_1(z_{d\alpha})$ and $G_2(z_{d\alpha})$ are as defined in (4–36). When the dislocation lies on the x_1-axis, that is, $z_{da} = x_{1d} = x_d$, we simplify (5–14) and (5–15) as

$$\boldsymbol{\Phi}^1_{,1}(x_d) = g(x_d)(\boldsymbol{H}^{-1} - \boldsymbol{L})\boldsymbol{d}, \tag{5–16}$$

$$\boldsymbol{\Phi}^1_{,2}(x_d) = g(x_d)\operatorname{Im}\left\{\boldsymbol{B}\boldsymbol{A}^{-1}[\overline{\boldsymbol{A}}\langle p_\alpha\rangle\overline{\boldsymbol{B}}^T - \boldsymbol{A}\langle p_\alpha\rangle\boldsymbol{B}^T]\right\}\boldsymbol{d}, \tag{5–17}$$

where $g(x_d)$ is as defined in (4–41).

6. Numerical examples

The previous sections derived the explicit expressions for the field intensity factors and the forces on the dislocation. However they are not straightforward since several variables are involved. In this section, we present some numerical illustrations. As an example, we address the case when the dislocation lies

along $\theta_d = \pi/6$. The material is assumed to be PZT-5H, with the x_1-axis the polling direction. The material constants [Pak 1992b] are

$$
\begin{aligned}
c_{11} &= 117\,\text{GPa}, & c_{12} &= c_{13} = 53\,\text{GPa}, \\
c_{22} &= c_{33} = 126\,\text{GPa}, & c_{23} &= 55\,\text{GPa}, \\
c_{44} &= 35.5\,\text{GPa}, & c_{55} &= c_{66} = 35.3\,\text{GPa}, \\
e_{11} &= 23.3\,\text{C/m}^2, & e_{12} &= e_{13} = -6.5\,\text{C/m}^2, \\
e_{35} &= e_{26} = 17\,\text{C/m}^2, \\
\varepsilon_{11} &= 130 \times 10^{-10}\,\text{C/Vm}, \\
\varepsilon_{22} &= \varepsilon_{33} = 151 \times 10^{-10}\,\text{C/Vm}.
\end{aligned} \tag{6--1}
$$

For p_α ($\alpha = 1, 2, 3, 4$), the values of A and B are then calculated as follows:

$$
\begin{aligned}
p_1 &= -0.17351 + 0.93175i, \\
p_2 &= 0.17351 + 0.93175i, \\
p_3 &= 0.93367i, \\
p_4 &= 0.99718i,
\end{aligned} \tag{6--2}
$$

$$
\begin{aligned}
A_{11} &= -.8521 \times 10^{-6} + .3117 \times 10^{-5}i, & A_{12} &= .3117 \times 10^{-5} - .8521 \times 10^{-6}i, \\
A_{13} &= .4133 \times 10^{-5} + .1433 \times 10^{-5}i, & A_{14} &= 0, \\
A_{21} &= -.3561 \times 10^{-5} + .4268 \times 10^{-6}i, & A_{22} &= -.4268 \times 10^{-6} + .3561 \times 10^{-5}i, \\
A_{23} &= -.1189 \times 10^{-5} + .1189 \times 10^{-5}i, & A_{24} &= 0, \\
A_{31} &= 0, \qquad A_{32} = 0, \\
A_{33} &= 0, \qquad A_{34} = -.2657 \times 10^{-5} + .2657 \times 10^{-5}i, \\
A_{41} &= 722.3288 + 2351.6593i, & A_{42} &= 2351.6593 + 722.3288i, \\
A_{43} &= -3006.4445 - 3006.4445i, & A_{44} &= 0.
\end{aligned} \tag{6--3}
$$

$$
\begin{aligned}
B_{11} &= -262382.5644 - 27548.9152i, & B_{12} &= 27548.9157 + 262382.5653i, \\
B_{13} &= -41491.1280 + 41491.1353i, & B_{14} &= 0, \\
B_{21} &= -22107.3141 - 277484.1268i, & B_{22} &= -277484.1276 - 22107.3141i, \\
B_{23} &= 44438.6631 - 44438.6550i, & B_{24} &= 0, \\
B_{31} &= 0, \quad B_{32} = 0, \quad B_{33} = 0, \quad B_{34} = -94074.2510 - 94074.2510i, \\
B_{41} &= -.7241 \times 10^{-4} - .1944 \times 10^{-4}i, & B_{42} &= .1944 \times 10^{-4} + .7241 \times 10^{-4}i, \\
B_{43} &= -.8535 \times 10^{-4} + .8535 \times 10^{-4}i, & B_{44} &= 0.
\end{aligned} \tag{6--4}
$$

6.1. *Field intensity factors.* The expression (4–31) gives the field intensity factors at the right rigid line tip arising from the dislocation $\boldsymbol{d} = (d_1, d_2, d_3, d_4)^T$ located at z_d near a rigid dielectric line. Expression (5–10) does the same for a rigid conducting line. When these intensity factors have the same sign as

those arising from the remote applied stress or electric displacement, the total intensity factors increase. The dislocation then anti-shields the rigid line tip; otherwise the dislocation shields it. Shielding effects from d_1, d_2, and d_4 on K_I, K_{II}, K_{III}, K_D for the dislocation located along $\theta_d = \pi/6$ near a rigid line are illustrated in Figures 3 to 8, in relation to the normalized dislocation radial location r_d/a. To plot the four field intensity factors in one figure, the values of K_I, K_{II}, K_{III}, K_D were properly normalized in the figures with positive values. The normalized intensity factors are denoted as K_I^*, K_{II}^*, K_{III}^*, K_D^* in the figures, where

$$K_j^*(d_j) = \frac{K_j(d_j)}{K_{j0}(d_j)}, \quad j = I, II, III, D, \tag{6–5}$$

with

$$K_{j0}(d_j) = \frac{d_j}{2\sqrt{\pi a}} \times 10^{10}\,\text{N/m}^2, \qquad K_{D0}(d_j) = \frac{d_j}{\sqrt{\pi a}} \times 2\,\text{N/Vm}, \quad j = I, II, III$$

$$K_{j0}(d_4) = \frac{d_4}{\sqrt{\pi a}} \times 2\,\text{N/Vm}, \quad j = I, II, III, \qquad K_{D0}(d_4) = \frac{d_4}{\sqrt{\pi a}} \times 10^{-9}\,\text{N/V}^2. \tag{6–6}$$

In the above equations, $d_I = d_1$, $d_{II} = d_2$, $d_{III} = d_3$.

Figure 3 shows that the glide dislocation d_1 always shields K_I while anti-shielding K_{II} and K_D when it is near a dielectric line tip. The shielding effects from the glide dislocation on K_{II} and K_D appear
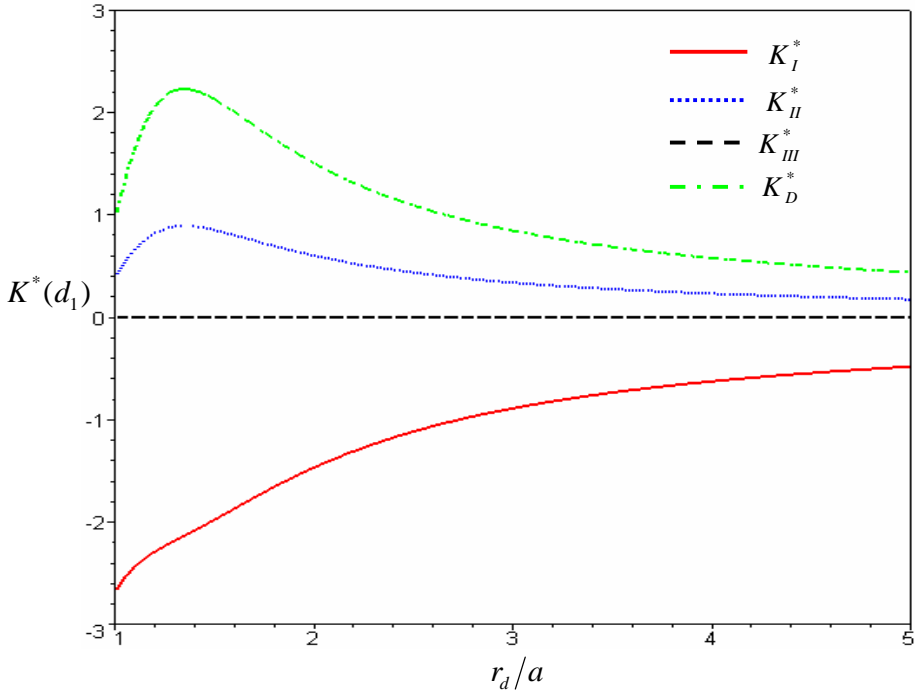
Figure 3. The shielding effect from the glide dislocation d_1 located along $\theta_d = \pi/6$ on the field intensity factors for a rigid dielectric inclusion.
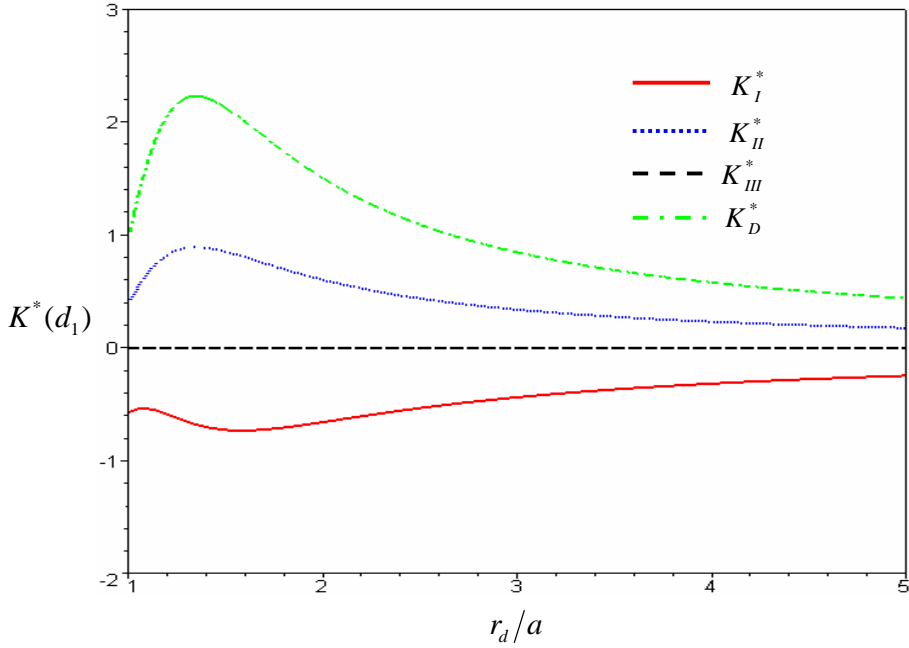
Figure 4. The shielding effect from the glide dislocation d_1 located along $\theta_d = \pi/6$ on the field intensity factors for a rigid conducting inclusion.

in a very similar way. But the glide dislocation d_1 does not affect K_{III}. This occurs because the glide dislocation does not contribute any anti-plane deformations.

Figure 4 also shows that the glide dislocation d_1 always shields K_I while anti-shielding K_{II} and K_D, but does not affect K_{III} when it is near a conducting line tip. A comparison of Figures 3 and 4 indicates that the conductivity of the inclusion only has apparent effects on K_I.

Figures 5 and 6 show the shielding effects from the climb dislocation d_2 for a rigid dielectric line and a rigid conducting line, respectively. We find that the two figures are nearly the same, which indicates that the conductivity of the rigid line is not sensitive to the shielding effects from d_2.

Figures 7 and 8 show the shielding effects from the electrical dislocation d_4 for a rigid dielectric line and a rigid conducting one, respectively. The comparison of these two figures also indicates that the conductivity of the rigid line only has apparent effects on K_I. For a rigid dielectric line, it first anti-shields and then shields K_I when increasing r_d/a; while for a rigid conducting one, it always shields K_I.

6.2. *Image force on dislocation.* Expressions for the image forces on the dislocation due to existence of the inclusion are calculated using (4–33) and (4–34) together with (4–37) and (4–38) for a rigid dielectric line, and by (5–12) to (5–15) for a rigid conducting one. As such, the slip and climb parts of the image forces can be calculated as follows:
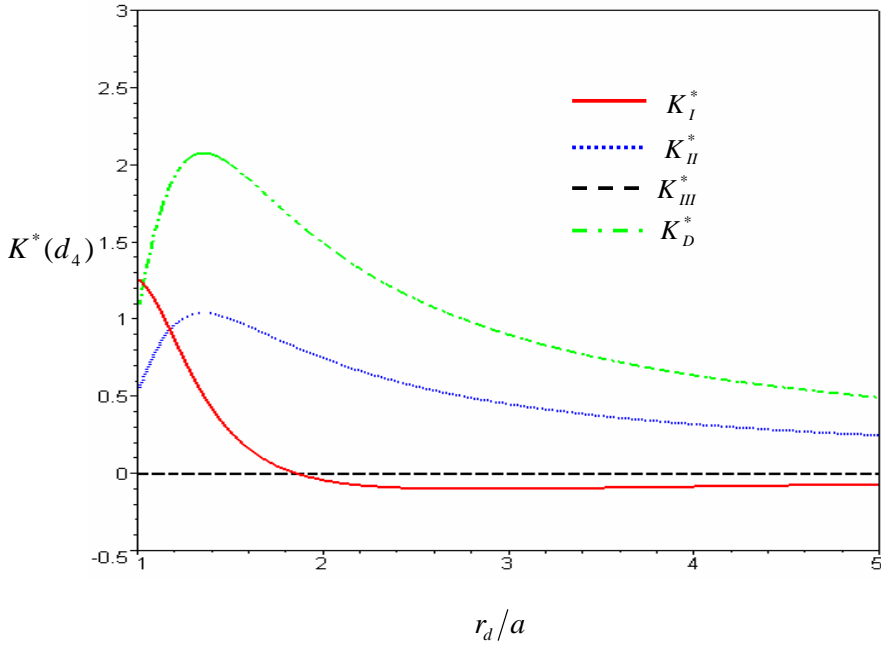
$$\begin{aligned} F_r &= F_x \cos\theta_d + F_y \sin\theta_d, \\ F_t &= -F_x \sin\theta_d + F_y \cos\theta_d. \end{aligned} \tag{6–7}$$
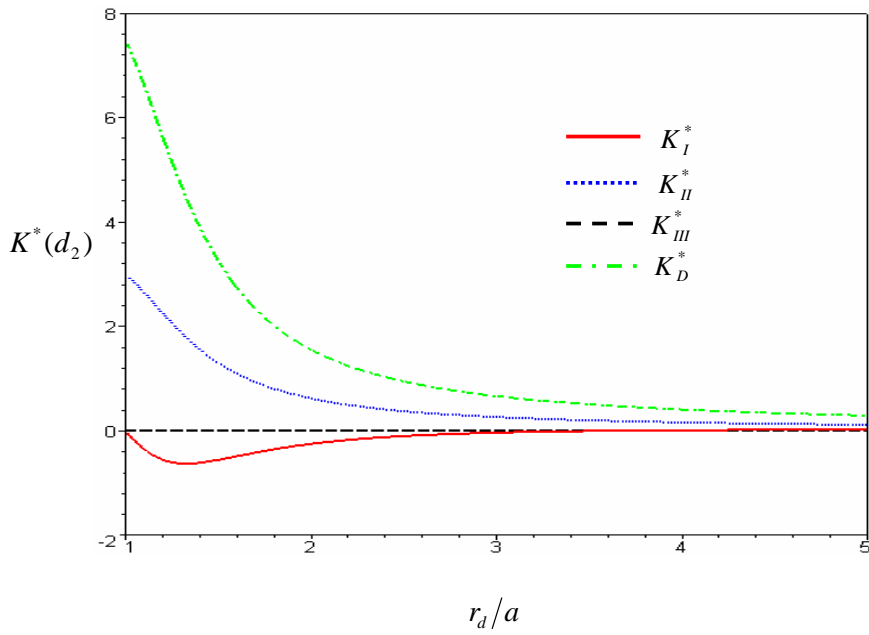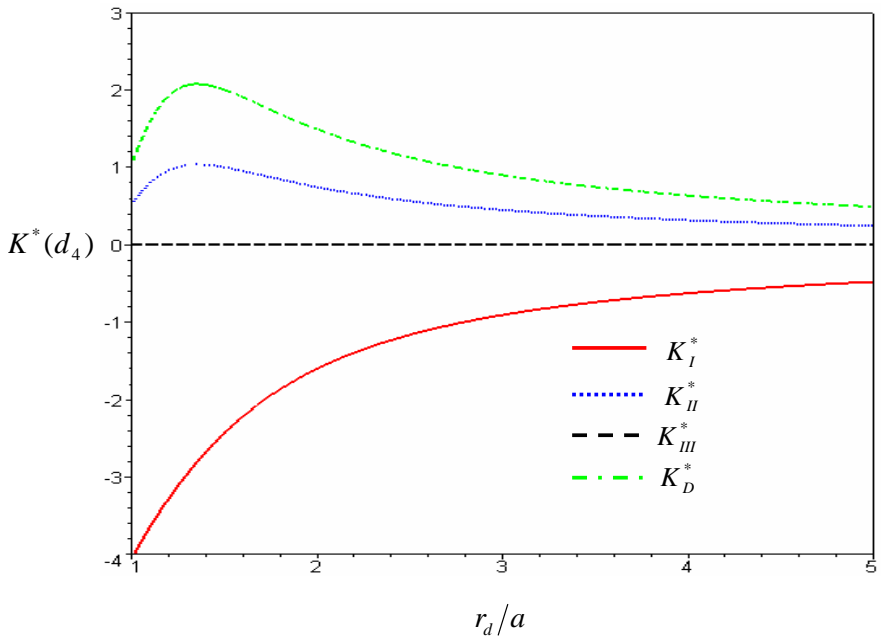
Figure 5. The shielding effect from the climb dislocation d_2 located along $\theta_d = \pi/6$ on the field intensity factors for a rigid dielectric inclusion.
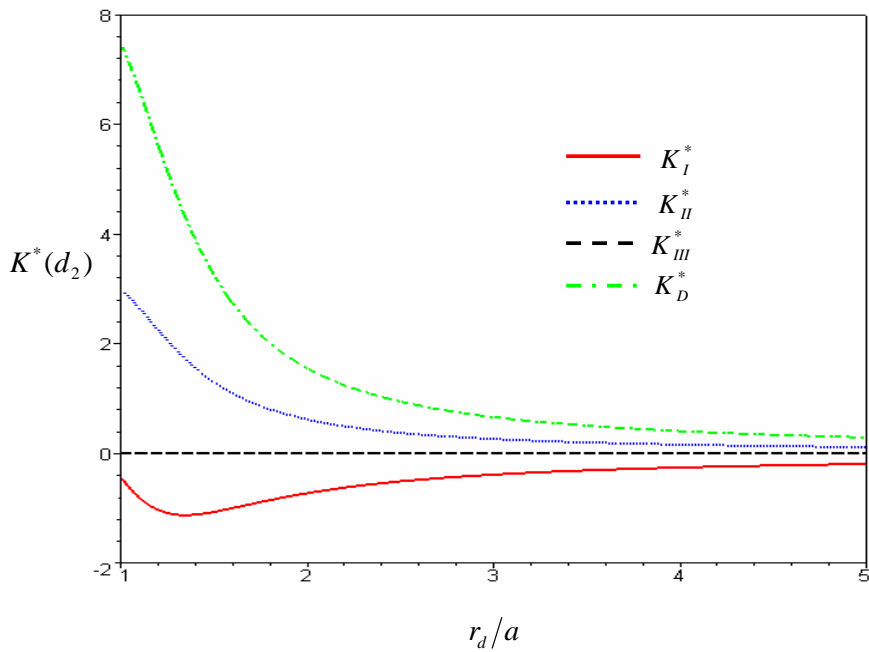
Figure 6. The shielding effect from the climb dislocation d_2 located along $\theta_d = \pi/6$ on the field intensity factors for a rigid conducting inclusion.

Figure 7. The shielding effect from the electrical dislocation d_4 located along $\theta_d = \pi/6$ on the field intensity factors for a rigid dielectric inclusion.


Figure 8. The shielding effect from the electrical dislocation d_4 located along $\theta_d = \pi/6$ on the field intensity factors for a rigid conducting inclusion.

Figures 9 and 10 plot the normalized slip image force F_r/F_0 and climb image force F_t/F_0 varied with the normalized radial location r_d/a, respectively, for a rigid *dielectric* line.
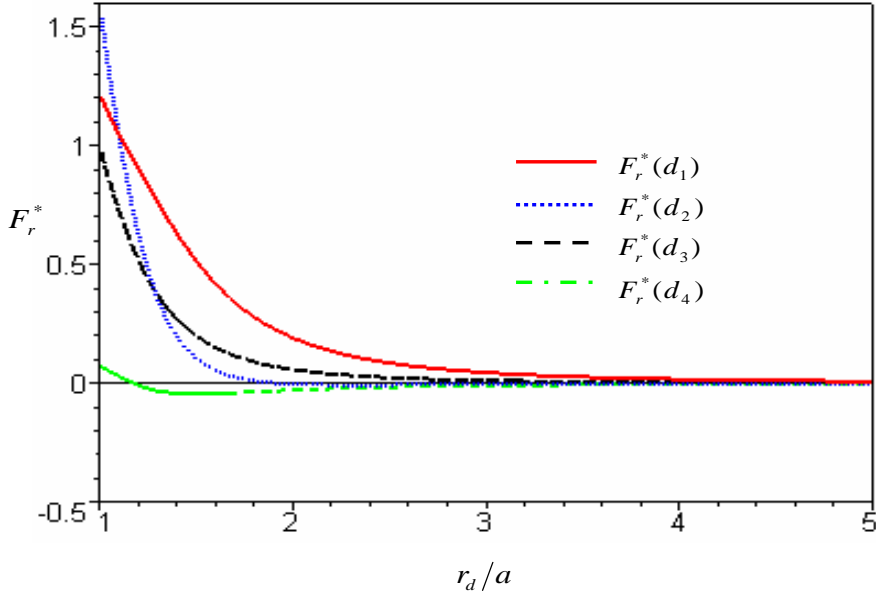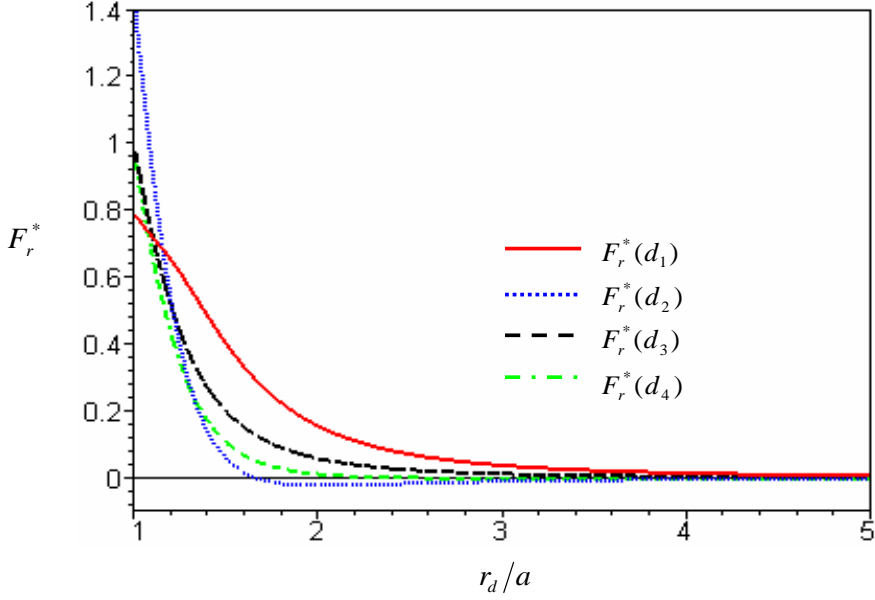

Figure 9. Variations of the radial normalized image forces on the dislocation located along $\theta_d = \pi/6$ near a rigid dielectric inclusion.
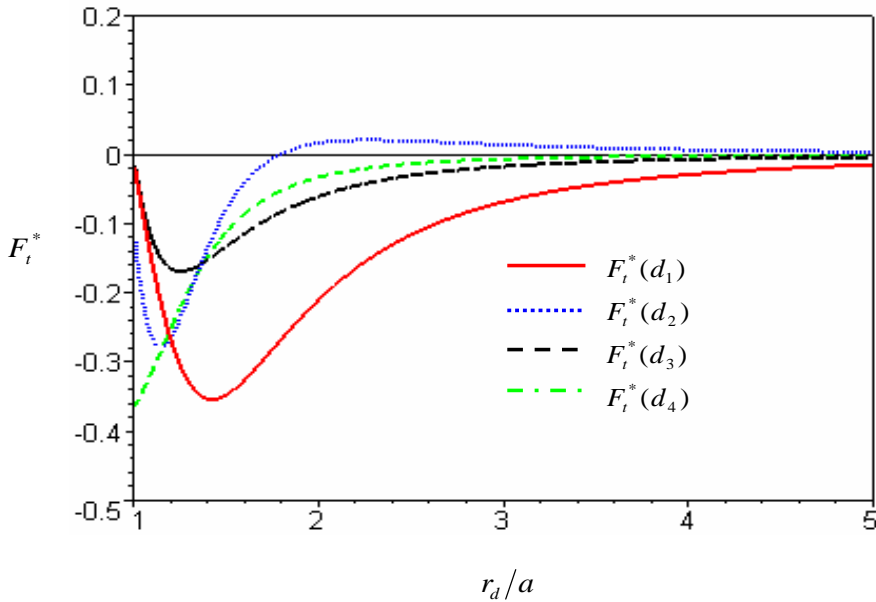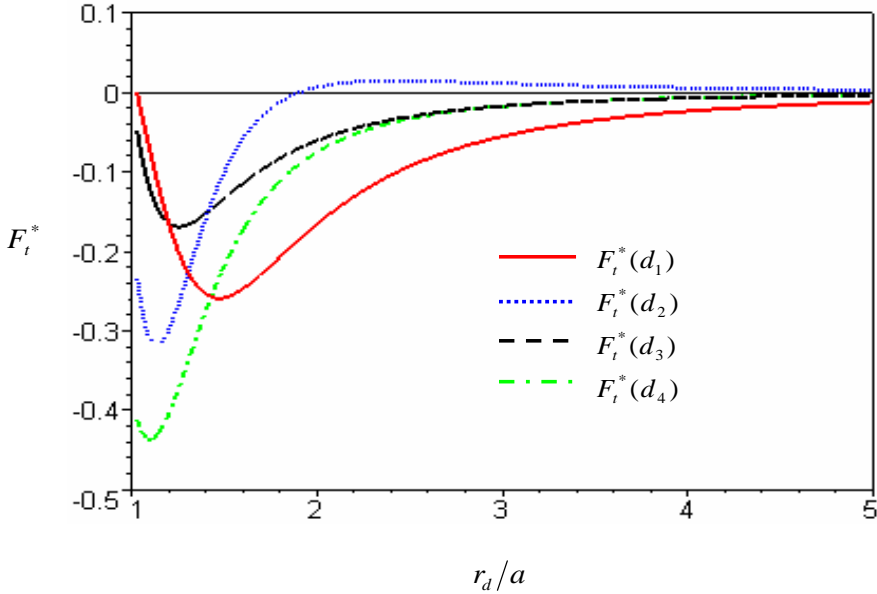

Figure 10. Variations of the tangential normalized image forces on the dislocation located along $\theta_d = \pi/6$ near a rigid dielectric inclusion.

Figures 11 and 12 plot those for a rigid *conducting* line. The dislocation has four different dislocation strength characteristics (d_1, d_2, d_3, d_4). We allow the dislocation to have only one non-zero strength

Figure 11. Variations of the radial normalized image forces on the dislocation located along $\theta_d = \pi/6$ near a rigid conducting inclusion.

Figure 12. Variations of the tangential normalized image forces on the dislocation located along $\theta_d = \pi/6$ near a rigid conducting inclusion.

characteristic. The other three are zero in each plotted curve. The normalizing factors in each curve are given by

$$F_0 = \frac{d^T L d}{4\pi a}. \tag{6–8}$$

Figures 9 and 10 show that, a rigid dielectric line always repels the mechanical dislocation in the radial direction, while it does little on the electrical dislocation; it always attracts the dislocation to the real axis when it is close to the rigid line tip. On the other hand, Figures 11 and 12 show that a rigid conducting line always repels the dislocation in the radial direction and attracts the dislocation in the tangential direction when the dislocation is close to the inclusion.

7. Conclusions

The interaction problem of a dislocation and collinear rigid lines embedded in a piezoelectric media is addressed. The lines considered are for either conductors or dielectrics. We obtain a closed form solution using the complex potential method, and explicitly derive field intensity factors and the forces on the dislocation for a single inclusion case. We present numerical examples and discuss the results.

References

[Chen et al. 2002] B. J. Chen, Z. M. Xiao, and L. K. M., "On the interaction between a semi-infinite anti-crack and a screw dislocation in piezoelectric solid", *Int. J. Solids Struct.* **39**:6 (2002), 1505–1513.

[Deng and Meguid 1998] W. Deng and S. A. Meguid, "Analysis of conducting rigid inclusions at the interface of two dissimilar piezoelectric materials", *J. Appl. Mech. (ASME)* **65** (1998), 76–84.

[Deng and Meguid 1999] W. Deng and S. A. Meguid, "Analysis of a screw dislocation inside an elliptical inhomogeneity in piezoelectric solids", *Int. J. Solids Struct.* **36**:10 (1999), 1449–1469.

[Fan and Keer 1993] H. Fan and L. M. Keer, "Two-dimensional line defects in anisotropic elastic solids", *Int. J. Fract.* **62**:1 (1993), 25–42.

[Gao and Fan 2000] C. F. Gao and W. X. Fan, "The generalized 2D problem of piezoelectric media with collinear rigid line inclusions", *Chin. J. Appl. Mech.* **17** (2000), 126–130.

[Huang and Kuang 2001] Z. Huang and Z. B. Kuang, "Dislocation inside a piezoelectric media with an elliptical inhomogeneity", *Int. J. Solids Struct.* **38**:46–47 (2001), 8459–8479.

[Kattis et al. 1998] M. A. Kattis, E. Providas, and A. L. Kalamkarov, "Two-phone potentials in the analysis of smart composites having piezoelectric components", *Compos. B Eng.* **29**:1 (1998), 9–14.

[Liang et al. 1995] J. Liang, J. C. Han, and S. Y. Du, "Rigid line inclusions and cracks in anisotropic piezoelectric solids", *Mech. Res. Commun.* **22**:1 (1995), 43–49.

[Liu and Fang 2003] Y. W. Liu and Q. H. Fang, "Electro-elastic interaction between a piezoelectric screw dislocation and circular interfacial rigid lines", *Int. J. Solids Struct.* **40**:20 (2003), 5353–5370.

[Meguid and Zhong 1997] S. A. Meguid and Z. Zhong, "Electroelastic analysis of a piezoelectric elliptical inhomogeneity", *Int. J. Solids Struct.* **34**:26 (1997), 3401–3414.

[Muskhelishvili 1975] N. I. Muskhelishvili, *Some basic problems of the mathematical theory of elasticity*, Noordhoff, Leiden, 1975.

[Pak 1990] Y. E. Pak, "Force on a piezoelectric screw dislocation", *J. Appl. Mech. (ASME)* **57** (1990), 863–869.

[Pak 1992a] Y. E. Pak, "Circular inclusion problem in anti-plane piezoelectricity", *Int. J. Solids Struct.* **29**:19 (1992), 2403–2419.

[Pak 1992b] Y. E. Pak, "Linear electro-elastic fracture mechanics of piezoelectric materials", *Int. J. Fract.* **54**:1 (1992), 79–100.

[Shi 1997] W. Shi, "Rigid line inclusions under anti-plane deformation and in-plane electric field in piezoelectric materials", *Eng. Fract. Mech.* **56**:2 (1997), 265–274.

BINGJIN CHEN: mbjchen@ntu.edu.sg
School of Mechanical and Aerospace Engineering, Nanyang Technological University, Nanyang Avenue, Singapore 639798

DONGWEI SHU: mdshu@ntu.edu.sg
School of Mechanical and Aerospace Engineering, Nanyang Technological University, Nanyang Avenue, Singapore 639798

ZHONGMIN XIAO: mzxiao@ntu.edu.sg
School of Mechanical and Aerospace Engineering, Nanyang Technological University, Nanyang Avenue, Singapore 639798

A DAMAGE INDEX FOR STRUCTURAL HEALTH MONITORING BASED ON THE EMPIRICAL MODE DECOMPOSITION

NADER CHERAGHI AND FARID TAHERI

This paper presents two novel damage indices based on empirical mode decomposition (EMD) and fast Fourier integration for identifying structural damage caused by a change in structural stiffness. The paper also demonstrates the effectiveness of the proposed damage indices formulated based on a series of coupled mathematical/engineering approaches that are used to detect damage in pipes reliably and accurately. The main approach is based on monitoring the vibration response of pipes using piezoelectric sensors and the first intrinsic mode functions (IMFs). Finite element analysis is used to simulate the response of a healthy pipe, as well as pipes with various sizes of damage. Damages are meant to represent the outcome of local corrosion (damage) with varying reduction in areas around the circumference of the pipe. The evaluated damage indices could effectively establish the location of the defects. Moreover, the evaluated energy indices could also distinguish various size defects. To demonstrate further the effectiveness of our proposed damage indices, the results are compared with other effective indices based on wavelet packet and other statistical methods reported in the literature.

Introduction

Vital energy resources such as oil and gas are transported through pipelines that span various terrains. They are critical transport elements, and their health and reliability through their designed service life is an important issue for design and maintenance engineers. Ground movement, resulting from natural and unavoidable circumstances, could significantly change the support condition of pipelines, thus subjecting them to loads and boundary conditions that would not have been considered during the design phase. Moreover, as pipes age, their component materials deteriorate. Therefore, many factors such as corrosion, damage caused by excavation equipment, cracks, and defective welds could severely impact the integrity of pipelines. There are several outcomes resulting from such changes to the original status of the pipe, causing massive costly dilemmas for industry stakeholders, including the producers, pipeline operators, regulatory agencies, and the public. The establishment of a safe and reliable method for detecting damage in pipelines is an important issue for not one, but several parties.

There are currently several industrially established nondestructive and in-line inspection methodologies available which provide some success in detecting the factors that affect the safe performance of pipelines. Most in-line inspection tools that are available today use either the magnetic flux leakage

(MFL) method [Reber et al. 2002] or the ultrasonic guided wave method [Wilkie et al. 2002]. Alternatively, experimental studies have also demonstrated the potential of piezoceramic actuators for controlling vibration in cylindrical shell structures [Fuller et al. 1992; Silcox et al. 1992].

Sun et al. [1995] and later Ayres et al. [1998] reported the use of PZT transducers for damage detection on a laboratory sized truss structure and a prototype truss joint, respectively. Their damage detection methods are based on the principle of electromechanical coupling between the host structure and the bonded PZT transducer. Several other workers have also explored the use of piezoelectric patches for detecting damage in structures. A review of damage detection methods using piezoelectric sensors and actuators can be found in [Zou et al. 2000] or [Cheraghi et al. 2005]. Its main objective is to demonstrate the effectiveness and integrity of two novel damage indices that were developed based on the EMD and fast Fourier integration (FFT) for identifying structural damage caused by a change in structural stiffness. A series of coupled mathematical/engineering approaches were used in the development of these indices, which would reliably and accurately detect damage in pipes. This demonstration will be based on the simulation of the response of a healthy pipe, as well as pipes with various sizes of damage by the finite element method. Our case studies will demonstrate that the proposed indices could also establish the location of the defects, as well as the relative sizes of the defects. In addition, comparisons will be made using the results reported in the literature that were established based on the wavelet packet and other statistical methods.

Modeling and formulation of the piezoelectric sensors

Various finite element formulations have been presented by several researchers for the assessment of dynamic response of piezoelectric materials. For instance, Tzou and Tseng [1990] and Rao and Sunar [1994] used the following equations to represent the dynamic response

$$[M]\{\ddot{u}\} + [K_{uu}]\{u\} + [K_{u\phi}]\{\phi\} = \{F\},$$
$$[K_{\phi u}]\{u\} + [K_{\phi\phi}]\{\phi\} = \{Q\},$$

(1)

where

$$[M] = \int_V \rho [N_u]^T [N_u] \, dV \qquad \text{is the kinematically consistent mass matrix;}$$

$$[K_{uu}] = \int_V [B_u]^T [C^E][B_u] \, dV \qquad \text{is the elastic stiffness matrix;}$$

$$[K_{u\phi}] = \int_V [B_u]^T [e]^T [B_\phi] \, dV \qquad \text{is the piezoelectric coupling matrix;}$$

$$[K_{\phi\phi}] = - \int_V [B_\phi]^T [\varepsilon][B_\phi] \, dV \qquad \text{is the dielectric stiffness matrix;}$$

$$\{F\} = \int_V [N_u]^T \{f_b\} \, dV + \int_{S_1} [N_u]^T \{f_S\} d\Omega + [N_u]^T \{f_c\} \qquad \text{is the mechanical force vector;}$$

$$\{Q\} = - \int_{S_2} [N_\phi]^T q_s d\Omega - [N_\phi]^T q_c \qquad \text{is the electrical force vector.}$$

In these equations, u is the displacement, ϕ is the electric potential, Q represents the applied concentrated electric charges, ρ is the mass density, $[B_u]$ and $[B_\phi]$ are the derivatives of the shape functions $[N_u]$ and $[N_\phi]$, $[C^E]$, $[\varepsilon]$, and $[e]$ are the elasticity, dielectric, and piezoelectric matrices, respectively, f_b denotes the body force, f_s is the surface force, f_c is the concentrated force, q_s is the surface charge, q_c is the point charge, S_1 is the area where mechanical forces are applied, and S_2 is the area where electrical charges are applied. The above matrix equations are written in partitioned form to reflect the coupling between the elastic and electric fields. Equation (1) can be condensed to represent the sensor's potential in terms of the sensor displacement in the form

$$\{\phi_s\} = [K_{\phi\phi}]^{-1}(-[K_{u\phi}^T]\{u\}). \tag{2}$$

The commercial finite element program ANSYS was employed for modeling the piezoelectric sensors. The three-dimensional coupled element (SOLID5) of ANSYS was used for modeling the piezoelectric patch. Note that this formulation is essentially used to obtain the voltage-time domain data of the excited pipe through the sensors attached to it.

FFT-based damage detection method

All the methods presented here for comparison purposes are based on the assumption that damage is located between two locations that exhibit the greatest damage indices. The selection of the sensor locations is arbitrary. The methodology relies on vibration data obtained through the sensors located on these points. If more than one defect is located in between two sensors, then the methodologies in their present form could not indicate the existence of more than one defect. However these methodologies could detect muti-defects, as long as each defect is located in between a pair of sensors.

The calculation of discrete approximation of FFT of the transient response data can be represented by (see [Santamarina and Dante 1998])

$$X(\omega) = \sum_{r=0}^{N-1} x(r\Delta t)e^{-i\omega r\Delta t}\Delta t, \quad \Delta t = \frac{T}{N}, \tag{3}$$

where $x(t)$ is a periodic function (containing the output of the piezoelectric sensors) with a period of T, N is the total number of samples, $X(\omega)$ is the frequency response of $x(t)$.

The equivalent energy can be represented by

$$E_{xx} = \int_{-\infty}^{+\infty} |X(\omega)|^2 d\omega. \tag{4}$$

The equivalent FFT energy index is assumed to be

$$\text{FRF} - E_\omega = \sum_\omega \left| \frac{E_{xx}^{\text{damaged}}}{E_{xx}^{\text{healthy}}} \right| \frac{2}{N} \times 100, \tag{5}$$

where E_{xx}^{damaged} and E_{xx}^{healthy} are the before and after damage energies in the pipeline, respectively.

This research proposes the integral of the amplitude of the frequency response function (FRF) evaluated over various frequency ranges as a novel quantity, that is, a damage index. The selected frequency
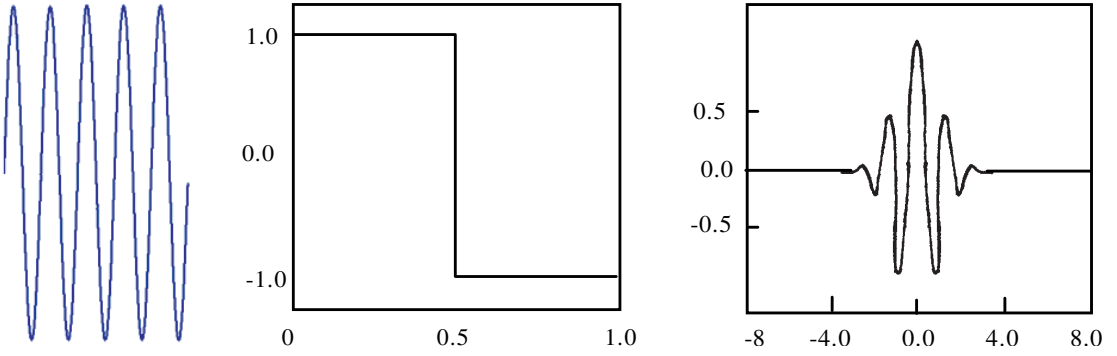
Figure 1. Schematics of a typical FFT function (left) and two typical wavelet functions (from Haar and Morlet, respectively).

intervals should be such that their limits bound the natural frequencies of the original undamaged system, because these are the regions most sensitive to the changes in response to the damage causing parameters.

This integral is then defined by

$$I_x = \int_{-\infty}^{+\infty} |X(\omega)| \, d\omega. \tag{6}$$

The damage index of FFT integration is defined as

$$\text{FRF } I_\omega = \left| \frac{I_x^{\text{damaged}} - I_x^{\text{healthy}}}{I_x^{\text{healthy}}} \right| \times 100, \tag{7}$$

where I_x^{damaged} and I_x^{healthy} are the integral of the pipe's signals at the damaged and undamaged state.

Wavelet transformation and damage index

The discrete wavelet transform. The following paragraphs provide brief reviews of wavelets and wavelet transformation methodologies with the aim of offering the reader a better perspective of the work carried out in this paper.

Transformation of a signal is just another form of representing a signal; such a transformation, however, would not alter the content of a given signal. In the context of the work presented here, the wavelet transform (WT) provides a time-frequency representation of a signal. It was developed to overcome the limitations of the short time Fourier transform (STFT), which is commonly used to analyze nonstationary signals. While STFT provides a constant resolution at all frequencies, WT uses a multiresolution technique by which different frequencies are analyzed with different resolutions.

While a wave is an oscillating function of time or space and is periodic, wavelets are localized waves. They have their energies concentrated in time or space and are suited for analysis of transient signals. The Fourier Transform and STFT use waves of regular shapes to analyze signals, while the Wavelet Transform uses wavelets of finite energy to do the same. Figure 1 schematically illustrates typical FFT and wavelet waves.

A wavelet analysis is very similar to a STFT analysis. In STFT analysis, the signal to be analyzed is multiplied by a window function, while in wavelet analysis the function is multiplied with a wavelet function. However, as shown in the above figure, unlike the STFT, in WT, the width of the wavelet function changes with each spectral component. As a rule of thumb, the WT provides good time resolution but relatively poor frequency resolution at high frequencies. However, when used at low frequencies, it provides good frequency resolution, but relatively poor time resolution.

Wavelet-based damage detection method

Wavelet packets consist of a set of linearly combined usual wavelet functions. A wavelet packet function has three indices, $\psi^i_{j,k}(t)$, where the integers i, j and k are the modulation, the scale, and translation parameters, respectively, and

$$\psi^i_{j,k}(t) = 2^{j/2}\psi^i(2^j t - k). \tag{8}$$

The wavelets ψ^i are obtained from the following recursive relationships

$$\psi^{2i}(t) = \sqrt{2}\sum_{k=-\infty}^{\infty} h(k)\psi^i(2t - k),$$

$$\psi^{2i+1}(t) = \sqrt{2}\sum_{k=-\infty}^{\infty} g(k)\psi^i(2t - k). \tag{9}$$

Note that the first wavelet is the so-called mother wavelet function

$$\psi^0(t) = \varphi(t), \qquad \psi^1(t) = \psi(t). \tag{10}$$

The discrete filters $h(k)$ and $g(k)$ are the quadrature mirror filters associated with the scaling function $\varphi(t)$ and the mother wavelet function $\psi(t)$. Any measurable and square-integratable function can be decomposed into wavelet packet component functions. The decomposition process is a recursive filter-decimation operation. The decomposed wavelet packet component signals $f^i_j(t)$ can be expressed by a linear combination of wavelet packet functions $\psi^i_{j,k}(t)$ as follows

$$f^i_j(t) = \sum_{k=-\infty}^{\infty} c^i_{j,k}\psi^i_{j,k}(t). \tag{11}$$

The wavelet packet coefficients $c^i_{j,k}(t)$ can be obtained from

$$c^i_{j,k} = \int_{-\infty}^{\infty} f(t)\psi^i_{j,k}(t). \tag{12}$$

Each component in the wavelet packet decomposition (WPD) tree can be viewed as the output of a filter tuned to a particular basis function. Thus the whole tree can be regarded as a filter bank. At the top of the WPD tree (lower decomposition level), the WPD yields good resolution in the time domain but poor resolution in the frequency domain. On the other hand, at the bottom of the WPD tree (higher decomposition level), the WPD results in good resolution in the frequency domain, yet poor resolution in the time domain. For the purpose of structural health monitoring, frequency domain information tends

to be more important, and thus a high level of the WPD is often required to detect the minute changes in the signals.

After understanding the basis of WPD, methodologies that use these signals for structural condition assessment are briefly summarized. [2002] demonstrated numerically, using a three-span bridge, that wavelet packet component energies were sensitive parameters and could be used as structural condition signatures. These component energies were defined as

$$E_j^i = \int_{-\infty}^{\infty} f_j^i(t)^2 dt. \tag{13}$$

It can be shown that when the mother wavelet is semiorthogonal or orthogonal, the signal energy E_f would be the summation of the jth level component energies, as

$$E_f = \int_{-\infty}^{\infty} f^2(t) dt = \sum_{i=1}^{2j} E_j^i. \tag{14}$$

Since each wavelet packet component contains information of the signal in a specific time-frequency window, the magnitude of the component energy could therefore vary quite significantly.

Mathematical description of the Hilbert–Huang transform (HHT). The Hilbert transform $Y(t)$ of an arbitrary function $X(t)$, in lower pass (Lp-) class [Titchmarsh 1986] is defined by

$$Y(t) = \frac{1}{\pi} P \int_{-\infty}^{\infty} \frac{X(t')}{t - t'} dt', \tag{15}$$

where P indicates the Cauchy principal value. Therefore an analytic signal, $Z(t)$, can be produced by

$$Z(t) = X(t) + iY(t) = a(t)e^{i\theta(t)}, \tag{16}$$

where

$$a(t) = (X^2(t) + Y^2(t))^{1/2} \quad \text{and} \quad \theta(t) = \arctan \frac{Y(t)}{X(t)} \tag{17}$$

are the instantaneous amplitude and phase angle of $X(t)$.

Since the Hilbert transform $Y(t)$ is defined as the convolution of $X(t)$ and $1/t$ by (12), it emphasizes the local properties of $X(t)$, even though the transform is global. In (13), the polar coordinate expression further clarifies the local nature of this representation. With (13), the instantaneous frequency of $X(t)$ can be defined by

$$\omega(t) = \frac{d\theta(t)}{dt}. \tag{18}$$

The method of EMD was recently proposed in [Huang et al. 1998] to decompose a measured response signal $x(t)$ into intrinsic mode functions (IMFs) that would admit well-behaved Hilbert transforms. The procedure of EMD is to construct the upper and lower envelopes of the signal by spline-fitting, and compute the average (mean) of both envelopes. Then the signal is subtracted from the mean (a process known as the sifting process). By repeating the sifting process until the resulting signal becomes a mono component (that is, one up-crossing or down-crossing) of zero, it will result in one local peak or (trough), indicating that the number of up-crossings (or down-crossings) of zero is equal to the number of peaks (or troughs). Such a mono component signal would then admit a well-behaved Hilbert transform and is

referred to as an IMF. The original signal is then subtracted from the IMF and the repeated sifting process is applied to the remaining signal to obtain another IMF. The process is repeated to obtain n IMFs:

$$x(t) = \sum_{j=1}^{n} c_j(t) + r_n(t), \tag{19}$$

where $c_j(t)$ $(j = 1, 2, \ldots, n)$ are the IMFs of the measured signal $x(t)$, and $r_n(t)$ are the residues that could be viewed as the mean trend of the signal or a constant.

The above set of operations is referred to as the EMD method, which has been patented by Huang [1998; 1999]. He showed that the characteristics of the signal could be extracted through the behavior of the IMFs, and that the EMD is applicable to nonstationary or nonlinear signals. Based on the EMD approach described above, the first IMF has the highest frequency contents of the signal. During the EMD process, a specified frequency is referred to as the intermittency frequency ω_{int}, which can be imposed so that the resulting IMF will have frequencies higher than ω_{int}; see [Huang 1998]. This is accomplished by removing the data that have frequencies lower than ω_{int} from the IMFs by a straightforward counting process.

The Hilbert–Huang transform (HHT) method was also proposed in [Huang 1998]. It consists of two parts: an EMD, and a Hilbert spectral analysis. The method is based on decomposing a signal into intrinsic mode functions (IMFs) using the described EMD method, with the condition that each IMF admits a well-behaved HHT. Then, the HHT is applied to each intrinsic mode function to obtain a decomposition of the signal in the frequency-time domain. This approach is also referred to as the Hilbert–Huang spectral analysis (HHSA) and it is applicable to a nonstationary signal [Huang et al. 1998; 1999].

In this paper, the EMD method proposed in [Huang 1998] will be used to decompose the measured response signal (output voltage of the piezoelectric sensors) into IMFs that would admit a well-behaved Hilbert transform. Based on the EMD, the modal response of each mode can then be extracted from the output voltage of a piezoelectric sensor (or any other similar sensors). The key advantage of using the HHT and EMD, rather than FFT or wavelet methodologies is that one is enabled to use the instantaneous frequency to display the data in a time-frequency-energy format. This would produce a more accurate, real-life representation of the data, thereby eliminating the artifacts associated with the nonlocal and adaptive limitations imposed by the FFT or wavelet methodologies. Moreover, the conventional Fourier-based methods are designed to work with linear data or linear representations of nonlinear data. Therefore, they are not efficient for studying nonlinear waves and other nonlinear phenomena.

In this paper, a damage index is also introduced that is based on the first (IMFs) of the output voltages obtained through piezoelectric sensors, which are passed through the band pass filter to ensure that they only contain the first natural frequency of the system. The energy of the first (IMFs) is defined as

$$E = \int_0^{t_0} (\text{IMF})^2 dt. \tag{20}$$

The damage index is therefore defined as

$$DI_{mn} = \left| \frac{E_{mn}^{\text{healthy}} - E_{mn}^{\text{damaged}}}{E_{mn}^{\text{healthy}}} \right| \times 100, \tag{21}$$

where m is the sensor's number or the considered degree of freedom of structure, n is the mode shape and (IMF) is the first calculated intrinsic mode function of the signal which has been passed through the band-pass criterion.

Band-pass filtering and EMD. The isolation of the modal responses using the EMD method presented above has an advantage in that the frequency content of the signal at each time instant can be effectively obtained. However, the associated computation could be quite involved, in particular when the modal frequencies are high, and/or when the signal is polluted by an elevated noise level. In these cases, to obtain accurate modal responses, one should increase the number of siftings in the EMD procedure. Therefore, to simplify and decrease the computational efforts, an alternative approach based on the band-pass filter was proposed in [Yang et al. 2003]. With that approach one could determine the approximate frequency range for each natural frequency from the Fourier spectrum of the output voltage. For example, if one looks at the power spectrum analysis of sensor 3, as illustrated in 3, one would see that the first mode is between 60 to 65 Hz. Each signal is then processed through the band-pass filters with a set frequency band. The time history obtained from the jth band-pass filter (jth natural frequency) is then processed through EMD. In this way, the first resulting IMF would be quite close to the jth modal response. By repeating the above procedure for the other natural frequencies, one could then obtain n modal responses. In Table 1 the result of calculating natural frequency based on EMD method is tabulated. Here we pass all of the output signals of piezoelectric sensors through band pass filter which only has a first natural frequency because our damage index is based on first IMFs of first natural frequency.

Examples. To investigate the effectiveness of the proposed piezoelectric-based vibrational sensing damage detection methodology for assessing the health of pipeline systems, we examine the response of aluminum pipes bearing various levels of damage. In each analysis, the pipe hosts nine piezoelectric patches bonded onto it. The physical and material properties of the pipes, which are made of aluminum, are provided in Table 2.

Nine PZT BM500 patches with dimensions of 50 mm long, 50 mm wide and 1 mm thick, with mass density of 7650 kg/m^3 were used in this analysis. The elasticity matrix $[C^E]$, piezoelectric matrix $[e]$ and dielectric matrix $[\varepsilon^S]$ of PZT BM500 piezoceramic are listed in [Sensor 2001] as

$$[C^E] = \begin{bmatrix} 12.1 & 7.54 & 7.52 & 0 & 0 & 0 \\ 7.54 & 12.1 & 7.52 & 0 & 0 & 0 \\ 7.52 & 7.52 & 11.1 & 0 & 0 & 0 \\ 0 & 0 & 0 & 2.11 & 0 & 0 \\ 0 & 0 & 0 & 0 & 2.26 & 0 \\ 0 & 0 & 0 & 0 & 0 & 2.26 \end{bmatrix} \times 10^{10} \text{ [N / m}^2\text{]},$$

$$[e] = \begin{bmatrix} 0 & 0 & 0 & 0 & 0 & 12.3 \\ 0 & 0 & 0 & 0 & 12.3 & 0 \\ -5.4 & -5.4 & 15.1 & 0 & 0 & 0 \end{bmatrix} \text{ [C/m}^2\text{]}, \qquad [\varepsilon^S] = \begin{bmatrix} 8.11 & 0 & 0 \\ 0 & 8.11 & 0 \\ 0 & 0 & 7.349 \end{bmatrix} \times 10^{-9} \text{ [F / m]},$$

The commercial finite element program ANSYS was employed for modeling the response of pipes and the piezoelectric sensors. The three-dimensional coupled element (SOLID5) of ANSYS was used for modeling. The pipes were cantilevered (fully supported at one end, and free at the other end). The mesh

| Pipe Condition	Modes	FE (eigenvalue) solution (Hz)	FRF solution (Hz)	EMD solution
Healthy pipe	1	62.4	63.8	62.45
	2	339.1	332.1	332.28
	3	379.2	380.1	379.04
Damaged pipe (DL2)	1	62.3	63.7	62.41
	2	333.1	326.6	326.91
	3	377.1	376.3	376.59

Table 1. Comparison of computed natural frequencies.

Outside diameter	273.5 mm
Wall thickness	9.3 mm
Length	2000 mm
Young's modulus	67×10^3 N/mm^2
Poisson ratio	$\nu = 0.33$
Mass density	2730 kg/m^3

**Table 2.** Geometry and material properties of the pipe.

density had 40 rows of elements along the axial direction, 18 elements along the pipe's circumference in each row, and two layers through the thickness, as shown in Figure 2a. The pipe was assumed to have been impacted at its free end by a pendulum, which was simulated by applying a concentrated load with magnitude of 1000N applied in a time interval of 2.5 μs. Figure 2d shows a graphical representation of the applied load. Different damage locations, sizes and stiffness reductions (as a damage form) were considered, which will be described in the following sections.

Case 1: dynamical response of piezoelectric sensors for different damage locations. To evaluate the integrity of the proposed methodologies, three different cantilevered aluminum pipes, each having damage at different locations along their length, were considered. This form of damage was assumed to have resulted from corrosion, and the subsequent reduction of material at that location. This is simulated by removing one layer (interior layers) element within two rows (that is, a 100 mm width) off the mesh forming the pipe. The defects are assumed to be located halfway between sensors 2 and 3, sensors 4 and 5, and sensors 7 and 8. These damage locations will be referred to as DL1, DL2 and DL3. A comparison of the natural frequencies obtained by the FEM (eigenvalue) analysis with those obtained from the frequency response function and EMD analysis of the sensors for the healthy and damaged pipes (DL2) is made in Table 1. The first and second mode shapes for the healthy pipe are shown in Figures 2b and 2c. As indicated in Table 1, there is fairly close agreement among the results obtained from the three approaches, indicating that the sensors' response from a modal analysis could be effectively used to evaluate the dynamic behavior of the system, since there are distinct differences between the two signals.

(a)

(b)

(c)

(d)
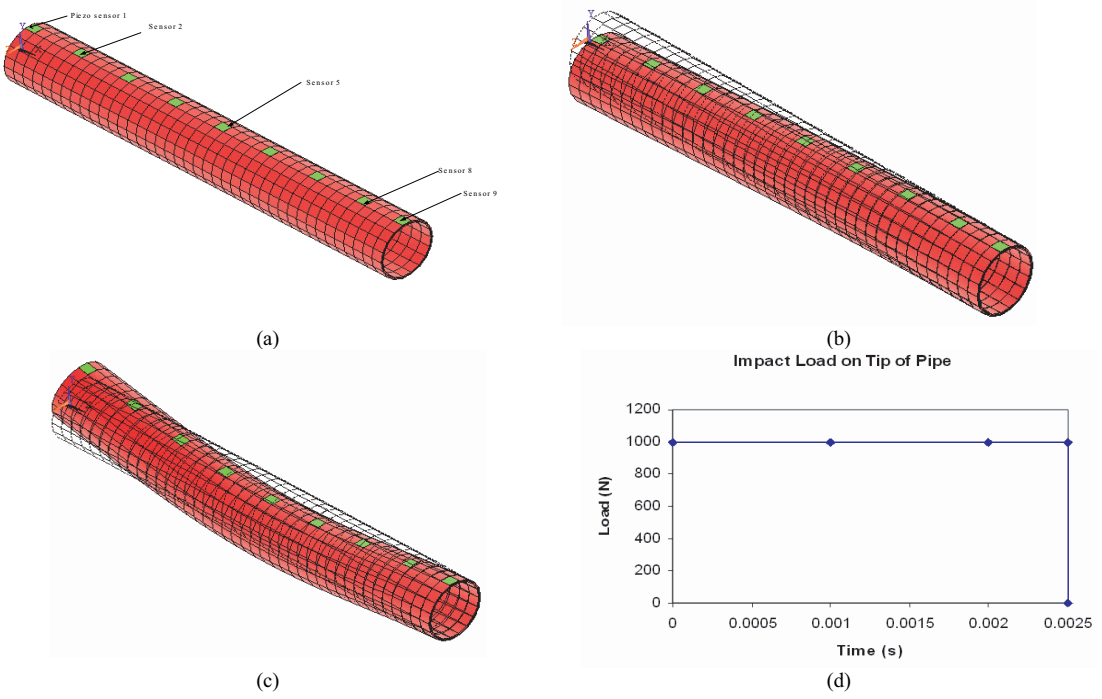
Figure 2. Computational dynamic response analysis of the pipe for (a) FEM mesh, (b) first vibration mode, (c) second vibration mode, and (d) impact load-time history of the tip of the pipe.

Typical FRF response curves of one of the sensors (sensor 5) for the healthy and damaged pipes (where damage is located on sensor location DL2) are shown in Figure 3. Figure 4 illustrates the FRF response
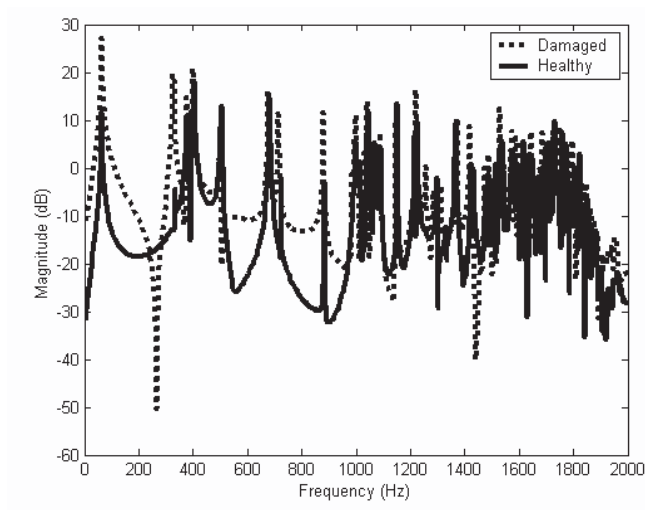

Figure 3. Typical FRF response curves of sensor 5 for healthy and damaged pipes.
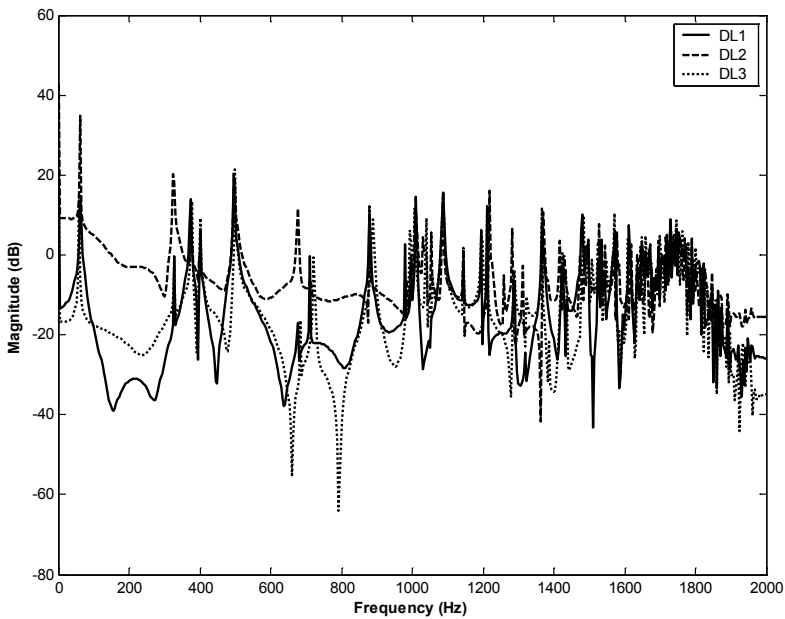
Figure 4. Comparison of FRF response for sensor 5 for damage cases DL1, DL2 and DL3.

curves of sensor 5 for the pipes having damage at three locations (DL1, DL2 and DL3). The response of sensors 2, 4 and 7 when damage is located in location 2 (DL2) is illustrated in Figure 5. A careful examination of the FRF responses shown in Figures 4 and 5 indicates that identical piezoelectric sensors,
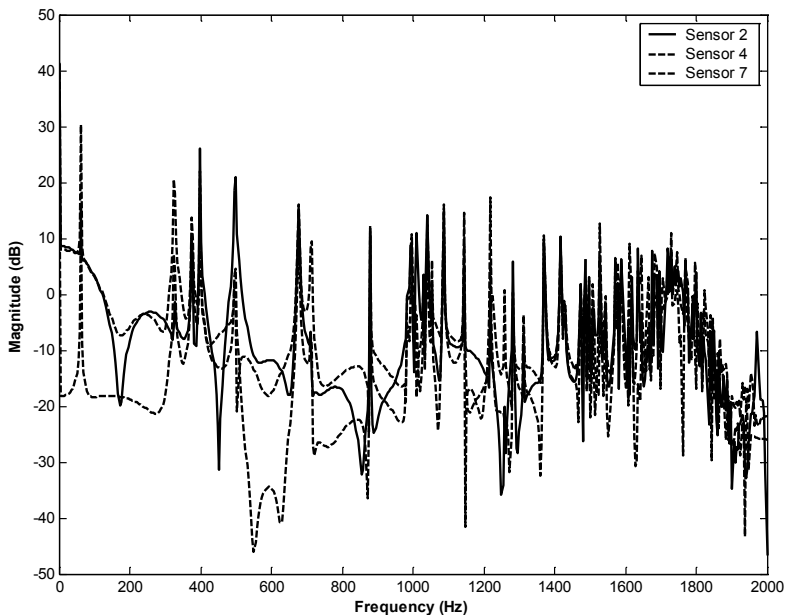
Figure 5. Comparison of FRF response for sensors 2, 4 and 7 for the damage case DL2.
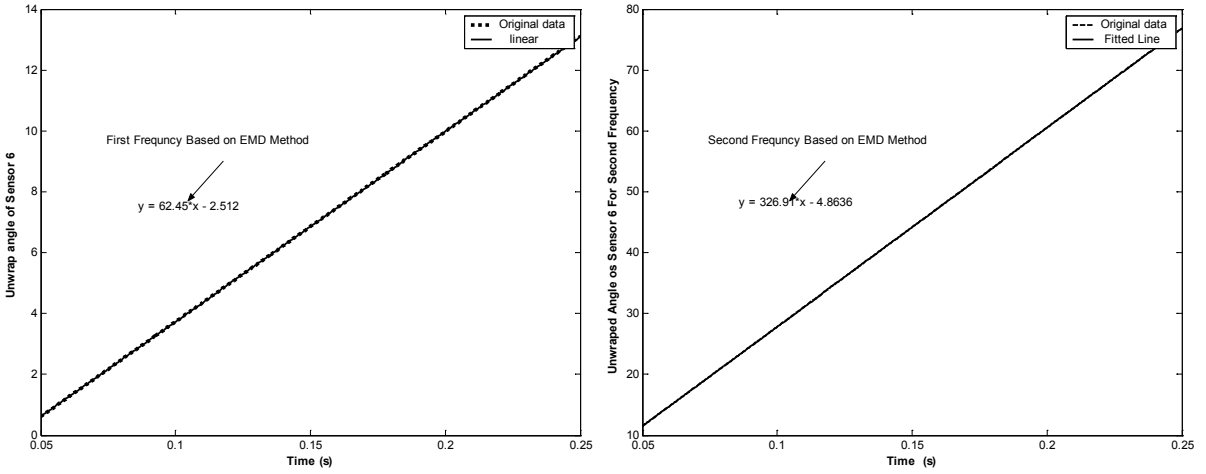
**Figure 6.** Empirical mode decomposition (EMD) for calculating first and second natural frequency based on first IMF.

mounted under a similar condition on a pipe, would respond differently depending on the presence and location of damage in the substrate. Figure 6 shows calculation of the first and second natural frequencies based on EMD calculations for sensor 6 for the case of DL2. This is a significant observation, in that health monitoring of pipeline systems could be effectively achieved by using an array of piezoelectric transducers. The following section will provide justification for this statement.

Wavelet analysis was also applied to the three cases. Specifically, the db4 wavelet and wavelet packet were used to conduct the analyses. Detailed wavelet responses obtained through the analysis of sensor 4 for the healthy and DL2 damaged pipeline cases are shown in Figure 7. Similarly, the information obtained for the wavelet packet analysis is shown in Figure 8. The EMD was also applied to the all cases. Detailed results of EMD for calculation of IMFs of sensor 3 for healthy pipe and sensor 6 for
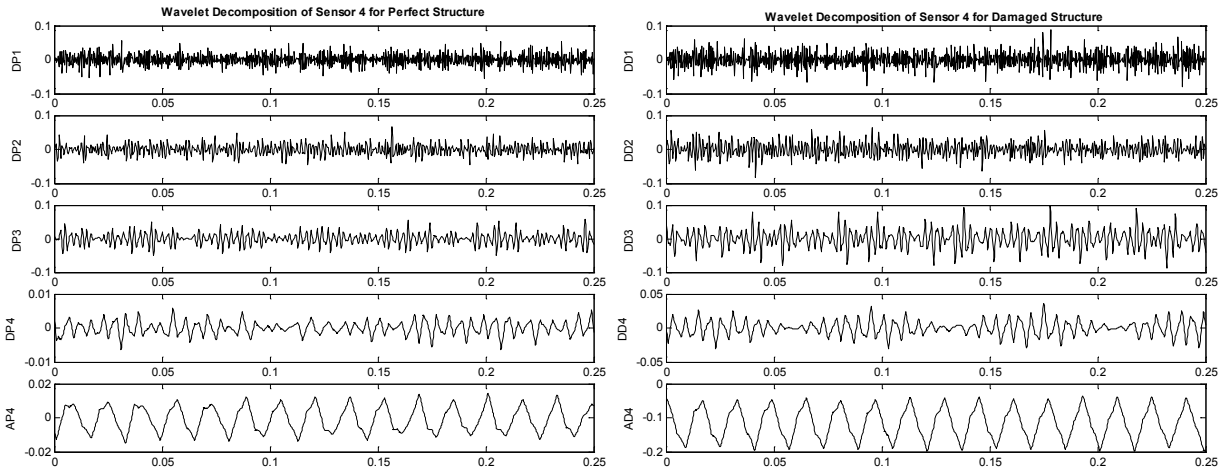

Figure 7. Wavelet simulation of (left) the healthy pipe, and (right) the damaged pipe (at DL2).
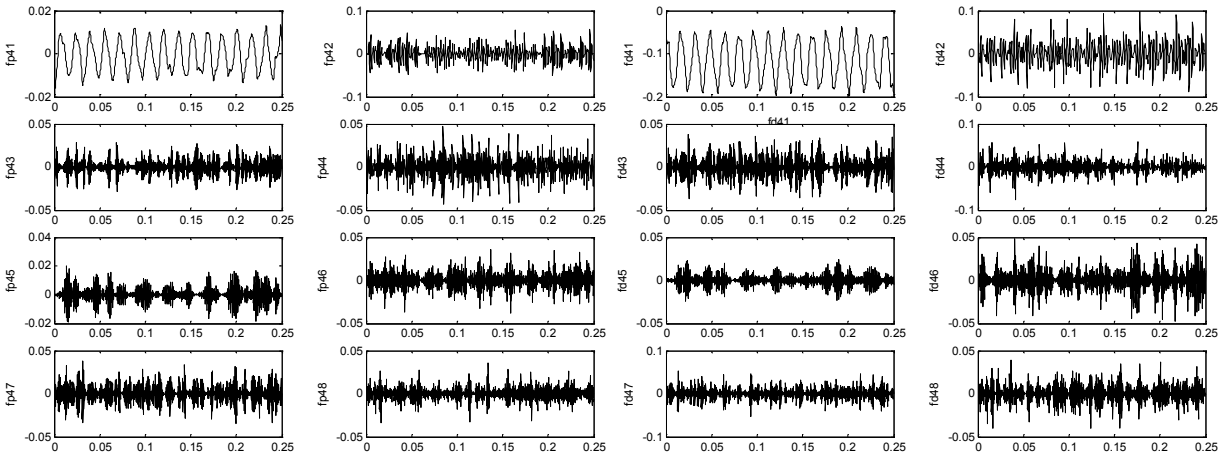
Figure 8. Wavelet packet simulation of (left) the healthy pipe, and (right) the damaged pipe (at DL2).

DL1 are shown in Figure 9. Notice that the wavelet methodology adopted here involves a multiresolution analysis for a piece of data windowed by shifted and scaled wavelets generated from the so-called mother wavelet [Wickerhauser 1994]. Only the higher-resolution details were used to make the above observation. Therefore, to detect a potential damage at a particular point in time would only require a small portion of data neighboring that particular time. This is an attractive feature of this approach and an effective means for on-line heath monitoring of pipelines. As seen from Figures 8 and 9, the initial signal has been decomposed to its IMFs and baby wavelets. One could reach the original signal by inversing the process.

The energy components obtained by the FFT, EMD, WT and WPT and EMD are tabulated in Table 3. In this table, the WT and WPT energy components are evaluated based on the db3 wavelet at the fourth
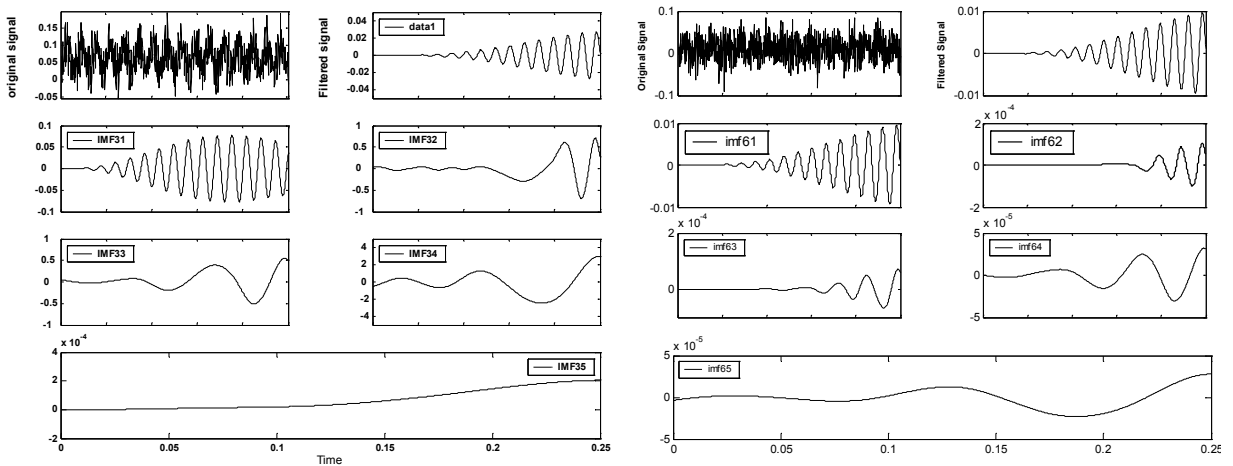
Figure 9. EMD of the healthy pipe for (left) sensor 3, and (right) sensor 6.

| Method	Components	E_{healthy} (0–0.25 s)	E_{damaged} (0–0.25 s)	Change (%)
FFT	—	394.2	2426.2	515.5
WT	$d_4^a(t)$	1.2687×10^{-5}	3.9225×10^{-3}	30816.7
	$d_4^d(t)$	8.6086×10^{-7}	2.5979×10^{-5}	2917.8
	$d_3^d(t)$	6.0146×10^{-5}	1.5819×10^{-4}	163.0
	$d_2^d(t)$	5.0762×10^{-5}	8.3846×10^{-5}	65.2
	$d_1^d(t)$	7.2237×10^{-5}	1.2242×10^{-4}	69.5
WPT	$d_4^1(t)$	8.6086×10^{-7}	2.5979×10^{-5}	2917.8
	$d_4^2(t)$	4.6565×10^{-5}	5.9677×10^{-5}	28.2
	$d_4^3(t)$	1.3367×10^{-5}	9.8914×10^{-5}	640.0
	$d_4^4(t)$	8.7762×10^{-6}	1.6786×10^{-5}	91.3
	$d_4^5(t)$	6.8594×10^{-6}	1.3166×10^{-5}	91.9
	$d_4^6(t)$	1.7970×10^{-5}	1.7382×10^{-5}	3.3
	$d_4^7(t)$	1.6655×10^{-5}	3.6173×10^{-5}	117.2
	$d_4^8(t)$	2.8572×10^{-7}	3.6739×10^{-7}	28.6
EMD	—	0.0115	1.0039	8629.56

Table 3. Comparison of computed energies for FFT, WT and WPT for the damage case DL2.

level decomposition. In the case of the WT approach, the $d_4^a(t)$ and $d_4^d(t)$ component of energies shows sensitivity to damage. However, in the case of the WPT approach, the $d_4^1(t)$ component of energy exhibits more sensitivity to damage.

Figure 10 illustrates the damage signatures (damage energy indices evaluated based on the EMD, FFT integration, WT, and WPT methodologies at the damage locations) as a function of the sensor number mounted along the axial direction of the pipe for the case where the damage is located in location 2 (DL2). It is observed that all four approaches could detect the defect locations within a range of a pair of sensors. However, it is noted that the WT , WPT, and EMD methodologies could predict the damage location more accurately than the FFT methods (that is, the differences in the energy indices from the sensors have much larger margin in WT and WPT than in the other methods). The results also confirm the suitability of PZT sensors and their sensitivity for detecting damage in pipelines.

Figure 11, left, illustrates the damage indices based on EMD, WT, and WPT as a function of sensor number for the case where the damage is located in location (DL1). Figure 11, right, shows the damage indices based on EMD and WPT for the case where the damage is located in location (DL2).

Case 2: detection of damage due to reduction in flexural rigidity. To further examine the integrity and sensitivity of the selected methodologies, this case study examines a pipe having reduced flexural rigidity between sensors 4 and 5. This effect was simulated by reducing the Young's modulus of the two rows of elements between sensors 4 and 5. The reduction in flexural rigidity ranges from 10% to 50%,
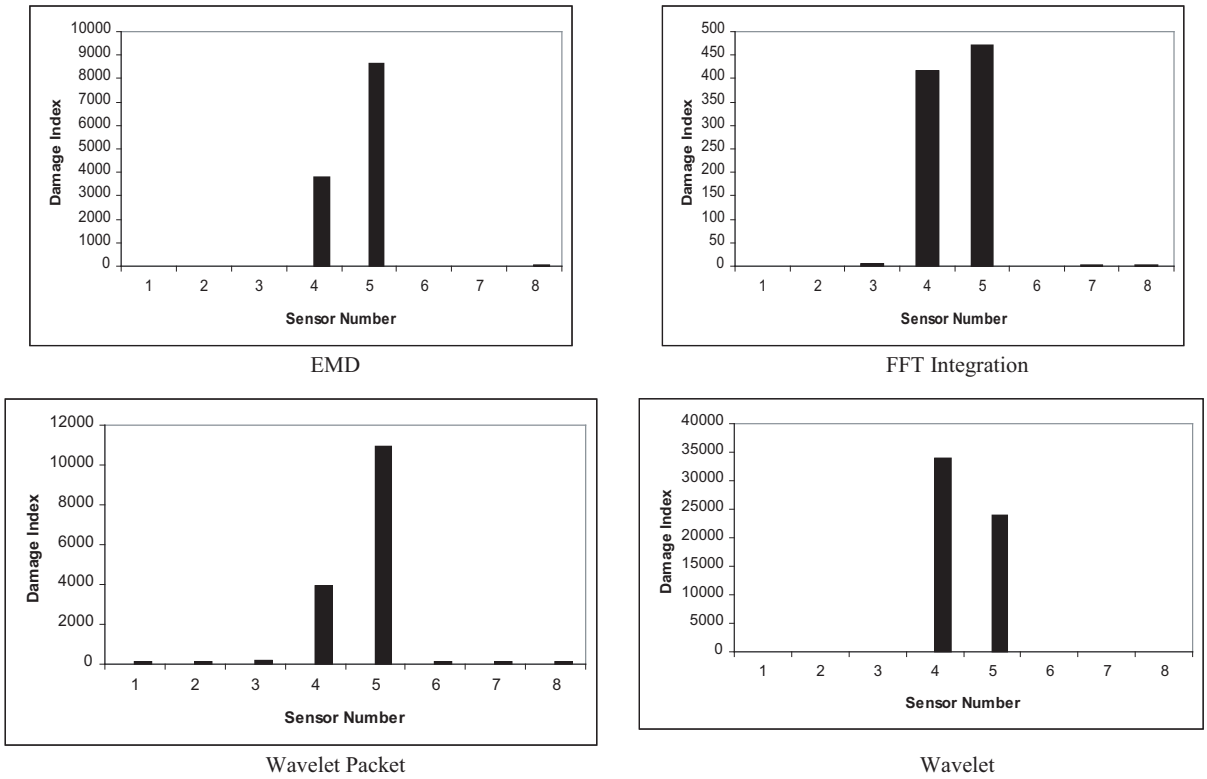
Figure 10. Damage indices for various percentiles of degradation based on the four methodologies (DL2).

representing different intensities of damage. The comparison of FRF response of sensor 4 for the cases of 10%, 30% and 50% reduction in rigidity is plotted in Figure 12. The comparison of the damage indices evaluated by EMD, WT, and WPT methodologies are illustrated in Figure 13. The damage indices are
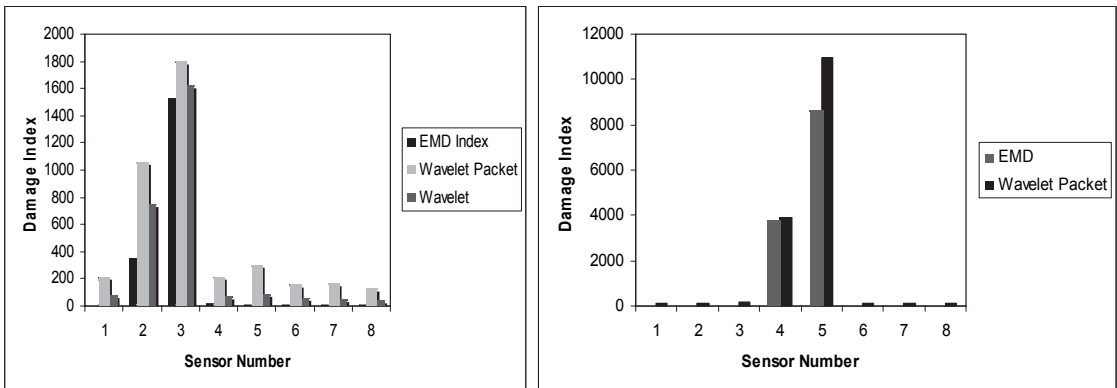
Figure 11. Damage index at (left) the damage location DL1, based on EMD, WT and WPT; (right) the damage location DL2 based on EMD and WPT.
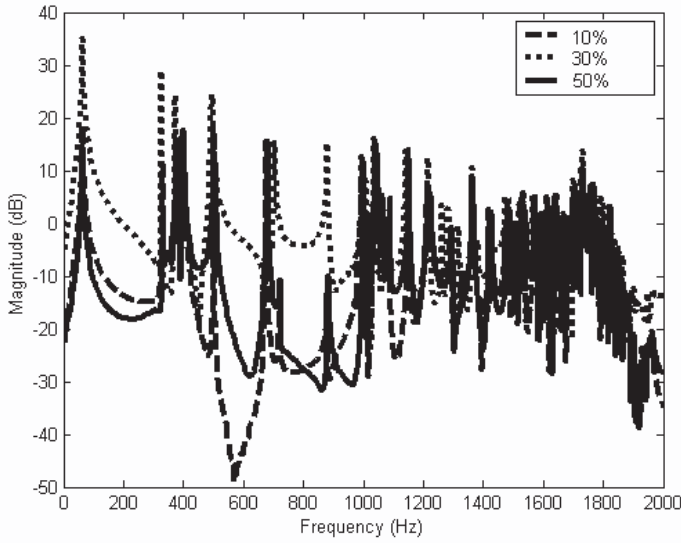
Figure 12. Comparison of the FRF responses for the pipe with 10%, 30% and 50% reduction in flexural rigidity.

clearly increased near the location where the pipe's rigidity is decreased. As can be clearly seen from Figure 13, the EMD method yields an approximately linear function for the damage index compared to WT or WPT methods.

As the case studies show, the Fourier transform method and the associated FFTs carry strong a priori assumptions about the source data, such as the linearity and status of the data. Signals associated with natural phenomena are essentially nonlinear and nonstationary. The accommodation of this fact in FFT-based analysis often involves using more data samples to assure acceptable convergence and nonalgorithmic procedural steps for the interpretation of FFT results. Wavelet-based analysis may yield
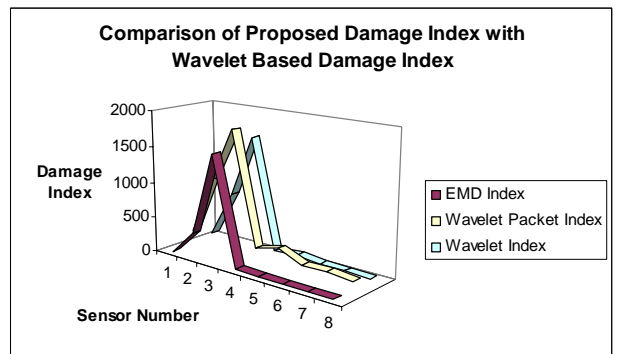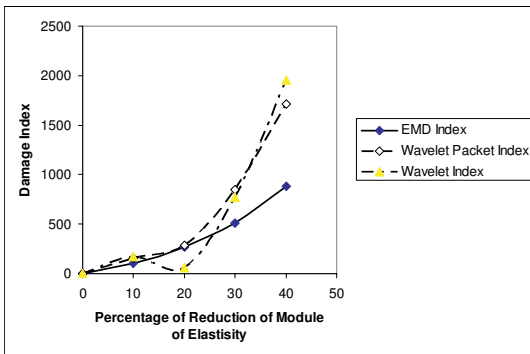
Figure 13. Comparison of variation in damage indices (left, as a function of axial direction; right, as a function of sensor number) for the pipe with reduction in flexure rigidity obtained by the FFT integration, WT and WPT methods (DL2).

some improvement over the FFT because it can handle nonstationary data. However, it retains the limitation of requiring the data set to be linear. The wavelet method may also prove inadequate, because notwithstanding the fact that it is well-suited for analyzing data with gradual frequency changes, its nonlocally adaptive approach causes leakage. This leakage can spread frequency energy over a wider range, removing definition from data and giving it an overly smooth appearance. Only recently has an alternative view for mechanics, the Hilbert view, and the associated processing tool, the empirical mode decomposition (EMD), been proposed.

The HHT, however, allows direct algorithmic analysis of nonlinear and nonstationary data functions by using an engineering and a posteriori data processing method, namely an EMD. This method enables one to perform unconstrained decomposition of the source data function into a finite set of intrinsic mode functions (IMFs) that can be effectively analyzed by the classical Hilbert transform, thus making the HHT devoid of the FFT limitations.

A case study was experimentally investigated to confirm the integrity of the proposed approach. The experimental investigation considered an adhesively bonded joint connecting two PVC plastic pipes. Three different specimen configurations were considered. In total, 24 test set-ups were considered with each specimen to examine the influence of several parameters. The parameters that were considered were the loading (excitation) location, support tightness, and debond location.

Each specimen had a different degree of disbond in its joint region; that is, one specimen was fully bonded, one bonded around half of its parameter and one only around a quarter of the parameter. The specimens were instrumented by piezoelectric sensors. The piezoelectric patches implemented in this investigation were QP15N PZT QuickPack strain sensors available from Mide Technology Corporation (Medford, MA). These patches were bonded to the surface of the pipe at the joint region using the West System's two-part epoxy. On the test specimens containing damage, piezoelectric sensors were positioned at the center of the damaged section of the joint and on the location 180° opposite to the first sensor. For the fully bonded pipe there was only one sensor bonded on the center of the joint.

To determine the existent and extent of damage in the adhesively bonded PVC pipe joints, the dynamic responses of the pipes were monitored at the joint region using a simply supported beam setup as schematically shown in Figure 14. The pipes were excited with an impulse hammer. The impulse hammer response was monitored continuously using a data acquisition card as well. The response of the piezoelectric sensors was also continuously monitored with a multipurpose data acquisition card in a PC. 40,000 data points were collected in each test at a rate of 10 kHz.

The results were used and processed based on the proposed methodologies. The integrity of the proposed damage index methodologies was verified and compared. A typical set of results of damage
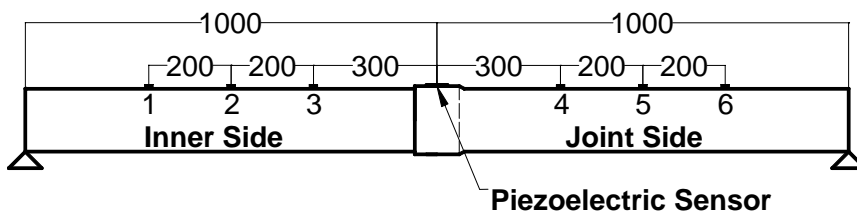
Figure 14. Schematic of the experimental setup of the adhesively bonded joint.
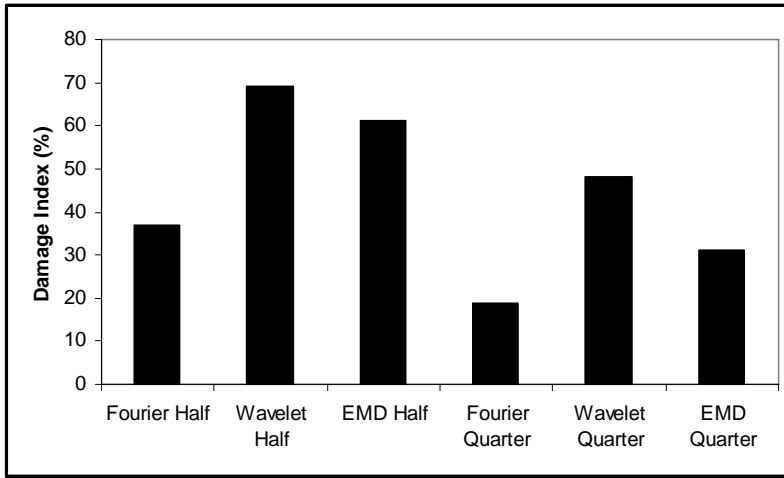
Figure 15. A typical set of experimental results based on different proposed damage indices.

indices evaluated by the various methods are illustrated in Figure 15. The terms *quarter* and *half* refer to the bonding status (that is, the joint has adhesive around a quarter of half of its circumference). The results clearly show that the energy based index obtained through the proposed EMD approach provides the most distinctive results.

Conclusions

Access to an effective health monitoring system is an important aspect of pipeline maintenance. The availability of an accurate and reliable damage detection system can significantly reduce the life-cycle cost of a pipeline system. There are some simple methods, such as root mean square, that in some cases can predict the location of damage, but the method is not effective in all cases. This research introduced a new health monitoring approach based on sensing of the vibration response of a pipe using smart piezoelectric transducers, and then evaluating the vibration response of the pipe using the data obtained by the transducers. In conjunction with the use of three-dimensional piezoelectric FE analysis, a novel approach was proposed for evaluating the damage energy indices established based on (FFT) and (EMD), which has been compared with wavelet transform methodologies. The damage indices proposed in this paper can reveal the location of the defect. Case studies were considered to evaluate the integrity of the proposed methodologies. For this, cantilevered pipes, having various forms of defects, were considered. The defects were assumed to be at various locations, having different intensities (that is, in the form of reduction of wall thickness to simulate a reduction in stiffness due to presence of corrosion). The numerical results confirm that the proposed approaches could effectively identify the existence and intensity of defects in the pipes. However, it was observed that the EMD-based procedure produced an almost linear relationship between the damage density and damage indices, while the relationship is nonlinear in the results produced by both the wavelet packet and wavelet methodologies. In our view, therefore, the EMD produced adequate accuracy for both detecting the location of the damage, and also establishing the severity of the damage. This was not the case for the observation on the wavelet and wavelet packet-based methods.

References

[Ayres et al. 1998] J. W. Ayres, F. Lalande, Z. Chaudhry, and C. A. Rogers, "Qualitative impedance-based health monitoring of civil infrastructures", *Smart Mater. Struct.* **7**:5 (1998), 599–605.

[Cheraghi et al. 2005] N. Cheraghi, G. P. Zou, and F. Taheri, "Piezoelectric-based pipeline damage assessment using Fourier and wavelet analyses", *Comput.-Aided Civ. Infrastruct. Eng.* **20**:5 (2005), 369–382.

[Fuller et al. 1992] C. R. Fuller, S. D. Snyder, C. H. Hansen, and R. J. Silcox, "Active control of interior noise in model aircraft fuselages using piezoceramic actuators", *AIAA J.* **30**:11 (1992), 2613–2617.

[Huang 1998] K. Huang, "A nondestructive instrument bridge safety inspection system (NIBSIS) using a transient load", US Patent 09/210.693, 1998.

[Huang et al. 1998] N. E. Huang, Z. Shen, S. R. Long, M. C. Wu, H. H. Shih, Q. Zheng, N.-C. Yen, C. C. Tung, and H. H. Liu, "The EMD and Hilbert spectrum for nonlinear and nonstationary time series analysis", *Proc. R. Soc. A* **454**:1971 (1998), 903–995.

[Huang et al. 1999] N. E. Huang, Z. Shen, and S. R. Long, "A new view of nonlinear water waves: the Hilbert spectrum", *Annu. Rev. Fluid Mech.* **31** (1999), 417–457.

[Rao and Sunar 1994] S. S. Rao and M. Sunar, "Piezoelectricity and its use in disturbance sensing and control of flexible structures: a survey", *Appl. Mech. Rev.* **47** (1994), 113–136.

[Reber et al. 2002] K. Reber, M. Beller, and N. I. Uzelac, "How do defect assessment methods influence the choice and construction of in-line inspection tools", pp. 2039–2044 in *Proceedings of the 4th International Pipeline Conference* (Calgary, Alberta), ASME, 2002.

[Santamarina and Dante 1998] J. C. Santamarina and F. Dante, *Introduction to discrete signal and inverse problems in civil engineering*, ASCE, Virginia, 1998.

[Sensor 2001] "Comparison chart of piezoelectric materials", Technical report, Sensor Technology Limited, Toronto, 2001, Available at http://209.41.160.145/site/index.cfm?DSP=Section&ID=29.

[Silcox et al. 1992] R. J. Silcox, S. Lefebvre, V. L. Metcalf, T. B. Beyer, and C. R. Fuller, "Evaluation of piezoceramic actuators for control of aircraft interior noise", pp. 542–551 (paper 92–02–091) in *Proceedings of the DGLR/AIAA 14th Aeroacoustics Conference* (Aachen), 1992.

[Sun and Chang 2002] Z. Sun and C. C. Chang, "Structural damage assessment based on wavelet packet transform", *J. Struct. Eng.* (*ASCE*) **128**:10 (2002), 1354–1361.

[Sun et al. 1995] F. P. Sun, Z. Chaudhry, C. A. Rogers, M. Majumdar, and C. Liang, "Automated real-time structure health monitoring via signature pattern recognition", pp. 236–247 in *Smart Structures and Materials 1995: Smart Structures and Integrated Systems* (San Diego, CA), edited by I. Chopra, Proceedings of SPIE **2443**, SPIE, Bellingham, Wash., 1995.

[Titchmarsh 1986] E. C. Titchmarsh, *Introduction to the theory of Fourier integrals*, 3rd ed., Chelsea, New York, 1986. MR 89c:42002 Zbl 63.0367.05

[Tzou and Tseng 1990] H. S. Tzou and C. I. Tseng, "Distributed piezoelectric sensor/actuator design for dynamic measurement/control of distributed parameter systems: a piezoelectric finite element approach", *J. Sound Vib.* **138**:1 (1990), 17–34.

[Wickerhauser 1994] M. V. Wickerhauser, *Adapted wavelet analysis from theory to software*, A K Peters, Wellesley, MA, 1994.

[Wilkie et al. 2002] G. H. Wilkie, T. J. Elam, and D. L. Enbridge, "Comparison of crack detection in-line inspection tools", pp. 69–77 in *Proceedings of the International Pipeline Conference* (Calgary, Alberta), 2002.

[Yang et al. 2003] J. N. Yang, Y. Lei, S. Pan, and N. E. Huang, "System identification of linear structures based on Hilbert–Huang spectral analysis, I: Normal modes", *Earthq. Eng. Struct. Dyn.* **32**:9 (2003), 1443–1467.

[Zou et al. 2000] Y. Zou, L. Tong, and G. P. Steven, "Vibration-based model-dependent damage (delamination) identification and health monitoring for composite structures: a review", *J. Sound Vib.* **230**:2 (2000), 357–378.

NADER CHERAGHI: Cheraghi.Nader@colteng.com
Colt Engineering Corporation, Canada Department of Civil & Resource Engineering, Calgary, AB, Canada

FARID TAHERI: farid.taheri@dal.ca
Department of Civil & Resource Engineering, Dalhousie University, 1360 Barrington St., Halifax, NS B3J 1Z1, Canada
http://myweb.dal.ca/farid

THE FLEXIBILITY OF FUNCTIONALLY GRADED MATERIAL PLATES SUBJECTED TO UNIFORM LOADS

YEN-LING CHUNG AND WEI-TING CHEN

We analyze functionally graded material (FGM) plates with two opposite edges simply supported and the other two edges free subjected to a uniform load. Even though an FGM plate is a kind of composite material, if the Young's modulus of the FGM plates varies along the thickness direction and the Poisson's ratio is constant in the whole FGM plate, the bending and in-plane problems in FGM plates under transverse load only are uncoupled. Therefore, the analytical solution to the bending problem of FGM plates is obtained in this study by Fourier series expansions, which agrees very well with a finite element calculation. Results show that the maximum tensile stresses are located at the bottom of the FGM plates. However, the maximum compressive stresses move to the inside of the FGM plates. The coefficients A_{11}, B_{11}, C_{11} defined in this paper relate to the area and to the first and the second moments of the area under the $E(z)$ curve from $z = -h/2$ to $z = h/2$. The parameter Q_{11}, representing the location of the centroid of the area under the $E(z)$ curve, is related to the location of the neutral surfaces, and S_{11} represents the bending stiffness of the FGM plates.

1. Introduction

Functionally graded materials (FGMs), a type of composite material produced by continuously varying the volume fractions in the thickness direction to obtain a predetermined profile, have received much attention recently because of the advantages of decreasing the mismatch in material properties and reducing residual and thermal stresses [Chung and Chi 2001; Lee and Erdogan 1994]. Many researchers have been working toward an understanding of the material constituent [Chi and Chung 2002; Bao and Wang 1995; Suresh and Mortensen 1998], fracture mechanics [Chi and Chung 2003; Jin and Noda 1994; Jin and Batra 1996; Delale and Erdogan 1983; Gu and Asaro 1997; Cai and Bao 1998; Jin and Paulino 2001; Erdogan and Wu 1996; Erdogan and Chen 1998], and processing of FGMs [Kwon and Crimp 1997; Kesler et al. 1997].

FGMs may be applied to plate structures in aircraft, space vehicles, reactor vessels, and other engineering applications as a thermal barrier. Studies of thermoelastic deformations of FGM plates can be found in many references in the literature. Obata and Noda [1996] theoretically analyzed and numerically calculated the steady thermal stresses in an FGM plate composed of PSZ and Ti-6Al-4V, and determined the optimal FGM plates. Praveen and Reddy [1998] investigated nonlinear transient thermoelastic responses of functionally graded ceramic-metal plates by using a plate finite element that accounts for the transverse shear strains, rotary inertia and moderately large rotations in the Von Karman sense. An exact solution was obtained in [Vel and Batra 2002] for three-dimensional deformations of a simply supported FGM thick rectangular plate subjected to mechanical and thermal loads on its top and/or bottom surfaces.

The exact solutions for mechanical and thermal loads are used to assess the accuracy of classical plate theory, first-order shear deformation theory, and a third-order shear deformation theory. Transient thermal stresses in FGM plates with a simple power-law distribution were investigated in [Vel and Batra 2003].

Buckling behavior plays an important role in plate structures. Elastic bifurcation buckling of FGM plates under in-plane compressive loading was studied in [Feldman and Aboudi 1997], based on a combination of micromechanical and structural approaches. Ma and Wang [2004] investigated the axisymmetric bending and buckling solutions for an FGM circular plate based on third-order plate theory and classical plate theory. The results showed that the first-order shear deformation plate theory is enough to consider the effect of shear deformation on the axisymmetric bending and buckling of FGM plates. The problems of thermal buckling in the axial direction of cylindrical shells made of FGMs varying as a power form were discussed in [Wu et al. 2005]. Moreover, the dynamic stability of conical FGM shells subjected to a periodic impulsive pressure was studied in [Sofiyev 2004] by applying Galerkin's method.

Understanding of the mechanical behavior of an FGM plate becomes very important in assessing the safety of the plate structure. Woo and Meguid [2001] applied Karman theory for large deformations to obtain the analytical solution for plates and shells under transverse mechanical loads and a temperature field. He et al. [2001] studied the vibration control of the FGM plates with integrated piezoelectric sensors and actuators by a finite element formulation based on the classical laminated plate theory. Chi and Chung [2006a; 2006b] analyzed the mechanical behaviors of a simply supported rectangular FGM plate with sigmoid functions of the volume fraction of the constituents by the Fourier series expansion. The collocation multiquadric radial basis is used in [Ferreira et al. 2005] to analyze static deformations of simply supported FGMs modeled by a third-order shear deformation theory and a meshless method.

The closed-form solution to the problems of FGM plates subjected to transverse loads with two opposite edges simply supported and the other two edges free is not found in the literature. Therefore, this study will focus on the simple but important problems of FGM plates with two opposite edges simply supported and the other two edges free. The material properties of the FGM plates considered here are assumed to change continuously throughout the thickness of the plate, according to the volume fraction of the constituent material based on the power-law and sigmoid functions. The analytical solution is obtained by the Fourier series expansion and compared with the finite element calculation.

2. Governing equations

Consider a linearly elastic, moderately thick, rectangular FGM plate subjected to a transverse load. Assume the plate has a uniform thickness h in the range $1/20 \sim 1/100$ of its span. The deformations and the stresses of the FGM plate are derived under the following assumptions:

1. Line elements perpendicular to the middle surface of the plate before deformation remain normal and unstretched after deformation.

2. The deflection of the FGM plate is small in comparison with its thickness h, so the linear strain-displacement relations are valid.

3. The normal stress in the thickness direction can be neglected because of the thickness assumption.

4. For the nonhomogeneous elastic FGM plate, the Young's modulus and Poisson's ratio of the FGM plate are functions of the spatial coordinate z.

2.1. *Stress field of FGM plates.* According to assumption 1, the transverse strain components ε_{zz}, γ_{xz}, and γ_{yz} are negligibly small. Under the assumption of small deformation, the strain field of the FGM plate is

$$\varepsilon_x = \frac{\partial u}{\partial x} = \varepsilon_{x_0} - z\frac{\partial^2 w(x, y)}{\partial x^2}, \tag{1a}$$

$$\varepsilon_y = \frac{\partial v}{\partial y} = \varepsilon_{y_0} - z\frac{\partial^2 w(x, y)}{\partial y^2}, \tag{1b}$$

$$\gamma_{xy} = \frac{\partial u}{\partial y} + \frac{\partial v}{\partial x} = \gamma_{xy_0} - 2z\frac{\partial^2 w(x, y)}{\partial x \partial y}, \tag{1c}$$

$$\varepsilon_z = \gamma_{xz} = \gamma_{yz} = 0, \tag{1d}$$

where

$$\varepsilon_{x_0} = \frac{\partial u_0(x, y)}{\partial x} \qquad \varepsilon_{y_0} = \frac{\partial v_0(x, y)}{\partial y} \qquad \gamma_{xy_0} = \frac{\partial u_0}{\partial y} + \frac{\partial v_0}{\partial x}$$

are strains at the middle surface. The quantities $u_0(x, y)$, $v_0(x, y)$, $w_0(x, y)$ are the displacements at the middle surface. It is known that neglecting the transverse shear deformations may lead to significant errors when applied to moderately thick plates with thickness larger than 0.1 of span [Tauchert 1986]. However, Shames and Dym [1985] indicated that for a plate with a thickness less than 0.1 of its span, the classical theory of plates is expected to give good results. In this paper, the thickness of the moderately thick FGM plate is assumed to be in the range $1/20 \sim 1/100$ of its span, therefore the transverse shear deformations are negligible.

Based on assumptions 3 and 4, the stress-strain relation of an FGM plate for plane stress condition is

$$\sigma_x = \frac{E(z)}{1 - v(z)^2}\left(\varepsilon_{x_0} + v(z)\varepsilon_{y_0} - z\left(\frac{\partial^2 w}{\partial x^2} + v(z)\frac{\partial^2 w}{\partial y^2}\right)\right), \tag{2a}$$

$$\sigma_y = \frac{E(z)}{1 - v(z)^2}\left(\varepsilon_{y_0} + v(z)\varepsilon_{x_0} - z\left(\frac{\partial^2 w}{\partial y^2} + v(z)\frac{\partial^2 w}{\partial x^2}\right)\right), \tag{2b}$$

$$\tau_{xy} = \frac{E(z)}{1 - v(z)^2}\left(\frac{1 - v(z)}{2}\right)\left(\gamma_{xy_0} - 2z\frac{\partial^2 w}{\partial x \partial y}\right). \tag{2c}$$

2.2. *Axial forces, shear forces, and bending moments of FGM plates.* The stress resultants per unit length of the middle surface are defined by integrating stresses along the thickness. Thus the in-plane axial forces N_x, N_y, and N_{xy}, and the bending moments per unit length of the middle surface, M_x, M_y, and M_{xy} are defined as follows, with $\alpha = x, y$:

$$N_\alpha = \int_{-h/2}^{h/2} \sigma_\alpha \, dz, \qquad N_{xy} = \int_{-h/2}^{h/2} \tau_{xy} \, dz, \qquad M_\alpha = \int_{-h/2}^{h/2} z\sigma_\alpha \, dz, \qquad M_{xy} = \int_{-h/2}^{h/2} z\tau_{xy} \, dz.$$

Substituting the relations (2) into these defining equations, we obtain the in-plane axial forces and the bending moments in terms of the middle-surface strains and deflection:

$$
\left\{ \begin{array}{c} N_x \\ N_y \\ N_{xy} \end{array} \right\} = \left[\begin{array}{ccc} A_{11} & A_{12} & 0 \\ A_{12} & A_{11} & 0 \\ 0 & 0 & A_{66} \end{array} \right] \left\{ \begin{array}{c} \varepsilon_{x0} \\ \varepsilon_{y0} \\ \gamma_{xy0} \end{array} \right\} + \left[\begin{array}{ccc} B_{11} & B_{12} & 0 \\ B_{12} & B_{11} & 0 \\ 0 & 0 & B_{66} \end{array} \right] \left\{ \begin{array}{c} -\dfrac{\partial^2 w}{\partial x^2} \\ -\dfrac{\partial^2 w}{\partial y^2} \\ -2\dfrac{\partial^2 w}{\partial x \partial y} \end{array} \right\},
\tag{3}
$$

$$
\left\{ \begin{array}{c} M_x \\ M_y \\ M_{xy} \end{array} \right\} = \left[\begin{array}{ccc} B_{11} & B_{12} & 0 \\ B_{12} & B_{11} & 0 \\ 0 & 0 & B_{66} \end{array} \right] \left\{ \begin{array}{c} \varepsilon_{x0} \\ \varepsilon_{y0} \\ \gamma_{xy0} \end{array} \right\} + \left[\begin{array}{ccc} C_{11} & C_{12} & 0 \\ C_{12} & C_{11} & 0 \\ 0 & 0 & C_{66} \end{array} \right] \left\{ \begin{array}{c} -\dfrac{\partial^2 w}{\partial x^2} \\ -\dfrac{\partial^2 w}{\partial y^2} \\ -2\dfrac{\partial^2 w}{\partial x \partial y} \end{array} \right\},
\tag{4}
$$

where the coefficients of A_{ij}, B_{ij} and C_{ij} are the integration of the material properties of the FGM plate

$$
(A_{11}, B_{11}, C_{11}) = \int_{-h/2}^{h/2} \frac{1}{1 - \nu(z)^2} \big(E(z), z E(z), z^2 E(z) \big) \, dz,
\tag{5a}
$$

$$
(A_{12}, B_{12}, C_{12}) = \int_{-h/2}^{h/2} \frac{\nu}{1 - \nu(z)^2} \big(E(z), z E(z), z^2 E(z) \big) \, dz,
\tag{5b}
$$

$$
(A_{66}, B_{66}, C_{66}) = \int_{-h/2}^{h/2} \frac{1}{2(1 + \nu(z))} \big(E(z), z E(z), z^2 E(z) \big) \, dz.
\tag{5c}
$$

2.3. *Equilibrium and compatibility equations for FGM plates.* Assume that the FGM plate is subjected to the distributed loads q_x, q_y and q_z along the x, y and z directions. Then the equilibrium equations of the FGM plate are (see [Chi and Chung 2003])

$$
\frac{\partial N_x}{\partial x} + \frac{\partial N_{yx}}{\partial y} + q_x = 0
\tag{6}
$$

$$
\frac{\partial N_{yx}}{\partial x} + \frac{\partial N_y}{\partial y} + q_y = 0
\tag{7}
$$

$$
\frac{\partial^2 M_x}{\partial x^2} + 2 \frac{\partial^2 M_{xy}}{\partial x \partial y} + \frac{\partial^2 M_y}{\partial y^2} = -q_z(x, y).
\tag{8}
$$

If the FGM plate is only subjected to the transverse load q_z, that is, if $q_x = q_y = 0$, the in-plane Equations (6) and (7) can be solved in term of a stress function $\phi(x, y)$ defined by

$$
N_x = \frac{\partial^2 \phi}{\partial y^2}; \qquad N_y = \frac{\partial^2 \phi}{\partial x^2}; \qquad N_{xy} = -\frac{\partial^2 \phi}{\partial x \partial y}.
\tag{9}
$$

Using Equations (3) and (9), the strains at the middle surface are then expressed in terms of the stress function $\phi(x, y)$ and the deflection w as

$$\begin{Bmatrix} \varepsilon_{x_0} \\ \varepsilon_{y_0} \\ \gamma_{xy_0} \end{Bmatrix} = \begin{bmatrix} P_{11} & P_{12} & 0 \\ P_{12} & P_{11} & 0 \\ 0 & 0 & P_{66} \end{bmatrix} \begin{Bmatrix} \dfrac{\partial^2 \phi}{\partial y^2} \\ \dfrac{\partial^2 \phi}{\partial x^2} \\ \dfrac{\partial^2 \phi}{\partial x \partial y} \end{Bmatrix} + \begin{bmatrix} Q_{11} & Q_{12} & 0 \\ Q_{12} & Q_{11} & 0 \\ 0 & 0 & Q_{66} \end{bmatrix} \begin{Bmatrix} -\dfrac{\partial^2 w}{\partial x^2} \\ -\dfrac{\partial^2 w}{\partial y^2} \\ -2\dfrac{\partial^2 w}{\partial x \partial y} \end{Bmatrix}. \tag{10}$$

Consequently, the bending moments rearranged by substituting (10) into (4) are

$$\begin{Bmatrix} M_x \\ M_y \\ M_{xy} \end{Bmatrix} = \begin{bmatrix} -Q_{11} & -Q_{12} & 0 \\ -Q_{12} & -Q_{11} & 0 \\ 0 & 0 & -Q_{66} \end{bmatrix} \begin{Bmatrix} \dfrac{\partial^2 \phi}{\partial y^2} \\ \dfrac{\partial^2 \phi}{\partial x^2} \\ \dfrac{\partial^2 \phi}{\partial x \partial y} \end{Bmatrix} + \begin{bmatrix} S_{11} & S_{12} & 0 \\ S_{12} & S_{11} & 0 \\ 0 & 0 & S_{66} \end{bmatrix} \begin{Bmatrix} -\dfrac{\partial^2 w}{\partial x^2} \\ -\dfrac{\partial^2 w}{\partial y^2} \\ -2\dfrac{\partial^2 w}{\partial x \partial y} \end{Bmatrix}, \tag{11}$$

where

$$\begin{aligned} P_{11} &= A_{11}/\Delta, & Q_{11} &= (A_{12}B_{12} - A_{11}B_{11})/\Delta, & S_{11} &= B_{11}Q_{11} + B_{12}Q_{12} + C_{11}, \\ P_{12} &= -A_{12}/\Delta, & Q_{12} &= (A_{12}B_{11} - A_{11}B_{12})/\Delta, & S_{12} &= B_{11}Q_{12} + B_{12}Q_{11} + C_{12}, \\ P_{66} &= -1/A_{66}, & Q_{66} &= -B_{66}/A_{66}, & S_{66} &= C_{66} + B_{66}Q_{66}, \end{aligned} \tag{12}$$

and

$$\Delta = A_{11}^2 - A_{12}^2.$$

Consequently, we substitute (11) into (8) and the equilibrium equation becomes

$$Q_{12}\frac{\partial^4 \phi}{\partial x^4} + 2(Q_{11} - Q_{66})\frac{\partial^4 \phi}{\partial x^2 \partial y^2} + Q_{12}\frac{\partial^4 \phi}{\partial y^4} + S_{11}\frac{\partial^4 w}{\partial x^4} + 2(S_{12} + 2S_{66})\frac{\partial^4 w}{\partial x^2 \partial y^2} + S_{11}\frac{\partial^4 w}{\partial y^4} = q_z(x, y). \tag{13}$$

In a similar manner, the compatibility equation for a plane problem expressed in terms of stress function $\phi(x, y)$ and the deflection w are derived as

$$P_{11}\frac{\partial^4 \phi}{\partial x^4} + (2P_{12} - P_{66})\frac{\partial^4 \phi}{\partial x^2 \partial y^2} + P_{11}\frac{\partial^4 \phi}{\partial y^4} - Q_{12}\frac{\partial^4 w}{\partial x^4} - 2(Q_{11} - Q_{66})\frac{\partial^4 w}{\partial x^2 \partial y^2} - Q_{12}\frac{\partial^4 w}{\partial y^4} = 0. \tag{14}$$

Equations (13) and (14) provide the simultaneous equations to solve the stress function $\phi(x, y)$ and the deflection w. They are particular cases of the nonlinear equations presented in [Woo and Meguid 2001]. Similar formulae for the equilibrium and compatibility equations in (13) and (14) can also be found in [Nowinski and Turski 1953] and [Sokolowski 1958].

If both the Young's modulus and Poisson's ratio are considered for calculating the coefficient, the integration will turn out to be very complex. Chi and Chung [2003] showed that the influence of Poisson's ratio on the mechanics of FGM plates is much less than that of the Young's modulus. Therefore, the

solutions for the material with Poisson's ratio assumed to be constant and Young's modulus varying in the thickness direction are derived in Section 3.

For material with $\nu =$ constant and $E = E(z)$, it can be found that

$$
\begin{aligned}
(A_{12}, B_{12}, C_{12}) &= \nu(A_{11}, B_{11}, C_{11}), \\
(A_{66}, B_{66}, C_{66}) &= \frac{1-\nu}{2}(A_{11}, B_{11}, C_{11}), \\
(P_{12}, Q_{12}, S_{12}) &= \nu(-P_{11}, 0, S_{11}), \\
(P_{66}, Q_{66}, S_{66}) &= \left(-2(1+\nu)P_{11}, Q_{11}, \frac{1-\nu}{2}S_{11}\right),
\end{aligned}
\tag{15}
$$

where

$$
P_{11} = \frac{1}{(1-\nu^2)A_{11}}, \qquad Q_{11} = -\frac{B_{11}}{A_{11}}, \qquad \text{and} \qquad S_{11} = B_{11}Q_{11} + C_{11}.
$$

Consequently, the equilibrium and compatibility equations are simplified as

$$
S_{11}\nabla^4 w = q(x, y), \tag{16}
$$

$$
\nabla^4 \phi = 0. \tag{17}
$$

It can be seen that for the FGM plate with constant Poisson's ratio, the governing equations of the bending problem expressed in Equation (16) and the in-plane problem in Equation (17) are uncoupled.

3. Solution to FGM plates with two opposite edges simply supported and two other edges free

Consider an FGM plate with length a, width b, and uniform thickness h subjected to the lateral load $q_z(x, y)$. The coordinates x and y define the plane of the plate, whereas the z-axis originating at the middle surface of the plate is in the thickness direction. The Poisson's ratio of the FGM plate is assumed to be constant and the Young's modulus varies functionally in the thickness direction. Further assume that two opposite edges of the FGM plate are simply supported and the other edges are free, as shown in Figure 1.

The deflection w must satisfy the boundary conditions of $w = 0$ and $w'' = 0$ at $x = 0$ and $x = a$. Therefore the deflection of the FGM plate can be assumed as

$$
w(x, y) = \sum_{m=1}^{\infty} w_m(y) \sin\frac{m\pi x}{a}. \tag{18}
$$

Consequently the distributed loading $q_z(x, y)$ can be expanded by Fourier series

$$
q_z(x, y) = \sum_{m=1}^{\infty} q_m(y) \sin kx,
$$

where $q_m(y) = \int q_z(x, y) \sin kx \, dx$ and $k = m\pi/a$. For the special case when the FGM plate is under a uniform load with magnitude $q_z(x, y) = q_0$, the quantity $q_m(y) = 4q_0/(m\pi)$ where m is an odd number.
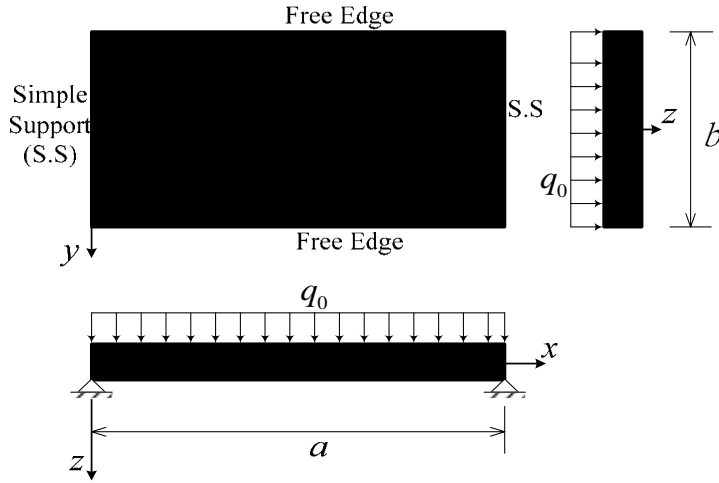
Figure 1. The configuration of an FGM plate.

To satisfy the governing equation of $\nabla^4 \phi = 0$, the stress function is also assumed as

$$\phi(x, y) = \sum_{m=1}^{\infty} \phi_m(y) \sin \frac{m\pi x}{a}. \tag{19}$$

Substituting (18) and (19) into (16) and (17), we rewrite the governing equations as

$$k^4 w_m(y) - 2k^2 w''_m(y) + w''''_m(y) = \frac{q_m(y)}{S_{11}}, \tag{20}$$

$$k^4 \phi_m(y) - 2k^2 \phi''_m(y) + \phi''''_m(y) = 0. \tag{21}$$

The solution of (20) consists of a homogeneous part $w_{mh}(y)$, and a particular part $w_{mp}(y)$. The particular part cannot be determined until $q_m(y)$ is specified. However, the homogeneous part can be easily determined as

$$w_{mh}(y) = A_{1m} \cosh ky + A_{2m} ky \sinh ky + A_{3m} \sinh ky + A_{4m} ky \cosh ky. \tag{22}$$

Similarly, $\phi_m(y)$ is obtained in the form

$$\phi_m(y) = B_{1m} \cosh ky + B_{2m} ky \sinh ky + B_{3m} \sinh ky + B_{4m} ky \cosh ky. \tag{23}$$

Because of symmetry with respect to the y-axis,

$$A_{3m} = A_{4m} = B_{3m} = B_{4m} = 0.$$

The unknown constants A_{im} and B_{im} can be determined from the boundary conditions on the free edges $(y = \pm b/2)$ as

$$\begin{cases} M_y = 0, \\ V_y + \dfrac{\partial M_{xy}}{\partial y} = 0, \end{cases} \quad \text{and} \quad \begin{cases} N_y = 0, \\ N_{xy} = 0. \end{cases}$$

The conditions $N_y(y = \pm b/2) = 0$ and $N_{xy}(y = \pm b/2) = 0$ give $B_{1m} = B_{2m} = 0$. Consequently, the stress function $\phi(x, y) = 0$. The boundary conditions $M_y = 0$ and $V_y + \partial M_{xy}/\partial y = 0$ at $y = \pm b/2$ yield

$$A_{1m} = \frac{\nu w_{mp}(y)\left(\frac{1+\nu}{1-\nu}\sinh\frac{kb}{2} - \frac{kb}{2}\cosh\frac{kb}{2}\right)}{\frac{3+\nu}{2}\sinh kb - (1-\nu)\frac{kb}{2}}, \qquad A_{2m} = \frac{\nu w_{mp}(y)\sinh\frac{kb}{2}}{\frac{3+\nu}{2}\sinh kb - (1-\nu)\frac{kb}{2}}. \tag{24}$$

With the aid of $\phi(x, y) = 0$, the complete solution of the FGM plate with two opposite edges simply supported and two other edges free is

$$w(x, y) = \sum_m \left(A_{1m}\cosh ky + A_{2m}ky\sinh ky + w_{mp}(y)\right)\sin kx, \tag{25a}$$

$$N_x = N_y = N_{xy} = 0, \tag{25b}$$

$$\begin{Bmatrix} M_x \\ M_y \\ M_{xy} \end{Bmatrix} = S_{11}\begin{bmatrix} 1 & \nu & 0 \\ \nu & 1 & 0 \\ 0 & 0 & (1-\nu)/2 \end{bmatrix}\begin{Bmatrix} \kappa_x \\ \kappa_y \\ \kappa_{xy} \end{Bmatrix}, \tag{25c}$$

$$\begin{Bmatrix} \varepsilon_{x0} \\ \varepsilon_{y0} \\ \gamma_{xy0} \end{Bmatrix} = Q_{11}\begin{Bmatrix} \kappa_x \\ \kappa_y \\ \kappa_{xy} \end{Bmatrix}, \tag{25d}$$

$$\begin{Bmatrix} \varepsilon_x \\ \varepsilon_y \\ \gamma_{xy} \end{Bmatrix} = (Q_{11} + z)\begin{Bmatrix} \kappa_x \\ \kappa_y \\ \kappa_{xy} \end{Bmatrix}, \tag{25e}$$

$$\begin{Bmatrix} \sigma_x \\ \sigma_y \\ \tau_{xy} \end{Bmatrix} = \left(\frac{E(z)}{1-\nu^2}\right)\left(\frac{Q_{11} + z}{S_{11}}\right)\begin{Bmatrix} M_x \\ M_y \\ M_{xy} \end{Bmatrix}, \tag{25f}$$

where $\kappa_x = -\dfrac{\partial^2 w}{\partial x^2}$, $\kappa_y = -\dfrac{\partial^2 w}{\partial y^2}$, $\kappa_{xy} = -2\dfrac{\partial^2 w}{\partial x\partial y}$, and

$$\frac{\partial^2 w}{\partial x^2} = -\sum_m k^2\left(A_{1m}\cosh ky + A_{2m}ky\sinh ky + w_{mp}(y)\right)\sin kx,$$

$$\frac{\partial^2 w}{\partial y^2} = \sum_m k^2\left(A_{1m}\cosh ky + A_{2m}(2\cosh ky + ky\sinh ky) + w_{mp}''(y)\right)\sin kx,$$

$$\frac{\partial^2 w}{\partial x\partial y} = \sum_m k^2\left(A_{1m}\sinh ky + A_{2m}(\sinh ky + ky\cosh ky) + w_{mp}'(y)\right)\cos kx,$$

for an FGM plate under a uniform load with magnitude $q_z(x, y) = q_0$, the particular solution w_{mp} equals $4q_0/(ak^5 S_{11})$.

4. Material gradient and the physical meaning of the coefficients

For the FGM plate in Figure 1, Poisson's ratio is assumed to be constant. The Young's moduli on the upper and lower surfaces of the FGM plate differ and are preassigned according to the performance demands, but the Young's modulus inside FGM plates varies continuously in the thickness direction with power-law functions (P-FGM) or sigmoid functions (S-FGM).

4.1. *Material properties and parameters of P-FGM plates.* The volume fraction of the P-FGM is assumed to obey a power-law function

$$g(z) = \left(\frac{z + h/2}{h}\right)^p, \tag{26}$$

where p is the material parameter and h is the thickness of the plate. Once the local volume fraction $g(z)$ has been defined, the material properties of a P-FGM can be determined by the rule of mixture (see [Bao and Wang 1995])

$$E(z) = g(z)E_1 + [1 - g(z)]E_2, \tag{27}$$

where E_1 and E_2 are the Young's moduli of the bottom and top surfaces of the FGM plate, respectively ($z = \pm h/2$). The variation of the Young's modulus of a P-FGM plate in the thickness direction with different material parameters p is plotted in Figure 2, which indicates that the overall stiffness of the FGM plate increases as the parameter p decreases. It is seen from Figure 2 that the Young's modulus varies rapidly at the top surface ($z/h = -0.5$) of the plate, therefore it must be very carefully defined in finite element analysis when dividing the meshes near the top surface.
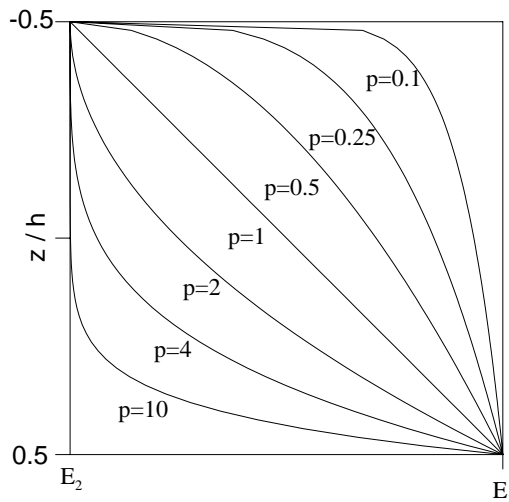
Figure 2. Variation of the Young's modulus of a P-FGM plate with differing material parameters p.

Substituting the gradation of the Young's modulus of P-FGM plates in (27) into the definition of coefficients in Equations (5), we obtain the coefficients of P-FGM plates:

$$A_{11} = \frac{h}{1-v^2}\Big(E_2 + (E_1 - E_2)\frac{1}{p+1}\Big),$$

$$B_{11} = \frac{h^2}{2(1-v^2)}(E_1 - E_2)\frac{p}{(p+1)(p+2)},$$

$$C_{11} = \frac{h^3}{12(1-v^2)}\Big(E_2 + (E_1 - E_2)\frac{3(p^2+p+2)}{(p+1)(p+2)(p+3)}\Big), \tag{28}$$

$$Q_{11} = \frac{-ph}{2(p+2)}\frac{(E_1 - E_2)}{(pE_2 + E_1)},$$

$$S_{11} = \frac{h^3}{12(1-v^2)}\Big(E_2 + \frac{3(p^2+p+2)(E_1-E_2)}{(p+1)(p+2)(p+3)} - \frac{3p^2(E_1-E_2)^2}{(p+1)(p+2)^2(pE_2+E_1)}\Big).$$

4.2. *Material properties of S-FGM plates.* In the case of adding an FGM of a single power-law function to the multilayered composite, stress concentrations appear on one of the interfaces where the material is continuous but changes rapidly [Lee and Erdogan 1994; Bao and Wang 1995]. Therefore, we defined the volume fraction using two power-law functions to ensure smooth distribution of stresses among all the interfaces. The Young's modulus of the S-FGM plate is defined based on two power-law functions [Chung and Chi 2001]

$$g_1(z) = 1 - \frac{1}{2}\Big(\frac{h/2-z}{h/2}\Big)^p \quad \text{for } 0 \le z \le h/2, \tag{29a}$$

$$g_2(z) = \frac{1}{2}\Big(\frac{h/2+z}{h/2}\Big)^p \qquad \text{for } -h/2 \le z \le 0. \tag{29b}$$

By using the rule of mixture, the Young's modulus of the S-FGM plate can be calculated by

$$E(z) = g_1(z)E_1 + [1 - g_1(z)]E_2 \quad \text{for } 0 \le z \le h/2, \tag{30a}$$
$$E(z) = g_2(z)E_1 + [1 - g_2(z)]E_2 \quad \text{for } -h/2 \le z \le 0. \tag{30b}$$

The variation of the Young's modulus of a P-FGM plate in the thickness direction with different material parameters p is plotted in Figure 3 which shows that the material properties rapidly change near the top and bottom surfaces for $p \ll 1$ but vary rapidly near the middle surface for $p \gg 1$. Therefore, if the S-FGM plate is used as the undercoat in a laminated material, the material distribution with $p \gg 1$ is the better choice.
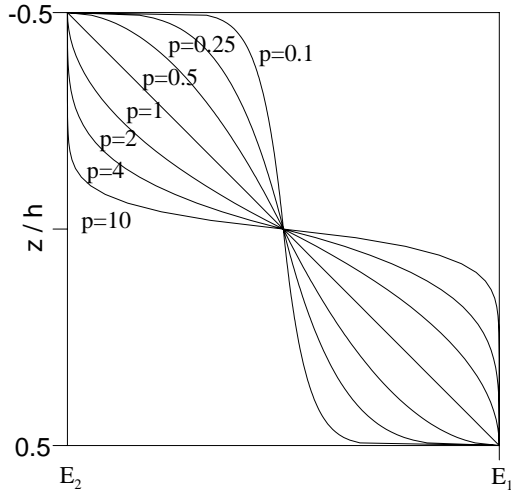
Figure 3. Variation of the Young's modulus of an S-FGM plate with differing material parameters p.

A similar approach to that used for P-FGM plates yields for the coefficients of S-GFM plates

$$
A_{11} = \frac{h}{1-v^2}\left(\frac{E_1+E_2}{2}\right),
$$

$$
B_{11} = \frac{h^2}{8(1-v^2)}(E_1-E_2)\frac{p^2+3p}{(p+1)(p+2)},
$$

$$
C_{11} = \frac{h^3}{12(1-v^2)}\frac{E_1+E_2}{2},
$$

$$
Q_{11} = \frac{-h(E_1-E_2)(p^2+3p)}{4(E_1+E_2)(p+1)(p+2)},
$$

$$
S_{11} = \frac{h^3}{8(1-v^2)}\left(\frac{E_1+E_2}{3} - \frac{(E_1-E_2)^2(p^2+3p)^2}{4(E_1+E_2)(p+1)^2(p+2)^2}\right).
$$

$$(31)$$

4.3. *Physical meaning of the quantities A_{11}, B_{11}, and C_{11}.* For FGM plates with constant Poisson's ratio, the parameters A_{11}, B_{11}, and C_{11} are defined in (5a) as

$$
(A_{11}, B_{11}, C_{11}) = \frac{1}{1-v^2}\int_{-h/2}^{h/2}\left(E(z), zE(z), z^2E(z)\right)dz
$$

Therefore, it is clear that $(1-v^2)A_{11}$ equals the area under the $E(z)$ curve from $z = -h/2$ to $z = h/2$, referred to in Figure 4, as indicated in [Mushelishvili 1953]. Similarly, the parameters B_{11}, and C_{11} are related to the first and second moments of the area under the $E(z)$ curve from $z = -h/2$ to $z = h/2$ with
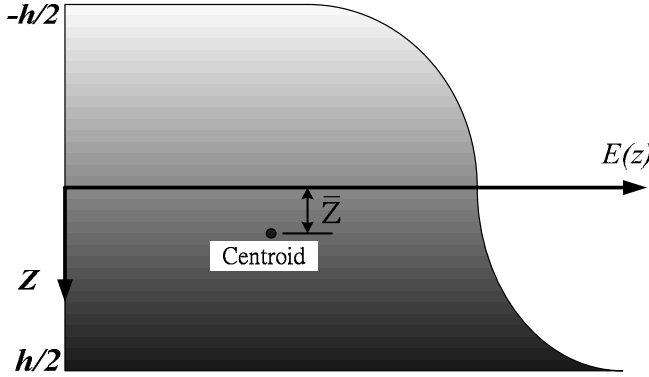
Figure 4. Distribution of the Young's modulus in the thickness direction of an FGM plate.

respect to the $z = 0$ axis. They are simplified as

$$(1 - v^2)A_{11} = \text{the area under the } E(z) \text{ curve from } z = -h/2 \text{ to } z = h/2, \tag{32a}$$

$$(1 - v^2)B_{11} = (1 - v^2)A_{11} \times \bar{z}, \tag{32b}$$

$$(1 - v^2)C_{11} = \bar{I} + (1 - v^2)A_{11} \times \bar{z}^2, \tag{32c}$$

where $\bar{z}$ is the distance from the centroid of the area $(1 - v^2)A_{11}$ to the axis $z = 0$, and $\bar{I}$ is the second moment of the area $(1 - v^2)A_{11}$ with respect to the axis passing through the centroid. It can be seen from Equation (32c) that the location of the centroid $\bar{z}$ can be expressed by the parameters A_{11} and B_{11} as

$$\bar{z} = \frac{B_{11}}{A_{11}}. \tag{33}$$

From Equations (28) and (31), the quantity B_{11} is positive if the Young's moduli satisfy $E_1 > E_2$; in this case the location of the centroid $\bar{z}$ is also positive.

4.4. *Physical meaning of the parameters Q_{11} and S_{11}.* Because of the zero strains at the neutral surface, the neutral surface is located at $Q_{11} + z = 0$ according to (25e). Therefore, the physical meaning of the parameter Q_{11} is the negative of the location of the neutral surface of the FGM plates. Based on (15) where $Q_{11} = -B_{11}/A_{11}$ and (33) where $\bar{z} = B_{11}/A_{11}$, we obtain $Q_{11} + \bar{z} = 0$ which means that the axes of the neutral surface and the centroid of the area under the $E(z)$ curve coincide. Therefore, the neutral surface of the FGM plates for bending problems can be evaluated directly by determining the location of the centroid of the $E(z)$ curve, which is related to the quantity B_{11} in (33). Consequently, it is concluded that when the origin of the z-axis is located at the central axis of the area under the $E(z)$ curve parallel to the middle surface, the quantity $B_{11} = 0$.

The neutral surfaces versus the material parameter p with different ratios of Young's moduli are plotted in Figure 5 for P-FGM and S-FGM plates. The two halves of the figure indicate that the neutral axes move far away from the $z = 0$ axis as the parameter p increases for $E_1/E_2 > 1$ (with E_1 fixed). With the
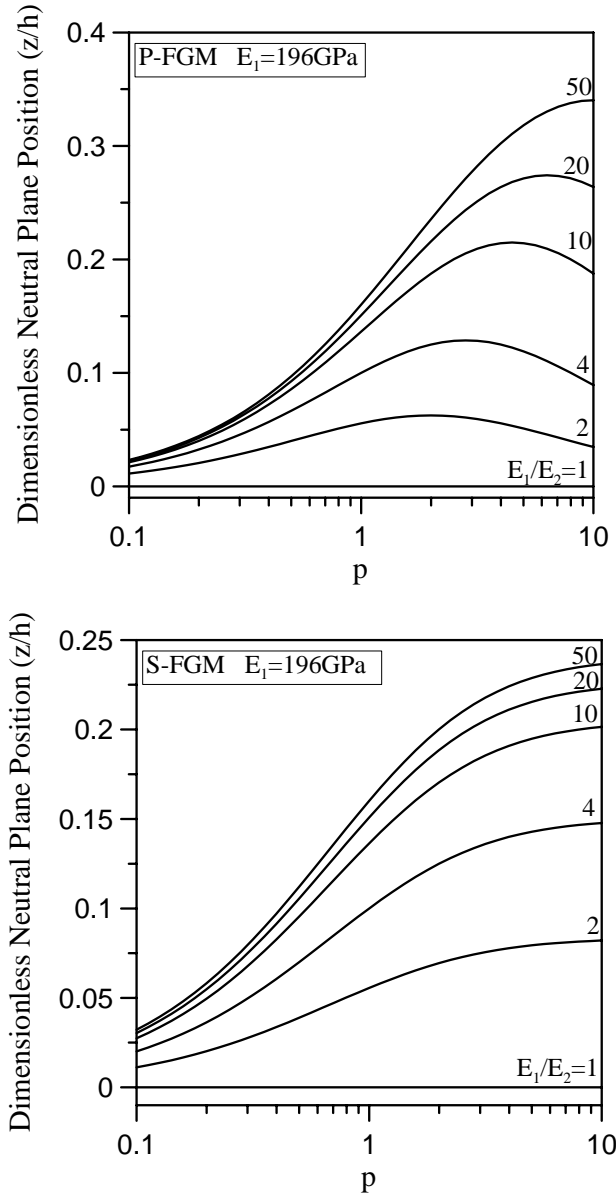
Figure 5. Locations of the neutral surfaces versus the material parameter p for $E_1 = 196 \, \text{GPa}$ and varying E_2. Top: P-FGM plate. Bottom: S-FGM plate.

same parameter p and Young's moduli E_1 and E_2, the locations of the neutral surfaces of the S-FGM plates are closer to the middle surfaces than those of the P-FGM plates.

It is also worthwhile to investigate the quantity S_{11}. With the aid of (15), (32c) and (33), the parameter S_{11} can be rewritten as

$$S_{11} = \frac{\bar{I}}{1 - v^2}, \tag{34}$$

where $\bar{I}$ is the second moment of the area $(1 - v^2)A_{11}$ with respect to the axis passing through the centroid. For homogeneous plates ($E_1 = E_2 = E$), the quantity S_{11} equals $Eh^3/12(1 - v^2)$ according to (28) and (31), and this is the bending stiffness of a homogeneous plate. By comparing the equilibrium equation of FGM plates in (16) with that of homogeneous plates, it is shown that parameter S_{11} is related to the bending stiffness of FGM plates. Therefore, the parameter S_{11} is here called the bending stiffness of FGM plates.
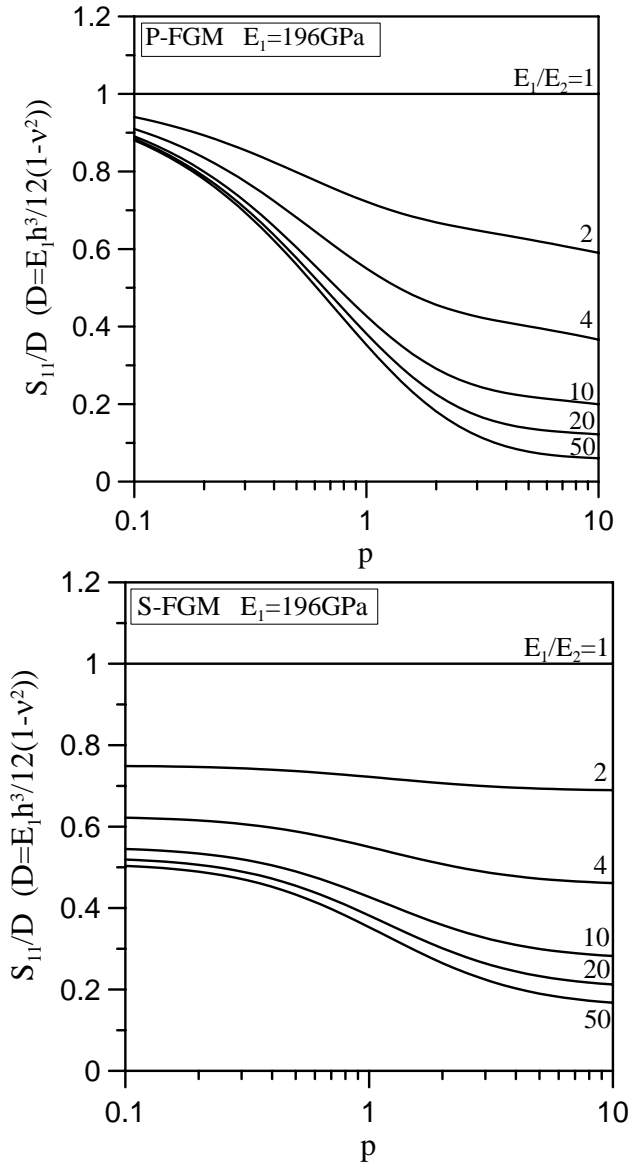

Figure 6. Bending stiffness versus material parameter p for $E_1 = 196$ GPa and varying E_2. Top: P-FGM plate. Bottom: S-FGM plate.

The ratios of S_{11} to the bending stiffness of homogeneous plates $Eh^3/12(1 - v^2)$ are plotted in Figure 6 for P-FGM and S-FGM plates. The figure shows that $S_{11} = Eh^3/12(1 - v^2)$ for a homogeneous plate in which $E_1 = E_2$. The bending stiffness of FGM plates S_{11} decreases with increase of p for $E_1/E_2 > 1$. However for P-FGM plates, the bending stiffnesses S_{11} are almost the same and close to that of the homogeneous plate for $p \ll 1$. It also can be seen that the bending stiffness S_{11} decreases when E_1/E_2 (E_1 fixed) increases for both S-FGM and P-FGM plates, because the overall stiffnesses of the plates decrease with the increase of E_1/E_2.

5. Numerical results

For the problem in Figure 1, if the aspect ratio a/b is large, the behavior of the plate will be similar to that of a beam. Therefore, consider a homogeneous plate in which $E_1 = E_2 = E$ and Poisson's ratio is $v = 0$ subjected to a uniform load q_0. If the aspect ratio a/b of the plate is large, the maximum deflection located at $x = a/2$ is approximated by $5q_0ba^4/384EI = 15q_0a^4/96Eh^3 = 0.15625q_0a^4/Eh^3$. This value will be compared with the solution to a homogeneous plate given in Equation (25a).

When $E_1 = E_2 = E$, and $v = 0$, Equations (28) and (31) become

$$(1 - v^2)A_{11} = Eh, \qquad B_{11} = Q_{11} = 0, \qquad C_{11} = S_{11} = Eh^3/12(1 - v^2).$$

As mentioned previously, the quantity $(1 - v^2)A_{11}$ represents the area under the $E(z)$ curve from $z = -h/2$ to $z = h/2$ which is equal to Eh. The results of $Q_{11} = 0$ and $B_{11} = 0$ reveal that the location of the neutral surface is at the origin of the z-axis, and that the axes of the neutral surface and the centroid of the area under the $E(z)$ curve coincide, respectively. Moreover, the term $(1 - v^2)C_{11}$, the second moment of the area under the $E(z)$ curve from $z = -h/2$ to $z = h/2$ with respect to $z = 0$ axis, is equal to the bending stiffness of FGM plates S_{11} times $(1 - v^2)$.

The coefficients A_{1m} and A_{2m} in (24) are approximated by zero as the aspect ratio a/b becomes large. Then, the displacement of a homogeneous rectangular plate based on (25a) is simplified as $w(x, y) = \sum_m w_{mp}(y) \sin kx$. Hence, the maximum displacement of the homogeneous rectangular plate located at $y = 0$, $x = a/2$ is obtained as

$$w(x = a/2, y = 0) = \frac{48q_0a^4}{\pi^5 Eh^3} \sum_{m=1,3,5,\ldots} \frac{1}{m^5} \sin \frac{m\pi}{2},$$

$$\approx 0.15625 \frac{q_0a^4}{Eh^3}. \tag{35}$$

The result of (35) derived from (25a) with $E_1 = E_2 = E$, $v = 0$ and large a/b is almost the same as the result from beam theory. The comparison of the deflections of a homogeneous plate and a beam is shown in Figure 7 for different aspect ratios. The figure shows that if the aspect ratio a/b is large, the deflections at the line $x = a/2$ based on the plate theory and beam formulation are almost the same for zero or nonzero Poisson's ratio. However if the aspect ratio a/b is small, the deflection at the center of the homogeneous plate will be identical to that of the beam theory only for Poisson's ratio $v = 0$.

Next, consider an FGM plate in which the boundary and load conditions are shown in Figure 1. Because of the symmetry about the x- and y-axes, only one quarter of the full plate in Figure 1 is under consideration when using the finite element program MARC. On the edge $y = 0$ of the one-quarter plate,
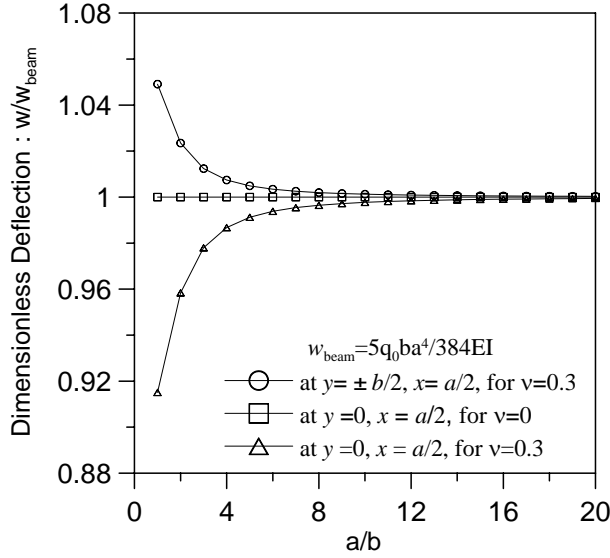
Figure 7. Comparison of the deflections of a homogeneous plate and beam.
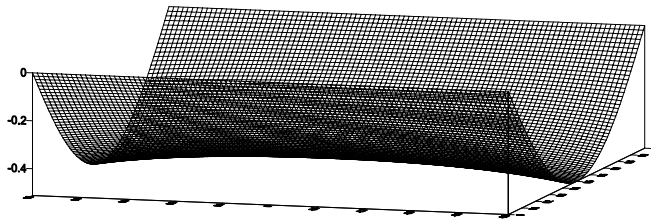
Figure 8. Deformation of an FGM plate at the neutral surface.

hinges are put at the neutral surface, while on the symmetric edges (that is, $y = 0$ and $x = a/2$), rollers are used such that displacements in z-direction are allowed. In the finite element mesh, because there is no stress singularity in the plate, solid eight-node elements are applied and 20×20 equally divided elements are used in the x- and y-directions. In order to simulate the variation of the material properties of the FGM plate, sixty layers in the thickness direction are used. Each layer has constant material properties, but the material properties differ from layer to layer. The material properties of all layers in the mesh are determined from the functions of volume fractions, according to the given E_1, E_2, v.

The dimensions of the FGM plate in Figure 1 are taken as $a = b = 100$ cm and $h = 2$ cm, so the width to thickness ratio is equal to 50. The Poisson's ratio of the FGM plate is assumed to be constant for the whole plate and is taken as $v = 0.3$. It is assumed that the Young's modulus at the bottom surface of the FGM plate E_1, is 196 GPa, while that at the top surface of the S-FGM plate E_2, varies with the ratio of E_1/E_2. The deflections and strains of the FGM plate for the material parameter $p = 2$ and the ratios of Young's modulus $E_1/E_2 = 1, 2, 4, 10, 20, 50$ are under investigation.

The deformed configuration of an FGM plate at the neutral surface is shown in Figure 8. The dimensionless deflections along the $x = a/2$ axis from $y = 0$ to $y = b/2$ and those along the $y = 0$ axis from
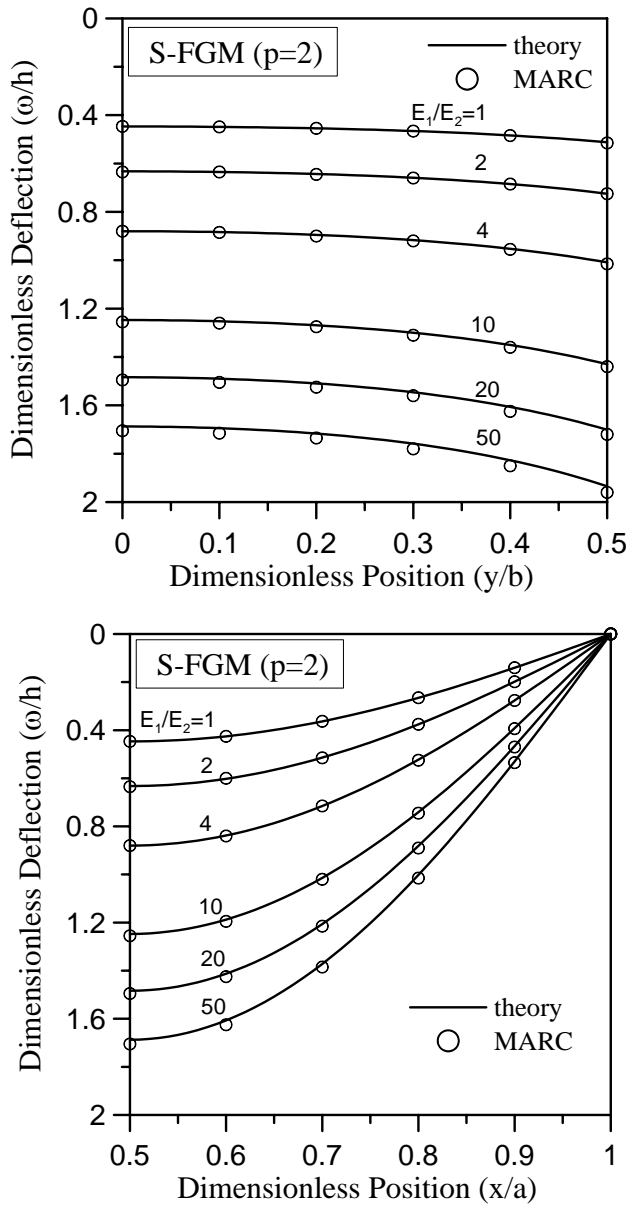
Figure 9. Deflection of an S-FGM plate. Top: from $y = 0$ to $y = b/2$ along the line $x = a/2$. Bottom: from $x = a/2$ to $x = a$ along the line $y = 0$.

$x = a/2$ to $x = a$ are plotted in Figure 9. Figures 8 and 9 reveal that the FGM plate exhibits saddle deformation which is the same as in homogeneous plates. The analytical and numerical results agree very well for small E_1/E_2 and are slightly different for large E_1/E_2. However, the error is less than 5%.

The dimensionless stresses σ_x/q_0 and σ_y/q_0 at the center of the plate along the thickness direction for $p = 2$ and different E_1/E_2 ratios are presented in Figure 10. These figures show that the stresses of the
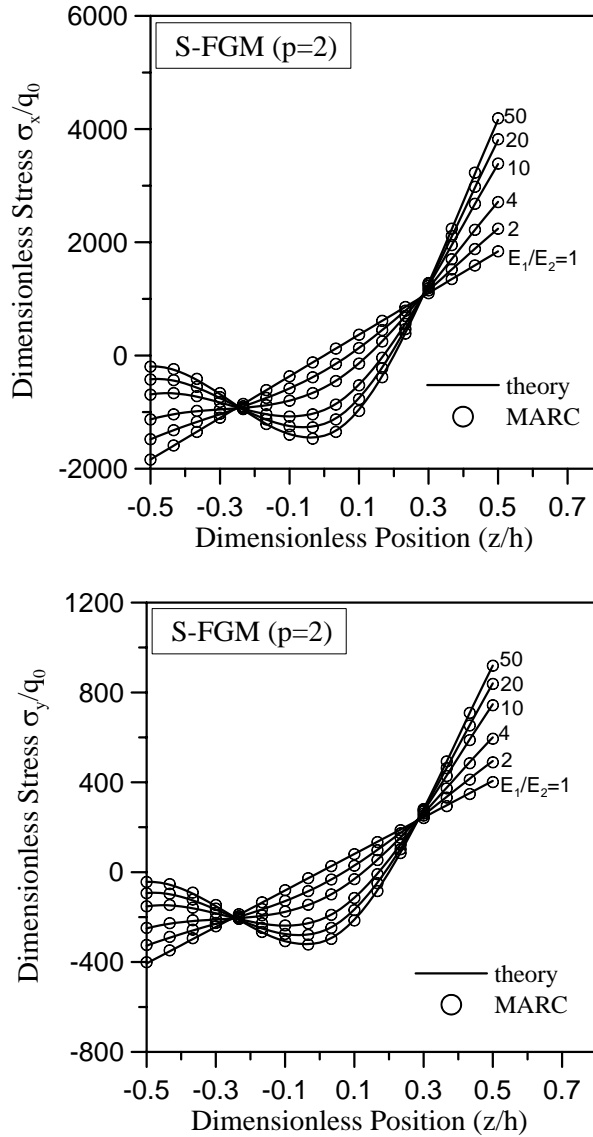
Figure 10. Distribution of stresses σ_x (top) and σ_y (bottom) at the center of an S-FGM plate along the thickness direction for different E_1/E_2 ratios.

S-FGM plate along the thickness direction are cubed. This is reasonable because the material parameter $p = 2$. For a homogeneous plate in which $E_1/E_2 = 1$, the magnitude of the tensile and compressive stresses are equal and located at the top and bottom surfaces. However, as the ratio of E_1/E_2 increases, the magnitudes of the tensile and compressive stresses are no longer equal. The maximum stress is tensile and is located at the bottom surface of the plate. However, the maximum compressive stress moves from the top surface to inside of the plate, and this phenomenon becomes clear for large E_1/E_2.
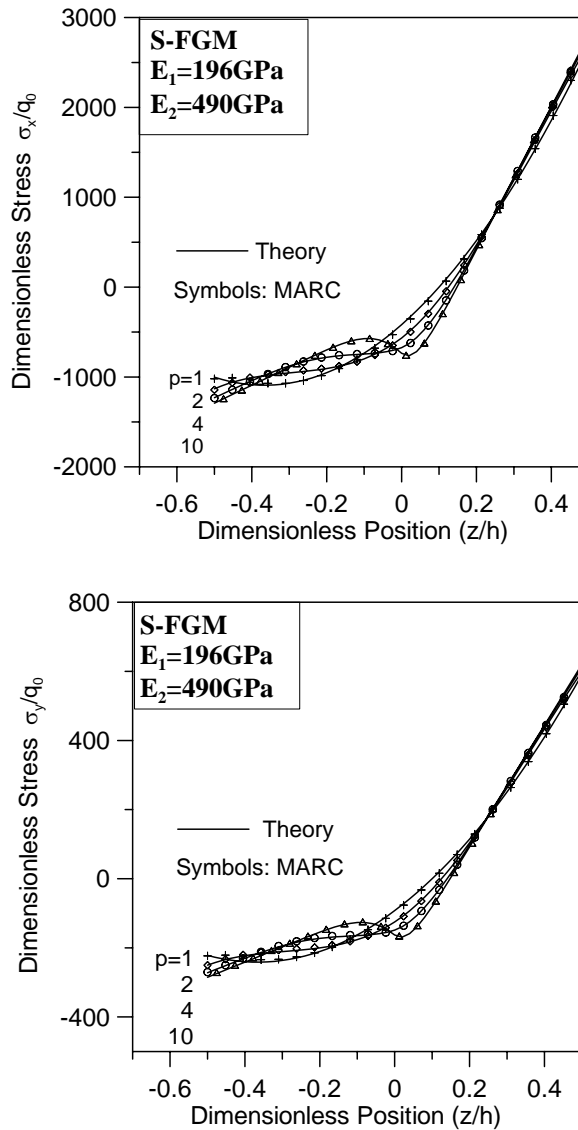
Figure 11. Distribution of stresses σ_x (top) and σ_y (bottom) at the center of an S-FGM plate along the thickness direction for differing material parameters $p \geq 1$.

Next we focus on a fixed value $E_1/E_2 = 4$, with changing material parameters $p = 1, 2, 4$, and 10, and $p = 1/2, 1/4$, and $1/10$. The dimensionless stresses σ_x/q_0 and σ_y/q_0 at the center of the FGM plates are plotted in Figure 11 for $p = 1, 2, 4$, and 10 and in Figure 12 for $p = 1/2, 1/4$, and $1/10$. It is clear from these four figures that the stress distributions differ little for different parameters p when E_1/E_2 is fixed. Specifically, the stresses at the top and bottom surfaces are almost the same for $p < 1$. This phenomenon occurs because the bending stiffness S_{11} for $E_1/E_2 = 4$ doesn't change very much for different values of p.
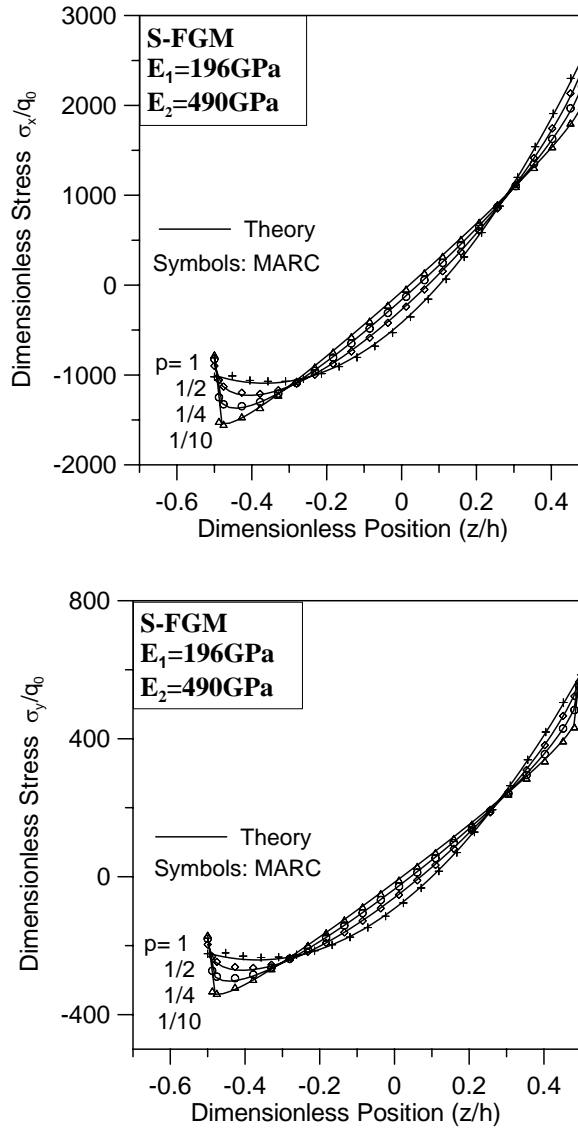
Figure 12. Distribution of stresses σ_x (top) and σ_y (bottom) at the center of an S-FGM plate along the thickness direction for differing material parameters $p < 1$.

So far, the results in this paper show that the analytical solution agrees very well with FEM simulation. However, the limitations and range of validity of the proposed model need to be investigated. Therefore, further considerations will focus on how thick the FGM plate is, or how steep the material gradient can be for the theoretical solution to fail.

The theoretical solutions in this paper are based on the assumption that the thickness of a moderately thick FGM plate is in the range $1/20 \sim 1/100$ of its span, and thus transverse shear deformations can be negligible. To examine this assumption, we fix the ratio $E_1/E_2 = 10$ but take the thickness of the
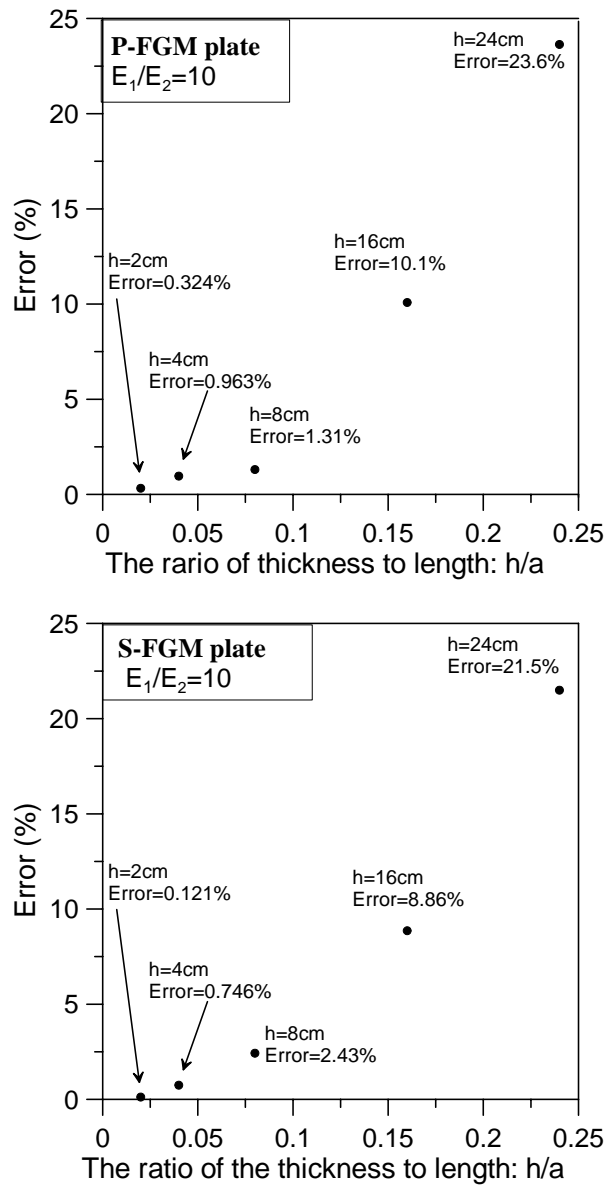
Figure 13. Error in maximum deflection versus thickness-to-length ratio h/a (fixed a). Top: P-FGM plate; bottom: S-FGM plates. In both cases $E_1/E_2 = 10$.

plate $h = 2\,\mathrm{cm}$, $4\,\mathrm{cm}$, $8\,\mathrm{cm}$, $16\,\mathrm{cm}$, or $24\,\mathrm{cm}$, and the corresponding ratios of thickness to length $h/a = 0.02, 0.04, 0.08, 0.16, 0.24$. The maximum deflections located at the center of the plate are evaluated by theoretical equation and FEM simulation. The errors, which are the differences between theoretical and numerical results divided by the theoretical results, are plotted in Figure 13 for P-FGM and S-FGM plates for various ratios h/a. These figures indicate that for moderately thick FGM plates with thickness less than 0.1 of the span, the error is less than 5%. This means that for an FGM plate with thickness
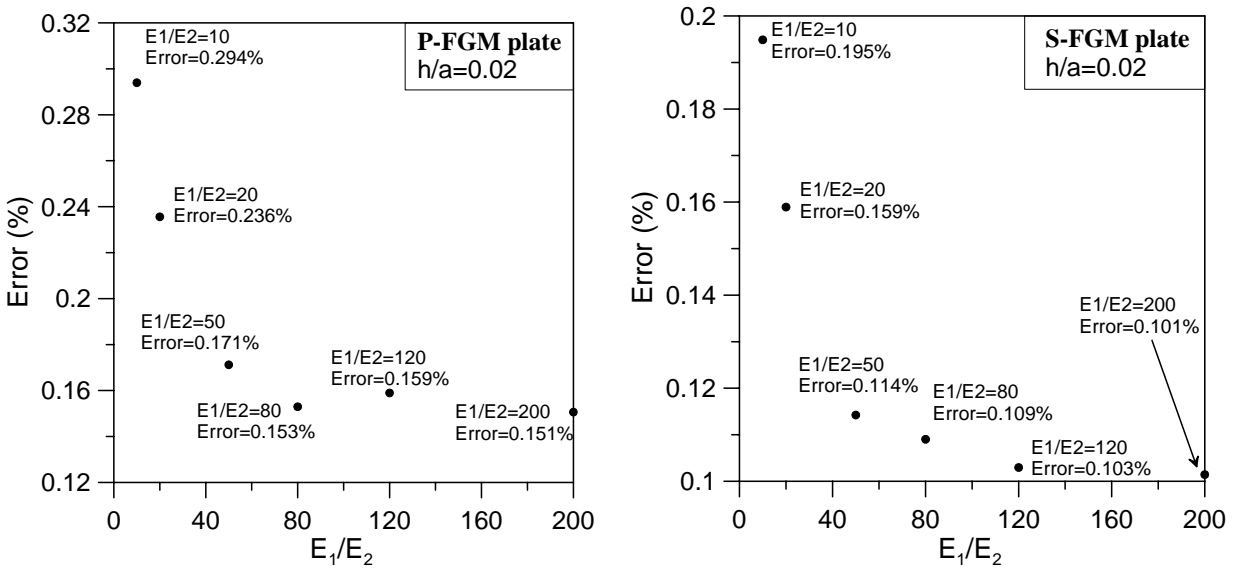
Figure 14. Error of maximum deflection of P-FGM plates versus ratio E_1/E_2 between Young's moduli. Top: P-FGM plate; bottom: S-FGM plates. In both cases $h/a = 0.02$.

less than 0.1 of its span, the classical theory of plates will give good results, as indicated in [Shames and Dym 1985] for homogeneous plates.

To investigate the effect of the steepness of the material gradient on the FGM plates, the ratio of thickness to length is fixed at 0.02 (that is, $h/a = 0.02$), but the ratios of Young's moduli are taken as $E_1/E_2 = 1, 10, 20, 50, 80, 120,$ and 200. The errors in maximum deflections versus the ratios E_1/E_2, plotted in Figure 14 for P-FGM and S-FGM plates, are all in the range 0.1% to 0.5%. Therefore, the linear assumption for the displacement field is still accurate for FGMs with steep material gradients.

6. Conclusions

We applied a Fourier series expansion to the analysis of FGM plates with two opposite edges simply supported and the other two edges free, subjected to uniform load. The results lead to these conclusions:

(1) The analytical solution obtained agrees very well with the finite element solution. The deformed configuration of the FGM plates is a saddle deformation, which is the same as that of a homogeneous plate. The maximum tensile stresses are located at the bottom of the FGM plates. However, the maximum compressive stresses move to the inside of the FGM plates, especially for larger E_1/E_2.

(2) In general, the bending and in-plane problems in FGM plates are coupled. But if the material properties of the FGM plate are such that the Young's modulus varies along the thickness direction but the Poisson's ratio is constant for the whole FGM plate, as in the problem solved in this paper, then the governing equations for the bending and in-plane problem become uncoupled.

(3) The parameters of A_{11}, B_{11}, C_{11}, Q_{11}, and S_{11} defined in this paper have physical meaning. The quantity $(1 - \nu^2)A_{11}$ represents the area under the $E(z)$ curve from $z = -h/2$ to $z = h/2$. The

parameters B_{11} and C_{11} are related to the first and second moment of the area under the $E(z)$ curve from $z = -h/2$ to $z = h/2$ with respect to the $z = 0$ axis. The ratio of B_{11}/A_{11} is equal to the centroid location $\bar{z}$, of the area under the $E(z)$ curve. The parameter $Q_{11} = -B_{11}/A_{11} = -\bar{z}$ represents the location of the centroid of the area under the $E(z)$ curve. The parameter S_{11} is called here the bending stiffness of FGM plates.

References

[Bao and Wang 1995] G. Bao and L. Wang, "Multiple cracking in functionally graded ceramic/metal coatings", *Int. J. Solids Struct.* **32**:19 (1995), 2853–2871.

[Cai and Bao 1998] H. Cai and G. Bao, "Crack bridging in functionally graded coatings", *Int. J. Solids Struct.* **35**:7–8 (1998), 701–717.

[Chi and Chung 2002] S. H. Chi and Y. L. Chung, "Cracking in sigmoid functionally graded coating", *J. Mech.* **18** (2002), 41–53.

[Chi and Chung 2003] S. H. Chi and Y. L. Chung, "Cracking in coating-substrate composites of multi-layered and sigmoid FGM coatings", *Eng. Fract. Mech.* **70**:10 (2003), 1227–1243.

[Chi and Chung 2006a] S. H. Chi and Y. L. Chung, "Mechanical behavior of functionally graded material plates under transverse load, I: Analysis", *Int. J. Solids Struct.* **43**:13 (2006), 3657–3674.

[Chi and Chung 2006b] S. H. Chi and Y. L. Chung, "Mechanical behavior of functionally graded material plates under transverse load, II: Numerical results", *Int. J. Solids Struct.* **43**:13 (2006), 3675–3691.

[Chung and Chi 2001] Y. L. Chung and S. H. Chi, "The residual stress of functionally graded materials", *J. Chin. Inst. Civil. Hydraul. Eng.* **13** (2001), 1–9.

[Delale and Erdogan 1983] F. Delale and F. Erdogan, "The crack problem for a nonhomogeneous plane", *J. Appl. Mech.* (*ASME*) **50** (1983), 609–614.

[Erdogan and Chen 1998] F. Erdogan and Y. F. Chen, "Interfacial cracking of FGM/metal bonds", pp. 29–37 in *Ceramic coating*, edited by K. Kokini, 1998.

[Erdogan and Wu 1996] F. Erdogan and B. H. Wu, "Crack problems in FGM layers under thermal stresses", *J. Therm. Stresses* **19** (1996), 237–265.

[Feldman and Aboudi 1997] E. Feldman and J. Aboudi, "Buckling analysis of functionally graded plates subjected to uniaxial loading", *Compos. Struct.* **38**:1–4 (1997), 29–36.

[Ferreira et al. 2005] A. J. M. Ferreira, R. C. Batra, C. M. C. Roque, L. F. Qian, and P. A. L. S. Martins, "Static analysis of functionally graded plates using third-order shear deformation theory and a meshless method", *Compos. Struct.* **69**:4 (2005), 449–457.

[Gu and Asaro 1997] P. Gu and R. J. Asaro, "Crack deflection in functionally graded materials", *Int. J. Solids Struct.* **34**:24 (1997), 3085–3098.

[He et al. 2001] X. Q. He, T. Y. Ng, S. Sivashanker, and K. M. Liew, "Active control of FGM plates with integrated piezoelectric sensors and actuators", *Int. J. Solids Struct.* **38**:9 (2001), 1641–1655.

[Jin and Batra 1996] Z. H. Jin and R. C. Batra, "Stress intensity relaxation at the tip of an edge crack in a functionally graded material subjected to a thermal shock", *J. Therm. Stresses* **19** (1996), 317–339.

[Jin and Noda 1994] Z. H. Jin and N. Noda, "Crack tip singular fields in nonhomogeneous materials", *J. Appl. Mech.* (*ASME*) **61** (1994), 738–740.

[Jin and Paulino 2001] Z. H. Jin and G. H. Paulino, "Transient thermal stress analysis of an edge crack in a functionally graded material", *Int. J. Fract.* **107**:1 (2001), 73–98.

[Kesler et al. 1997] O. Kesler, M. Finot, S. Suresh, and S. Sampath, "Determination of processing-induced stresses and properties of layered and gradedcoatings: experimental method and results for plasma-sprayed Ni-Al$_2$O$_3$", *Acta Mater.* **45**:8 (1997), 3123–3134.

[Kwon and Crimp 1997] P. Kwon and M. Crimp, "Automating the design process and powder processing of functionally gradient materials", pp. 73–88 in *Composites and functionally graded materials: 1997 ASME International Mechanical Engineering Congress and Exposition*, edited by T. S. Srivatsan et al., ASME MD **80**, AMSE, New York, 1997.

[Lee and Erdogan 1994] Y. D. Lee and F. Erdogan, "Residual/thermal stress in FGM and laminated thermal barrier coatings", *Int. J. Fract.* **69**:2 (1994), 145–165.

[Ma and Wang 2004] L. S. Ma and T. J. Wang, "Relationships between axisymmetric bending and buckling solutions of FGM circular plates based on third-order plate theory and classical plate theory", *Int. J. Solids Struct.* **41**:1 (2004), 85–101.

[Mushelishvili 1953] N. I. Mushelishvili, *Some basic problems of the mathematical theory of elasticity*, Noordhoff, Groningen, 1953.

[Nowinski and Turski 1953] J. Nowinski and S. Turski, "On the theory of elasticity of isotropic non-homogeneous bodies", *Arch. Mech.* **5** (1953), 67–83. In Polish.

[Obata and Noda 1996] Y. Obata and N. Noda, "Optimum material design for functionally gradient material plate", *Arch. Appl. Mech.* **66**:8 (1996), 581–589.

[Praveen and Reddy 1998] G. N. Praveen and J. N. Reddy, "Nonlinear transient thermoelastic analysis of functionally graded ceramic-metal plates", *Int. J. Solids Struct.* **35**:33 (1998), 4457–4476.

[Shames and Dym 1985] I. H. Shames and C. L. Dym, *Energy and finite element methods in structural mechanics*, McGraw-Hill, New York, 1985.

[Sofiyev 2004] A. H. Sofiyev, "The stability of functionally graded truncated conical shells subjected to aperiodic impulsive loading", *Int. J. Solids Struct.* **41**:13 (2004), 3411–3424.

[Sokolowski 1958] M. Sokolowski, "The bending of transversally non-homogeneous plates of moderate thickness", *Arch. Mech.* **10** (1958), 315–328.

[Suresh and Mortensen 1998] S. Suresh and A. Mortensen, *Fundamentals of functionally graded materials*, Cambridge University Press, 1998.

[Tauchert 1986] T. R. Tauchert, "Thermal stresses in plates: static problems", pp. 23–141 in *Thermal stresses, I*, edited by R. B. Hetnarski, Elsevier, Amsterdam, 1986.

[Vel and Batra 2002] S. S. Vel and R. C. Batra, "Exact solution for thermoelastic deformations of functionally graded thick rectangular plates", *AIAA J.* **40**:7 (2002), 1421–1433.

[Vel and Batra 2003] S. S. Vel and R. C. Batra, "Three-dimensional analysis of transient thermal stresses in functionally graded plates", *Int. J. Solids Struct.* **40**:25 (2003), 7181–7196.

[Woo and Meguid 2001] J. Woo and S. A. Meguid, "Nonlinear analysis of functionally graded plates and shallow shells", *Int. J. Solids Struct.* **38**:42–43 (2001), 7409–7421.

[Wu et al. 2005] L. Wu, Z. Jiang, and J. Liu, "Thermoelastic stability of functionally graded cylindrical shells", *Compos. Struct.* **70**:1 (2005), 60–68.

YEN-LING CHUNG: chungyl@mail.ntust.edu.tw
Department of Construction Engineering, National Taiwan University of Science and Technology, P. O. Box 90-130, Taipei 10672, Taiwan

WEI-TING CHEN: *Department of Construction Engineering, National Taiwan University of Science and Technology, P. O. Box 90-130, Taipei 10672, Taiwan*

THERMOMECHANICS OF MARTENSITIC PHASE TRANSITIONS IN SHAPE MEMORY ALLOYS
I. CONSTITUTIVE THEORIES FOR SMALL AND LARGE DEFORMATIONS

DIRK HELM

This article deals with the geometrically linear and nonlinear modeling of martensitic phase transitions in shape memory alloys. A geometrically nonlinear theory is required for the thermomechanical simulation of complex structures like endoscopic devices and stents. However, in certain situations like the simulation of pipe couplers, it is sufficient to apply a geometrically linear theory. In both cases, a free energy function is introduced, evolution equations for internal variables are postulated, and the dependence of the fraction of oriented martensite on the transformation strains is represented by a novel constitutive equation. In all, the developed constitutive theories are able to depict the thermomechanically coupled behavior of shape memory alloys. This is demonstrated in Part II of this article (to appear in this journal, in coauthorship with M. Schäfers). For this purpose, the theories are numerically treated in the framework of the finite element method in order to solve initial-boundary-value problems. These illustrate the main features of the constitutive theories by means of numerical test calculations. The results are compared with experimental data.

1. Introduction

The exceptional material behavior of shape memory alloys is based on martensitic phase transitions, which can be initiated and propagated by thermomechanical processes. In contrast to other kinds of phase changes, martensitic phase transitions take place without diffusion processes. These phase transitions are the result of cooperative movements of atomic layers until the crystal structure of the product phase is reached. The underlying physical processes on the micro scale are well understood [Funakubo 1987; Otsuka and Ren 1999; Otsuka and Wayman 1998; Patoor et al. 2006]. During the last decades, the material behavior including the fatigue properties of different shape memory alloys like NiTi and CuAlNi has been elaborately investigated in uniaxial tests; see, for example, [Funakubo 1987; Huo and Müller 1993; Otsuka and Wayman 1998; Shaw and Kyriakides 1995; Eggeler et al. 2004]. Moreover, the material properties under combined tension-torsion loads were studied by [Rogueda et al. 1996; Lim and McDowell 1999; Helm and Haupt 2001; Raniecki et al. 2001; McNaney et al. 2003]. Above the so-called austenite finish temperature A_f, martensitic phase transitions from austenite into oriented (detwinned) martensite occur at a certain stress level. Due to the involved crystal structure of the austenite and martensite phase, the occurring phase transitions are dominated by shear deformations and lead to macroscopic inelastic deformations. If the material is unloaded, the material returns back to its parent
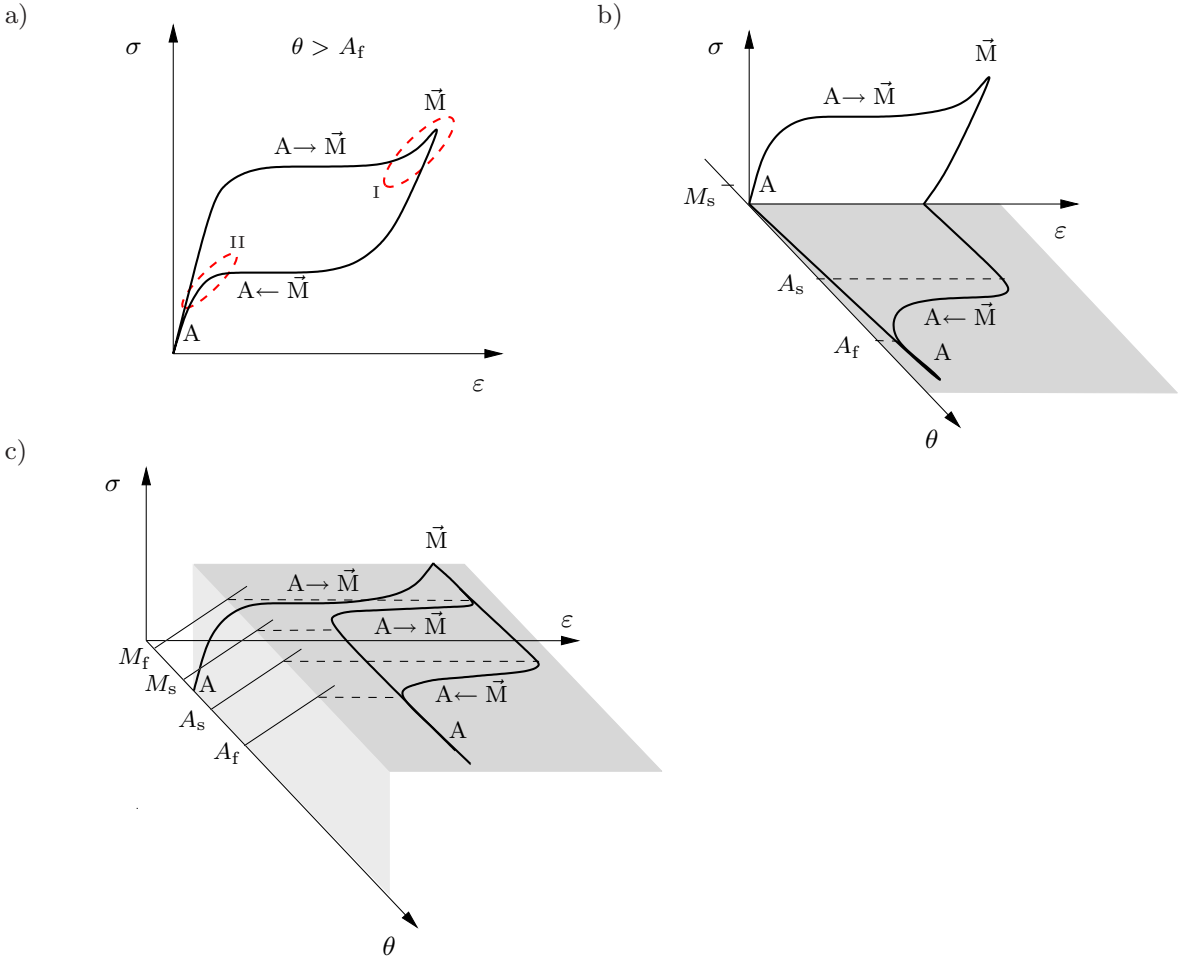
Figure 1. Sketch of the pseudoelasticity and the shape memory effects. A: austenite; $\vec{\mathrm{M}}$: oriented (detwinned) martensite.

phase (austenite) and initial shape. This behavior is called pseudoelasticity or superelasticity, and is illustrated in Figure 1a. In the case of polycrystalline nickel-titanium shape memory alloys, the pseudoelastic deformations are in the magnitude of about 5–10% engineering strain.

On condition that the austenitic material is loaded below the austenite finish temperature A_f but above the martensite start temperature M_s (see Figure 1b and c), martensitic phase transitions occur during mechanical loading, but after unloading inelastic deformations remain in the shape memory alloy, because the detwinned martensite still exists (see Figure 1b). This effect is called pseudoplasticity due to martensitic phase transitions. Of course, the pseudoplastic behavior (r-pseudoplasticity) is also observed below M_f: in this situation, the shape memory alloy consists of martensite twins in the stress-free state, which can be oriented and reoriented by appropriate mechanical loads. In the present study, this effect is not regarded in the model, but the basic structure of the constitutive theory [Helm 2001; Helm and Haupt 2003] also includes the description of this phenomenon.

In addition to the pseudoelastic and pseudoplastic behavior, appropriate thermomechanical processes lead to one-way and two-way shape memory effects. The one-way shape memory effect takes place if the detwinned martensite is heated at sufficient small mechanical loads. Between the A_s- and A_f-temperature, the oriented martensite transforms back into austenite (see Figure 1b), the inelastic deformations disappear, and the material regains its original shape. Therefore, this material behavior is called one-way shape memory effect.

Under certain circumstances, shape memory alloys exhibit a two-way shape memory effect. Therefore, oriented martensite must be produced by an appropriate stress field in the microstructure, which can be the result of residual stresses or external forces. This stress field must be affected on the microstructure during a subsequent heating and cooling process between the A_f- and M_f-temperature (see Figure 1c). In analogy to the one way-shape memory effect, the material regains approximately its undeformed shape during heating. However, the required temperature to initiate and propagate the martensitic phase transitions is higher than in the case of the one-way shape memory effect, because the existing stress state increases the characteristic phase transition temperatures. In contrast to the one-way shape memory effect, the induced stress state during the cooling process leads to phase transitions from austenite into oriented martensite. Consequently, the material regains its deformed shape. In the used definition of the two-way shape memory effect, which is advantageously for the modeling of the material behavior, the two-way shape memory effect is released by a suitable stress field, which interacts with the microstructure, and an appropriate variation in the temperature field. This usage of the term two-way shape memory effect differs from the classical definition (see the explanations in [Funakubo 1987; Otsuka and Wayman 1998]): in the classical definition, the two-way shape memory effect is only released by residual stress fields. The other phenomenon is called two-way behavior of a shape memory alloy with a one-way characteristic [Funakubo 1987].

More than twenty years ago, the first constitutive theories for shape memory alloys were published [Achenbach and Müller 1982; Bertram 1982; Tanaka and Nagaki 1982; Falk 1983]. Since these pioneering studies, many different constitutive theories have been developed, and a number of models are able to predict the uniaxial behavior of shape memory alloys; see, for example, [Liang and Rogers 1990; Khan and Lagoudas 2002; Seelecke 2002; Paiva et al. 2005]. Such theories are well applicable to simulate the behavior of one-dimensional structures like the usage of wires in actuator applications. However, the simulation of applications like stents or pipe couplers requires three-dimensional formulated constitutive theories. For this purpose, a large number of phenomenological models were suggested: for example, Bertram [1982] and Graesser and Cozzarelli [1994] developed constitutive theories, which are not discussed in a thermodynamic framework. In contrast to these concepts, constitutive theories in the framework of continuum thermomechanics have been proposed in [Boyd and Lagoudas 1994; Raniecki et al. 1992; Raniecki and Lexcellent 1994; Leclercq and Lexcellent 1996; Souza et al. 1998; Juhász et al. 2000; Entchev and Lagoudas 2002; Helm and Haupt 2003; Lexcellent et al. 2006]. These models consist of a thermodynamic function for the free energy (Helmholtz free energy) or the free enthalpy (Gibbs free energy), which depends on state and internal variables. Moreover, evolution equations for certain internal variables are introduced to represent the history dependent material behavior as well as dissipation phenomena. An elaborate review about the phenomenological modeling of shape memory alloys was recently published in [Lagoudas et al. 2006]. In addition to the discussions in that paper, it should be mentioned that a part of the phenomenological models subdivide the evolution of the phase

transition strains into an evolution equation for the forward phase transition and an evolution equation for the reverse phase transition; see, for example, [Bondaryev and Wayman 1988; Boyd and Lagoudas 1994; Auricchio et al. 1997; Helm 2001; Lagoudas et al. 2006]. In contrast to this, the approaches in [Graesser and Cozzarelli 1994; Delobelle and Lexcellent 1996; Souza et al. 1998; Juhász et al. 2000; Helm and Haupt 2003; Auricchio and Stefanelli 2004] utilize only one evolution equation for both directions of phase transitions. In addition to these phenomenological concepts, different types of micromechanically motivated theories have also been proposed in the literature; see, for instance, [Patoor et al. 1994; Lexcellent et al. 1996; Huang et al. 2000; Lim and McDowell 2002; Tanaka et al. 2002; Anand and Gurtin 2003; Thamburaja and Anand 2003; Jung et al. 2004; Novák and Sittner 2004; Patoor et al. 2006], which are able to model the influence of the microstructure on the macroscopic behavior. Most of the proposed constitutive theories are formulated in the framework of a geometrically linear theory. However, the simulation of certain problems like stents or endoscopic devices requires a geometrically nonlinear theory. Referring to this, only a few geometrically nonlinear concepts have been proposed in the common literature: on the one hand, phenomenological theories were published in [Auricchio and Taylor 1997; Qidwai and Lagoudas 2000; Helm 2001; Müller and Bruhns 2004]. On the other hand, in [Anand and Gurtin 2003; Thamburaja and Anand 2003; Jung et al. 2004], the focus has been on micromechanical models at finite deformations.

For many applications, it is sufficient to apply a geometrically linear theory. However, a geometrically nonlinear constitutive theory is generally required, because different types of applications are characterized by large rotations. Therefore, the present work is concerned with the thermomechanical modeling in the case of small and also finite deformations. Our previous studies [Helm and Haupt 2003; Helm 2005] are geometrically linear theories and contain singularities in the phase transition function. Moreover, the concept of the former paper also contains a singularity in the phase transition rule. In certain cases, both types of singularities are removable if a simple von Mises phase transition function is applied. In contrast to these previous studies, the present constitutive theory does not contain such types of singularities, because the dependence of the fraction of oriented martensite on the transformation strains is modeled by a novel constitutive equation. In addition to this mathematical improvement, the modified constitutive relation leads also to a more precise depiction of the observed material behavior: e.g., the modeling of residual martensite after unloading at temperatures above A_f.

The first part of the article is organized as follows: in Section 2, the kinematics for representing inelasticity with respect to small and finite deformations are outlined. Thereafter, the basic structure of the constitutive theories to model the multiaxial behavior of shape memory alloys in the framework of continuum thermomechanics is developed (geometrically linear theory: Section 3; geometrically nonlinear theory: Section 4). In both cases, a free energy function and two evolution equations for internal variables are introduced. Both models are able to represent the basic phenomena of shape memory alloys due to martensitic phase transitions: i.e. pseudoelasticity and pseudoplasticity as well as one-way and two-way shape memory effect. Moreover, the representation of other effects like tension-compression asymmetries or the cyclic behavior of shape memory alloys is possible, if certain parts of the model are slightly changed. A second part of this article ([Helm and Schäfers 2006]) will deal with the numerical treatment of these constitutive theories in the framework of the finite element method. For this purpose, the system of differential equations is numerically integrated to obtain the stress state as well as the
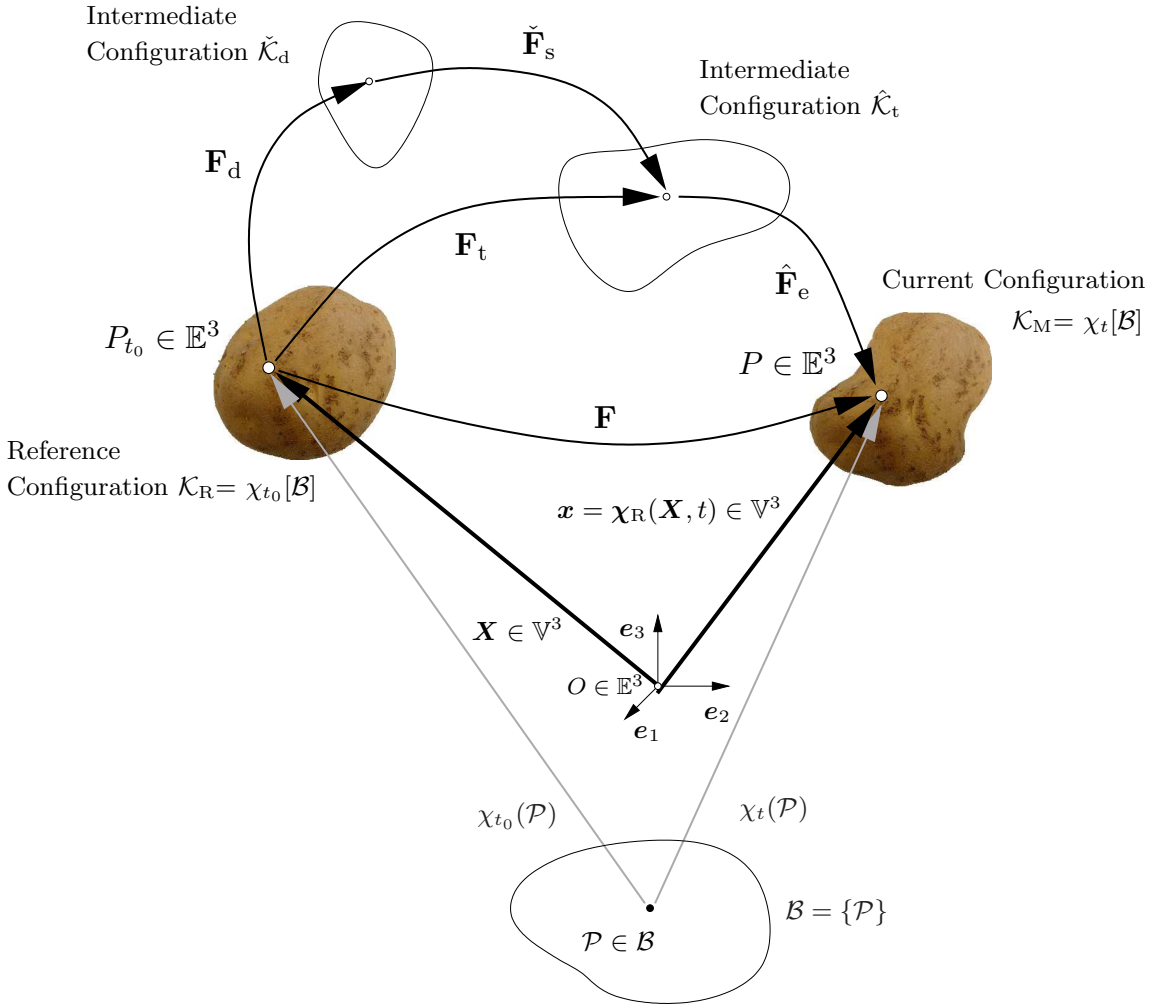
Figure 2. Reference, current, and intermediate configuration.

accompanying heat production. The capabilities of these constitutive theories are demonstrated with illustrative examples and the results of the constitutive theories are compared to experimental data.

2. Kinematics

The continuum mechanics is based on the assumption that a material body $\mathcal{B}$ consists of material points $\mathcal{P}$ and its motion is depicted by a continuous sequence of configurations (see Figure 2). If a reference configuration is selected, the motion is representable by the one-to-one mapping: $x = \chi_R(X, t)$. The local changes in space of the motion are depicted by the deformation gradient $\mathbf{F}(X, t) = \text{Grad } \chi_R(X, t)$, which is the Fréchet-derivative of the motion $x = \chi_R(X, t)$. The deformation gradient transforms material line elements dX of the reference configuration $\mathcal{K}_R$ into material line elements of the current configuration $\mathcal{K}_M$: i.e., $dx = \mathbf{F}dX$.

The following theory for finite deformations makes use of the multiplicative split $\mathbf{F} = \mathbf{F}^* \bar{\mathbf{F}}$, which can be traced back to [Flory 1961]: in this multiplicative split, the deformation gradient $\mathbf{F}$ is decomposed into a volumetric part $\mathbf{F}^*$ and an isochoric part $\bar{\mathbf{F}}$ if the operators

$$(\cdot)^* : \mathbf{F} \mapsto \mathbf{F}^* = (\det \mathbf{F})^{1/3} \mathbf{1} \qquad \text{and} \qquad \overline{(\cdot)} : \mathbf{F} \mapsto \bar{\mathbf{F}} = (\det \mathbf{F})^{-1/3} \mathbf{F} \tag{1}$$

are applied. Throughout the whole article, these operators are used in a more general sense: the tensor $\bar{\mathbf{A}} = (\det \mathbf{A})^{-1/3} \mathbf{A}$ is the unimodular part of $\mathbf{A}$ and the remaining nonunimodular part of $\mathbf{A}$ is denoted by $\mathbf{A}^* = (\det \mathbf{A})^{1/3} \mathbf{1}$.

2.1. *Multiplicative decompositions of the deformation gradient.*

In finite deformation theories for modeling the inelastic behavior of different types of materials, the multiplicative decomposition of the deformation gradient $\mathbf{F} = \hat{\mathbf{F}}_e \mathbf{F}_i$ into an elastic part $\hat{\mathbf{F}}_e$ and an inelastic part $\mathbf{F}_i$ is often applied (see [Kröner 1960; Lee 1969; Lee and Liu 1967; Lubliner 1985; Haupt 2002]). In the present framework, the related multiplicative decomposition $\mathbf{F} = \hat{\mathbf{F}}_e \mathbf{F}_t$ is used: therein, $\hat{\mathbf{F}}_e$ is the elastic part of the deformation gradient and $\mathbf{F}_t$ represents the inelastic part of the deformation gradient resulting from martensitic phase transitions see [Auricchio and Taylor 1997; Helm 2001]. The multiplicative decomposition of the deformation gradient implies a stress-free intermediate configuration $\hat{\mathcal{K}}_t$ (see Figure 2). Already in [Eckart 1948] and [Kröner 1958], stress-free intermediate configurations were introduced to define inelastic states. It is common knowledge that the multiplicative decomposition $\mathbf{F} = \hat{\mathbf{F}}_e \mathbf{F}_t$ leads to an incompatible intermediate configuration; see [Eckart 1948; Lee 1969; Mandel 1972; Haupt 2002].

As a result of our previous studies [Helm and Haupt 2003; Helm 2005], the consideration of internal stress fields is a useful concept to model the material behavior of shape memory alloys. It is known from viscoplasticity [Lion 2000] that an additional multiplicative decomposition of the inelastic part is appropriate to model internal stress fields in a geometrically nonlinear theory. Therefore, this concept is transferred to the present study (see [Helm 2001]): the inelastic part $\mathbf{F}_t = \check{\mathbf{F}}_s \mathbf{F}_d$ of the deformation gradient is decomposed into two parts $\check{\mathbf{F}}_s$ and $\mathbf{F}_d$. In the present theory, the part $\check{\mathbf{F}}_s$ is used to model energy storage effects during the evolution of internal stress fields while the remainder part $\mathbf{F}_d$ is introduced to account for the accompanied dissipative phenomena. In addition to the intermediate configuration $\hat{\mathcal{K}}_t$, the additional decomposition of $\mathbf{F}_t = \check{\mathbf{F}}_s \mathbf{F}_d$ formally results in a further intermediate configuration $\check{\mathcal{K}}_d$ (see Figure 2).

2.2. *Strain tensors.*

2.2.1. *Finite strains.*
Provided that the multiplicative decomposition is used, the Green strain tensor $\mathbf{E} = [\mathbf{C} - \mathbf{1}]/2$ cannot be separated into purely elastic and inelastic parts. Therein, the tensor $\mathbf{C} = \mathbf{F}^T \mathbf{F}$ is the right Cauchy–Green tensor. However, the transformation of the Green strain tensor to the intermediate configuration $\hat{\mathcal{K}}_t$ leads to a strain measure (see [Haupt 1985])

$$\hat{\boldsymbol{\Gamma}} = \mathbf{F}_t^{-T} \mathbf{E} \mathbf{F}_t^{-1} = \hat{\boldsymbol{\Gamma}}_e + \hat{\boldsymbol{\Gamma}}_t \text{ with } \hat{\boldsymbol{\Gamma}}_e = \tfrac{1}{2}(\hat{\mathbf{C}}_e - \mathbf{1}) \text{ and } \hat{\boldsymbol{\Gamma}}_t = \tfrac{1}{2}(\mathbf{1} - \hat{\mathbf{B}}_t^{-1}), \tag{2}$$

which is additively decomposable into an elastic part $\hat{\boldsymbol{\Gamma}}_e$ and an inelastic part $\hat{\boldsymbol{\Gamma}}_t$. Therein, the tensors $\hat{\mathbf{C}}_e = \hat{\mathbf{F}}_e^T \hat{\mathbf{F}}_e$ and $\hat{\mathbf{B}}_t = \mathbf{F}_t \mathbf{F}_t^T$ are defined in analogy to the right and left Cauchy–Green tensors, $\mathbf{C} = \mathbf{F}^T \mathbf{F}$ and $\mathbf{B} = \mathbf{F} \mathbf{F}^T$. If $\hat{\boldsymbol{\Gamma}}_e$ and $\hat{\boldsymbol{\Gamma}}_t$ are expressed in terms of the reference configuration $\mathcal{K}_R$,

$$\mathbf{E}_e = \mathbf{F}_t^T \hat{\boldsymbol{\Gamma}}_e \mathbf{F}_t = \tfrac{1}{2}(\mathbf{F}_t^T \hat{\mathbf{C}}_e \mathbf{F}_t - \mathbf{F}_t^T \mathbf{F}_t) \quad \text{and} \quad \mathbf{E}_t = \mathbf{F}_t^T \hat{\boldsymbol{\Gamma}}_t \mathbf{F}_t = \tfrac{1}{2}(\mathbf{F}_t^T \mathbf{F}_t - \mathbf{1}), \tag{3}$$

it becomes clear that the transformation strain state $\mathbf{E}_t$ depends only on $\mathbf{F}_t$, but the elastic strain state $\mathbf{E}_e$ is a function of $\hat{\mathbf{F}}_e$ and $\mathbf{F}_t$.

On the basis of the foregoing discussion, an internal variable to represent internal stress fields can be introduced with respect to the intermediate configuration $\check{\mathcal{K}}_d$: the transformation of $\mathbf{E}_t$ or $\hat{\boldsymbol{\Gamma}}_t$ to the intermediate configuration $\check{\mathcal{K}}_d$ leads to an internal variable $\check{\mathbf{Y}}$ of strain type,

$$\check{\mathbf{Y}} = \mathbf{F}_d^{-T}\mathbf{E}_t\mathbf{F}_d^{-1} = \check{\mathbf{F}}_s^T\hat{\boldsymbol{\Gamma}}_t\check{\mathbf{F}}_s = \check{\mathbf{Y}}_s + \check{\mathbf{Y}}_d, \tag{4}$$

which can be additively decomposed into $\check{\mathbf{Y}}_s$ and $\check{\mathbf{Y}}_d$:

$$\check{\mathbf{Y}}_s = \tfrac{1}{2}\left(\check{\mathbf{C}}_s - \mathbf{1}\right) \quad \text{and} \quad \check{\mathbf{Y}}_d = \tfrac{1}{2}\left(\mathbf{1} - \check{\mathbf{B}}_d^{-1}\right). \tag{5}$$

In analogy to the left and right Cauchy–Green tensors, the tensors $\check{\mathbf{C}}_s = \check{\mathbf{F}}_s^T\check{\mathbf{F}}_s$ and $\check{\mathbf{B}}_d = \mathbf{F}_d\mathbf{F}_d^T$ are defined.

Remark 1 (Notation). In order to distinguish between the different configurations the following terminology is applied (see Figure 2): Stress and strain tensors operating in the intermediate configuration $\hat{\mathcal{K}}_t$ are denoted by $(\hat{\cdot})$. In contrast to this, the stress and strain measures in the second intermediate configuration $\check{\mathcal{K}}_d$ are denoted by $(\check{\cdot})$. For the stress tensors in the reference configuration $\mathcal{K}_R$ the notation $(\tilde{\cdot})$ is used and for the strain tensors the letters like $\mathbf{E}$ and $\mathbf{C}$ are applied. In the case of the theory for small deformations (see Eq.(6) and (7)), the distinction of different configurations is not required. Moreover, the quantities $\check{\mathbf{F}}_s$ and $\hat{\mathbf{F}}_e$ are denoted with $(\check{\cdot})$ and $(\hat{\cdot})$, because they transforms material line elements from different intermediate configurations.

2.2.2. *Small strains.* The previously introduced strain measures on the basis of the multiplicative decompositions are not required in their exact forms if the special case of a theory for small deformations is considered: according to [Casey 1985], the multiplicative decomposition of the deformation gradient $\mathbf{F} = \hat{\mathbf{F}}_e\mathbf{F}_t$ corresponds in a geometrically linear theory to the additive decomposition of the linearized Green strain tensor,

$$\mathbf{E} = \mathbf{E}_e + \mathbf{E}_t, \tag{6}$$

into an elastic part $\mathbf{E}_e$ and an inelastic part $\mathbf{E}_t$, which represent the transformation strain state. Finally, the other multiplicative decomposition $\mathbf{F}_t = \check{\mathbf{F}}_s\mathbf{F}_d$ merge into the additive decomposition

$$\mathbf{Y} = \mathbf{E}_t = \mathbf{Y}_s + \mathbf{Y}_d, \tag{7}$$

if the assumption of small deformations is applied. Consequently, the geometrically linear theory can be formulated on the basis of the additive decomposition (6) and (7).

3. Constitutive theory in relation to small deformations

3.1. *Free energy.* In shape memory alloys different types of energy storage mechanisms play an important role: for example the change in internal energy due to the thermoelasticity of a single-phase material, the energy change on account of the phase transitions, as well as energy storage phenomena resulting from internal stress fields. Consequently, it is assumed that the free energy of the proposed model depends on the elastic part of the linearized Green strain tensor $\mathbf{E}_e$ (see Equation (6)), the absolute thermodynamic temperature θ, the fraction $z \in [0, 1]$ of oriented martensite, and the internal variable $\mathbf{Y}_s$:

$$\psi(\mathbf{E}_e, \theta, z, \mathbf{Y}_s) = \hat{\psi}_e(\mathbf{E}_e, \theta, z) + \hat{\psi}_s(\mathbf{Y}_s, \theta). \tag{8}$$

In this assumption, the thermoelastic part ψ_e represents the mixture of two thermoelastic single-phase materials (austenite (A) and martensite (M)):

$$\rho\psi_e = \rho\hat{\psi}_e(\mathbf{E}_e, \theta, z) = z\rho\psi_e^M(\mathbf{E}_e, \theta) + (1-z)\rho\psi_e^A(\mathbf{E}_e, \theta)$$

$$= \tilde{\mu}(\theta, z)\mathbf{E}_e^D \cdot \mathbf{E}_e^D + \frac{\tilde{\kappa}(\theta, z)}{2}(\operatorname{tr}\mathbf{E}_e)^2 - 3\tilde{\alpha}(\theta, z)(\operatorname{tr}\mathbf{E}_e)(\theta - \theta_0)$$

$$+ z\rho\int_{\theta_0}^{\theta} c_{d_0}^M(\bar{\theta})\mathrm{d}\bar{\theta} + (1-z)\rho\int_{\theta_0}^{\theta} c_{d_0}^A(\bar{\theta})\mathrm{d}\bar{\theta} + \rho\left[u_0^A + z\Delta u_0\right]$$

$$- \theta\left[z\rho\int_{\theta_0}^{\theta}\frac{c_{d_0}^M(\bar{\theta})}{\bar{\theta}}\mathrm{d}\bar{\theta} + (1-z)\rho\int_{\theta_0}^{\theta}\frac{c_{d_0}^A(\bar{\theta})}{\bar{\theta}}\mathrm{d}\bar{\theta} + \rho\left[\eta_0^A + z\Delta\eta_0\right]\right]. \quad (9)$$

Therein, the effective elasticity parameters

$$\tilde{\mu}(\theta, z) = z\mu^M(\theta) + (1-z)\mu^A(\theta), \quad (10)$$

$$\tilde{\kappa}(\theta, z) = z\kappa^M(\theta) + (1-z)\kappa^A(\theta), \text{ and} \quad (11)$$

$$\tilde{\alpha}(\theta, z) = z\alpha^M(\theta)\kappa^M(\theta) + (1-z)\alpha^A(\theta)\kappa^A(\theta) \quad (12)$$

contain the elasticity parameters of the different phases ($\omega = $ A, M): μ^ω is the shear modulus, κ^ω the bulk modulus, and α^ω the linear expansion coefficient. Moreover, θ_0 represents the reference temperature, $c_{d_0}^\omega$ is a certain part of the specific heat at constant deformation, and the initial internal energy and the initial entropy are denoted by u_0^ω and η_0^ω. Furthermore the constants $\Delta u_0 = u_0^M - u_0^A$ and $\Delta\eta_0 = \eta_0^M - \eta_0^A$ are of special interest in the thermomechanical modeling of phase transitions (see [Huo and Müller 1993; Helm and Haupt 2003]): for instance, they play a dominant role in the description of latent heat effects. The thermomechanical interactions between the austenite and martensite phase in the microstructure of the material are strongly simplified due to the assumption of equal thermoelastic strain and temperature states in both phases.

The other part $\hat{\psi}_s(\mathbf{Y}_s)$ of the free energy models the energy storage due to the generation and variation of internal stresses. Each grain of a polycrystalline shape memory alloy contains a lot of imperfections like precipitations and impurities. Consequently, the martensitic phase transitions are obstructed by the imperfections and by the surrounding grains. As a macroscopical result of these microstructural phenomena, the associated part ψ_s of the free energy function is assumed to be

$$\rho\psi_s = \rho\hat{\psi}_s(\theta, \mathbf{Y}_s) = \frac{c(\theta)}{2}\mathbf{Y}_s \cdot \mathbf{Y}_s. \quad (13)$$

Therein, $c(\theta)$ is a nonnegative material function of temperature.

3.2. *Evolution equations for internal variables.* In order to develop a thermodynamically consistent theory, the basic structure of the free energy function according to Equation (8) is introduced into the internal dissipation inequality $\rho\delta_i = -\rho\dot{\psi} - \rho\dot{\theta}\eta + \mathbf{T} \cdot \dot{\mathbf{E}} \geq 0$ (for details see [Helm and Haupt 2003] or Section 4):

$$\rho\delta_i = \left[\mathbf{T} - \rho\frac{\partial\psi_e}{\partial\mathbf{E}_e}\right] \cdot \dot{\mathbf{E}}_e - \rho\left[\frac{\partial\psi}{\partial\theta} + \eta\right]\dot{\theta} - \rho\frac{\partial\psi_e}{\partial z}\dot{z} - \rho\frac{\partial\psi_s}{\partial\mathbf{Y}_s} \cdot \dot{\mathbf{Y}}_s + \mathbf{T} \cdot \dot{\mathbf{E}}_t \geq 0. \quad (14)$$

Therein, η is the entropy and the material density is denoted by ρ. For arbitrary rates of $\mathbf{E}_e$, θ, z, $\mathbf{Y}_s$, and $\mathbf{E}_t$, this inequality implies potential relations for the stress tensor $\mathbf{T}$,

$$\mathbf{T} = \rho \frac{\partial \psi_e}{\partial \mathbf{E}_e} = 2\tilde{\mu}(\theta, z)\mathbf{E}_e^D + \tilde{\kappa}(\theta, z)(\operatorname{tr}\mathbf{E}_e)\mathbf{1} - 3\tilde{\alpha}(\theta, z)\,(\theta - \theta_0)\,\mathbf{1}, \tag{15}$$

and the entropy $\eta = -\partial \psi / \partial \theta$, if $\dot{z}$, $\dot{\mathbf{Y}}_s$, and $\dot{\mathbf{E}}_t$ do not depend on $\dot{\mathbf{E}}_e$ and $\dot{\theta}$ (see [Coleman and Gurtin 1967]). Furthermore, the remaining dissipation inequality motivates the definition of the thermodynamic quantity $\Xi = \rho \partial \psi_e / \partial z$,

$$\Xi = \frac{\partial \tilde{\mu}(\theta, z)}{\partial z}\mathbf{E}_e^D \cdot \mathbf{E}_e^D + \frac{1}{2}\frac{\partial \tilde{\kappa}(\theta, z)}{\partial z}\,(\operatorname{tr}\mathbf{E}_e)^2 - 3\frac{\partial \tilde{\alpha}(\theta, z)}{\partial z}\,(\operatorname{tr}\mathbf{E}_e)\,(\theta - \theta_0)$$
$$+ \rho\left[\int_{\theta_0}^{\theta}\left[c_{d0}^M(\bar{\theta}) - c_{d0}^A(\bar{\theta})\right]d\bar{\theta} + \Delta u_0\right] - \rho\theta\left[\int_{\theta_0}^{\theta}\frac{c_{d0}^M(\bar{\theta}) - c_{d0}^A(\bar{\theta})}{\bar{\theta}}d\bar{\theta} + \Delta\eta_0\right], \tag{16}$$

and the internal stress field $\mathbf{X}_\varepsilon$:

$$\mathbf{X}_\varepsilon = \rho \frac{\partial \psi_s}{\partial \mathbf{Y}_s} = c(\theta)\,\mathbf{Y}_s = c(\theta)\,[\mathbf{E}_t - \mathbf{Y}_d]. \tag{17}$$

The thermodynamic quantity Ξ plays an important role in view of the depiction of the stress state, which is required to initiate and propagate the martensitic phase transitions. The other internal variable $\mathbf{X}_\varepsilon$ incorporates the fact that the cooperative motion of the atoms during the martensitic phase transitions is limited by defects in the microstructure like impurities and precipitations. In classical theories of plasticity, $\mathbf{X}_\varepsilon$ is denoted as back stress.

With these definitions, the remaining dissipation inequality takes the following form:

$$\rho \delta_i = -\Xi\,\dot{z} + \mathbf{T}\cdot\dot{\mathbf{E}}_t - \mathbf{X}_\varepsilon\cdot\dot{\mathbf{Y}}_s \geq 0. \tag{18}$$

To complete the material model, constitutive equations for the internal variables z, $\mathbf{E}_t$, and $\mathbf{Y}_d = \mathbf{E}_t - \mathbf{Y}_s$ have to be defined. On account of the physical understanding of the deformation mechanisms (see [Miyazaki and Otsuka 1989], for instance) and also based on experimental studies, the martensitic phase transitions between austenite and oriented martensite are accompanied by inelastic deformations. In polycrystalline materials, the required constitutive relation between the oriented martensite fraction z and the transformation strain tensor $\mathbf{E}_t$ is quite difficult to identify. However, the following physical aspects should be considered in a constitutive theory for shape memory alloys: if the material is completely in the austenite phase, the transformation strains must vanish, i.e. $\mathbf{E}_t = \mathbf{0}$. Moreover, if a complex deformation path is performed, which starts and ends at $\mathbf{E}_t = \mathbf{0}$, it must be guaranteed that the fraction of oriented martensite is always zero if $\mathbf{E}_t = \mathbf{0}$. Both $z = \hat{z}(\mathbf{E}_t)$ with the restriction $\hat{z}(\mathbf{0}) = 0$ and $\mathbf{E}_t = \bar{\mathbf{E}}_t(z)$ with the constraint $\bar{\mathbf{E}}_t(0) = \mathbf{0}$ are appropriate strategies to model the observations. In the present concept the fraction of oriented martensite $z = \hat{z}(\mathbf{E}_t)$ is depicted as function of $\mathbf{E}_t$. It should be emphasized that such a relation is only meaningful between the fraction of detwinned martensite and the inelastic strain state, because the fraction of twinned martensite does not depend on the inelastic strain state.

Remark 2. Instead of a function $z = \hat{z}(\mathbf{E}_t)$, it is possible to apply an evolution equation for z, namely $\dot{z} = Z(\mathbf{E}_t) \cdot \dot{\mathbf{E}}_t$. Then, the relation

$$z = \oint Z(\mathbf{E}_t) \cdot \mathrm{d}\mathbf{E}_t = 0 \qquad (19)$$

must be fulfilled if an arbitrary deformation process starts at $\mathbf{E}_t = \mathbf{0}$. This relation guarantees that z vanishes after an arbitrary multiaxial process, which starts and ends at $\mathbf{E}_t = \mathbf{0}$. Of course, Equation (19) is fulfilled, if and only if $Z(\mathbf{E}_t)$ is equal to $\mathrm{d}z/\mathrm{d}\mathbf{E}_t$.

For an isotropic material, the fraction z of oriented martensite depends on the basic invariants ($J_{t1} = \mathrm{tr}\,\mathbf{E}_t$, $J_{t2} = \mathrm{tr}\,\mathbf{E}_t^2$, and $J_{t3} = \mathrm{tr}\,\mathbf{E}_t^3$): $z = \hat{z}(\mathbf{E}_t) = \tilde{z}(J_{t1}, J_{t2}, J_{t3})$. In the remaining dissipation inequality, the material time derivative of $z = \tilde{z}(J_{t1}, J_{t2}, J_{t3})$ is required:

$$\dot{z} = \frac{\mathrm{d}\hat{z}}{\mathrm{d}\mathbf{E}_t} \cdot \dot{\mathbf{E}}_t \qquad \text{with} \qquad \frac{\partial \hat{z}}{\partial \mathbf{E}_t} = \frac{\partial \tilde{z}}{\partial J_{t1}}\mathbf{1} + 2\frac{\partial \tilde{z}}{\partial J_{t2}}\mathbf{E}_t + 3\frac{\partial \tilde{z}}{\partial J_{t3}}\mathbf{E}_t^2. \qquad (20)$$

Martensitic phase transitions are accompanied by small volume changes (see [Shimizu and Tadaki 1987], for instance), which may be neglected. For example, in NiTi the volume change by phase transitions between austenite and martensite amounts 0.34%. Consequently, the underlying deformation mechanism is nearly volume preserving. As a result of this material property, the influence of the first invariant J_{t1} in the function of z can be omitted. Furthermore, the transformation strains are small and dominated by shear deformations. Therefore, the influence of the second invariant is much more important than that of the third invariant. However, for the modeling of tension-compression asymmetries in the strain space, the first and third invariants may be important quantities. Ignoring these possibilities, the fraction of oriented martensite is introduced to be a function of the second invariant J_{t2}: $z = \tilde{z}(J_{t2})$. In phenomenological theories for shape memory alloys; see, for example, [Levitas 1998; Juhász et al. 2000; Helm and Haupt 2003], the fraction of oriented martensite is commonly depicted in the following form:

$$z = \hat{z}(\mathbf{E}_t) = \tilde{z}(J_{t2}) = \frac{\|\mathbf{E}_t\|}{\sqrt{\frac{3}{2}}\gamma_t} \qquad \Rightarrow \qquad \dot{z} = \frac{\mathbf{E}_t \cdot \dot{\mathbf{E}}_t}{\sqrt{\frac{3}{2}}\gamma_t \|\mathbf{E}_t\|}. \qquad (21)$$

Therein, the norm of $\mathbf{E}_t$ is given by $\|\mathbf{E}_t\| = \sqrt{\mathbf{E}_t \cdot \mathbf{E}_t}$ and γ_t represents the maximum transformation strain, which can be measured in a uniaxial test. It should be mentioned that a similar relation was suggested by Bertram [1982] in terms of the so-called limit function. As pointed out in [Helm and Haupt 2003], the evolution equation (phase transition rule) for the transformation strains incorporates the time derivative of z according to Equation (21)$_2$. Therefore, the applied phase transition rule (see Equation (27) and the internal variable $\mathbf{X}_\theta$ according to Equation (24) for $\gamma_0 = 0$) and likewise the introduced phase transition function are singular, if a process starts at $\mathbf{E}_t = \mathbf{0}$. In certain cases, these singularities are removable, but difficulties in numerical implementation still remain. Similar problems exist in the theories of Souza et al. [1998], Juhász et al. [2000], and Auricchio and Stefanelli [2004]. In order to avoid this problem, Auricchio and Petrini [2004] introduce a regularized norm operator. Moreover, the shape memory materials often show a smooth transition from the retransformation plateau into the elastic region (see region II in Figure 1a): in previous models, such as that of [Helm and Haupt 2003], this smooth transition cannot be described. Therefore, an improved constitutive equation for representing the fraction

of oriented martensite as a function of the transformation strain tensor is proposed in the present article:

$$z = \hat{z}(\mathbf{E}_t) = \tilde{z}(J_{t2}) = \frac{\sqrt{\frac{2}{3}\mathbf{E}_t \cdot \mathbf{E}_t + \gamma_0^2}}{\gamma_t} - z_0. \tag{22}$$

In this constitutive relation, γ_t is still the maximum transformation strain. In contrast to the constitutive relation (21), the positive parameters γ_0 and z_0 are additionally introduced. The parameter z_0 is pre-determined, because the physical understanding of the occurring martensitic phase transitions between austenite and oriented martensite requires $z = \hat{z}(\mathbf{0}) = 0$. Consequently, this condition leads to $z_0 = \gamma_0/\gamma_t$. The parameter γ_0 has an important influence on the rate of z (Equation (22)),

$$\dot{z} = \frac{\mathbf{E}_t \cdot \dot{\mathbf{E}}_t}{\sqrt{\frac{3}{2}}\gamma_t \sqrt{\mathbf{E}_t \cdot \mathbf{E}_t + \frac{3}{2}\gamma_0^2}}, \tag{23}$$

because the influence of γ_0 on z is only negligible if $\|\mathbf{E}_t\| \gg \gamma_0$. In order to obtain the final form of the internal dissipation inequality (18), the time derivative of z according to Equation (23) is inserted, the time derivative of $\mathbf{Y}_s = \mathbf{E}_t - \mathbf{Y}_d$ is replaced by usage of Equation (7), and the internal variable $\mathbf{X}_\theta$ of stress type (see the discussion in [Helm and Haupt 2003]):

$$\mathbf{X}_\theta = \Xi \frac{d\hat{z}}{d\mathbf{E}_t} = \frac{\Xi \mathbf{E}_t}{\sqrt{\frac{3}{2}}\gamma_t \sqrt{\mathbf{E}_t \cdot \mathbf{E}_t + \frac{3}{2}\gamma_0^2}}, \tag{24}$$

as well as $\mathbf{X} = \mathbf{X}_\varepsilon + \mathbf{X}_\theta$ is considered:

$$\rho\delta_i = [\mathbf{T} - \mathbf{X}] \cdot \dot{\mathbf{E}}_t + \mathbf{X}_\varepsilon \cdot \dot{\mathbf{Y}}_d \geq 0. \tag{25}$$

The introduced internal variable $\mathbf{X}_\theta$ has a physical meaning, because $\mathbf{X}_\theta$ is responsible for the depiction of the temperature-dependence of the required stress state to initiate and progress the martensitic phase transitions. Due to the applied thermoelastic mixture, the thermodynamic quantity Ξ strongly depends on temperature. The most important term in Ξ is given by $\rho(\Delta u_0 - \theta\Delta\eta_0)$. Therefore, if suitable material parameters are used, the model predicts a nearly linear temperature-dependence of the required phase transition stress over a certain temperature range. This is the stress state, which is necessary to initiate and progress the martensitic phase transitions. In contrast to [Helm 2001; Helm and Haupt 2003], the internal variable $\mathbf{X}_\theta$ is a continuous function of $\mathbf{E}_t$. For a simple tension-compression load, the 11-component of $\mathbf{X}_\theta$ is proportional to

$$\frac{\varepsilon_t}{\sqrt{\varepsilon_t^2 + \gamma_0^2}}.$$

This function is plotted in Figure 3 for different values of γ_0.

The final inequality (25) is an excellent basis to introduce a phase transition function

$$f = \|\mathbf{T}^D - \mathbf{X}^D\| - \sqrt{\frac{2}{3}}k(\theta) \tag{26}$$

and the evolution equations for the internal variables $\mathbf{E}_t$ and $\mathbf{Y}_d$. In the phase transition function, the quantity $k(\theta)$ is the radius of the phase transition surface. In general, it is also possible to introduce the phase transition radius as function of the fraction of oriented martensite in order to model isotropic
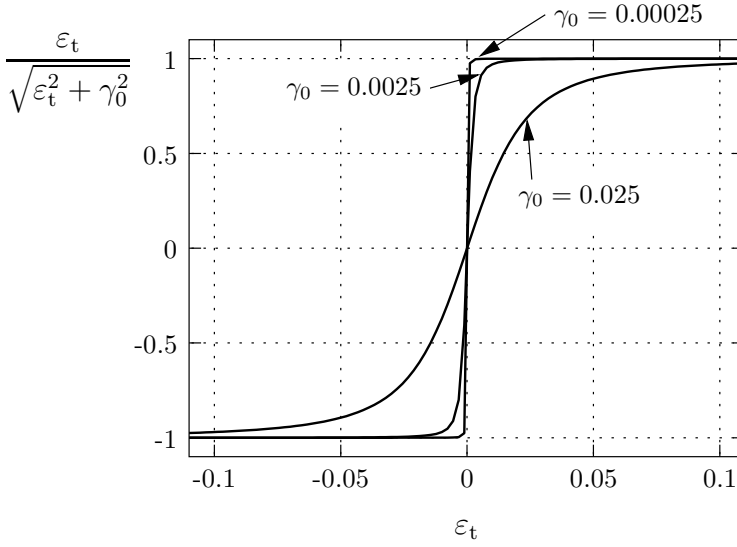
Figure 3. Illustration of $\boldsymbol{e}_1 \cdot \mathbf{X}_\theta \boldsymbol{e}_1 \sim \varepsilon_t / \sqrt{\varepsilon_t^2 + \gamma_0^2}$ for uniaxial tension-compression load.

transformation hardening. Such transformation hardening functions are commonly used in the modeling of shape memory alloys (see discussions in [Lagoudas et al. 2006]). Moreover, it is assumed that only deviatoric stress states influence the value of the phase transition function: $\mathbf{T}^D = \mathbf{T} - (\mathrm{tr}\,\mathbf{T})/3\,\mathbf{1}$. Due to the fact that phase transition function f depends on the internal variable $\mathbf{X}_\theta$ according to Equation (24), the model is restricted to a temperature range, which implies $\Xi \geq 0$ at $\mathbf{E}_e = \mathbf{0}$.

It should be mentioned that the simple v. Mises-type phase transition function leads initially to a symmetric tension-compression behavior. Such a behavior is almost observable for the first cycle in the uniaxial tension-compression experiments of Lim and McDowell [1995] on NiTi. In the case of a polycrystalline NiTi shape memory alloy without texture, the micromechanical studies of Gall and Sehitoglu [1999] lead to the result that, at the macroscopic level, merely a small tension-compression asymmetry is observable. In contrast to these results, a tension-compression asymmetry is experimentally observed and theoretically investigated in different types of shape memory alloys: see [Patoor et al. 1996; Gall and Sehitoglu 1999; Lim and McDowell 1999; Qidwai and Lagoudas 2000; Raniecki et al. 2001; Lexcellent et al. 2006]. Both the induced set of active martensite variants by the applied stress state and the texture of the material influence the tension-compression asymmetry. Consequently, depending on the underlying shape memory alloy and its microstructure, an appropriate phase transition function should be applied; see [Patoor et al. 1996; Qidwai and Lagoudas 2000].

Finally, the evolution equations for the internal variables $\mathbf{E}_t$ and $\mathbf{Y}_d$ are postulated.

- It is assumed that the transformation strain state $\mathbf{E}_t$ evolves according to the phase transition rule

$$\dot{\mathbf{E}}_t = \lambda_t\,\mathbf{N} \qquad \text{with the normal} \qquad \mathbf{N} = \frac{\partial f}{\partial \mathbf{T}} = \frac{\mathbf{T}^D - \mathbf{X}^D}{\|\mathbf{T}^D - \mathbf{X}^D\|}. \tag{27}$$

In analogy to [Helm and Haupt 2003] and [Helm 2005], a nonnegative inelastic multiplier

$$
\lambda_t =
\begin{cases}
\dfrac{1}{\eta_t(\theta)} \left\langle \dfrac{f}{r_t} \right\rangle^{m_t(\theta)} & \text{A} \rightarrow \vec{\text{M}} \text{ if } z < 1 \text{ and } \mathbf{E}_t \cdot \mathbf{N} \geq 0, \\[2mm]
& \vec{\text{M}} \rightarrow \text{A} \text{ if } z > 0 \text{ and } \mathbf{E}_t \cdot \mathbf{N} < 0, \\[2mm]
0 & \text{in all other cases}
\end{cases}
\tag{28}
$$

of Perzyna-type is assumed [Perzyna 1963; Hohenemser and Prager 1932]. Therein, $\eta_t(\theta) > 0$ and $m_t(\theta)$ are temperature-dependent material functions and r_t is introduced to obtain a dimensionless argument to the operator: $\langle x \rangle = (|x| + x)/2$. The introduced inelastic multiplier leads to a rate-dependent theory. However, if $\eta_t(\theta) \rightarrow 0$ (but always $\eta_t(\theta) > 0$) or if sufficiently slow processes are considered, the material model approximates a rate-independent theory in the sense of an asymptotic limit. This property is well known in thermoviscoplasticity [Haupt et al. 1992; Haupt 2002].

For representing the history-dependent material behavior of shape memory alloys, a few case distinctions are introduced: the phase transition from austenite to oriented martensite takes place if the phase transition function f is positive, austenite is available ($z < 1$), and the fraction of oriented martensite increases ($\mathrm{d}z \sim \mathbf{E}_t \cdot \mathbf{N} \geq 0$). In contrast to the forward transition, the retransformation occurs if oriented martensite is available ($z > 0$) and the fraction of oriented martensite decreases ($\mathrm{d}z \sim \mathbf{E}_t \cdot \mathbf{N} < 0$). In comparison with the magnitude of the isochoric deformations, the occurring volume changes during the martensitic phase transitions are negligible. Therefore, a deviatoric evolution of $\mathbf{E}_t$ is assumed; that is,

$$
\mathbf{E}_t^{\mathrm{D}} = \mathbf{E}_t - (\operatorname{tr} \mathbf{E}_t)/3\, \mathbf{1}.
$$

As pointed out in [Helm and Haupt 2003], the applied evolution equation (27) is able to predict the direction of the transformation strain-rate in accordance with the experimental studies of [Lim and McDowell 1999]. The main reason for this result is that the internal variable $\mathbf{X}_\theta$ significantly influences the direction of the transformation strain-rate.

- Furthermore, the evolution of $\mathbf{Y}_d$ is proposed to be proportional to the internal stress tensor $\mathbf{X}_\varepsilon$:

$$
\dot{\mathbf{Y}}_d = \zeta_d\, \mathbf{X}_\varepsilon.
\tag{29}
$$

The introduced proportional factor $\zeta_d \geq 0$ is assumed to be

$$
\zeta_d = \frac{B(\theta, z, \dot{z})}{c(\theta)} \dot{s}_t \quad \text{with} \quad \dot{s}_t = \sqrt{\tfrac{2}{3}} \|\dot{\mathbf{E}}_t\|
\tag{30}
$$

and the function

$$
B(\theta, z, \dot{z}) =
\begin{cases}
\tfrac{1}{2}\big(\tanh\left[-\beta(\theta)(z - \gamma(\theta))\right] + 1\big) b(\theta) & \text{if } \dot{z} > 0, \\[2mm]
b(\theta) & \text{if } \dot{z} < 0.
\end{cases}
\tag{31}
$$

Here, $\dot{s}_t$ is the rate of the accumulated phase transition strain s_t. Therein, b, β, and γ are nonnegative and generally temperature-dependent material functions. The constitutive model for the evolution of the internal stress fields (Equation (13), (30), and (31)) is a modification of a classical Armstrong–Frederick type approach: thus the strong stress slope as well as the different slope in the loading and unloading paths at the end of the phase transition plateau (see region I in Figure 1a and the experiments in [Huo and

Müller 1993; Shaw and Kyriakides 1995; Helm and Haupt 2001]) are all incorporated in the suggested constitutive theory.

On account of the internal stress tensor $\mathbf{X}_\varepsilon$ (Equation (17)) and the accompanying evolution equation for the internal variable $\mathbf{Y}_d$ (Equation (29)), the evolution of the internal stress state $\mathbf{X}_\varepsilon$ depends on the deformation history and leads to an anisotropic behavior of the model, because the value of the phase transition function f (Equation (26)) depends on $\mathbf{X}_\varepsilon$. Therefore, the characteristic phase transition stresses and temperatures depends also on the deformation history.

If both evolution equations are introduced into the remaining dissipation inequality (25),

$$\rho \delta_i = \lambda_t \| \mathbf{T}^D - \mathbf{X}^D \| + \zeta_d \, \| \mathbf{X}_\varepsilon \|^2 \geq 0, \tag{32}$$

it is discernible that the proposed constitutive theory is thermodynamically consistent, because of $\lambda_t \geq 0$ and $\zeta_d \geq 0$ according to Equation (28) and (30).

4. Constitutive theory in relation to finite deformations

In the foregoing section, a small strain theory has been constructed to model the thermomechanical behavior of shape memory alloys due to martensitic phase transitions. To formulate a relation between the fraction of oriented martensite and the transformation strain tensor, a new constitutive equation in form of Equation (22) was introduced. In this section, the developed constitutive theory is enhanced on the basis of [Helm 2001] to a finite strain theory. In that work we introduced a basic concept for shape memory alloys at finite deformations. This concept is based on a twofold multiplicative decomposition of the deformation gradient in order to distinguish between elastic and inelastic deformations as well as to incorporate the influences of internal stress states. Furthermore, the theory contains two evolution equations for the phase transition strain: one evolution equation models the phase transition from austenite into oriented martensite and the other evolution equation represents the retransformation. In the present section, the finite deformation theory of our earlier work is revised in order to obtain a constitutive theory, which requires only one simple constitutive equation to describe the evolution of the phase transition strains, which is valid for the forward and the reverse phase transition as well.

4.1. *Free energy.* According to [Helm 2001] and in analogy to the proposed geometrically linear theory in the foregoing section, the main energy storage phenomena are describable if the free energy is introduced as a function of the elastic strain state $\hat{\mathbf{\Gamma}}_e$, the absolute thermodynamic temperature θ, and the fraction of martensite z as well as an internal variable $\check{\mathbf{Y}}_s$:

$$\psi = \hat{\psi}(\hat{\mathbf{\Gamma}}_e, \theta, z, \check{\mathbf{Y}}_s) = \hat{\psi}_e(\hat{\mathbf{\Gamma}}_e, \theta, z) + \hat{\psi}_s(\check{\mathbf{Y}}_s, \theta). \tag{33}$$

In analogy to the small strain theory, the thermoelastic part ψ_e of the free energy results from the simple mixture of two single phase materials:

$$\psi_e(\theta, \hat{\mathbf{\Gamma}}_e, z) = z \psi_e^M(\theta, \hat{\mathbf{\Gamma}}_e) + (1-z) \psi_e^A(\theta, \hat{\mathbf{\Gamma}}_e). \tag{34}$$

Here, it is assumed that the elastic strains in the austenite and martensite phase are equal. Each single phase material is depicted by a finite thermoelasticity relation (see [Helm 2001; 2006]):

$$\psi_e^\omega = \frac{1}{2\rho_R}\kappa^\omega(\theta)\left(\ln\left(\det\hat{\mathbf{C}}_e\right)^{1/2}\right)^2 + \frac{1}{2\rho_R}\mu^\omega(\theta)\left(\operatorname{tr}\bar{\hat{\mathbf{C}}}_e - 3\right)$$

$$-\frac{1}{\rho_R}\kappa^\omega(\theta)\ln\left(1+\alpha^\omega(\theta)\left[\theta-\theta_0\right]\right)^3\ln\left(\det\hat{\mathbf{C}}_e\right)^{1/2} + \int_{\theta_0}^\theta c_d^\omega(\bar{\theta})\mathrm{d}\bar{\theta} + u_0^\omega - \theta\left[\int_{\theta_0}^\theta \frac{c_d^\omega(\bar{\theta})}{\bar{\theta}}\mathrm{d}\bar{\theta} + \eta_0^\omega\right]. \quad (35)$$

Therein, the first part describes the energy storage due to volumetric deformations (see [Simo and Pister 1984]), and the free energy contribution of isochoric deformations is given by the second term (see [Simo 1985: 1988]), which is of neo-Hooke type. Moreover, the third term represents the thermoelastic coupling phenomena. Applying the useful assumption of small thermoelastic strains $\alpha^\omega(\theta)\left[\theta-\theta_0\right]$, this term can be written in its approximation $\kappa^\omega(\theta)\ln\left[(1+\alpha^\omega(\theta)\left[\theta-\theta_0\right])^3\right] \approx 3\kappa^\omega(\theta)\alpha^\omega(\theta)\left[\theta-\theta_0\right]$. The last term in Equation (34) models the energy storage due to caloric effects. The meaning of the material parameters in the free energy function of a single-phase material are already known from the small strain theory (see Section 3.1).

If the free energy of the single phase material (35) is inserted into the mixture relation (34), the free energy of the two-phase material is given by

$$\rho_R\psi_e = \frac{\tilde{\kappa}(\theta,z)}{2}\left(\ln\left(\det\hat{\mathbf{C}}_e\right)^{1/2}\right)^2 + \frac{1}{2}\tilde{\mu}(\theta,z)\left(\operatorname{tr}\bar{\hat{\mathbf{C}}}_e - 3\right) - 3\tilde{\alpha}(\theta,z)\left(\theta-\theta_0\right)\ln\left(\det\hat{\mathbf{C}}_e\right)^{1/2}$$

$$+z\rho_R\int_{\theta_0}^\theta c_{d_0}^M(\bar{\theta})\mathrm{d}\bar{\theta} + (1-z)\rho_R\int_{\theta_0}^\theta c_{d_0}^A(\bar{\theta})\mathrm{d}\bar{\theta} + \rho_R\left[u_0^A + z\Delta u_0\right]$$

$$-\theta\left[z\rho_R\int_{\theta_0}^\theta \frac{c_{d_0}^M(\bar{\theta})}{\bar{\theta}}\mathrm{d}\bar{\theta} + (1-z)\rho_R\int_{\theta_0}^\theta \frac{c_{d_0}^A(\bar{\theta})}{\bar{\theta}}\mathrm{d}\bar{\theta} + \rho_R\left[\eta_0^A + z\Delta\eta_0\right]\right]. \quad (36)$$

According to Equation (10)–(12), the material functions $\tilde{\kappa}(\theta,z)$, $\tilde{\mu}(\theta,z)$, and $\tilde{\alpha}(\theta,z)$ are already known. Altogether, the main thermoelastic effects are representable by the proposed finite thermoelasticity relation.

In addition to the thermoelastic part of the free energy, a constitutive equation for the inelastic part is assumed to be (see [Helm 2001])

$$\psi_s = \frac{1}{4\rho_R}c(\theta)\left(\operatorname{tr}\bar{\check{\mathbf{C}}}_s - 3\right). \quad (37)$$

Therein, the tensor $\bar{\check{\mathbf{C}}}_s$ is the unimodular part of $\check{\mathbf{C}}_s$.

4.2. Evolution equations for internal variables.

In a finite deformation theory it is important to introduce conjugate variables and associated time derivatives. The concept of dual variables [Haupt and Tsakmakis 1989; Haupt 2002] implies that the variables $\tilde{\mathbf{T}}$ (second Piola–Kirchhoff stress tensor) and $\mathbf{E}$ are not only conjugate but also dual variables. Other dual variables result from the postulate that the invariance of the following physically significant inner products is fulfilled: the scalar product between the second Piola–Kirchhoff stress tensor $\tilde{\mathbf{T}}$ and the Green strain tensor $\mathbf{E}$ ($\tilde{\mathbf{T}}\cdot\mathbf{E}$), the stress power $\tilde{\mathbf{T}}\cdot\dot{\mathbf{E}}$, the complementary stress power $\dot{\tilde{\mathbf{T}}}\cdot\mathbf{E}$, and finally the incremental stress power $\overset{\triangle}{\tilde{\mathbf{T}}}\cdot\dot{\mathbf{E}}$. In relation to the

intermediate configuration $\hat{\mathcal{K}}_t$, the stress tensor $\hat{\mathbf{S}} = \mathbf{F}_t \tilde{\mathbf{T}} \mathbf{F}_t^T$ and the strain tensor $\hat{\mathbf{\Gamma}}$ (see Equation (2)) are dual variables, because this pair does not influence, for example, $\tilde{\mathbf{T}} \cdot \mathbf{E} = \hat{\mathbf{S}} \cdot \hat{\mathbf{\Gamma}}$ and

$$\tilde{\mathbf{T}} \cdot \dot{\mathbf{E}} = \text{tr} \, (\underbrace{\mathbf{F}_t \tilde{\mathbf{T}} \mathbf{F}_t^T}_{\hat{\mathbf{S}}} \underbrace{\mathbf{F}_t^{-T} \dot{\mathbf{E}} \mathbf{F}_t^{-1}}_{\overset{\triangle}{\hat{\mathbf{\Gamma}}}}) = \hat{\mathbf{S}} \cdot \overset{\triangle}{\hat{\mathbf{\Gamma}}}. \tag{38}$$

Therein, $\overset{\triangle}{\hat{\mathbf{\Gamma}}}$ represents the Oldroyd derivative of $\hat{\mathbf{\Gamma}}$,

$$\overset{\triangle}{\hat{\mathbf{\Gamma}}} = \dot{\hat{\mathbf{\Gamma}}} + \hat{\mathbf{L}}_t^T \hat{\mathbf{\Gamma}} + \hat{\mathbf{\Gamma}} \hat{\mathbf{L}}_t \qquad \text{with} \qquad \overset{\triangle}{(\hat{\cdot})} = \dot{(\hat{\cdot})} + \hat{\mathbf{L}}_t^T (\hat{\cdot}) + (\hat{\cdot}) \hat{\mathbf{L}}_t, \tag{39}$$

which is an associated time derivative, formulated relative to the intermediate configuration $\hat{\mathcal{K}}_t$. This Oldroyd derivative of $\hat{\mathbf{\Gamma}}_t$ is calculated on the basis of the inelastic deformation rate $\hat{\mathbf{L}}_t = \dot{\mathbf{F}}_t \mathbf{F}_t^{-1}$. Furthermore, the relation

$$\overset{\triangle}{\hat{\mathbf{\Gamma}}} = \overset{\triangle}{\hat{\mathbf{\Gamma}}}_e + \overset{\triangle}{\hat{\mathbf{\Gamma}}}_t, \text{ with } \overset{\triangle}{\hat{\mathbf{\Gamma}}}_e = \dot{\hat{\mathbf{\Gamma}}}_e + \hat{\mathbf{L}}_t^T \hat{\mathbf{\Gamma}}_e + \hat{\mathbf{\Gamma}}_e \hat{\mathbf{L}}_t \text{ and } \overset{\triangle}{\hat{\mathbf{\Gamma}}}_t = \dot{\hat{\mathbf{\Gamma}}}_t + \hat{\mathbf{L}}_t^T \hat{\mathbf{\Gamma}}_t + \hat{\mathbf{\Gamma}}_t \hat{\mathbf{L}}_t \tag{40}$$

is valid, because the Oldroyd derivative is a linear operator. It should be mentioned that the relation

$$\overset{\triangle}{\hat{\mathbf{\Gamma}}}_t = \frac{1}{2} [\hat{\mathbf{L}}_t + \hat{\mathbf{L}}_t^T] = \hat{\mathbf{D}}_t \tag{41}$$

is valid for the Oldroyd derivative of $\hat{\mathbf{\Gamma}}_t$. This relation underlines that the Oldroyd rate of $\hat{\mathbf{\Gamma}}_t$ depends only on $\mathbf{F}_t$ and its material time derivative. In contrast to this, the Oldroyd derivative of $\hat{\mathbf{\Gamma}}_e$ is influenced by $\hat{\mathbf{F}}_e$, $\mathbf{F}_t$ and their material time derivatives.

In analogy to Section 3.2, the basic structure of the constitutive theory is developed on the basis of the internal dissipation inequality, given by $\rho_R \delta_i = -\rho_R \dot{\psi} - \rho_R \dot{\theta} \eta + \tilde{\mathbf{T}} \cdot \dot{\mathbf{E}} \geq 0$. Here, ρ_R is the mass density with respect to the reference configuration. Inserting the free energy function (33), the identity (38), and the relation (40) into the internal dissipation inequality, the resulting inequality is given by

$$\delta_i = -\frac{\partial \hat{\psi}_e}{\partial \hat{\mathbf{\Gamma}}_e} \cdot \dot{\hat{\mathbf{\Gamma}}}_e - \frac{\partial \hat{\psi}_e}{\partial z} \dot{z} - \left[\eta + \frac{\partial \hat{\psi}}{\partial \theta} \right] \dot{\theta} - \frac{\partial \hat{\psi}_s}{\partial \check{\mathbf{Y}}_s} \cdot \dot{\check{\mathbf{Y}}}_s + \frac{1}{\rho_R} \hat{\mathbf{S}} \cdot \overset{\triangle}{\hat{\mathbf{\Gamma}}}_e + \frac{1}{\rho_R} \hat{\mathbf{S}} \cdot \overset{\triangle}{\hat{\mathbf{\Gamma}}}_t. \tag{42}$$

In the next step, $\dot{\hat{\mathbf{\Gamma}}}_e$ is replaced by its Oldroyd derivative according to Equation (40)$_2$. In the same way, $\dot{\check{\mathbf{Y}}}_s$ is substituted by an associated time derivative: with respect to the intermediate configuration $\check{\mathcal{K}}_d$, an internal stress tensor $\check{\mathbf{X}}_\varepsilon = \mathbf{F}_t \tilde{\mathbf{X}}_\varepsilon \mathbf{F}_t^T$ is defined, which represents the transformation of the internal stress state $\tilde{\mathbf{X}}_\varepsilon$ from the reference configuration to the intermediate configuration $\check{\mathcal{K}}_d$. Its dual strain tensor in the reference configuration is named as $\tilde{\mathbf{Y}}$ and the variable $\check{\mathbf{Y}}$ is the associated strain tensor in the intermediate configuration $\check{\mathcal{K}}_d$. The analysis of the stress power,

$$\tilde{\mathbf{X}}_\varepsilon \cdot \dot{\tilde{\mathbf{Y}}} = \text{tr} \, (\underbrace{\mathbf{F}_d \tilde{\mathbf{X}}_\varepsilon \mathbf{F}_d^T}_{\check{\mathbf{X}}_\varepsilon} \underbrace{\mathbf{F}_d^{-T} \dot{\tilde{\mathbf{Y}}} \mathbf{F}_d^{-1}}_{\overset{\triangle}{\check{\mathbf{Y}}}}) = \check{\mathbf{X}}_\varepsilon \cdot \overset{\triangle}{\check{\mathbf{Y}}}, \tag{43}$$

leads to the associated time derivative:

$$\overset{\triangle}{\check{\mathbf{Y}}} = \dot{\check{\mathbf{Y}}} + \check{\mathbf{L}}_d^T \check{\mathbf{Y}} + \check{\mathbf{Y}} \check{\mathbf{L}}_d, \qquad \overset{\triangle}{(\check{\cdot})} = \dot{(\check{\cdot})} + \check{\mathbf{L}}_d^T (\check{\cdot}) + (\check{\cdot}) \check{\mathbf{L}}_d, \tag{44}$$

with $\check{\mathbf{L}}_\mathrm{d} = \dot{\mathbf{F}}_\mathrm{d}\mathbf{F}_\mathrm{d}^{-1}$. Consequently, $\overset{\triangle}{\check{\mathbf{Y}}}$ represents an Oldroyd derivative relative to the intermediate config-uration $\check{\mathcal{K}}_\mathrm{d}$. Since this Oldroyd derivative is also a linear operator, the relation

$$\overset{\triangle}{\check{\mathbf{Y}}} = \overset{\triangle}{\check{\mathbf{Y}}}_\mathrm{s} + \overset{\triangle}{\check{\mathbf{Y}}}_\mathrm{d} \text{ with } \overset{\triangle}{\check{\mathbf{Y}}}_\mathrm{s} = \dot{\check{\mathbf{Y}}}_\mathrm{s} + \check{\mathbf{L}}_\mathrm{d}^\mathrm{T}\check{\mathbf{Y}}_\mathrm{s} + \check{\mathbf{Y}}_\mathrm{s}\check{\mathbf{L}}_\mathrm{d} \text{ and } \overset{\triangle}{\check{\mathbf{Y}}}_\mathrm{d} = \dot{\check{\mathbf{Y}}}_\mathrm{d} + \check{\mathbf{L}}_\mathrm{d}^\mathrm{T}\check{\mathbf{Y}}_\mathrm{d} + \check{\mathbf{Y}}_\mathrm{d}\check{\mathbf{L}}_\mathrm{d} \tag{45}$$

is likewise valid. In analogy to Equation (41), the Oldroyd derivative of $\check{\mathbf{Y}}_\mathrm{d}$ is representable as

$$\overset{\triangle}{\check{\mathbf{Y}}}_\mathrm{d} = \tfrac{1}{2}\big[\check{\mathbf{L}}_\mathrm{d} + \check{\mathbf{L}}_\mathrm{d}^\mathrm{T}\big] = \check{\mathbf{D}}_\mathrm{d}. \tag{46}$$

Consequently, the identities according to Equation $(40)_2$ and also Equation $(45)_2$ are used to replace in Equation (42) the material time derivative of $\hat{\mathbf{\Gamma}}_\mathrm{e}$ and $\check{\mathbf{Y}}_\mathrm{s}$ by their Oldroyd derivatives. Additionally, the additive relation according to Equation $(45)_1$ is applied in Equation (42):

$$\delta_\mathrm{i} = \frac{1}{\rho_\mathrm{R}}\left[\hat{\mathbf{S}} - \rho_\mathrm{R}\frac{\partial\hat{\psi}_\mathrm{e}}{\partial\hat{\mathbf{\Gamma}}_\mathrm{e}}\right]\cdot\overset{\triangle}{\hat{\mathbf{\Gamma}}}_\mathrm{e} - \left[\eta + \frac{\partial\hat{\psi}}{\partial\theta}\right]\dot{\theta} - \frac{\partial\hat{\psi}_\mathrm{e}}{\partial z}\dot{z} - \frac{\partial\hat{\psi}_\mathrm{s}}{\partial\check{\mathbf{Y}}_\mathrm{s}}\cdot\overset{\triangle}{\check{\mathbf{Y}}} + \frac{1}{\rho_\mathrm{R}}\hat{\mathbf{S}}\cdot\overset{\triangle}{\hat{\mathbf{\Gamma}}}_\mathrm{t}$$

$$+ \underbrace{\frac{\partial\hat{\psi}_\mathrm{s}}{\partial\check{\mathbf{Y}}_\mathrm{s}}\cdot\big[\overset{\triangle}{\check{\mathbf{Y}}}_\mathrm{d} + \check{\mathbf{L}}_\mathrm{d}^\mathrm{T}\check{\mathbf{Y}}_\mathrm{s} + \check{\mathbf{Y}}_\mathrm{s}\check{\mathbf{L}}_\mathrm{d}\big]}_{\left[\check{\mathbf{C}}_\mathrm{s}\frac{\partial\hat{\psi}_\mathrm{s}}{\partial\check{\mathbf{Y}}_\mathrm{s}}\right]\cdot\overset{\triangle}{\check{\mathbf{Y}}}_\mathrm{d}} + \underbrace{\frac{\partial\hat{\psi}_\mathrm{e}}{\partial\hat{\mathbf{\Gamma}}_\mathrm{e}}\cdot\big[\hat{\mathbf{L}}_\mathrm{t}^\mathrm{T}\hat{\mathbf{\Gamma}}_\mathrm{e} + \hat{\mathbf{\Gamma}}_\mathrm{e}\hat{\mathbf{L}}_\mathrm{t}\big]}_{\left[\hat{\mathbf{C}}_\mathrm{e}\frac{\partial\hat{\psi}_\mathrm{e}}{\partial\hat{\mathbf{\Gamma}}_\mathrm{e}}\right]\cdot\overset{\triangle}{\hat{\mathbf{\Gamma}}}_\mathrm{t}} \geq 0. \tag{47}$$

As shown in the last line of Equation (47), these terms can be replaced if $\partial\hat{\psi}_\mathrm{s}/\partial\check{\mathbf{Y}}_\mathrm{s}$ is an isotropic tensor function of $\check{\mathbf{Y}}_\mathrm{s}$ and if $\partial\hat{\psi}_\mathrm{e}/\partial\hat{\mathbf{\Gamma}}_\mathrm{e}$ is an isotropic tensor function of $\hat{\mathbf{\Gamma}}_\mathrm{e}$ [Mandel 1972; Haupt 2002]. Furthermore, the relation

$$\frac{\partial\hat{\psi}_\mathrm{s}}{\partial\check{\mathbf{Y}}_\mathrm{s}}\cdot\overset{\triangle}{\check{\mathbf{Y}}} = \check{\mathbf{F}}_\mathrm{s}\frac{\partial\hat{\psi}_\mathrm{s}}{\partial\check{\mathbf{Y}}_\mathrm{s}}\check{\mathbf{F}}_\mathrm{s}^\mathrm{T}\cdot\check{\mathbf{F}}_\mathrm{s}^{-\mathrm{T}}\overset{\triangle}{\check{\mathbf{Y}}}\check{\mathbf{F}}_\mathrm{s}^{-1} = \check{\mathbf{F}}_\mathrm{s}\frac{\partial\hat{\psi}_\mathrm{s}}{\partial\check{\mathbf{Y}}_\mathrm{s}}\check{\mathbf{F}}_\mathrm{s}^\mathrm{T}\cdot\overset{\triangle}{\hat{\mathbf{\Gamma}}}_\mathrm{t}. \tag{48}$$

is valid for the last term in the first line of the inequality (47). Considering these identities into the internal dissipation inequality (47), the resulting inequality

$$\rho_\mathrm{R}\delta_\mathrm{i} = \left[\hat{\mathbf{S}} - \rho_\mathrm{R}\frac{\partial\hat{\psi}_\mathrm{e}}{\partial\hat{\mathbf{\Gamma}}_\mathrm{e}}\right]\cdot\overset{\triangle}{\hat{\mathbf{\Gamma}}}_\mathrm{e} - \rho_\mathrm{R}\left[\eta + \frac{\partial\hat{\psi}}{\partial\theta}\right]\dot{\theta} - \rho_\mathrm{R}\frac{\partial\hat{\psi}_\mathrm{e}}{\partial z}\dot{z} + \left[\check{\mathbf{C}}_\mathrm{s}\rho_\mathrm{R}\frac{\partial\hat{\psi}_\mathrm{s}}{\partial\check{\mathbf{Y}}_\mathrm{s}}\right]\cdot\overset{\triangle}{\check{\mathbf{Y}}}_\mathrm{d} + \left[\hat{\mathbf{C}}_\mathrm{e}\hat{\mathbf{S}} - \check{\mathbf{F}}_\mathrm{s}\rho_\mathrm{R}\frac{\partial\hat{\psi}_\mathrm{s}}{\partial\check{\mathbf{Y}}_\mathrm{s}}\check{\mathbf{F}}_\mathrm{s}^\mathrm{T}\right]\cdot\overset{\triangle}{\hat{\mathbf{\Gamma}}}_\mathrm{t}$$

$$\geq 0 \tag{49}$$

implies a potential relation for the stress tensor

$$\hat{\mathbf{S}} = \rho_\mathrm{R}\frac{\partial\hat{\psi}_\mathrm{e}}{\partial\hat{\mathbf{\Gamma}}_\mathrm{e}} = 2\rho_\mathrm{R}\frac{\partial\tilde{\psi}_\mathrm{e}}{\partial\hat{\mathbf{C}}_\mathrm{e}} = \tilde{\mu}(\theta, z)\left(\det\hat{\mathbf{C}}_\mathrm{e}\right)^{-1/3}\left[\mathbf{1} - \tfrac{1}{3}\big(\mathrm{tr}\,\hat{\mathbf{C}}_\mathrm{e}\big)\hat{\mathbf{C}}_\mathrm{e}^{-1}\right]$$

$$+ \left[\tilde{\kappa}(\theta, z)\ln\left(\det\hat{\mathbf{C}}_\mathrm{e}\right)^{1/2} - 3\tilde{\alpha}(\theta, z)\,(\theta - \theta_0)\right]\hat{\mathbf{C}}_\mathrm{e}^{-1}, \tag{50}$$

which is related to the intermediate configuration $\hat{\mathcal{K}}_\mathrm{t}$, and the entropy $\eta = -\partial\hat{\psi}/\partial\theta$, if $\dot{z}$, $\overset{\triangle}{\check{\mathbf{Y}}}_\mathrm{d}$, and $\overset{\triangle}{\hat{\mathbf{\Gamma}}}_\mathrm{t}$ do

not depend on $\overset{\triangle}{\hat{\mathbf{\Gamma}}}_{\mathrm{e}}$ and $\dot{\theta}$ [Coleman and Gurtin 1967]. Furthermore, the remaining internal dissipation inequality

$$\rho_{\mathrm{R}}\delta_{\mathrm{i}} = -\underbrace{\rho_{\mathrm{R}}\frac{\partial\hat{\psi}_{\mathrm{e}}}{\partial z}}_{\Xi}\,\dot{z} + \left[\overbrace{\check{\mathbf{C}}_{\mathrm{s}}\,\rho_{\mathrm{R}}\frac{\partial\hat{\psi}_{\mathrm{s}}}{\partial\check{\mathbf{Y}}_{\mathrm{s}}}}^{\check{\mathbf{X}}_{\varepsilon}}\right]\cdot\overset{\triangle}{\check{\mathbf{Y}}}_{\mathrm{d}} + \left[\underbrace{\hat{\mathbf{C}}_{\mathrm{e}}\hat{\mathbf{S}}}_{\hat{\mathbf{P}}} - \underbrace{\check{\mathbf{F}}_{\mathrm{s}}\,\rho_{\mathrm{R}}\overbrace{\frac{\partial\hat{\psi}_{\mathrm{s}}}{\partial\check{\mathbf{Y}}_{\mathrm{s}}}}^{\check{\mathbf{X}}_{\varepsilon}}\check{\mathbf{F}}_{\mathrm{s}}^{\mathrm{T}}}_{\hat{\mathbf{P}}_{\mathbf{X}_{\varepsilon}}}\right]\cdot\overset{\triangle}{\hat{\mathbf{\Gamma}}}_{\mathrm{t}} \tag{51}$$

motivates the introduction of four definitions: the partial derivative in the first term is interpretable as a thermodynamic force $\Xi = \rho_{\mathrm{R}}\,\partial\psi_{\mathrm{e}}/\partial z$,

$$\Xi = \frac{1}{2}\frac{\partial\tilde{\mu}}{\partial z}\left(\operatorname{tr}\bar{\hat{\mathbf{C}}}_{\mathrm{e}} - 3\right) + \frac{1}{2}\frac{\partial\tilde{\kappa}}{\partial z}\left(\ln\left(\det\hat{\mathbf{C}}_{\mathrm{e}}\right)^{1/2}\right)^{2} - 3\frac{\partial\tilde{\alpha}}{\partial z}\,(\theta - \theta_{0})\ln\left(\det\hat{\mathbf{C}}_{\mathrm{e}}\right)^{1/2}$$
$$+ \rho_{\mathrm{R}}\left[\int_{\theta_{0}}^{\theta}\left[c_{\mathrm{d}_{0}}^{\mathrm{M}}(\bar{\theta}) - c_{\mathrm{d}_{0}}^{\mathrm{A}}(\bar{\theta})\right]\mathrm{d}\bar{\theta} + \Delta u_{0}\right] - \rho_{\mathrm{R}}\theta\left[\int_{\theta_{0}}^{\theta}\frac{c_{\mathrm{d}_{0}}^{\mathrm{M}}(\bar{\theta}) - c_{\mathrm{d}_{0}}^{\mathrm{A}}(\bar{\theta})}{\bar{\theta}}\mathrm{d}\bar{\theta} + \Delta\eta_{0}\right], \tag{52}$$

which is already known from the geometrically linear theory. Furthermore, the partial derivative in the second term,

$$\check{\mathbf{X}}_{\varepsilon} = \rho_{\mathrm{R}}\frac{\partial\hat{\psi}_{\mathrm{s}}}{\partial\check{\mathbf{Y}}_{\mathrm{s}}} = 2\rho_{\mathrm{R}}\frac{\partial\hat{\psi}_{\mathrm{s}}}{\partial\check{\mathbf{C}}_{\mathrm{s}}} = \frac{c(\theta)}{2}\left(\det\check{\mathbf{C}}_{\mathrm{s}}\right)^{-1/3}\left[\mathbf{1} - \tfrac{1}{3}\left(\operatorname{tr}\check{\mathbf{C}}_{\mathrm{s}}\right)\check{\mathbf{C}}_{\mathrm{s}}^{-1}\right], \tag{53}$$

can be understood as the internal stress tensor (back stress tensor) on the intermediate configuration $\check{\mathcal{K}}_{\mathrm{d}}$. The stress tensor

$$\hat{\mathbf{P}} = \hat{\mathbf{C}}_{\mathrm{e}}\hat{\mathbf{S}} = \tilde{\kappa}(\theta, z)\ln\left(\det\hat{\mathbf{C}}_{\mathrm{e}}\right)^{1/2}\mathbf{1} + \tilde{\mu}(\theta, z)\bar{\hat{\mathbf{C}}}_{\mathrm{e}}^{\mathrm{D}} - 3\tilde{\alpha}(\theta, z)\,(\theta - \theta_{0})\,\mathbf{1} \tag{54}$$

is known as the Mandel stress tensor [1972] (see also [Lubliner 1990]). Due to the assumption that $\partial\hat{\psi}_{\mathrm{e}}/\partial\hat{\mathbf{\Gamma}}_{\mathrm{e}}$ is an isotropic tensor function of $\hat{\mathbf{\Gamma}}_{\mathrm{e}}$, the Mandel-stress tensor $\hat{\mathbf{P}}$ is symmetric. In contrast to this, the stress tensor

$$\check{\mathbf{M}}_{\mathbf{X}_{\varepsilon}} = \check{\mathbf{C}}_{\mathrm{s}}\check{\mathbf{X}}_{\varepsilon} = \frac{c(\theta)}{2}\bar{\bar{\check{\mathbf{C}}}}_{\mathrm{s}}^{\mathrm{D}} \tag{55}$$

has the structure of a Mandel stress tensor and the stress tensor

$$\hat{\mathbf{P}}_{\mathbf{X}_{\varepsilon}} = \check{\mathbf{F}}_{\mathrm{s}}\check{\mathbf{X}}_{\varepsilon}\check{\mathbf{F}}_{\mathrm{s}}^{\mathrm{T}} = \frac{c(\theta)}{2}\bar{\hat{\mathbf{B}}}_{\mathrm{s}}^{\mathrm{D}} \tag{56}$$

is the transformation of $\check{\mathbf{X}}_{\varepsilon}$ from the intermediate configuration $\check{\mathcal{K}}_{\mathrm{d}}$ onto $\hat{\mathcal{K}}_{\mathrm{t}}$. The stress tensor $\hat{\mathbf{P}}_{\mathbf{X}_{\varepsilon}}$ is of Mandel-type, too.

Using these definitions, the remaining dissipation inequality (see [Helm 2001]) is given by

$$\rho_{\mathrm{R}}\delta_{\mathrm{i}} = -\Xi\,\dot{z} + \check{\mathbf{M}}_{\mathbf{X}_{\varepsilon}}\cdot\overset{\triangle}{\check{\mathbf{Y}}}_{\mathrm{d}} + \left[\hat{\mathbf{P}} - \hat{\mathbf{P}}_{\mathbf{X}_{\varepsilon}}\right]\cdot\overset{\triangle}{\hat{\mathbf{\Gamma}}}_{\mathrm{t}} \geq 0. \tag{57}$$

In shape memory alloys, the martensitic phase transitions between austenite and oriented martensite result from a cooperative movement of the atomic lattice. In analogy to Equation (22), a constitutive equation is required for incorporating this coupling phenomenon between the fraction of oriented martensite and the transformation strain. Already in [Helm 2001] the coupling between the fraction z of oriented martensite

and the inelastic Cauchy–Green tensor $\mathbf{C}_t$ was represented in a finite-strain concept by the constitutive relation

$$z = \frac{1}{\sqrt{3}\gamma_t}\sqrt{\mathrm{tr}\left[\bar{\mathbf{C}}_t\right] - 3}. \tag{58}$$

According to the definition in Equation (1), the tensor $\bar{\mathbf{C}}_t$ is the unimodular part of $\mathbf{C}_t = \mathbf{F}_t^T\mathbf{F}_t$. However, if the relation (58) was applied in the present context, the model would contain a phase transition criterion and a phase transition rule, which would be singular at $\bar{\mathbf{C}}_t = \mathbf{1}$ (see the discussions in [Helm 2001; Helm and Haupt 2003]). Moreover, the smooth transition from the retransformation plateau into the elastic region (see region II in Figure 1a) cannot be depicted. Therefore, a new constitutive equation is suggested in analogy to Equation (22):

$$z = \frac{1}{\sqrt{3}\gamma_t}\sqrt{\mathrm{tr}\left[\bar{\mathbf{C}}_t\right] - 3(1 - \gamma_0^2)} - z_0. \tag{59}$$

Therein, γ_0 is a positive material parameter and $z_0 = \gamma_0/\gamma_t$ follows from the condition $\hat{z}(\bar{\mathbf{C}}_t = \mathbf{1}) = 0$. On account of the introduced material parameter $\gamma_0 > 0$, the resulting model does not contain any singularity.

In the dissipation inequality (57), the material time derivative of z is required:

$$\dot{z} = \frac{(\det \mathbf{C}_t)^{-1/3}\left[\mathbf{1} - \frac{1}{3}\mathrm{tr}\,(\mathbf{C}_t)\,\mathbf{C}_t^{-1}\right]}{\sqrt{3}\gamma_t\sqrt{\mathrm{tr}\,\bar{\mathbf{C}}_t - 3(1 - \gamma_0^2)}} \cdot \frac{1}{2}\dot{\mathbf{C}}_t. \tag{60}$$

Multiplying the time derivative of z with the thermodynamic quantity Ξ and transforming the participated variables from the reference configuration $\mathcal{K}_R$ to the intermediate configuration $\hat{\mathcal{K}}_t$, the resulting relation $(\hat{\mathbf{B}}_t = \mathbf{F}_t\mathbf{F}_t^T)$

$$\Xi\,\dot{z} = \frac{\Xi\,\bar{\hat{\mathbf{B}}}_t^D \cdot \overset{\triangle}{\hat{\mathbf{\Gamma}}}_t}{\sqrt{3}\gamma_t\sqrt{\mathrm{tr}\,\bar{\hat{\mathbf{B}}}_t - 3(1 - \gamma_0^2)}} = \hat{\mathbf{P}}_{\mathbf{X}_\theta} \cdot \overset{\triangle}{\bar{\hat{\mathbf{\Gamma}}}}_t, \tag{61}$$

motivates the definition of an internal variable $\hat{\mathbf{P}}_{\mathbf{X}_\theta}$ of stress type:

$$\hat{\mathbf{P}}_{\mathbf{X}_\theta} = \frac{\Xi\bar{\hat{\mathbf{B}}}_t^D}{\sqrt{3}\gamma_t\sqrt{\mathrm{tr}\,\bar{\hat{\mathbf{B}}}_t - 3(1 - \gamma_0^2)}}. \tag{62}$$

Owing to $\hat{\mathbf{P}}_{\hat{\mathbf{X}}_\theta}$, which is a continuous function of $\bar{\hat{\mathbf{B}}}_t$, the present constitutive model is able to represent the temperature-dependence of the phase transition stress.

Remark 3 (Interpretation of $\hat{\mathbf{P}}_{\mathbf{X}_\theta}$). The internal variable $\hat{\mathbf{P}}_{\mathbf{X}_\theta}$ can be better understood if a simple inelastic shear deformation is regarded: $\mathbf{F}_t = \mathbf{1} + \gamma_{12}\,\boldsymbol{e}_1 \otimes \boldsymbol{e}_2$. On account of

$$\hat{\mathbf{B}}_t = \bar{\hat{\mathbf{B}}}_t = \mathbf{1} + \gamma_{12}\,(\boldsymbol{e}_1 \otimes \boldsymbol{e}_2 + \boldsymbol{e}_2 \otimes \boldsymbol{e}_1) + \gamma_{12}^2\,\boldsymbol{e}_1 \otimes \boldsymbol{e}_1, \tag{63}$$

the 12-component of $\hat{\mathbf{P}}_{\mathbf{X}_\theta}$ can be calculated:

$$\boldsymbol{e}_1 \cdot \hat{\mathbf{P}}_{\mathbf{X}_\theta}\boldsymbol{e}_2 = \frac{\Xi}{\sqrt{3}\gamma_t}\frac{\gamma_{12}}{\sqrt{\gamma_{12}^2 + 3\,\gamma_0^2}}. \tag{64}$$

For $\gamma_{12} \gg \gamma_0$, the value of this shear stress is given by $\Xi/(\sqrt{3}\gamma_t)$, because the other term is approximately ± 1. Consequently, the effect of the introduced constitutive relation for $\hat{\mathbf{P}}_{\mathbf{X}_\theta}$ on the whole theory is similar to the influence of the internal variable $\mathbf{X}_\theta$ in the small strain theory (see Equation (24) and Figure 3).

Remark 4 (Trace of a unimodular tensor). The first invariant $\mathrm{I}_{\mathbf{A}}$ of a unimodular tensor $\mathbf{A}$ (i.e., $\mathrm{III}_{\mathbf{A}} = \det \mathbf{A} = 1$ is valid) has a lower bound $\mathrm{I}_{\mathbf{A}} = \mathrm{tr}\, \mathbf{A} \geq 3$ [Haupt 2002, (9.91)]. Therefore, the term

$$f(\bar{\bar{\mathbf{B}}}_t) = \sqrt{\mathrm{tr}\, \bar{\bar{\mathbf{B}}}_t - 3(1 - \gamma_0^2)} \geq \sqrt{3}\gamma_0 \tag{65}$$

in Equation (62) has likewise a lower bound and the ratio $1/f(\bar{\bar{\mathbf{B}}}_t)$ is always defined, because $\gamma_0 > 0$ is required in the model.

If the important relation $\Xi\, \dot{z} = \hat{\mathbf{P}}_{\mathbf{X}_\theta} \cdot \overset{\triangle}{\hat{\mathbf{\Gamma}}}_t$ according to Equation (61) is inserted into the remaining dissipation inequality (57), the resultant inequality (see [Helm 2001])

$$\rho_R \delta_i = \check{\mathbf{M}}_{\mathbf{X}_\varepsilon} \cdot \overset{\triangledown}{\check{\mathbf{Y}}}_d + \left[\hat{\mathbf{P}} - \hat{\mathbf{P}}_{\mathbf{X}} \right] \cdot \overset{\triangle}{\hat{\mathbf{\Gamma}}}_t \geq 0 \tag{66}$$

with the definition $\hat{\mathbf{P}}_{\mathbf{X}} = \hat{\mathbf{P}}_{\mathbf{X}_\varepsilon} + \hat{\mathbf{P}}_{\mathbf{X}_\theta}$, is a suitable basis to specify the phase transition function

$$f = \|\hat{\mathbf{P}}^D - \hat{\mathbf{P}}_{\mathbf{X}}^D\| - \sqrt{\frac{2}{3}} k(\theta) \tag{67}$$

and the required evolution equations for the internal variables $\hat{\mathbf{\Gamma}}_t$ and $\check{\mathbf{Y}}_d$.

• In the case of the transformation strain tensor $\hat{\mathbf{\Gamma}}_t$ the phase transition rule

$$\overset{\triangle}{\hat{\mathbf{\Gamma}}}_t = \lambda_t \hat{\mathbf{P}}_{\mathbf{N}} \qquad \text{with} \qquad \hat{\mathbf{P}}_{\mathbf{N}} = \frac{\partial f}{\partial \hat{\mathbf{P}}} = \frac{\hat{\mathbf{P}}^D - \hat{\mathbf{P}}_{\mathbf{X}}^D}{\|\hat{\mathbf{P}}^D - \hat{\mathbf{P}}_{\mathbf{X}}^D\|} \tag{68}$$

is suggested. Therein, $\lambda_t \geq 0$ is the inelastic multiplier. This evolution equation states that $\overset{\triangle}{\hat{\mathbf{\Gamma}}}_t$ is a deviatoric tensor. Consequently, the model incorporates the assumption of isochoric inelastic deformations: $\det \mathbf{F}_t = 1$.

In analogy to the inelastic multiplier of the small deformation theory, a Perzyna-type (see [Perzyna 1963; Hohenemser and Prager 1932]) multiplier λ_t is introduced:

$$\lambda_t = \begin{cases} \dfrac{1}{\eta_t(\theta)} \left\langle \dfrac{f}{r_t} \right\rangle^{m_t(\theta)} & \text{A} \to \vec{\mathbf{M}} \text{ if } z < 1 \text{ and } \bar{\bar{\mathbf{B}}}_t^D \cdot \hat{\mathbf{P}}_{\mathbf{N}} \geq 0, \\[2ex] \qquad\qquad\qquad & \vec{\mathbf{M}} \to \text{A} \text{ if } z > 0 \text{ and } \bar{\bar{\mathbf{B}}}_t^D \cdot \hat{\mathbf{P}}_{\mathbf{N}} < 0, \\[2ex] \qquad 0 & \text{in all other cases.} \end{cases} \tag{69}$$

The material parameters and the case distinctions have the same meaning as in the small strain theory, but the condition of increasing martensite requires $\mathrm{d}z \sim \bar{\bar{\mathbf{B}}}_t^D \cdot \hat{\mathbf{P}}_{\mathbf{N}} \geq 0$ and the martensite decreases, if $\mathrm{d}z \sim \bar{\bar{\mathbf{B}}}_t^D \cdot \hat{\mathbf{P}}_{\mathbf{N}} < 0$ is fulfilled.

- For the internal variable $\check{\mathbf{Y}}_d$, the evolution equation

$$\overset{\triangle}{\check{\mathbf{Y}}}_d = \zeta_d \, \check{\mathbf{M}}_{\mathbf{X}_\varepsilon} = \zeta_d \, \check{\mathbf{C}}_s \check{\mathbf{X}}_\varepsilon, \tag{70}$$

is proposed. Likewise in the case of finite deformations, ζ_d is introduced in form of

$$\zeta_d = \frac{B(\theta, z, \dot{z})}{c(\theta)} \dot{s}_t \qquad \text{with} \qquad \dot{s}_t = \sqrt{\tfrac{2}{3}} \|\overset{\triangle}{\hat{\boldsymbol{\Gamma}}}_t\|. \tag{71}$$

Therein, $B(\theta, z, \dot{z})$ is given according to Equation (31) and s_t is the accumulated transformation strain.

It should be mentioned that no further constitutive equations are required to represent the evolution of the internal variables $\hat{\boldsymbol{\Gamma}}_t$ and $\check{\mathbf{Y}}_d$ according to (68) and (70), because it is not necessary to determine the orthogonal part $\mathbf{R}_t$ of the polar decomposition $\mathbf{F}_t = \mathbf{R}_t \mathbf{U}_t$ and the orthogonal part $\mathbf{R}_d$ of the polar decomposition $\mathbf{F}_d = \mathbf{R}_d \mathbf{U}_d$ in the proposed constitutive theory for an isotropic elastic material (see [Haupt 2002] or [Helm and Schäfers 2006], for example). Only the evolution of the stretch tensors $\mathbf{U}_t$ and $\mathbf{U}_d$ is represented by the evolution equations (68) and (70).

If the evolution equations (68) and (70) are inserted into the inequality (66) the internal dissipation is written in the following form:

$$\rho_R \delta_i = \zeta_d \, \|\check{\mathbf{M}}_{\mathbf{X}_\varepsilon}\|^2 + \lambda_t \|\hat{\mathbf{P}}^D - \hat{\mathbf{P}}^D_{\mathbf{X}}\|. \tag{72}$$

Obviously ($\lambda_t \geq 0$ and $\zeta_d \geq 0$), the postulated geometrically nonlinear constitutive theory is thermodynamically consistent for arbitrary thermomechanical processes.

Remark 5 (Mandel stress tensors). In the context of a constitutive theory for viscoplastic materials, Mandel [1972] proposed to consider the stress tensor $\hat{\mathbf{P}} = \hat{\mathbf{C}}_e \hat{\mathbf{S}}$ in the yield function. Mandel's theory has been formulated on the basis of the multiplicative decomposition of the deformation gradient in an elastic and inelastic part. In order to describe the kinematic hardening behavior of metals in a finite deformation theory using continuum thermomechanics, Tsakmakis [1996] found out that the yield function should depend on a back stress tensor of Mandel-type.

5. Conclusions

In the present article, two basic concepts for modeling martensitic phase transitions in shape memory alloys are developed: the first model is based on the assumption of small deformations, and the second concept is formulated in the context of finite deformations. In both cases, the energy storage and release phenomena during thermomechanical processes are represented by a free energy function. Moreover, evolution equations for two internal variables are introduced in order to model the history-dependent material behavior and the dissipation phenomena. An essential element of the developed theories is that the deformation and the strain-like internal variables are decomposed into volumetric and isochoric parts. This leads to a simple representation of the occurring mechanisms. In contrast to other constitutive theories for shape memory alloys, the developed concept is formulated in the framework of thermoviscoplasticity. Therefore, the system of constitutive equations has a strong resemblance to classical models, which depict the viscoplastic behavior of metals by using the concept of kinematic hardening. The present approach of

finite thermoviscoplasticity is based on [Lion 2000], which introduces a multiple multiplicative decomposition of the deformation gradient for the modeling of kinematic hardening in the framework of finite deformations. In analogy to [Helm 2001], only a double multiplicative decomposition of the deformation gradient is introduced without any thermal intermediate configuration. Therefore, the entropy results immediately from the free energy function by means of a potential relation. Similar strategies for incorporating the kinematic hardening at finite strains were discussed in [Dettmer and Reese 2004; Tsakmakis and Willuweit 2004]. In the present constitutive theory, all energy storage phenomena due to isochoric deformations are depicted by modified neo-Hooke-type models. This strategy leads to a simple representation of the occurring energy storage mechanisms and the kinematic hardening behavior. In all, the developed concept can be easily transformed to give the thermoviscoplastic behavior of metals if only a few modifications are considered: e.g. $\gamma_t = \infty$, $\mathbf{X}_\theta = \mathbf{0}$ or $\hat{\mathbf{P}}_{\mathbf{X}_\theta} = \mathbf{0}$, and a single phase material is modeled.

It is important to mention that the number of material parameters or functions is identical for both theories. Provided that the material functions do not depend on temperature, the model includes 20 material parameters: the modeling of the thermoelastic material properties of a two-phase material requires eleven material parameters (μ^A, μ^M, κ^A, κ^M, α^A, α^M, $c_{d_0}^A$, $c_{d_0}^M$, ρ, Δu_0, and $\Delta \eta_0$). The evolution of the transformation strain tensor is adjusted by the parameters η_t and m_t. The limit case $\eta_t \to 0$ results in a rate-independent theory. Moreover, the material parameters c (modulus for $\mathbf{X}_\varepsilon$), b (saturation value), γ (parameter in $B(\theta, z, \dot{z})$), and β (parameter in $B(\theta, z, \dot{z})$) are used to model the internal stress field $\mathbf{X}_\varepsilon$. The height of the hysteresis is influenced by the phase transition radius k and the relation between the fraction of oriented martensite and the transformation strain state is adjusted by γ_t (maximum transformation strain) and γ_0. Of course, the identification of all these parameters is a challenge: e.g. the determination of all thermoelasticity parameters requires an elaborate testing equipment. In [Helm 2005] it is demonstrated that a certain part of the set of material parameters can be identified by common experiments in combination with the method of neural networks.

The present constitutive theory models only the material behavior of shape memory alloys due to martensitic phase transitions. For simplicity, the influence of the orientation and reorientation of martensite twins on the material behavior of shape memory alloys is not considered. However, it is possible to combine the current theory with the proposed strategy in [Helm and Haupt 2003] for the representation of the orientation and reorientation of martensite twins. To do this, it is necessary to separate the fraction of martensite into the fraction of self-accommodated martensite (twinned martensite) and the fraction of oriented martensite (detwinned martensite); compare the discussion in [Lagoudas et al. 2006].

From a mathematical point of view, the theories developed are particularly suitable for the numerical solution of initial-boundary value problems, because the introduced internal variables to describe the temperature-dependent phase transition stress are continuous functions of the transformation strain tensor. The numerical treatment of the proposed material models is discussed in the second part of this article [Helm and Schäfers 2006]. Moreover, the main features of the theories are demonstrated in numerical examples, which include the comparison to experimental data.

References

[Achenbach and Müller 1982] M. Achenbach and I. Müller, "A model for shape memory", *Journal de Physique, Colleque C4, ICOMAT–82* **43** (1982), 163–167.

[Anand and Gurtin 2003] L. Anand and M. E. Gurtin, "Thermal effects in the superelasticity of crystalline shape-memory materials", *J. Mech. Phys. Solids* **51**:6 (2003), 1015–1058. MR 2004c:74066

[Auricchio and Petrini 2004] F. Auricchio and L. Petrini, "A three-dimensional model describing stress-temperature induced solid phase transformations: solution algorithm and boundary value problems", *Internat. J. Numer. Methods Engrg.* **61**:6 (2004), 807–836. MR 2005d:74032

[Auricchio and Stefanelli 2004] F. Auricchio and U. Stefanelli, "Numerical analysis of a three-dimensional super-elastic constitutive model", *Internat. J. Numer. Methods Engrg.* **61**:1 (2004), 142–155. MR 2005b:74100

[Auricchio and Taylor 1997] F. Auricchio and R. Taylor, "Shape-memory alloys: modelling and numerical simulations of the finite-strain superelastic behavior", *Computer Methods in Applied Mechanics and Engineering* **143** (1997), 175–194.

[Auricchio et al. 1997] F. Auricchio, R. Taylor, and J. Lubliner, "Shape-memory alloys: macromodelling and numerical simulations of the superelastic behavior", *Computer Methods in Applied Mechanics and Engineering* **146** (1997), 281–312.

[Bertram 1982] A. Bertram, "Thermo-mechanical constitutive equations for the description of shape memory effects in alloys", *Nuclear Engineering and Design* **74** (1982), 173–182.

[Bondaryev and Wayman 1988] E. Bondaryev and C. Wayman, "Some stress-strain-temperature relationships for shape memory alloys", *Metallurgical Transactions A* **19A** (1988), 2407–2413.

[Boyd and Lagoudas 1994] J. Boyd and D. Lagoudas, "A constitutive model for simultaneous transformation and reorientation in shape memory materials", pp. 159–177 in *Mechanics of phase transformations and shape memory alloys* (Chicago, 1994), edited by L. C. Brinson and B. Moran, AMD **189**, The American Society of Mechanical Engineers, New York, 1994.

[Casey 1985] J. Casey, "Approximate kinematical relations in plasticity", *Internat. J. Solids Structures* **21**:7 (1985), 671–682. MR 88c:73033

[Coleman and Gurtin 1967] B. Coleman and M. Gurtin, "Thermodynamics with internal state variables", *J. Chem. Phys.* **47** (1967), 597–613.

[Delobelle and Lexcellent 1996] P. Delobelle and C. Lexcellent, "A phenomenological three dimensional model for pseudoelastic behavior of shape memory", *Journal de Physique IV* **6** (1996), 293–300.

[Dettmer and Reese 2004] W. Dettmer and S. Reese, "On the theoretical and numerical modelling of Armstrong-Frederick kinematic hardening in the finite strain regime", *Comput. Methods Appl. Mech. Engrg.* **193** (2004), 87–116.

[Eckart 1948] C. Eckart, "The thermodynamics of irreversible processes, IV: The theory of elasticity and anelasticity", *Physical Rev.* (2) **73** (1948), 373–382. MR 9,394a

[Eggeler et al. 2004] G. Eggeler, E. Hornbogen, A. Yawny, and M. Wagner, "Structural and functional fatigue of NiTi shape memory alloys", *Materials Science and Engineering A* **378** (2004), 24–33.

[Entchev and Lagoudas 2002] P. Entchev and D. Lagoudas, "Modeling porous shape memory alloys using micromechanical averaging techniques", *Mechanics of materials* **34**:11 (2002), 1–24.

[Falk 1983] F. Falk, "One-dimensional model of shape memory", *Archives of Mechanics* **35** (1983), 63–84.

[Flory 1961] P. J. Flory, "Thermodynamic relations for high elastic materials", *Trans. Faraday Soc.* **57** (1961), 829–838. MR 23 #B1161

[Funakubo 1987] H. Funakubo, *Shape memory alloys*, Gordon and Breach, New York, 1987.

[Gall and Sehitoglu 1999] K. Gall and H. Sehitoglu, "The role of texture in tension-compression asymmetry in polycrystalline NiTi", *International Journal of Plasticity* **15**:1 (1999), 69–92. Corrigendum in **15**:7, 781.

[Graesser and Cozzarelli 1994] E. Graesser and F. Cozzarelli, "A proposed three dimensional constitutive model for shape memory alloys", *Journal of Intelligent Material Systems and Structures* **5** (1994), 78–89.

[Haupt 1985] P. Haupt, "On the concept of an intermediate configuration and its application to a representation of viscoelastic-plastic material behaviour", *International Journal of Plasticity* **1** (1985), 303–316.

[Haupt 2002] P. Haupt, *Continuum mechanics and theory of materials*, 2nd ed., Advanced Texts in Physics, Springer, Berlin, 2002. MR 2004h:74001

[Haupt and Tsakmakis 1989] P. Haupt and C. Tsakmakis, "On the application of dual variables in continuum mechanics", *Contin. Mech. Thermodyn.* **1**:3 (1989), 165–196. MR 91m:73002

[Haupt et al. 1992] P. Haupt, M. Kamlah, and C. Tsakmakis, "On the thermodynamics of rate-independent plasticity as an asymptotic limit of viscoplasticity for slow processes", pp. 107–116 in *Finite inelastic deformations: Theory and applications* (Hannover, 1991), edited by D. Besdo and E. Stein, Berlin, 1992.

[Helm 2001] D. Helm, *Formgedächtnislegierungen: Experimentelle Untersuchung, phänomenologische Modellierung und numerische Simulation der thermomechanischen Materialeigenschaften*, Ph.D. thesis, Institut für Mechanik, Universität Gesamthochschule Kassel, Kassel, 2001.

[Helm 2005] D. Helm, "Pseudoelastic behavior of shape memory alloys: Constitutive theory and identification of the material parameters using neural networks", *Technische Mechanik* **25** (http://www.uni-magdeburg.de/ifme/techmech/ 2005), 39–58.

[Helm 2006] D. Helm, "Stress computation in finite thermoviscoplasticity", *International Journal of Plasticity* **22** (2006), 1699–1727.

[Helm and Haupt 2001] D. Helm and P. Haupt, "Thermomechanical behaviour of shape memory alloys", pp. 302–313 in *Smart structures and materials: Active materials, behavior and mechanics* (Newport Beach, CA, 2001), edited by C. S. Lynch, Proceedings of SPIE **4333**, Internat. Soc. Optical Eng., Bellingham, WA, 2001.

[Helm and Haupt 2003] D. Helm and P. Haupt, "Shape memory behaviour: modelling within continuum thermomechanics", *International Journal of Solids and Structures* **40** (2003), 825–849.

[Helm and Schäfers 2006] D. Helm and M. Schäfers, "Thermomechanics of martensitic phase transitions in shape memory alloys, II: numerical treatment", *Journal of Mechanics and Materials of Structures* (2006), 1–30. prepared.

[Hohenemser and Prager 1932] K. Hohenemser and W. Prager, "Über die Ansätze der Mechanik isotroper Kontinua", *ZAMM* **12** (1932), 216–226.

[Huang et al. 2000] M. Huang, X. Gao, and L. C. Brinson, "A multivariant micromechanical model for SMAs, 2: Polycrystal model", *International Journal of Plasticity* **16** (2000), 1371–1390.

[Huo and Müller 1993] Y. Huo and I. Müller, "Nonequilibrium thermodynamics of pseudoelasticity", *Contin. Mech. Thermodyn.* **5**:3 (1993), 163–204. MR 94h:73015

[Juhász et al. 2000] L. Juhász, H. Andrä, and O. Hesebeck, "Simulation of the thermomechanical behaviour of shape memory alloys under multi-axial non-proportional loading", pp. 484–495 in *Smart structures and materials: Active materials, behavior and mechanics* (Newport Beach, CA, 2000), edited by C. S. Lynch, Proceedings of SPIE **3992**, Internat. Soc. Optical Eng., Bellingham, WA, 2000.

[Jung et al. 2004] Y. Jung, P. Papadopoulos, and R. O. Ritchie, "Constitutive modelling and numerical simulation of multivariant phase transformation in superelastic shape-memory alloys", *Internat. J. Numer. Methods Engrg.* **60**:2 (2004), 429–460. MR 2005a:74076

[Khan and Lagoudas 2002] M. Khan and D. Lagoudas, "Modeling of shape memory alloy springs using Preisach model for passive vibration isolation", pp. 336–347 in *Smart structures and materials: Modeling, signal processing, and control* (San Diego, 2002), edited by V. Rao, Proceedings of SPIE **4693**, Internat. Soc. Optical Eng., Bellingham, WA, 2002.

[Kröner 1958] E. Kröner, *Kontinuumstheorie der Versetzungen und Eigenspannungen*, Ergebnisse der angewandten Mathematik **5**, Springer, Berlin, 1958. MR 20 #2117

[Kröner 1960] E. Kröner, "Allgemeine Kontinuumstheorie der Versetzungen und Eigenspannungen", *Arch. Rational Mech. Anal.* **4** (1960), 273–334. MR 23 #B26

[Lagoudas et al. 2006] D. Lagoudas, P. Entchev, P. Popov, E. Patoor, L. Brinson, and X. Gao, "Shape memory alloys, I: Modeling of polycrystals", *Mechanics of Materials* **38** (2006), 430–462.

[Leclercq and Lexcellent 1996] S. Leclercq and C. Lexcellent, "A general macroscopic description of the thermomechanical behavior of shape memory alloys", *Journal of the Mechanics and Physics of Solids* **44**:6 (1996), 953–980.

[Lee 1969] E. Lee, "Elastic-plastic deformation at finite strains", *Journal of Applied Mechanics* **36** (1969), 59–67.

[Lee and Liu 1967] E. Lee and D. Liu, "Finite-strain elastic-plastic theory with application to plane-wave analysis", *Journal of Applied Physics* **38** (1967), 19–27.

[Levitas 1998] V. I. Levitas, "Thermomechanical theory of martensitic phase transformations in inelastic materials", *Internat. J. Solids Structures* **35**:9-10 (1998), 889–940. MR 98k:73012

[Lexcellent et al. 1996] C. Lexcellent, B. Goo, Q. Sun, and J. Bernardini, "Characterization, Thermomechanical Behaviour and Micromechanical-Based Constitutive Model of Shape-Memory Cu-Zn-Al Single Crystals", *Acta Materialia* **44** (1996), 3773–3780.

[Lexcellent et al. 2006] C. Lexcellent, M. Boubakar, C. Bouvet, and S. Calloch, "About modelling the shape memory alloy behaviour based on the phase transformation surface identification under proportional loading and anisothermal conditions", *International Journal of Solids and Structures* **43** (2006), 613–626.

[Liang and Rogers 1990] C. Liang and C. Rogers, "One dimensional thermomechanical constitutive relations for shape memory materials", *Journal of Intelligent Material Systems and Structures* **1** (1990), 207–234.

[Lim and McDowell 1995] T. Lim and D. McDowell, "Path dependence of shape memory alloys during cyclic loading", *Journal of Intelligent Material Systems and Structures* **6** (1995), 817–830.

[Lim and McDowell 1999] T. Lim and D. McDowell, "Mechanical behavior of an Ni-Ti shape memory alloy under axial-torsional proportional and nonproportional loading", *Journal of Engineering Materials and Technology* **121** (1999), 9–19.

[Lim and McDowell 2002] T. Lim and D. McDowell, "Cyclic thermomechanical behavior of a polycrystalline pseudoelastic shape memory alloy", *Journal of the Mechanics and Physics of Solids* **50**:26 (2002), 651–676.

[Lion 2000] A. Lion, "Constitutive modelling in finite thermoviscoplasticity: a physical approach based on nonlinear rheological models", *InternationalJournal of Plasticity* **16** (2000), 469–494.

[Lubliner 1985] J. Lubliner, "A model of rubber viscoelasticity", *Mechanics Research Communications* **12** (1985), 93–99.

[Lubliner 1990] J. Lubliner, *Plasticity theory*, New York, London, 1990.

[Mandel 1972] J. Mandel, *Plasticité classique et viscoplasticité*, CIMS Courses and Lectures **97**, Springer, Vienna, 1972. MR 49 #8463

[McNaney et al. 2003] J. McNaney, V. Imbeni, Y. Jung, P. Papadopoulos, and R. O. Ritchie, "An experimental study of the superelastic effect in a shape-memory Nitinol alloy under biaxial loading", *Mechanics of Materials* **35** (2003), 969–986.

[Miyazaki and Otsuka 1989] S. Miyazaki and K. Otsuka, "Development of shape memory alloys", *ISIJ International* **29**:5 (1989), 353–377.

[Müller and Bruhns 2004] C. Müller and O. Bruhns, "An Eulerian model for pseudoelastic shape memory alloys", *Material Science and Engineering Technology* **35** (2004), 260–271.

[Novák and Sittner 2004] V. Novák and P. Sittner, "Micromechanical modelling of NiTi polycrystalline aggregates transforming under tension and compression stress", *Materials Science and Engineering, A* **378** (2004), 490–498.

[Otsuka and Ren 1999] K. Otsuka and X. Ren, "Recent developments in the research of shape memory alloys", *Intermetallics* **7** (1999), 511–528.

[Otsuka and Wayman 1998] K. Otsuka and C. Wayman, *Shape memory materials*, Cambridge University Press, 1998.

[Paiva et al. 2005] A. Paiva, M. Savi, A. Braga, and P. Pacheco, "A constitutive model for shape memory alloys considering tensile-compressive asymmetry and plasticity", *International Journal of Solids and Structures* **42** (2005), 3439–3457.

[Patoor et al. 1994] E. Patoor, A. Eberhardt, and M. Berveiller, "Micromechanical modelling of the shape memory behavior", pp. 23–37 in *Mechanics of phase transformations and shape memory alloys* (Chicago, 1994), edited by L. Brinson and B. Moran, AMD **189**, The American Society of Mechanical Engineers, New York, 1994.

[Patoor et al. 1996] E. Patoor, A. Eberhardt, and M. Berveiller, "Micromechanical modelling of superelasticity in shape memory alloys", *Journal de Physique IV* **6** (1996), 277–292.

[Patoor et al. 2006] E. Patoor, D. Lagoudas, P. Entchev, L. Brinson, and X. Gao, "Shape memory alloys, Part I: General properties and modeling of single crystals", *Mechanics of Materials* **38** (2006), 391–429.

[Perzyna 1963] P. Perzyna, "The constitutive equations for rate sensitive plastic materials", *Quart. Appl. Math.* **20** (1963), 321–332. MR 26 #2080

[Qidwai and Lagoudas 2000] M. A. Qidwai and D. C. Lagoudas, "On thermomechanics and transformation surfaces of polycrystalline NiTi shape memory alloy material", *International Journal of Plasticity* **16** (2000), 1309–1343.

[Raniecki and Lexcellent 1994] B. Raniecki and C. Lexcellent, "R_L-models of pseudoelasticity and their specification for some shape memory solids", *European J. Mech. A Solids* **13**:1 (1994), 21–50. MR 94m:73012

[Raniecki et al. 1992] B. Raniecki, C. Lexcellent, and K. Tanaka, "Thermodynamic models of pseudoelastic behaviour of shape memory alloys", *Arch. Mech.* (*Arch. Mech. Stos.*) **44**:3 (1992), 261–284. MR 94j:73012

[Raniecki et al. 2001] B. Raniecki, K. Tanaka, and A. Ziółkowski, "Testing and modeling of NiTi SMA at complex stress state: Selected results of Polish-Japanese research cooperation", *Materials Science Research International* Special Technical Publication **2** (2001), 327–334.

[Rogueda et al. 1996] C. Rogueda, C. Lexcellent, and L. Bocher, "Experimental study of pseudoelastic behaviour of a CuZnAl polycrystalline shape memory alloy under tension-torsion proportional and non-proportional loading tests", *Archives of Mechanics* **48** (1996), 1025–1045.

[Seelecke 2002] S. Seelecke, "Modeling the dynamic behavior of shape memory alloys", *International Journal of Non-Linear Mechanics* **37** (2002), 1363–1374.

[Shaw and Kyriakides 1995] J. Shaw and S. Kyriakides, "Thermomechanical aspects of NiTi", *Journal of the Mechanics and Physics of Solids* **8** (1995), 1243–1281.

[Shimizu and Tadaki 1987] K. Shimizu and T. Tadaki, "Shape memory effect: Mechanism", pp. 1–60 in *Shape memory alloys*, edited by H. Funakubo, Gordon and Breach, New York, 1987.

[Simo 1985] J. Simo, "On the computational significance of the intermediate configuration and hyperelastic stress relations in finite deformation elastoplasticity", *Mechanics of Materials* **4** (1985), 439–451.

[Simo 1988] J. C. Simo, "A framework for finite strain elastoplasticity based on maximum plastic dissipation and the multiplicative decomposition, I: Continuum formulation", *Comput. Methods Appl. Mech. Engrg.* **66**:2 (1988), 199–219. MR 89a:73029

[Simo and Pister 1984] J. Simo and K. Pister, "Remarks on rate constitutive equations for finite deformation problems", *Computer Methods in Applied Mechanics and Engineering* **46** (1984), 201–215.

[Souza et al. 1998] A. Souza, E. Mamiya, and N. Zouain, "Three-dimensional model for solids undergoing stress-induced phase transitions", *Eur. J. Mech. A/Solids* **17** (1998), 789–806.

[Tanaka and Nagaki 1982] K. Tanaka and S. Nagaki, "A thermomechanical description of materials with internal variables in the process of phase transitions", *Ingenieur-Archiv* **51** (1982), 287–299.

[Tanaka et al. 2002] K. Tanaka, D. Ohnami, T. Watanabe, and J. Kosegawa, "Micromechanical simulations of thermomechanical behavior in shape memory alloys: transformation conditions and thermomechanical hystereses", *Mechanics of Materials* **34** (2002), 279–298.

[Thamburaja and Anand 2003] P. Thamburaja and L. Anand, "Thermo-mechanically coupled superelastic repsonse of initially-textured Ti-Ni sheet", *Acta Materialia* **51** (2003), 325–338.

[Tsakmakis 1996] C. Tsakmakis, "Kinematic hardening rules in finite plasticity, I: A constitutive approach", *Continuum Mechanics and Thermodynamics* **8** (1996), 215–231.

[Tsakmakis and Willuweit 2004] C. Tsakmakis and A. Willuweit, "A comparative study of kinematic hardening rules at finite deformations", *Int. J. of Non-Linear Mechanics* **39** (2004), 539–554.

DIRK HELM: dirk.helm@iwm.fraunhofer.de
Institute of Mechanics, Department of Mechanical Engineering, University of Kassel, Mönchebergstraße 7, D–34109 Kassel, Germany
Current address: *Fraunhofer Institute for Mechanics of Materials, Wöhlerstraße 11, D–79108 Freiburg, Germany*
http://www.iwm.fraunhofer.de

MAGNETOTHERMOELASTIC STRESSES INDUCED BY A TRANSIENT MAGNETIC FIELD IN AN INFINITE CONDUCTING PLATE

MASAHIRO HIGUCHI, RYUUSUKE KAWAMURA, YOSHINOBU TANIGAWA AND HIDEKI FUJIEDA

We investigate the dynamic and quasistatic behavior of magnetothermoelastic stresses induced by a transient magnetic field in an infinite conducting plate. A transient magnetic field defined by an arbitrary function of time acts on both surfaces of the infinite plate and parallel to them. The fundamental equations of one-dimensional electromagnetic, temperature and elastic fields are formulated, and solutions for the magnetic field, eddy current, temperature change and dynamic and quasistatic solutions for stresses and deformations are analytically derived, in terms of the excitation function. The stress solutions are determined to be sums of a thermal stress component caused by eddy current loss and a magnetic stress component caused by the Lorentz force. The case of a magnetic field defined by a smoothed ramp function with a sine-function profile is examined in particular, and the dynamic and quasistatic behavior of the stresses are numerically calculated.

1. Introduction

Mechanical structures that are activated when a magnetic field is applied has been of increasing interest in recent years. When a time-dependent magnetic field acts on a conducting medium, an eddy current is induced, which generates heat; this is the eddy current energy loss due to the Joule effect. The conducting medium is also subjected to a Lorentz force. Thus, two kinds of stress arise: thermal stress caused by eddy current loss magnetic stress caused by the Lorentz force.

In the field of magnetoelasticity or magnetothermoelasticity, many studies have employed an analytical treatment of the interaction between elastic, electromagnetic and temperature fields; see, for instance, [Kaliski and Nowacki 1962; Kaliski and Michalec 1963; Paria 1967; Wauer 1996; Banerjee and Roychoudhuri 1997; Wang et al. 2002; 2003; Librescu et al. 2003; Ezzat and Youssef 2005; Zheng et al. 2005]. However, there have been only a few analytical studies of thermal stresses induced by time-dependent magnetic fields [Moon and Chattopadhyay 1974; Chian and Moon 1981; Wauer 1995]. Moon and Chattopadhyay [1974] have studied thermal stresses and magnetic stresses in a conducting half-space caused by an applied jump in tangential magnetic field at the boundary. Chian and Moon [1981] have extended that work, investigating the same stresses in a hollow cylindrical conductor caused by a pulsed magnetic field at the cavity. Wauer [1995] has studied the dynamic behavior of a magnetothermoelastic plate layer whose surfaces are subjected to a magnetic field composed of a constant and a harmonically oscillating part in the direction parallel to the surfaces. He has mentioned the stability of the plate due to the external magnetic field. Pantelyat and Féliachi [2002] have studied the mechanical behavior of metals

Keywords: magnetothermoelasticity, eddy current loss, Lorentz force.

in induction heating devices by using of finite element method. They have calculated thermoelastic-plastic stresses induced by an alternating magnetic field, taking into account the temperature dependence of the material properties.

Here we investigate the dynamic and quasistatic behavior of magnetothermoelastic stresses induced by a transient magnetic field on an infinite conducting plate made of a nonferromagnetic metal such as copper or aluminum. Assuming an applied magnetic field defined by an arbitrary function of time, acting on both sides of the plate and parallel to it, we formulate the fundamental equations of the one-dimensional electromagnetic, temperature and elastic fields. We then solve for the electromagnetic field, temperature change and dynamic and quasistatic solutions of stresses and displacements, analytically deriving expressions for these fields in terms of the arbitrary excitation function. The stresses solutions are determined to be the sums of a thermal stress and a magnetic stress component.

We then focus on the case of an excitation given by a smoothed ramp function with sine-function profile, studying numerically the dynamic and quasistatic behavior of the induced thermal and magnetic stresses.

2. Fundamental equations

2.1. *Electromagnetic field.* Figure 1 shows an infinite conducting plate of thickness $2b$ with a Cartesian coordinate system, subject to a time-dependent magnetic field $H_0\phi(t)$ that is uniformly distributed along the x and z directions and acts on both side surfaces of the infinite plate in the z direction, starting at time $t = 0$. Here H_0 is a reference magnetic field strength and $\phi(t)$ is an arbitrary function of time.

Let the magnetic field be $\boldsymbol{H} = (0, 0, H_z(y, t))$ in the infinite plate, and let the electric field vector be $\boldsymbol{E} = (E_x(y, t), 0, 0)$. Disregarding the displacement current, the governing equations and the constitutive relations of electromagnetics reduce to (see [Stoll 1974; Moon and Chattopadhyay 1974])

$$-\frac{\partial E_x}{\partial y} + \frac{\partial B_z}{\partial t} = 0, \quad \frac{\partial H_z}{\partial y} = J_x,$$

$$\sigma\left(E_x + B_z\frac{\partial v}{\partial t}\right) = J_x, \quad B_z = \mu H_z,$$

(1)

where B_z is the magnetic flux in the z direction, J_x is the electric current density in the x direction, v is the displacement in the y direction (as discussed later, no displacement is considered in the x and z directions), and σ and μ are the electric conductivity and the magnetic permeability in the infinite plate.
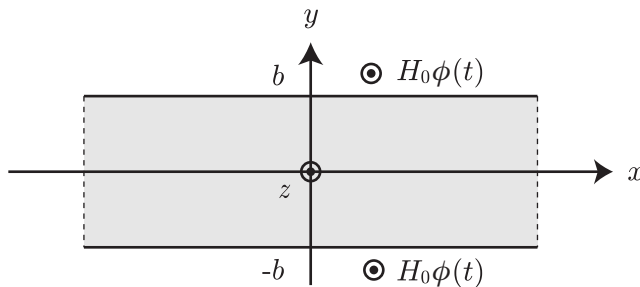
Figure 1. Conditions and coordinate system of infinite plate.

This leads to the fundamental equation of magnetic field [Moon and Chattopadhyay 1974]:

$$\frac{\partial^2 H_z}{\partial y^2} = \mu\sigma \frac{\partial H_z}{\partial t} + \mu\sigma \frac{\partial}{\partial y}\left(H_z \frac{\partial v}{\partial t}\right), \tag{2}$$

where the second term on the right is a nonlinear coupling term with elastic field. This coupling term is small compared with the first term $\mu\sigma \partial H_z/\partial t$, as shown in [Moon and Chattopadhyay 1974; Chian and Moon 1981]. Therefore, the coupled equation (2) with the elastic field reduces to the uncoupled equation

$$\frac{\partial^2 H_z}{\partial y^2} = \mu\sigma \frac{\partial H_z}{\partial t}. \tag{3}$$

The boundary conditions and initial condition are

$$\begin{aligned} \text{at } y = \pm b: \quad & H_z = H_0 \phi(t), \\ \text{at } t = 0: \quad & H_z = 0. \end{aligned} \tag{4}$$

The current density $J_x = \partial H_z/\partial y$ induced by the variation of the magnetic field is called the eddy current.

2.2. *Temperature field.* The eddy current J_x generates Joule heat, giving rise to the so-called eddy current loss $w(y, t)$. The eddy current loss per unit time per unit volume is given by (see [Moon and Chattopadhyay 1974])

$$w(y, t) = \sigma^{-1} J_x(y, t)^2. \tag{5}$$

We assume that the infinite plate with zero initial temperature change is heated by the eddy current loss $w(y, t)$ from time $t = 0$, and that both side surfaces are insulated, or subjected to surrounding media at temperature 0, with relative heat transfer coefficients h.

The one-dimensional heat conduction equation taking into account the eddy current loss [Moon and Chattopadhyay 1974] is then given by

$$\frac{\partial T}{\partial t} = \kappa \frac{\partial^2 T}{\partial y^2} + \frac{w}{C\rho}, \tag{6}$$

with boundary conditions and initial condition

$$\begin{aligned} \text{at } y = \pm b: \quad & \frac{\partial T}{\partial y} \pm hT = 0, \\ \text{at } t = 0: \quad & T(y, 0) = 0, \end{aligned} \tag{7}$$

where $T = T(y, t)$ is temperature change and κ, C and ρ denote the thermal conductivity, the specific heat and the mass density. If both surfaces are insulated, then h in (7) becomes zero. In (6), the coupling term with strain is neglected because the coupling effect mainly occurs at large times [Boley and Tolins 1962; Moon and Chattopadhyay 1974].

2.3. *Elastic field.* Besides the temperature change arising from the eddy current loss, the plate is subjected to a Lorentz force f, given by (see [Moon and Chattopadhyay 1974])

$$f = J \times B = \begin{pmatrix} \dfrac{\partial H_z}{\partial y} \\ 0 \\ 0 \end{pmatrix} \times \begin{pmatrix} 0 \\ 0 \\ \mu H_z \end{pmatrix} = \begin{pmatrix} 0 \\ -\dfrac{\mu}{2}\dfrac{\partial}{\partial y}\left[H_z(y,t)\right]^2 \\ 0 \end{pmatrix} \tag{8}$$

Thus the Lorentz force only has a y component:

$$f_y(y,t) = -\frac{\mu}{2}\frac{\partial}{\partial y}\left(H_z(y,t)\right)^2 \tag{9}$$

Because the temperature change and Lorentz force depend only on y and t, the displacement components are assumed to be $(0, v(y,t), 0)$. Thus the stress-displacement relations taking into account temperature change reduce to (see [Sternberg and Chakravorty 1959])

$$\sigma_{xx}(y,t) = \sigma_{zz}(y,t) = \frac{(1-v)E}{(1+v)(1-2v)}\left(\frac{v}{1-v}\frac{\partial v}{\partial y} - \frac{1+v}{1-v}\alpha T\right),$$

$$\sigma_{yy}(y,t) = \frac{(1-v)E}{(1+v)(1-2v)}\left(\frac{\partial v}{\partial y} - \frac{1+v}{1-v}\alpha T\right), \tag{10}$$

where $(\sigma_{xx}, \sigma_{yy}, \sigma_{zz})$ are the stress components and v, E and α denote the Poisson ratio, the Young's modulus and the coefficient of linear thermal expansion. The equation of motion in the y direction, taking into account Lorentz force, is given by (see [Moon and Chattopadhyay 1974])

$$\frac{\partial \sigma_{yy}}{\partial y} + f_y = \rho\frac{\partial^2 v}{\partial t^2}. \tag{11}$$

Substitution of (9) and $\bar{\sigma}_{yy}$ from (10) into (11) leads to the displacement equation of motion

$$\frac{\partial^2 v}{\partial y^2} = \frac{1}{C_L^2}\frac{\partial^2 v}{\partial t^2} + \frac{1+v}{1-v}\alpha\frac{\partial T}{\partial y} + \frac{(1+v)(1-2v)}{(1-v)E}\frac{\mu}{2}\frac{\partial}{\partial y}\left(H_z\right)^2, \tag{12}$$

where

$$C_L = \sqrt{\frac{(1-v)E}{(1+v)(1-2v)\rho}}. \tag{13}$$

is the velocity of longitudinal wave. The infinite plate is at rest before $t = 0$ and we suppose that the surfaces are traction-free ($\sigma_{yy} = 0$). Thus the mechanical boundary conditions and initial conditions are

$$\text{at } y = \pm b: \qquad \frac{\partial v}{\partial y} = \frac{1+v}{1-v}\alpha T,$$

$$\text{at } t = 0: \qquad v = \frac{\partial v}{\partial t} = 0. \tag{14}$$

2.4. _Dimensionless quantities._ We define the dimensionless quantities

$$\bar{y} = \frac{y}{b}, \quad \bar{H}_z = \frac{H_z}{H_0}, \quad \tau = \frac{t}{\mu \sigma b^2}, \quad \bar{J}_x = \frac{bJ_x}{H_0}, \quad \bar{w} = \frac{\sigma b^2 w}{H_0^2}, \quad \bar{T} = \frac{C\gamma T}{\mu H_0^2}, \quad \bar{h} = bh,$$

$$\bar{f}_y = \frac{bf_y}{\mu H_0^2}, \quad (\bar{\sigma}_{xx}, \bar{\sigma}_{yy}, \bar{\sigma}_{zz}) = \frac{(\sigma_{xx}, \sigma_{yy}, \sigma_{zz})}{\frac{\mu H_0^2}{2}}, \quad \bar{v} = \frac{(1-\nu)E}{(1+\nu)(1-2\nu)} \frac{2}{b\mu H_0^2} v \tag{15}$$

and

$$\chi_1 = \mu \sigma \kappa, \quad \chi_2 = \mu \sigma b C_L, \quad \chi_3 = \frac{2\alpha E}{(1-2\nu)C\rho}. \tag{16}$$

In terms of these dimensionless quantities, the equality $J_x = \partial H_z / \partial y$ and Equations (3)–(7), (9), (10), (12), (14) become:

(1) _Electromagnetic field:_

Equation system:
$$\frac{\partial^2 \bar{H}_z}{\partial \bar{y}^2} = \frac{\partial \bar{H}_z}{\partial \tau} \tag{17}$$

with conditions
$$\begin{aligned} \text{at } \bar{y} = \pm 1: \quad & \bar{H}_z = \phi(\tau) \\ \text{at } \tau = 0: \quad & \bar{H}_z = 0 \end{aligned} \tag{18}$$

Eddy current:
$$\bar{J}_x(\bar{y}, \tau) = \frac{\partial \bar{H}_z(\bar{y}, \tau)}{\partial \bar{y}} \tag{19}$$

(2) _Temperature field:_

Eddy current loss:
$$\bar{w}(\bar{y}, \tau) = \left(\bar{J}_x(\bar{y}, \tau) \right)^2 \tag{20}$$

Equation system:
$$\frac{\partial \bar{T}}{\partial \tau} = \chi_1 \frac{\partial^2 \bar{T}}{\partial \bar{y}^2} + \bar{w} \tag{21}$$

with conditions
$$\begin{aligned} \text{at } \bar{y} = \pm 1: \quad & \frac{\partial \bar{T}}{\partial \bar{y}} \pm \bar{h}\bar{T} = 0 \\ \text{at } \tau = 0: \quad & \bar{T} = 0 \end{aligned} \tag{22}$$

(3) _Elastic field:_

Lorentz force:
$$\bar{f}_y(\bar{y}, \tau) = -\frac{1}{2} \frac{\partial}{\partial \bar{y}} \left(\bar{H}_z(\bar{y}, \tau) \right)^2 \tag{23}$$

Stress-displacement relations:
$$\begin{aligned} \bar{\sigma}_{xx}(\bar{y}, \tau) = \bar{\sigma}_{zz}(\bar{y}, \tau) &= \frac{\nu}{1-\nu} \frac{\partial \bar{v}}{\partial \bar{y}} - \chi_3 \bar{T} \\ \bar{\sigma}_{yy}(\bar{y}, \tau) &= \frac{\partial \bar{v}}{\partial \bar{y}} - \chi_3 \bar{T} \end{aligned} \tag{24}$$

Equation system:
$$\frac{\partial^2 \bar{v}}{\partial \bar{y}^2} = \frac{1}{\chi_2^2} \frac{\partial^2 \bar{v}}{\partial \tau^2} + \chi_3 \frac{\partial \bar{T}}{\partial \bar{y}} + \frac{\partial}{\partial \bar{y}} (\bar{H}_z)^2 \tag{25}$$

with conditions
$$at \ \bar{y} = \pm 1 : \quad \frac{\partial \bar{v}}{\partial \bar{y}} = \chi_3 \bar{T} \tag{26}$$
$$at \ \tau = 0 : \quad \bar{u} = \frac{\partial \bar{u}}{\partial \tau} = 0$$

3. Solutions

3.1. *Magnetic field.* To transform the inhomogeneous boundary condition $\bar{H}_z = \phi(\tau)$ from (18) into a homogeneous one, we assume that the solution of (17) is given by

$$\bar{H}_z(\bar{y}, \tau) = h_z(\bar{y}, \tau) + \phi(\tau). \tag{27}$$

By substitution of (27) into (17)–(18), the equation system with respect to h_z becomes

$$\frac{\partial^2 h_z}{\partial \bar{y}^2} = \frac{\partial h_z}{\partial \tau} + \frac{\partial \phi(\tau)}{\partial \tau} \tag{28}$$

with boundary and initial conditions

$$at \ \bar{y} = \pm 1 : \quad h_z = 0, \tag{29}$$
$$at \ \tau = 0 : \quad h_z = -\phi(0).$$

By separation of variables, the solution of (28) will be assumed to be of the form

$$h_z(\bar{y}, \tau) = \sum_{n=1}^{\infty} a_n(\tau) \cos(k_n \bar{y}), \tag{30}$$

where the $a_n(\tau)$ are unknown functions of τ and the k_n are the positive roots of the eigenequation

$$\cos(k_n) = 0 \quad \therefore \quad k_n = \frac{(2n-1)\pi}{2} \quad (n = 1, 2, \dots) \tag{31}$$

The solution $h_z(\bar{y}, \tau)$ in (30) clearly satisfies the homogeneous boundary conditions in (29).

Substitution of (30) into (28) gives

$$-\sum_{n=1}^{\infty} k_n^2 a_n(\tau) \cos(k_n \bar{y}) = \sum_{n=1}^{\infty} \frac{da_n(\tau)}{d\tau} \cos(k_n \bar{y}) + \frac{d\phi(\tau)}{d\tau} \tag{32}$$

Multiplying both sides by $\cos(k_m \bar{y})$ and integrating it from -1 to 1, we obtain

$$-\sum_{n=1}^{\infty} k_n^2 a_n(\tau) \int_{-1}^{1} \cos(k_n \bar{y}) \cos(k_m \bar{y}) \, d\bar{y}$$
$$= \sum_{n=1}^{\infty} \frac{da_n(\tau)}{d\tau} \int_{-1}^{1} \cos(k_n \bar{y}) \cos(k_m \bar{y}) \, d\bar{y} + \int_{-1}^{1} \frac{d\phi(\tau)}{d\tau} \cos(k_m \bar{y}) \, d\bar{y}. \tag{33}$$

By virtue of the orthogonal property of trigonometric functions, we obtain

$$\int_{-1}^{1} \cos(k_n \bar{y}) \cos(k_m \bar{y}) \, \mathrm{d}\bar{y} = \begin{cases} 1 & (m = n), \\ 0 & (m \neq n). \end{cases} \tag{34}$$

Substituting (34) into (33) gives

$$\frac{\mathrm{d}a_n(\tau)}{\mathrm{d}\tau} + k_n a_n(\tau) = -\int_{-1}^{1} \frac{\mathrm{d}\phi(\tau)}{\mathrm{d}\tau} \cos(k_n \bar{y}) \, \mathrm{d}\bar{y}. \tag{35}$$

By use of the initial condition in (29), the solutions of (35) are determined to be

$$a_n(\tau) = \frac{2(-1)^n}{k_n} \hat{a}_n(\tau). \tag{36}$$

where the $\hat{a}_n(\tau)$ are determined by the function $\phi(\tau)$:

$$\hat{a}_n(\tau) = \int_0^{\tau} e^{-k_n^2(\tau - \tau')} \frac{\mathrm{d}\phi(\tau')}{\mathrm{d}\tau'} \, \mathrm{d}\tau'. \tag{37}$$

From (27), (30) and (36), the magnetic field $\bar{H}_z$ is written as

$$\bar{H}_z(\bar{y}, \tau) = \phi(\tau) + 2 \sum_{n=1}^{\infty} \frac{(-1)^n}{k_n} \cos(k_n \bar{y}) \hat{a}_n(\tau). \tag{38}$$

Substitution of (38) into (19) gives the eddy current $\bar{J}_x$ as follows:

$$\bar{J}_x(\bar{y}, \tau) = 2 \sum_{n=1}^{\infty} (-1)^{n+1} \sin(k_n \bar{y}) \hat{a}_n(\tau). \tag{39}$$

3.2. Temperature field. By separation of variables, the solution of (21) will be assumed to be of the form

$$\bar{T}(\bar{y}, \tau) = \sum_{j=\beta}^{\infty} b_j(\tau) \cos(p_j \bar{y}), \qquad \beta = \begin{cases} 0 & \text{for} \quad \bar{h} = 0, \\ 1 & \text{for} \quad \bar{h} > 0, \end{cases} \tag{40}$$

where the $b_j(\tau)$ are unknown functions of τ, and the p_j are the nonnegative roots of the eigenequations

$$\begin{aligned} \sin p_j &= 0 & (p_j \geq 0 \text{ for } j = 0, 1, 2, \dots) && \text{if } \bar{h} = 0, \\ \tan p_j &= \frac{h}{p_j} & (p_j > 0 \text{ for } j = 1, 2, 3, \dots) && \text{if } \bar{h} > 0. \end{aligned} \tag{41}$$

The solution $\bar{T}(\bar{y}, \tau)$ in (40) clearly satisfies the boundary conditions in (22).

By virtue of the orthogonal property of trigonometric functions, we have

$$\int_{-1}^{1} \cos(p_j \bar{y}) \cos(p_l \bar{y}) \, \mathrm{d}\bar{y} = \begin{cases} M_j & (l = j), \\ 0 & (l \neq j), \end{cases} \tag{42}$$

where
$$M_j = \begin{cases} 2 & (j = 0) \\ \begin{cases} 1 & \text{for} \quad \bar{h} = 0 \\ \dfrac{\bar{h} + \bar{h}^2 + p_j^2}{\bar{h}^2 + p_j^2} & \text{for} \quad \bar{h} > 0 \end{cases} & (j > 0) \end{cases} \tag{43}$$

Substituting (40) into (21) and using (42), we obtain

$$\frac{\mathrm{d}b_j(\tau)}{\mathrm{d}\tau} + \chi_1 p_j^2 b_j(\tau) = \frac{1}{M_j} \int_{-1}^{1} \bar{w}(\bar{y}, \tau) \cos(p_j \bar{y}) \, \mathrm{d}\bar{y} \tag{44}$$

Through the use of the initial condition in (21), the solutions of (44) are determined to be

$$b_j(\tau) = \begin{cases} \dfrac{1}{2} \int_{-1}^{1} \left(\int_{0}^{\tau} \bar{w}(\bar{y}, \tau') \, \mathrm{d}\tau' \right) \mathrm{d}\bar{y} & (j = 0) \\ \dfrac{1}{M_j} \int_{-1}^{1} \left(\int_{0}^{\tau} \mathrm{e}^{-\chi_1 p_j^2(\tau - \tau')} \bar{w}(\bar{y}, \tau') \, \mathrm{d}\tau' \right) \cos(p_j \bar{y}) \, \mathrm{d}\bar{y} & (j > 0) \end{cases} \tag{45}$$

Substituting (39) into (20), we obtain the eddy current loss:

$$\bar{w}(\bar{y}, \tau) = 4 \sum_{m=1}^{\infty} \sum_{n=1}^{\infty} (-1)^{m+n} \sin(k_m \bar{y}) \sin(k_n \bar{y}) \hat{a}_m(\tau) \hat{a}_n(\tau) \tag{46}$$

Substitution of (46) into (45) gives

$$b_j(\tau) = \begin{cases} 2 \sum_{n=1}^{\infty} \hat{b}_n^{(0)}(\tau) & (j = 0), \\ \dfrac{4}{M_j} \sum_{m=1}^{\infty} \sum_{n=1}^{\infty} I_{1jmn} \hat{b}_{jmn}(\tau) & (j > 0), \end{cases} \tag{47}$$

where

$$\begin{aligned} I_{1jmn} &= (-1)^{m+n} \int_{-1}^{1} \sin k_m \bar{y} \sin k_n \bar{y} \cos p_j \bar{y} \, \mathrm{d}\bar{y} \\ &= \begin{cases} \begin{cases} -\frac{1}{2}(-1)^{m+n} & (m + n = j + 1) \\ \frac{1}{2}(-1)^{m+n} & (|m - n| = j) \\ 0 & (\text{otherwise}) \end{cases} & \text{if } \bar{h} = 0, \\ \bar{h} \cos(p_j) \dfrac{2(k_m^2 + k_n^2 - p_j^2)}{(2k_m k_n)^2 - (k_m^2 + k_n^2 - p_j^2)^2} & \text{if } \bar{h} > 0, \end{cases} \end{aligned} \tag{48}$$

and where the $\hat{b}_n^{(0)}(\tau)$ and $\hat{b}_{jmn}(\tau)$ are determined by the function $\phi(\tau)$:

$$
\hat{b}_n^{(0)}(\tau) = \int_0^\tau \left(\hat{a}_n(\tau')\right)^2 \, d\tau',
$$
$$
\hat{b}_{jmn}(\tau) = \int_0^\tau e^{-\chi_1 p_j^2(\tau-\tau')} \hat{a}_m(\tau')\hat{a}_n(\tau') \, d\tau'. \tag{49}
$$

Substituting (47) into (40), we obtain for the temperature change

$$
\bar{T}(\bar{y}, \tau) = 2\sum_{n=1}^\infty \hat{b}_n^{(0)}(\tau) + 4\sum_{j=1}^\infty \frac{1}{M_j} \cos(p_j\bar{y}) \sum_{m=1}^\infty \sum_{n=1}^\infty I_{1jmn}\hat{b}_{jmn}(\tau) \tag{50}
$$

where, for $\bar{h} > 0$, the first term on the right-hand side in (50) is ignored.

3.3. *Elastic field.*

3.3.1. *Dynamic solutions.* To transform the inhomogeneous boundary condition $\frac{\partial \bar{v}}{\partial \bar{y}} = \chi_3 \bar{T}$ from (26) into a homogeneous one, we assume that the displacement $\bar{v}(\bar{y}, \tau)$ is given by

$$
\bar{v}(\bar{y}, \tau) = v_1(\bar{y}, \tau) + v_2(\bar{y}, \tau), \tag{51}
$$

where $v_1(\bar{y}, \tau)$ satisfies

$$
\frac{\partial^2 v_1}{\partial \bar{y}^2} = 0 \qquad \text{with boundary condition } \frac{\partial v_1}{\partial \bar{y}} = \chi_3 \bar{T} \text{ at } \bar{y} = \pm 1. \tag{52}
$$

The solution of (52) is

$$
v_1 = \chi_3 \bar{T}(\pm 1, \tau)\bar{y}, \tag{53}
$$

where $\bar{T}(1, \tau) = \bar{T}(-1, \tau)$ from (50).

Substitution of (51) with (52) into (25)–(26) gives the equation system with respect to v_2 as

$$
\frac{\partial^2 v_2}{\partial \bar{y}^2} = \frac{1}{\chi_2^2}\frac{\partial^2 v_2}{\partial \tau^2} + \frac{1}{\chi_2^2}\frac{\partial^2 v_1}{\partial \tau^2} + \chi_3\frac{\partial \bar{T}}{\partial \bar{y}} + \frac{\partial}{\partial \bar{y}}(\bar{H}_z)^2 \tag{54}
$$

with conditions

$$
\text{at } \bar{y} = \pm 1: \quad \frac{\partial v_2}{\partial \bar{y}} = 0,
$$
$$
\text{at } \tau = 0: \quad \frac{\partial v_2}{\partial \tau} = -\frac{\partial v_1}{\partial \tau}, \quad v_2 = -v_1. \tag{55}
$$

By separation of variables, the solution of (54) will be assumed to be of the form

$$
v_2(\bar{y}, \tau) = \sum_{i=1}^\infty c_i(\tau) \sin(\eta_i \bar{y}), \tag{56}
$$

where the $c_i(\tau)$ are unknown functions of τ and the η_i are the positive roots of the eigenequation

$$\cos(\eta_i) = 0 \quad \therefore \quad \eta_i = \frac{(2i-1)\pi}{2} \quad (i = 1, 2, \dots). \tag{57}$$

The solution $v_2(\bar{y}, \tau)$ in (56) clearly satisfies the homogeneous boundary conditions in (55).

By the orthogonality of trigonometric functions, we obtain

$$\int_{-1}^{1} \sin(\eta_i \bar{y}) \sin(\eta_q \bar{y}) \, d\bar{y} = \begin{cases} 1 & (q = i), \\ 0 & (q \neq i). \end{cases} \tag{58}$$

Substituting (56) into (54), and using (58) we obtain

$$\frac{\partial^2 c_i(\tau)}{\partial \tau^2} + \Omega_i^2 c_i(\tau)$$

$$= -\int_{-1}^{1} \frac{\partial^2 v_1}{\partial \tau^2} \sin(\eta_i \bar{y}) \, d\bar{y} - \chi_3 \chi_2^2 \int_{-1}^{1} \frac{\partial \bar{T}}{\partial \bar{y}} \sin(\eta_i \bar{y}) \, d\bar{y} - \chi_2^2 \int_{-1}^{1} \frac{\partial}{\partial \bar{y}} (\bar{H}_z)^2 \sin(\eta_i \bar{y}) \, d\bar{y}, \tag{59}$$

where the Ω_i are the natural angular frequencies of the i-th mode in dimensionless form:

$$\Omega_i = \chi_2 \eta_i. \tag{60}$$

By the use of the initial condition in (55), the solutions of (59) are determined to be

$$c_i(\tau) = \int_{-1}^{1} \left(-v_1(\bar{y}, \tau) + \Omega_i \int_{0}^{\tau} \sin \Omega_i(\tau - \tau') v_1(\bar{y}, \tau') \, d\tau' \right) \sin(\eta_i \bar{y}) \, d\bar{y}$$

$$- \chi_3 \frac{\chi_2}{\eta_i} \int_{-1}^{1} \frac{\partial}{\partial \bar{y}} \left(\int_{0}^{\tau} \sin \Omega_i(\tau - \tau') \bar{T}(\bar{y}, \tau') \, d\tau' \right) \sin(\eta_i \bar{y}) \, d\bar{y}$$

$$- \frac{\chi_2}{\eta_i} \int_{-1}^{1} \frac{\partial}{\partial \bar{y}} \left(\int_{0}^{\tau} \sin \Omega_i(\tau - \tau') \left(\bar{H}_z(\bar{y}, \tau') \right)^2 \, d\tau' \right) \sin(\eta_i \bar{y}) \, d\bar{y}. \tag{61}$$

Substitution of (38), (50) and (53) into (61) gives

$$c_i(\tau) = c_i^T(\tau) + c_i^M(\tau), \tag{62}$$

where

$$c_i^T(\tau) = \frac{4(-1)^i}{\eta_i^2} \chi_3 \left(\frac{1}{2} \sum_{n=1}^{\infty} \left(\hat{b}_n^{(0)}(\tau) - \Omega_i \hat{c}_{in}^{T(0)}(\tau) \right) \right.$$

$$\left. + \sum_{j=1}^{\infty} \frac{\cos(p_j)}{M_j} \sum_{m=1}^{\infty} \sum_{n=1}^{\infty} I_{1jmn} \left(\hat{b}_{jmn}(\tau) + \frac{\eta_i^2}{p_j^2 - \eta_i^2} \Omega_i \hat{c}_{ijmn}^T(\tau) \right) \right) \tag{63}$$

is the contribution from the temperature change (the first term on the right-hand side being ignored, for $\bar{h} = 0$), and

$$c_i^M(\tau) = \frac{4(-1)^i \chi_2}{\eta_i} \left(\hat{c}_{ii}^{M(1)}(\tau) + \sum_{m=1}^{\infty} \sum_{n=1}^{\infty} \frac{4\eta_i^2}{(k_m^2 + k_n^2 - \eta_i^2)^2 - (2k_m k_n^2)^2} \hat{c}_{imn}^{M(2)}(\tau) \right) \tag{64}$$

is the contribution from the Lorentz force. In these expressions $\hat{c}_{in}^{T(0)}(\tau)$, $\hat{c}_{ijmn}^{T}(\tau)$, $\hat{c}_{ii}^{M(1)}(\tau)$ and $\hat{c}_{imn}^{M(2)}(\tau)$ are defined in terms of the excitation function $\phi(\tau)$ by

$$
\begin{aligned}
\hat{c}_{in}^{T(0)}(\tau) &= \int_0^\tau \sin \Omega_i(\tau - \tau') \hat{b}_n^{(0)}(\tau') \, d\tau', \\
\hat{c}_{ijmn}^{T}(\tau) &= \int_0^\tau \sin \Omega_i(\tau - \tau') \hat{b}_{jmn}(\tau') \, d\tau', \\
\hat{c}_{ii}^{M(1)}(\tau) &= \int_0^\tau \sin \Omega_i(\tau - \tau') \phi(\tau') \hat{a}_i(\tau') \, d\tau', \\
\hat{c}_{imn}^{M(2)}(\tau) &= \int_0^\tau \sin \Omega_i(\tau - \tau') \hat{a}_m(\tau') \hat{a}_n(\tau') \, d\tau'.
\end{aligned}
\tag{65}
$$

From (51), (53), (56), and (62), we have

$$
\begin{aligned}
\bar{v}^T(\bar{y}, \tau) &= \chi_3 \bar{T}(\pm 1, \tau)\bar{y} + \sum_{i=1}^\infty c_i^T(\tau) \sin(\eta_i \bar{y}), \\
\bar{v}^M(\bar{y}, \tau) &= \sum_{i=1}^\infty c_i^M(\tau) \sin(\eta_i \bar{y}),
\end{aligned}
\tag{66}
$$

where $\bar{v}^T(\bar{y}, \tau)$ and $\bar{v}^M(\bar{y}, \tau)$ are the radial displacements due to temperature change and due to Lorentz force, respectively, and satisfy

$$
\bar{v}(\bar{y}, \tau) = \bar{v}^T(\bar{y}, \tau) + \bar{v}^M(\bar{y}, \tau).
\tag{67}
$$

Substituting (67) with (66) into (24), we obtain the dynamic solutions for the stress components:

$$
\bar{\sigma}_{xx}^T(\bar{y}, \tau) = \bar{\sigma}_{zz}^T(\bar{y}, \tau) = \frac{\nu}{1-\nu}\left(\chi_3 \bar{T}(\pm 1, \tau) + \sum_{i=1}^\infty c_i^T(\tau)\eta_i \sin(\eta_i \bar{y})\right) - \chi_3 \bar{T}(\bar{y}, \tau),
\tag{68}
$$

$$
\bar{\sigma}_{yy}^T(\bar{y}, \tau) = \chi_3\big(\bar{T}(\pm 1, \tau) - \bar{T}(\bar{y}, \tau)\big) + \sum_{i=1}^\infty c_i^T(\tau)\eta_i \sin(\eta_i \bar{y}),
$$

$$
\bar{\sigma}_{xx}^M(\bar{y}, \tau) = \bar{\sigma}_{zz}^M(\bar{y}, \tau) = \frac{\nu}{1-\nu} \sum_{i=1}^\infty c_i^M(\tau)\eta_i \sin(\eta_i \bar{y}),
\tag{69}
$$

$$
\bar{\sigma}_{yy}^M(\bar{y}, \tau) = \sum_{i=1}^\infty c_i^M(\tau)\eta_i \sin(\eta_i \bar{y}),
$$

where $(\bar{\sigma}_{xx}^T, \bar{\sigma}_{yy}^T, \bar{\sigma}_{zz}^T)$ and $(\bar{\sigma}_{xx}^M, \bar{\sigma}_{yy}^M, \bar{\sigma}_{zz}^M)$ are the thermal and magnetic stress components, satisfying

$$
\bar{\sigma}_{xx} = \bar{\sigma}_{xx}^T + \bar{\sigma}_{xx}^M, \quad \bar{\sigma}_{yy} = \bar{\sigma}_{yy}^T + \bar{\sigma}_{yy}^M, \quad \bar{\sigma}_{zz} = \bar{\sigma}_{zz}^T + \bar{\sigma}_{zz}^M.
\tag{70}
$$

3.3.2. *Quasistatic solutions.* We now derive the quasistatic solutions of the displacements and stresses. Neglect of the inertia term on the right-hand side of (25) gives the equilibrium equation

$$\frac{d^2\bar{v}}{d\bar{y}^2} = \chi_3 \frac{d\bar{T}}{d\bar{y}} + \frac{d}{d\bar{y}}(\bar{H}_z)^2 \tag{71}$$

Solving (71) with the boundary condition in (26), we obtain the quasistatic solutions of the displacements due to temperature change and due to Lorentz force:

$$\bar{v}^T(\bar{y}, \tau) = \chi_3 \int \bar{T}(\bar{y}, \tau)\, d\bar{y}, \qquad \bar{v}^M(\bar{y}, \tau) = \int \bar{H}_z(\bar{y}, \tau)^2\, d\bar{y} - \phi(\tau)^2. \tag{72}$$

Substituting (72) with the relation of (67) into (24), we obtain the quasistatic solutions of the stress components as follows:

$$\bar{\sigma}_{xx}^T(\bar{y}, \tau) = \bar{\sigma}_{zz}^T(\bar{y}, \tau) = -\frac{1-2\nu}{1-\nu}\chi_3\bar{T}(\bar{y}, \tau), \qquad \bar{\sigma}_{yy}^T(\bar{y}, \tau) = 0, \tag{73}$$

$$\bar{\sigma}_{xx}^M(\bar{y}, \tau) = \bar{\sigma}_{zz}^M(\bar{y}, \tau) = \frac{\nu}{1-\nu}(\bar{H}_z(\bar{y}, \tau)^2 - \phi(\tau)^2), \qquad \bar{\sigma}_{yy}^M(\bar{y}, \tau) = (\bar{H}_z(\bar{y}, \tau))^2 - (\phi(\tau))^2, \tag{74}$$

These quasistatic thermal stresses and magnetic stresses satisfy the relations in (70).

4. Numerical results and discussion

So far we have assume the excitation $\phi(\tau)$ to be arbitrary. Now we specialize to the case of a smoothed ramp function with a sine-function profile:

$$\phi(\tau) = \begin{cases} \sin\left(\frac{\pi}{2\tau_0}\tau\right) & (\tau < \tau_0), \\ 1 & (\tau \geq \tau_0), \end{cases} \tag{75}$$

where τ_0 is the (nondimensional) rise time. The particular expressions for the various functions of τ in (37), (49) and (65) — $\hat{a}_n(\tau)$, $\hat{b}_n^{(0)}(\tau)$, $\hat{b}_{jmn}(\tau)$, $\hat{c}_{in}^{T(0)}(\tau)$, $\hat{c}_{ijmn}^T(\tau)$, $\hat{c}_{ii}^{M(1)}(\tau)$, and $\hat{c}_{imn}^{M(2)}(\tau)$ — will not be spelled out because they can be easily derived.

We carried out numerical calculations corresponding to the analytical results above in the case of aluminum, whose material properties are

$$\mu = 4\pi \times 10^{-7}\,[\text{H/m}], \quad \sigma = 3.42 \times 10^7\,[\text{S/m}], \quad C = 2.7 \times 10^3\,[\text{J/kgK}], \quad \rho = 0.9 \times 10^3\,[\text{kg/m}^3],$$

$$\kappa = 92.6 \times 10^{-6}\,[\text{m}^2/\text{sec}], \quad \nu = 0.33, \quad E = 70\,[\text{GPa}], \quad \alpha = 24 \times 10^{-6}\,[1/\text{K}].$$

In addition, since the nondimensional variable χ_2 in (16) includes the half-thickness b, this dimension needs to be fixed. We chose $b = 1.0 \times 10^{-4}\,[\text{m}]$ to ensure the convergence of the solutions. The rise time τ_0 is given by

$$\tau_0 = \varepsilon\frac{1}{\chi_2},$$

where ε is a dimensionless parameter and $1/\chi_2$ is the nondimensional time needed by the stress waves created at the surfaces to arrive at the middle of the infinite plate.
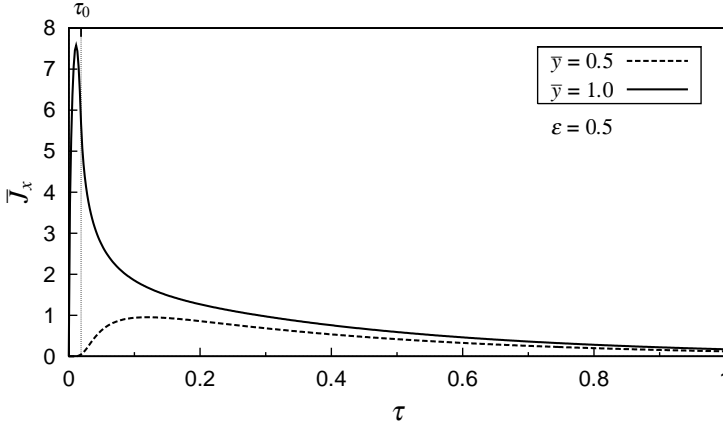
Figure 2. Time evolution of the eddy current $\bar{J}_x$, for $\varepsilon = 0.5$.

We first present the numerical results for $\varepsilon = 0.5$. Figure 2 shows the time evolution of eddy current $\bar{J}_x$. It shows a peak ahead of $\tau = \tau_0$ at the surface ($\bar{y} = 1.0$), then it decays slowly with time. Figure 3 shows the time evolution of the temperature change $\bar{T}$ for $\bar{h} = 0.0$ and 1.0 until they attain steady state. It can be seen from that figure that temperature changes take a long time to attain a steady state, in comparison with the eddy current $\bar{J}_x$. This is because the value of χ_1 in (16), which is the ratio of the diffusion coefficient of temperature field κ to that of magnetic field $(\mu\sigma)^{-1}$, is very small: $\chi_1 = \kappa\mu\sigma \cong 3.98 \times 10^{-3}$ for aluminum. In the case of $\bar{h} = 1.0$, the temperature change converges to zero, whereas in the case of $\bar{h} = 0.0$ (insulated plate), it converges to a value that can be determined from (45):

$$\bar{T} = \frac{1}{2} \int_{-1}^{1} \left(\int_0^{\infty} \bar{w}(\bar{y}, \tau')\, d\tau' \right) d\bar{y}. \tag{76}$$

However, as shown in Figure 4 (short-term time evolution of temperature), there is not a large difference between the insulated and noninsulated cases: the temperature changes always propagate from the surface more slowly than the eddy current. Therefore numerical results on the thermal stresses are shown only for the case of $\bar{h} = 0.0$. Figure 5 shows the dynamic and quasistatic behaviors of the
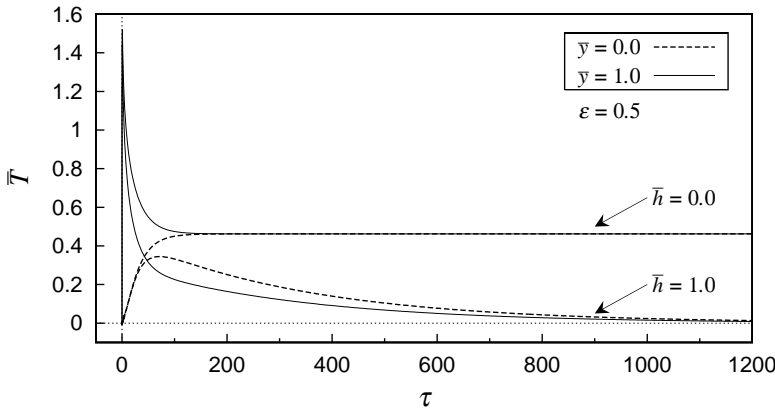
Figure 3. Time evolution of temperature changes $\bar{T}$, for $\bar{h} = 0.0$ and 1.0, $\varepsilon = 0.5$.
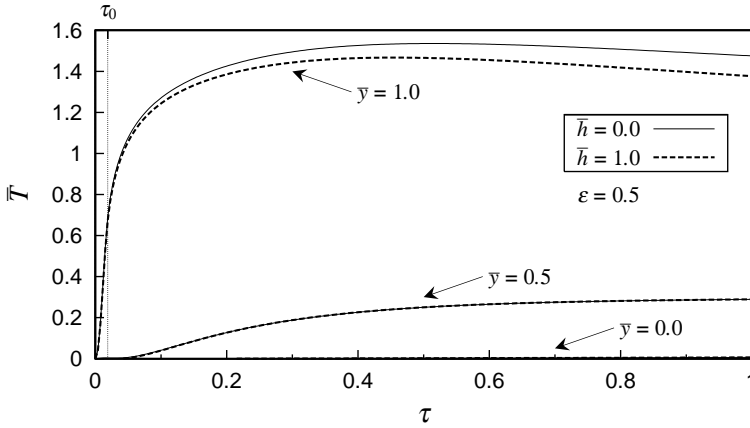
Figure 4. Short-term evolution of temperature change $\bar{T}$, for $\bar{h} = 0.0$ and 1.0, $\varepsilon = 0.5$.

thermal stress $\bar{\sigma}_{xx}^{T}(=\bar{\sigma}_{zz}^{T})$ at the middle ($\bar{y} = 0.0$) and the surface ($\bar{y} = 1.0$) of the infinite plate versus nondimensional time τ. Note that the dynamic solution of $\bar{\sigma}_{xx}^{T}$ corresponds to the quasistatic one at the surface (see (68) and (73)), and that the quasistatic solution is proportional to temperature change $\bar{T}$ with the negative constant $-(1-2\nu)\chi_3/(1-\nu) \cong -2.06$ for aluminum. Therefore, the thermal stress $\bar{\sigma}_{xx}^{T}$ is compressive at the surface. However, the dynamic stress at the middle shows different behavior from the quasistatic one as shown in Figure 5. The dynamic behavior of the thermal stress $\bar{\sigma}_{yy}^{T}$ is shown in Figure 6. Consequently, the quasistatic one is identically zero as shown by the second relation in (73). In Figure 6, a new nondimensional time τ_E is introduced for convenience. The nondimensional time τ_E is based on the longitudinal wave velocity C_L, defined as

$$\tau_E = \frac{\tau}{\chi_2} = \frac{C_L}{b}t.$$
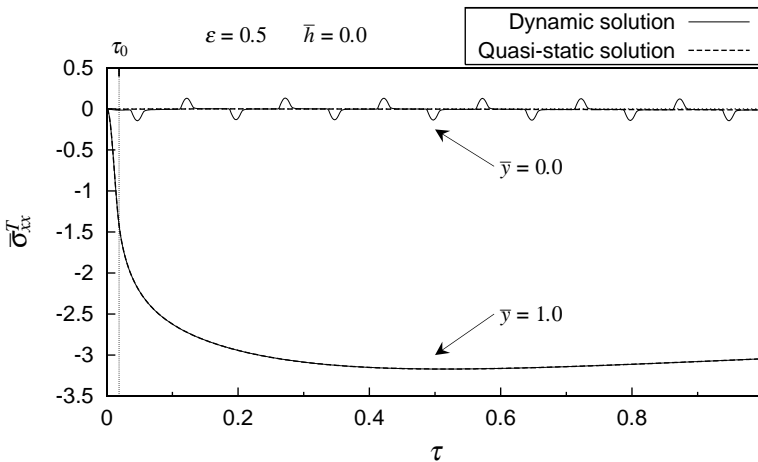
Figure 5. Dynamic and quasistatic behaviors of the thermal stress $\bar{\sigma}_{xx}^{T}$ versus nondimensional time τ, for $\bar{h} = 0.0$, $\varepsilon = 0.5$.

$$\tau_E = C_L t / b$$
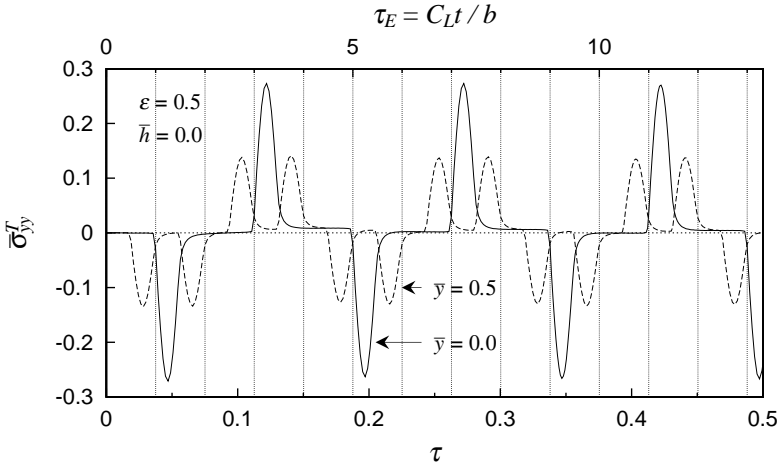
Figure 6. Dynamic behavior of the thermal stress $\bar{\sigma}_{yy}^T$ versus nondimensional time τ and τ_E, for $\bar{h} = 0.0$, $\varepsilon = 0.5$.

We see from Figure 6 that a pulsed stress wave is induced by the rapid surface temperature rise in Figure 4. As shown in Figure 7, the stress waves created on both surfaces propagate to the middle, and then interfere with each other at the middle. Therefore, the absolute value of the stress at the middle becomes about twice of those in distant positions from the middle as shown in Figures 6 and 7.

Figure 8 shows the dynamic and quasistatic behaviors of the magnetic stress $\bar{\sigma}_{yy}^M$ at the middle versus nondimensional time τ. The magnetic stress components $\bar{\sigma}_{xx}^M$ and $\bar{\sigma}_{zz}^M$ are omitted here because those components are proportional to the component $\bar{\sigma}_{yy}^M$ with $\nu/(1 - \nu) \cong 0.49$ as shown by (69) and (74). Although the maximum absolute value of the quasistatic stress $\bar{\sigma}_{yy}^M$ is less than 1, as shown by the second relation in (74), the absolute value of the dynamic stress can exceed 1, as shown in Figure 8. The variation in the y direction of the dynamic magnetic stress $\bar{\sigma}_{yy}^M$ is shown in Figure 9.

The stress waves, whose maximum absolute value is 1, created at both surfaces due to the Lorentz force propagate into the middle, and then get superimposed. Therefore, the maximum absolute value of the dynamic stress becomes 2 except near the surfaces, as shown in Figure 9. Comparing the magnetic
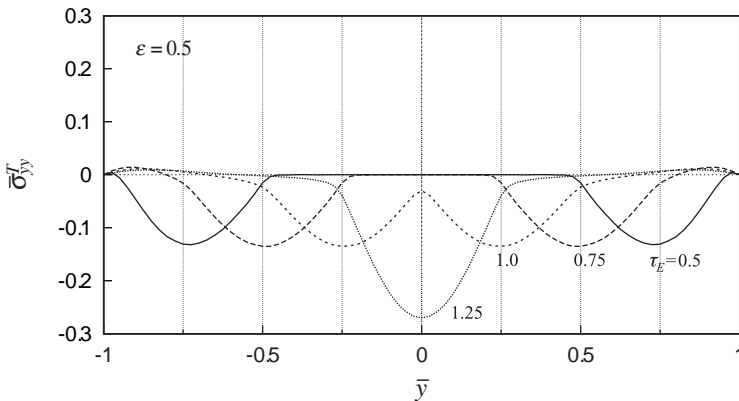
Figure 7. Variation in the y direction of the dynamic thermal stress $\bar{\sigma}_{yy}^T$.
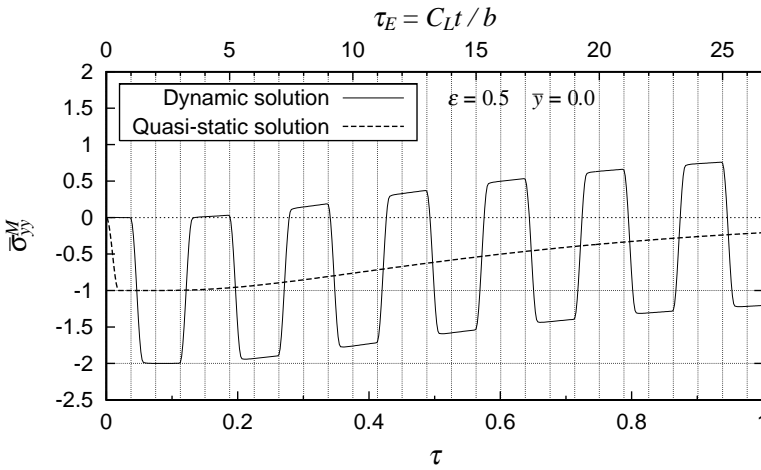
Figure 8. Dynamic and quasistatic behavior of the magnetic stress $\bar{\sigma}_{yy}^M$ versus nondimensional time τ and τ_E, for $\varepsilon = 0.5$.
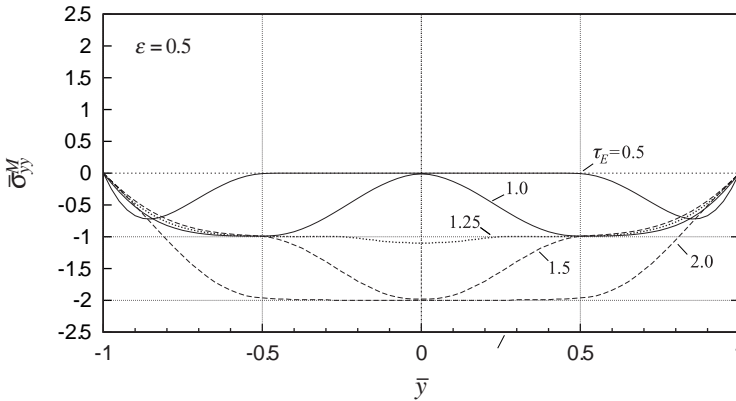
Figure 9. Variation in the y direction of the dynamic magnetic stress $\bar{\sigma}_{yy}^M$.

stress $\bar{\sigma}_{yy}^M$ in Figure 8 with the thermal stress $\bar{\sigma}_{yy}^T$ in Figure 6, we see that the former is the dominant stress component in the y direction.

Numerical results for $\varepsilon = 10.0$ — eddy current, thermal stress and magnetic stress — are presented in Figures 10–12. It can be seen from Figure 10 that the eddy current $\bar{J}_x$ is small and varies slowly in comparison with the case $\varepsilon = 0.5$. Therefore, the maximum absolute values of both the thermal stress $\bar{\sigma}_{xx}^T$ and the magnetic stress $\bar{\sigma}_{yy}^M$ are smaller and there is almost no difference in behavior between the dynamic and quasistatic solutions.

References

[Banerjee and Roychoudhuri 1997] S. Banerjee and S. K. Roychoudhuri, "Magneto-thermo-elastic interactions in an infinite isotropic elastic cylinder subjected to a periodic loading", *Int. J. Eng. Sci.* **35**:4 (1997), 437–444.

[Boley and Tolins 1962] B. A. Boley and I. S. Tolins, "Transient coupled thermoelastic boundary value problems in the half-space", *Trans. ASME Ser. E. J. Appl. Mech.* **29** (1962), 637–646. MR 26 #4570
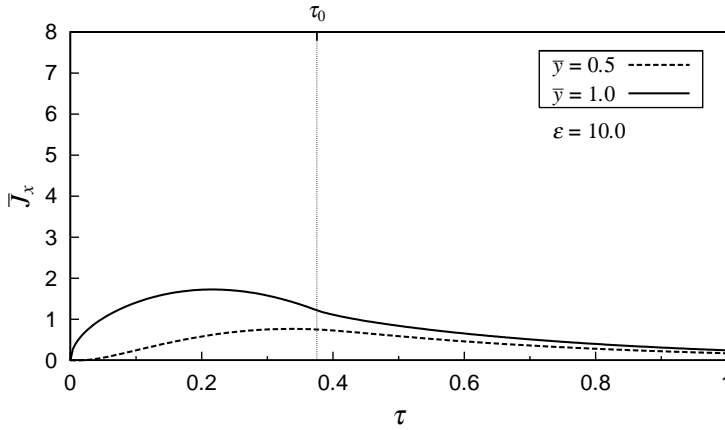
Figure 10. Time evolution of the eddy current $\bar{J}_x$ for $\varepsilon = 10.0$.
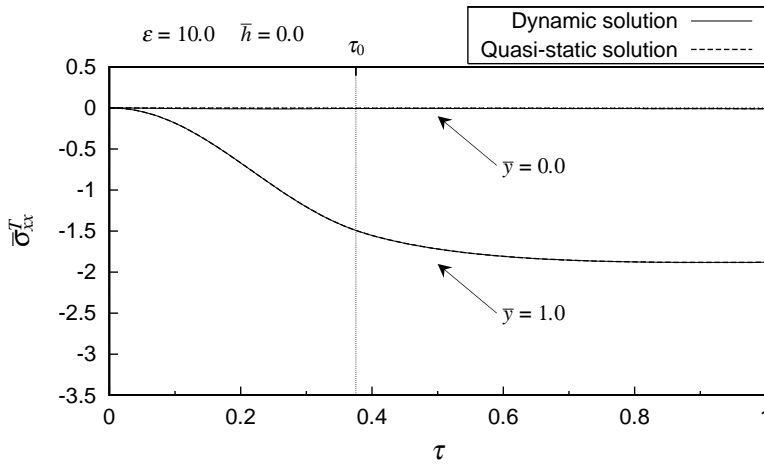
Figure 11. Dynamic and quasistatic behavior of the thermal stress $\bar{\sigma}_{xx}^T$ for $\varepsilon = 10.0$, $\bar{h} = 0.0$.
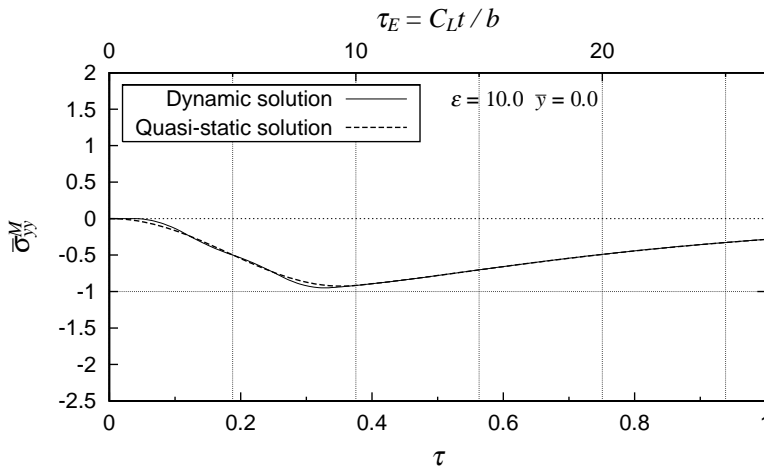
Figure 12. Dynamic and quasistatic behavior of the magnetic stress $\bar{\sigma}_{yy}^M$ for $\varepsilon = 10.0$.

[Chian and Moon 1981] C. T. Chian and F. C. Moon, "Magnetically induced cylindrical stress waves in a thermoelastic conductor", *Int. J. Solids Struct.* **17**:11 (1981), 1021–1035.

[Ezzat and Youssef 2005] M. A. Ezzat and H. M. Youssef, "Generalized magneto-thermoelasticity in a perfectly conducting medium", *Int. J. Solids Struct.* **42** (2005), 6319–6334.

[Kaliski and Michalec 1963] S. Kaliski and J. Michalec, "The resonance amplification of a magnetoelastic wave radiated from a cylindrical cavity", *Proc. Vibr. Prob.* **4**:1 (1963), 7–15.

[Kaliski and Nowacki 1962] S. Kaliski and W. Nowacki, "Combined elastic and electromagnetic waves produced by thermal shock in the case of a medium of finite electric conductivity", *Bull. Acad. Polon. Sci. Sér. Sci. Tech.* **10** (1962), 213–223.

[Librescu et al. 2003] L. Librescu, D. Hansanyan, Z. Qin, and D. R. Ambur, "Nonlinear magnetothermoelasticity of anisotropic plates immersed in a magnetic field", *J. Therm. Stresses* **26** (2003), 1277–1304.

[Moon and Chattopadhyay 1974] F. C. Moon and S. Chattopadhyay, "Magnetically induced stress waves in a conducting solid: Theory and experiment", *J. Appl. Mech.* (*ASME*) **41** (1974), 641–647.

[Pantelyat and Féliachi 2002] M. G. Pantelyat and M. Féliachi, "Magneto-thermo-elastic-plastic simulation of inductive heating of metals", *Eur. Phys. J. Appl. Phys.* **17** (2002), 29–33.

[Paria 1967] G. Paria, "Magneto-elasticity and magneto-thermo-elasticity", *Adv. Appl. Mech.* **10** (1967), 73–112.

[Sternberg and Chakravorty 1959] E. Sternberg and J. G. Chakravorty, "On inertia effects in a transient thermoelastic problem", *J. Appl. Mech.* **26** (1959), 503–509. MR 22 #8877

[Stoll 1974] R. L. Stoll, *The analysis of eddy currents*, Clarendon Press, Oxford, 1974.

[Wang et al. 2002] X. Wang, Y.-H. Zhou, and X. Zheng, "A generalized variational model of magneto-thermo-elasticity for nonlinearly magnetized ferroelastic bodies", *Internat. J. Engrg. Sci.* **40**:17 (2002), 1957–1973. MR 2003i:74015

[Wang et al. 2003] X. Wang, J. S. Lee, and X. Zheng, "Magneto-thermo-elastic instability of ferromagnetic plates in thermal and magnetic fields", *Int. J. Solids Struct.* **40** (2003), 6125–6142.

[Wauer 1995] J. Wauer, "Parametric vibrations in a magneto-thermo-elastic layer of finite thickness", pp. 407–414 in *Proceedings of the 1995 Design Engineering Technical Conferences*, vol. 3A, *Vibration of nonlinear, random, and time-varying systems*, edited by S. C. Sinha, Design Engineering Division **84-1**, ASME, New York, 1995.

[Wauer 1996] J. Wauer, "Free and forced magneto-thermo-elastic vibrations in a conducting plate layer", *J. Therm. Stresses* **19** (1996), 671–691.

[Zheng et al. 2005] X. Zheng, J. Zhang, and Y. Zhou, "Dynamic stability of a cantilever conductive plate in transverse impulsive magnetic field", *Int. J. Solids Struct.* **42** (2005), 2417–2430.

MASAHIRO HIGUCHI: higuchi@applied.me.osakafu-u.ac.jp
Department of Mechanical Systems Engineering, Osaka Prefecture University, Gakuencho 1-1, Nakaku, Sakai, Osaka 599-8531, Japan

RYUUSUKE KAWAMURA: kawamura@me.osakafu-u.ac.jp
Department of Mechanical Systems Engineering, Osaka Prefecture University, Gakuencho 1-1, Nakaku, Sakai, Osaka 599-8531, Japan

YOSHINOBU TANIGAWA: tanigawa@me.osakafu-u.ac.jp
Department of Mechanical Systems Engineering, Osaka Prefecture University, Gakuencho 1-1, Nakaku, Sakai, Osaka 599-8531, Japan

HIDEKI FUJIEDA: *Ebara Corporation, 11-1, Haneda Asahi-cho, Ohta-ku, Tokyo 144-8510, Japan*

EXPERIMENTAL EVALUATION OF TWO MULTIPHASE CONSTITUTIVE MODELS APPLICABLE TO METAL MATRIX COMPOSITES UNDER NONPROPORTIONAL VARIABLE AMPLITUDE LOADING

GBADEBO MOSES OWOLABI AND MEERA NAND KAUR SINGH

In a previous research investigation, using the Mróz model and the endochronic theory of plasticity as their bases, two sets of elastic-plastic constitutive relations were identified that account for the interaction in stress fields between adjacent particles in particulate metal matrix composites (PMMCs). In this paper the ability of the two models to predict the behavior of PMMCs under variable amplitude nonproportional cyclic loading paths is evaluated by comparing the models predictions with experimental results obtained from a series of biaxial (tension-torsion) cyclic tests performed on tubular specimens made from 6061-T6 aluminum with 10 and 20% volume fractions of alumina particles. For most of the investigated loading paths, both models predict satisfactorily the amplitudes of the experimental strains. However, the endochronic theory-based constitutive model generally gives better predictions of the measured strains.

Notation

m	matrix	i, j, k, l, r, s	indices = 1,2,3 (summation convention)
f	reinforcement	S_{ij}	components of deviatoric stress tensor
C_f	reinforcement stiffness tensor	S_{ijkl}	components of Eshelby's tensor
C_m	matrix stiffness tensor	V_f	reinforcement volume fraction
F	yield function	V_m	matrix volume fraction
I_{ijkl}	identity tensor	C_r	material constants
δ	Kronecker delta	α_{ij}^{ℓ}	components of back stress tensor of surface ℓ
Δ	increment of a variable	ξ_{ij}	deviatoric components of α_{ij}
ε_{ij}	components of strain tensor	$\mathrm{d}(\cdot)$	differential form of variable or constant
$\mathrm{d}\mu$	magnitude of translation	$(\cdot)^e$	elastic components of a variable
$\rho()$	hereditary (memory) function	$(\cdot)_{(f)}$	reinforcement component
σ_{ij}	components of stress tensor	$(\cdot)\ell$	component with reference to surface ℓ
σ_o^{ℓ}	yield stress of surface ℓ	$(\cdot)_{(m)}$	matrix components of a variable or constant
$\mathrm{d}\mu$	magnitude of translation	$(\cdot)^p$	plastic components of a variable
K_p	hardening modulus	$(\cdot)_q$	q-th step component of a variable
z	intrinsic time scale	$(\cdot)^T$	total components of a variable

1. Introduction

Due to their material properties, particulate metal matrix composites (PMMCs) are increasingly finding applications in aerospace, automotive, and related industries. However, due to the complexity of the geometry of the reinforcements and the nonlinear (inelastic) behavior of the matrix, the behavior of PMMCs particularly when subjected to complex service loading conditions is still not fully understood [Ji and Wang 2003; Lease et al. 1996; Ju and Chen 1994]. Thus, with increasing interest in the application of these materials in both structural and nonstructural applications, the need to understand, model, and predict the mechanical response and fatigue life of the materials to applied service loads also increases.

Most research studies that have described the constitutive behavior of PMMCs assume that the composites remain elastic as the loads are applied. Goodier [1933] worked on modeling a spherical and a cylindrical inclusion in a matrix, providing the first detailed analysis of the elastic stress-strain response of composite materials. Subsequently, Sadowsky and Sterberg [1952] derived relations defining the elastic stress-field around an ellipsoidal cavity under plane stress conditions. The general problem of elastic field inside and at the interface of an ellipsoidal inclusion was solved by Eshelby [1957]. His theory of equivalent inclusions is perhaps the most widely accepted elastic constitutive model applicable to composite materials. However, Eshelby's method is only applicable to composites with very small volume fraction of the reinforcement — at most 5%. For higher volume fractions of reinforcements, the method has to be modified to account for the interaction in the stress field between the reinforcements.

The concept of average stress and strain in the composite and its constituents has been used extensively in the past to account for the interactions in the stress field between the particles. The self-consistent theory [Hershey 1954; Kröner 1961] and the mean-field theory of Mori and Tanaka [1973], both based on the concept of average stress and strain, are the commonly used models. The self-consistent theory was originally developed to model the average constitutive behavior of polycrystals; it has been used to estimate the macroscopic elastic moduli of two-phase composites and also the average internal nonuniformity of strain and stresses in the matrix and particles of a composite system. Hutchison [1970] used this theory to estimate the elastic-plastic incremental relations of polycrystals and composites. Although straightforward, the method does not provide acceptable results when the matrix contains either voids or perfectly rigid inclusions [Mori and Wakashima 1990]. Consequently, Mori–Tanaka mean-field theory has been more widely used. The original approach of [Mori and Tanaka 1973] has been used mainly to evaluate the elastic behavior of composite materials. The emphasis on elasticity shows its importance in applications, and provides the means for developing practical design methods. It is, however, unrealistic to assume that all components being modeled behave linearly.

Tandon and Weng [1988] considered the elastic-plastic stress-strain behavior of spherical particle reinforced composites under multiaxial loading using the secant moduli of the ductile, work-hardening matrix. Specifically, they analyzed the elastic-plastic behavior of the composites by applying the concept of secant properties to the elastic mean field theory. In the Tandon–Weng model, the secant modulus of the matrix in the plastic range changes with an increase in plastic deformation. Since the change is not known beforehand, at each state of stress or strain an initial value has to be assumed for the matrix effective plastic strain. The model has received attention from the research community, but it is only applicable if the loads are applied in a proportional manner and not if there is load reversal.

In an attempt to study the elastic-plastic deformation of multiphase composite materials under nonproportional loading, Li and Chen [1990] reformulated the mean field theory in an incremental form. Their method is meant to be applied to multiphase materials in which the components exhibit different elastic-plastic material behavior under nonproportional or reverse loading. Theoretically, the model could be used to study the elastic-plastic deformation of composite materials under nonproportional monotonic and cyclic loadings; however, Li and Chen only implemented and validated the model for uniaxial monotonic loading. That is, in [Li and Chen 1990], the model was not validated for the case of multiaxial cyclic loading. Generally, their model can be used in conjunction with any cyclic plasticity model developed for homogeneous materials to predict the matrix plastic strain components.

Inelastic constitutive models for homogeneous metals subjected to cyclic loads (cyclic plasticity models) are still evolving. Chaboche [1986] describes two classes of such models. Those in the first class are based on thermodynamic concepts and assume that the present state of the material depends on the present values of observable variables and a set of internal variables. Included in this category are the Ziegler model [1959], the Mróz model [1967], the two-surface plasticity model [Dafalias and Popov 1975; Krieg 1975], and the Armstrong and Frederick model [1966], modified by Chaboche et al. [1979]. The second class of plasticity models is based on the assumption that the present state of material depends on the present values and the past history of observable variables only (total strains, temperature etc.), giving rise to hereditary theories. The endochronic theory of plasticity [Valanis 1971; 1980] is based on this concept. Several of these models and their various modifications have been used to predict the elastic-plastic, creep and ratcheting behaviors of homogeneous materials and are well documented in the literature, including recent work such as [Kang et al. 2003; Chiou and Yip 2003; Tong et al. 2004; Vincent et al. 2004; Chen et al. 2005; Hashiguchi et al. 2005].

Only a few cyclic plasticity models have been incorporated into a formulation targeted at describing the constitutive behavior of metal matrix composites under multiaxial loading conditions. Ogarevic [1992] formulated a composite constitutive model based on Li and Chen's incremental mean field theory, the incremental theory of plasticity, and a linear kinematic hardening rule to study the uniaxial cyclic deformation of discontinuously reinforced metal matrix composites (MMCs) both at room and elevated temperatures. The model was demonstrated only analytically for externally applied uniaxial cyclic loading. A major relevant model that addresses cyclic biaxial proportional external loading was developed in [Lease 1994; Lease et al. 1995], where the Li and Chen model was used together with Chaboche's incremental plasticity theory to simulate the constitutive behavior of the composite system. The model was demonstrated both analytically and experimentally for cyclic axial and biaxial proportional loading. Although the axial and torsional elastic-plastic strain and stress seemed to accurately simulate the monotonic tests, the elastic loading/unloading portions of the cyclic uniaxial and biaxial tests show obvious differences that increase with increasing strain range [Lease 1994]. Fleming and Temis [2002] used cyclic strain plasticity relationships based on the classical strain plasticity theory hypotheses in [Johnson and Mellor 1975] to predict cyclic stress-strain response of the matrix material. The constitutive equations lead to a nonlinear finite element problem that was solved using a special iterative procedure at every half-cycle of the loading or unloading. However, the model has only been demonstrated for monotonic and uniaxial cyclic loading conditions.

In [Owolabi and Singh 2003], two constitutive models capable of predicting the elastic-plastic strain-stress response of the matrix, reinforcement, and the PMMC under multiaxial cyclic loading conditions

were developed. Specifically, the elastic components of the matrix and reinforcement strains and stresses were obtained from the applied incremental stresses or strains by implementing known relations specific to composites. The matrix plastic strain components were obtained using two alternative cyclic plasticity routines. Specifically, the Mróz multisurface model [1967] and the endochronic theory of plasticity [Valanis 1971; 1980], originally developed for homogeneous materials, were used to model the matrix cyclic plasticity. The elastic and plastic (matrix only) strains were superimposed to obtain the constituents constitutive relations. These models are capable of predicting the constitutive behavior of PMMCs under a variety of loading conditions and are dependent on the properties of the matrix and the properties, volume fraction and geometry of the reinforcing particles. The constitutive models account for the interactions in stress fields between adjacent particles in PMMCs. In [Owolabi and Singh 2003] we compared the models predictions to limited experimental results given in [Lease 1994] for PMMCs under biaxial cyclic strain-controlled (proportional loading) tests with various strain amplitudes. However in our 2003 paper only preliminary comments could be made regarding the model's suitability in defining the constitutive behavior of composites, based on a comparison with the limited experimental results in [Lease 1994]. That is, more testing was required to make more meaningful conclusions, particularly when the material is subjected to more complex loadings. Investigations of the ability of the cyclic constitutive models to predict the elastic-plastic response of PMMCs under more complex loading conditions such as variable amplitude nonproportional cyclic loading is critical in engineering design.

To date, no cyclic plasticity model applicable to PMMCs has been validated experimentally for cyclic nonproportional variable amplitude external loading. In addition, experimental data that can be used to validate existing and newly developed models for PMMCs subjected to variable amplitude loads are very rare in the open literature. Thus, this paper is designed primarily to provide a complete formulation of the two models that completely define the constitutive response of the matrix, reinforcement, and PMMCs; and validate the ability of the models to predict the elastic-plastic behavior of PMMCs under complex external loading. The theoretical and experimental results of the constitutive response of PMMCs to such complex loading paths are reported. Note that the experimental results presented here were all conducted under load-controlled tests. In addition to the variable amplitude loads, one load-controlled biaxial proportional path was also included.

Section 2 presents a summary of the constitutive models. The experimental procedure and load paths used are presented in Section 3. In Section 4, the model's predictions are compared with experimental results. Conclusions are given in Section 5.

2. Constitutive models

The details of the elastic-plastic constitutive model appear in [Owolabi and Singh 2003], so only a summary is given here. For PMMCs, we assume that the matrix, consisting of a homogeneous metallic material, is initially isotropic and strain hardens at the onset of plastic deformation. Since it is additionally assumed to be cyclically stable, transient effects are not considered. The reinforcement, consisting of ceramic particles, behaves elastically throughout the loading paths and has higher stiffness relative to the matrix.

For small deformations, the total incremental matrix strain tensor $d\varepsilon_{ij(m)}^{T}$ can be decomposed into elastic and plastic components, denoted by superscript e and p:

$$d\varepsilon_{ij(m)}^{T} = d\varepsilon_{ij(m)}^{e} + d\varepsilon_{ij(m)}^{p}. \tag{1}$$

The reinforcement strain, $d\varepsilon_{ij(f)}^{T}$, only has an elastic component, since the reinforcement (ceramic particles) deforms elastically:

$$d\varepsilon_{ij(f)}^{T} = d\varepsilon_{ij(f)}^{e}. \tag{2}$$

The approach used to determine the incremental elastic stress and strain components in the matrix, reinforcement, and composite was presented in [Owolabi and Singh 2003] on the same basis as Li and Chen's [1990] incremental formulations of mean field theory. This approach is suitable for PMMCs with high volume fractions of reinforcement, since it accounts for interactions in the stress fields between reinforcing particles; it is summarized in Section 2.1. Once the matrix stress exceeds the material yield stress, a suitable cyclic plasticity model must be used to obtain the matrix strains. Two such cyclic plasticity models are presented in Section 2.2.

2.1. *Elastic model.* In [Owolabi and Singh 2003; Lease 1994; Lease et al. 1995] it was shown that the average incremental stress tensors in the matrix and the reinforcements, due to externally applied load tensor, can be obtained using the incremental form of Mori and Tanaka's mean field theory [1973]. A summary of this approach is presented here. Consider an elastic component subjected to an increment in external load or displacement tensor. In the absence of reinforcement, the external load would give rise to an increase in the uniform stress field, $\Delta\sigma_{ij}$, which can be related to the increment in the strain field, $\Delta\varepsilon_{ij}$. The average incremental stress in the matrix, $\Delta\sigma_{ij(m)}$, differs from the applied incremental stress by a perturbed incremental stress, $\Delta\tilde{\sigma}_{ij(m)}$:

$$\Delta\sigma_{ij(m)} = \Delta\sigma_{ij} + \Delta\tilde{\sigma}_{ij(m)} = C_{ijkl(m)}(\Delta\varepsilon_{kl} + \Delta\tilde{\varepsilon}_{kl(m)}), \tag{3}$$

where $C_{ijkl(m)}$ is the matrix stiffness tensor and $\Delta\tilde{\varepsilon}_{ij(m)}$ is the matrix incremental strain disturbance that results from the presence of the particles. The reinforcement average incremental stress, $\Delta\sigma_{ij(f)}$, and strain, $\Delta\varepsilon_{ij(f)}$ are also different from those of the matrix. The average incremental stress in the reinforcement is

$$\Delta\sigma_{ij(f)} = C_{ijkl(m)}(\Delta\varepsilon_{kl} + \Delta\tilde{\varepsilon}_{kl(m)} + \Delta\varepsilon_{kl}^{c} - \Delta\varepsilon_{kl}^{t}), \tag{4}$$

where $\Delta\varepsilon_{kl}^{c}$ is a constrained strain set up at all points in the matrix and the reinforcement, and $\Delta\varepsilon_{kl}^{t}$ is a transformation strain having a finite value within the reinforcements and zero outside them. Although the solution for the constrained strain field in the matrix is quite complex, an approximate relation between the constrained strain, the stress free transformation strain, and the 6×6 Eshelby tensor S is given by

$$\Delta\varepsilon_{ij}^{c} = S_{ijkl}\Delta\varepsilon_{kl}^{t}. \tag{5}$$

The incremental strain disturbance in the matrix can be found using Equations (3)–(5) and the rule of mixture as

$$\Delta\tilde{\varepsilon}_{ij(m)} = (1 - V_m)(\boldsymbol{I}_{ijkl} - \boldsymbol{S}_{ijkl})(\Delta\varepsilon_{kl}^{t}), \tag{6}$$

where V_m is the matrix volume fraction. and $\boldsymbol{I}$ is the identity tensor.

The incremental transformation strain, $\Delta\varepsilon_{ij}^t$, is found in [Owolabi and Singh 2003] to be

$$\Delta\varepsilon_{ij}^t = L_{ijkl}^{-1}(C_{klrs(f)} - C_{klrs(m)})(C_{klrs(m)}^{-1}\Delta\sigma_{kl}), \tag{7}$$

where

$$L_{ijkl} = (V_f - 1)C_{klrs(m)}(\boldsymbol{I}_{ijrs} - \boldsymbol{S}_{ijrs}) + C_{klrs(f)}\big(V_f(\boldsymbol{S}_{ijrs} - \boldsymbol{I}_{ijrs}) - \boldsymbol{S}_{ijrs}\big). \tag{8}$$

Substituting (7) into (6), and using the result in (3), we get the average incremental stress in the matrix:

$$\Delta\sigma_{ij(m)} = \big(\boldsymbol{I}_{ijkl} - V_f C_{ijrs(m)}(\boldsymbol{S}_{klrs} - \boldsymbol{I}_{klrs})L_{ijrs}^{-1}(C_{ijkl(f)} - C_{ijkl(m)})C_{klrs(m)}^{-1}\big)\Delta\sigma_{kl}, \tag{9}$$

where V_f is the volume fraction of reinforcement.

The incremental matrix elastic strain, $\Delta\varepsilon_{ij(m)}^e$, can be obtained from the incremental stress using the generalized Hooke's law:

$$\Delta\varepsilon_{ij(m)}^e = C_{ijkl(m)}^{-1}\Delta\sigma_{kl(m)}. \tag{10}$$

The mean incremental stress tensor in the reinforcement, $\Delta\sigma_{ij(f)}$, is obtained from (4), (5) and (7):

$$\Delta\sigma_{ij(f)} = \big(\boldsymbol{I}_{ijkl} + V_m C_{ijrs(m)}(\boldsymbol{S}_{klst} - \boldsymbol{I}_{klrs})L_{ijrs}^{-1}(C_{ijkl(f)} - C_{ijkl(m)})C_{klrs(m)}^{-1}\big)\Delta\sigma_{kl}. \tag{11}$$

The incremental elastic strain in the reinforcement can be obtained from the incremental stress using the generalized Hooke's law:

$$\Delta\varepsilon_{ij(f)}^e = C_{ijkl(f)}^{-1}\Delta\sigma_{kl(f)}. \tag{12}$$

The increment in average strains in the composite can be estimated using an approximate technique proposed by [Li and Chen 1990] for a multiphase system. The technique assumes that the work done by the average stress of the composite is equal to the weighted sum of the work done by the local stresses of the inclusions and the matrix. Under this assumption, the following expression is obtained for a two-phase composite material:

$$\Delta\sigma_{ik}\Delta\varepsilon_{kj} = V_m\Delta\sigma_{ik(m)}\Delta\varepsilon_{kj(m)} + V_f\Delta\sigma_{ik(f)}\Delta\varepsilon_{kj(f)}, \tag{13}$$

from which $\Delta\varepsilon_{ij}$ can be obtained in terms of other stress and strain increments. A similar expression of this work-based rule of mixture has been used in [Lease 1994; Lease et al. 1995] and is valid both in the elastic and the elastic-plastic regions.

2.2. *Cyclic plasticity models.* In [Owolabi and Singh 2003] we identified two sets of elastic-plastic constitutive relations as applicable to PMMCs. These are the based respectively on the Mróz model (Section 2.2.1) and the endochronic theory of plasticity (Section 2.2.2), and are used below to describe the increments in the matrix plastic strain given in (1).

2.2.1. *The Mróz model.* For a plastically deforming material, Mróz [1967] describes a field of ℓ initially concentric work hardening surfaces and prescribing a translation rule for the surfaces moving with respect to one another. The model assumes that each surface can be described by the same relationship as the yield criterion. Using the von Mises yield criterion on the matrix gives

$$F^\ell\big(S_{ij(m)}, \xi_{ij(m)}\big) = \tfrac{3}{2}\big(S_{ij(m)} - \xi_{ij(m)}^\ell\big)\big(S_{ij(m)} - \xi_{ij(m)}^\ell\big) - \sigma_{o(m)}^\ell{}^2 = 0, \tag{14}$$

where $S_{ij(m)}$ and $\xi_{ij(m)}^\ell$ are the deviatoric components of the current matrix stress tensor $\sigma_{ij(m)}$ and the backstress tensor α_{ij}^ℓ; F^ℓ is the yield function of the active surface (the one on which the stress state is located during elastic-plastic loading) at higher stress level; and σ_o^ℓ is the material yield stress.

For the active surface, the increment in the plastic strain tensor is related to the increment in the stress by the flow rule:

$$d\varepsilon_{ij(m)}^{p} = \frac{1}{K_p} \frac{\partial F^{\ell}}{\partial \sigma_{ij(m)}} \left(\frac{\partial F^{\ell}}{\partial \sigma_{kl(m)}} d\sigma_{kl(m)} \right), \tag{15}$$

where K_p is the hardening modulus obtained from the matrix uniaxial stress-strain curve. Mróz [1967] prescribed a translation rule for the determination of the active surface; in our case it takes the form

$$d\xi_{ij(m)}^{\ell} = d\mu \left(S_{ij(m)}^{\ell+1} - S_{ij(m)}^{\ell} \right), \tag{16}$$

where $d\mu$ is a scalar parameter of the active surface translation, which can be determined using the consistency condition, and the term $(S_{ij(m)}^{\ell+1} - S_{ij(m)}^{\ell})$ governs the direction of its translation. The quantity $S_{ij(m)}^{\ell+1}$ is the point on the surface $\ell+1$ immediately enclosing the active surface; it has the same unit normal as the active surface ℓ at the actual current stress state, $S_{ij(m)}^{\ell}$. It is obtained from the Mróz translation rule as

$$S_{ij(m)}^{\ell+1} = \xi_{ij(m)}^{\ell+1} + \frac{\sigma_{o(m)}^{\ell+1}}{\sigma_{o(m)}^{\ell}} \left(S_{ij(m)} - \xi_{ij(m)}^{\ell} \right). \tag{17}$$

2.2.2. *Endochronic theory.* The ability of the endochronic theory to model certain phenomena in cyclic plasticity and creep of homogeneous materials was demonstrated in [Wu and Yang 1983; Khan and Wang 1988; Watanabe and Atluri 1986; Hsu et al. 1991]. In [Owolabi and Singh 2003], the theory was used along with the incremental mean field theory to predict the constitutive behavior of PMMCs under biaxial proportional loading conditions. We give a brief description of the theory. For a plastically incompressible and time independent matrix material, the deviatoric stress is related to the matrix incremental plastic strain by the equation

$$S_{ij(m)} = 2 \int_0^z \rho(z - z') \frac{d\varepsilon_{ij(m)}^{p}(z')}{dz'} dz'. \tag{18}$$

Here z is the intrinsic time scale and $\rho(z)$ is the material function called the hereditary function, and given by

$$\rho(z) = \sum_{r=1}^{r} C_r e^{-\alpha_r z}, \tag{19}$$

where C_r and α_r are material constants determined from the uniaxial cyclic stress-strain curve of the matrix.

As described in [Hsu et al. 1991; Owolabi and Singh 2003], for a stress-controlled loading condition, the incremental matrix plastic strain tensor is related to the incremental intrinsic time scale by

$$\Delta\varepsilon_{ij(m)}^{p} = \frac{a_{ij}\Delta z}{b}, \tag{20}$$

where

$$a_{ij} = \frac{1}{2} \left((\Delta S_{ij(m)})_q + \sum_{r=1}^{r} (S_{ij(m)}^{r})_{q-1}(1 - e^{-\alpha_r \Delta z}) \right) \tag{21}$$

and

$$b = \left(\sum_{r=1}^{r} C_r \frac{(1 - e^{-\alpha_r \Delta z})}{\alpha_r} \right). \tag{22}$$

In these equations q and $q-1$ denote the current and the previous loading steps, and Δ is the difference between the current and previous steps. For a given increment of composite stress tensor, the increment in the intrinsic time scale, Δz, can be obtained, using the secant method or the Newton–Raphson method, as a root of the equation

$$b^2 - a_{ij}a_{ij} = 0 = R(\Delta z). \tag{23}$$

2.2.3. *Complete formulation of the constitutive models.* We now present two models that completely define the constitutive response of the matrix, reinforcement, and PMMCs. The first combines the elastic constitutive response defined by the incremental mean field theory with the Mróz model. The second model differs from the first in that the endochronic theory of plasticity is used to define the increments in the matrix plastic strain components.

Constitutive relations based on the Mróz model. For multiaxial cyclic loading, using the Mróz-based model, incremental mean field theory, and the work relation, the following constitutive relations can be developed to predict the constituents and the composite elastic-plastic strain and stress increments.

Matrix constitutive model. The matrix constitutive relation can be finalized by substituting (9), (10) and (15) into (1). Changing the differential to small increments for numerical implementation yields

$$\Delta\varepsilon_{ij(m)} = \frac{1+\upsilon_m}{E_m}\big(I_{ijkl} - V_f C_{ijrs(m)}(S_{klrs} - I_{klrs})L_{ijrs}^{-1}(C_{ijkl(f)} - C_{ijkl(m)})C_{klrs(m)}^{-1}\big)\Delta\sigma_{kl}$$
$$- \frac{\upsilon_m}{E_{(m)}}\big(\Delta\sigma_{kk} - V_f C_{ijrs(m)}(S_{klrs} - I_{klrs})L_{ijrs}^{-1}(C_{ijkl(f)} - C_{ijkl(m)})C_{ijrs(m)}^{-1}\Delta\sigma_{kk}\big)\delta_{ij}$$
$$+ \frac{\hat{n}_{ij}}{K_{p(m)}}\hat{n}_{kl}\big(I_{ijkl} - V_f C_{ijrs(m)}(S_{klrs} - I_{klrs})L_{ijrs}^{-1}(C_{ijkl(f)} - C_{ijkl(m)})C_{klrs(m)}^{-1}\big)\Delta\sigma_{kl}. \tag{24}$$

Reinforcement constitutive model. The reinforcement, being relatively stiff, only has elastic strain components. The reinforcement constitutive relation can be finalized by substituting (11) and (12) into (2). Changing the differential to small increments yields

$$\Delta\varepsilon_{ij(f)} = \frac{1+\upsilon_f}{E_f}\big(I_{ijkl} + V_m C_{ijrs(m)}(S_{klrs} - I_{klrs})L_{ijrs}^{-1}(C_{ijkl(f)} - C_{ijkl(m)})C_{klrs(m)}^{-1}\big)\Delta\sigma_{kl}$$
$$- \frac{\upsilon_f}{E_{(f)}}\big(\Delta\Delta\sigma_{kk} + V_m C_{ijrs(m)}(S_{klrs} - I_{klrs})L_{ijrs}^{-1}(C_{ijkl(f)} - C_{ijkl(m)})C_{ijrs(m)}^{-1}\Delta\sigma_{kk}\big)\delta_{ij}. \tag{25}$$

Composite constitutive model. The composite constitutive relation can be reached by substituting Equations (9), (11), (24), and (25) into (13). Changing the differential to small increments yields

$$\Delta\varepsilon_{ij} = V_m[\Delta\sigma_{kl}]^{-1}\big(I_{ijkl} - V_f C_{ijrs(m)}(S_{klrs} - I_{klrs})L_{ijrs}^{-1}(C_{ijkl(f)} - C_{ijkl(m)})C_{klrs(m)}^{-1}\big)\Delta\sigma_{kl}$$
$$\times\bigg(\frac{1+\upsilon_m}{E_m}\big(I_{ijkl} - V_f C_{ijrs(m)}(S_{klrs} - I_{klrs})L_{ijrs}^{-1}(C_{ijkl(f)} - C_{ijkl(m)})C_{klrs(m)}^{-1}\big)\Delta\sigma_{kl}$$
$$- \frac{\upsilon_m}{E_{(m)}}\big(\Delta\sigma_{kk} - V_f C_{ijrs(m)}(S_{klrs} - I_{klrs})L_{ijrs}^{-1}(C_{ijkl(f)} - C_{ijkl(m)})C_{ijrs(m)}^{-1}\Delta\sigma_{kk}\big)\delta_{ij}$$
$$+ \frac{\hat{n}_{ij}}{K_{p(m)}}\hat{n}_{kl}\big(I_{ijkl} - V_f C_{ijrs(m)}(S_{klrs} - I_{klrs})L_{ijrs}^{-1}(C_{ijkl(f)} - C_{ijkl(m)})C_{klrs(m)}^{-1}\big)\Delta\sigma_{kl}\bigg)+$$

$$+ V_f[\Delta\sigma_{kl}]^{-1}\big(I_{ijkl} + V_m C_{ijrs(m)}(S_{klrs} - I_{klrs})L_{ijrs}^{-1}(C_{ijkl(f)} - C_{ijkl(m)})C_{klrs(m)}^{-1}\big)\Delta\sigma_{kl}$$

$$\times\left(\frac{1+\upsilon_f}{E_f}\Big(I_{ijkl} + V_m C_{ijrs(m)}(S_{klrs} - I_{klrs})L_{ijrs}^{-1}(C_{ijkl(f)} - C_{ijkl(m)})C_{klrs(m)}^{-1}\Big)\Delta\sigma_{kl}\right.$$

$$\left.- \frac{\upsilon_f}{E_{(f)}}\big(\Delta\sigma_{kk} + V_m C_{ijrs(m)}(S_{klrs} - I_{klrs})L_{ijrs}^{-1}(C_{ijkl(f)} - C_{ijkl(m)})C_{ijrs(m)}^{-1}\Delta\sigma_{kk}\big)\delta_{ij}\right). \quad (26)$$

Constitutive relations based on endochronic theory. For multiaxial cyclic loading, using the endochronic theory-based model, incremental mean field theory, and the work relation, the following constitutive relations are developed to predict the constituents and the composite elastic-plastic strain and stress increments.

Matrix constitutive model. The matrix constitutive relation can be finalized by substituting (9), (10), and (20)–(22) into (1). Changing the differential to small increments yields

$$\Delta\varepsilon_{ij(m)} = \frac{1+\upsilon_m}{E_m}\big(\boldsymbol{I}_{ijkl} - V_f C_{ijrs(m)}(\boldsymbol{S}_{klrs} - \boldsymbol{I}_{klrs})L_{ijrs}^{-1}(C_{ijkl(f)} - C_{ijkl(m)})C_{klrs(m)}^{-1}\big)\Delta\sigma_{kl}$$

$$- \frac{\upsilon_m}{E_{(m)}}\big(\Delta\sigma_{kk} - V_f C_{ijrs(m)}(\boldsymbol{S}_{klrs} - \boldsymbol{I}_{klrs})L_{ijrs}^{-1}(C_{ijkl(f)} - C_{ijkl(m)})C_{ijrs(m)}^{-1}\Delta\sigma_{kk}\big)\delta_{ij}$$

$$+ \frac{\frac{1}{2}\Big((\Delta S_{ij(m)})_q + \sum_{r=1}^{n}(S_{ij(m)}^r)_{q-1}(1 - e^{-\alpha_r\Delta z})\Big)\Delta z}{\sum_{r=1}^{n}C_r\dfrac{(1 - e^{-\alpha_r\Delta z})}{\alpha_r}}. \quad (27)$$

Reinforcement constitutive model. The reinforcement, being relatively stiff, has only the elastic strain components. Consequently, the reinforcement constitutive relation is the same as in the Mróz-based PMMCs constitutive model given by Equation (25).

Composite constitutive model. The composite constitutive relation can be finalized by substituting (9), (11), (25) and (27) into (13). Changing the differentials to small increments yields

$$\Delta\varepsilon_{ij} = V_m[\Delta\sigma_{kl}]^{-1}\big(I_{ijkl} - V_f C_{ijrs(m)}(S_{klrs} - I_{klrs})L_{ijrs}^{-1}(C_{ijkl(f)} - C_{ijkl(m)})C_{klrs(m)}^{-1}\big)\Delta\sigma_{kl}$$

$$\times\left(\frac{1+\upsilon_m}{E_m}\big(I_{ijkl} - V_f C_{ijrs(m)}(S_{klrs} - I_{klrs})L_{ijrs}^{-1}(C_{ijkl(f)} - C_{ijkl(m)})C_{klrs(m)}^{-1}\big)\Delta\sigma_{kl}\right.$$

$$\left.- \frac{\upsilon_m}{E_{(m)}}\big(\Delta\sigma_{kk} - V_f C_{ijrs(m)}(S_{klrs} - I_{klrs})L_{ijrs}^{-1}(C_{ijkl(f)} - C_{ijkl(m)})C_{ijrs(m)}^{-1}\Delta\sigma_{kk}\big)\delta_{ij} + \frac{a_{ij}\Delta z}{b}\right)$$

$$+ V_f[\Delta\sigma_{kl}]^{-1}\big(\Delta\sigma_{kl} + V_m C_{klst(m)}(S_{klst} - I_{klst})L_{ijkl}^{-1}(C_{klst(f)} - C_{klst(m)})C_{klst(m)}^{-1}\Delta\sigma_{kl}\big)$$

$$\times\left(\frac{1+\upsilon_f}{E_f}\big(I_{ijkl} + V_m C_{ijrs(m)}(S_{klrs} - I_{klrs})L_{ijrs}^{-1}(C_{ijkl(f)} - C_{ijkl(m)})C_{klrs(m)}^{-1}\big)\Delta\sigma_{kl}\right.$$

$$\left.- \frac{\upsilon_f}{E_{(f)}}\big(\Delta\sigma_{kk} + V_m C_{ijrs(m)}(S_{klrs} - I_{klrs})L_{ijrs}^{-1}(C_{ijkl(f)} - C_{ijkl(m)})C_{ijrs(m)}^{-1}\Delta\sigma_{kk}\big)\delta_{ij}\right). \quad (28)$$

To obtain numerical results, two MATLAB programs were developed, one for each of the Mróz-based model and the endochronic theory-based model. Each program calculates either the elastic-plastic

composite strain or stress history given the composites material properties and the known stress or strain history. The Mróz-based PMMCs constitutive model uses the yield stresses and hardening moduli of the matrix yield surfaces, while the endochronic theory-based PMMCs constitutive model uses the materials constants as additional inputs. The matrix incremental stress-strain increments are obtained separately using (9), (10), and (24) for the Mróz-based model, while for the endochronic theory-based model, the elastic-plastic matrix stress-strain increments are obtained using (9), (10), and (27) after calculating the increment in the intrinsic time using (23). The final state of stress and strain for a loading step can then be obtained by adding the increments to the previous stress-strain history. The increments in the reinforcement stress and strain can be obtained from the elastic analysis using (11) and (25). For each loading step in the loading history the composite elastic-plastic strain or stress state can be obtained using the elastic-plastic matrix strains, the elastic reinforcement strains and stresses, and (26) and (28) respectively for the Mróz-based and the endochronic theory based models.

3. Experimental procedure

To assess the capability of the two constitutive models presented in Section 2.2.3 to predict the elastic-plastic constitutive behavior of PMMCs, biaxial cyclic (proportional and nonproportional) loads were applied to tubular PMMC specimens, machined from round bars as shown in Figure 1. The PMMC materials used are general purpose Duralcan materials made of 6061-T6 aluminum alloy reinforced with 10 and 20% by volume alumina (Al_2O_3). The composite and its constituents properties, obtained from [Bill 2003; Lease 1994], are shown in Table 1. In [Owolabi and Singh 2003], three terms in the series expansion of the Equation (19) were found to accurately model the stress-plastic strain response of the matrix cyclic stress-strain curve. The values of the material constants, C_r and α_r, associated with the endochronic theory-based PMMCs constitutive model for the matrix material 6061-T6 alloy are shown in Table 2. For the Mróz model, the values of the hardening moduli and yield stresses for ten surfaces used in the matrix uniaxial curve are shown in Table 3.

For the verification of any constitutive model, tubular specimens are normally used because they are more suitable for use for torsional and combined tensile-torsional tests than the corresponding smooth solid specimens. That is, the relationship between the applied torque, T, and the shear stress, τ, can easily be made for tubular specimens in both the elastic and the plastic regions than can be for solid specimens.
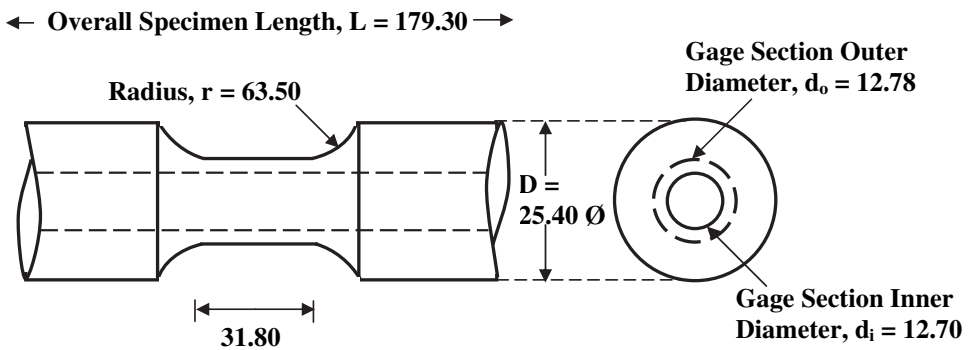
Figure 1. Geometry of the smooth tubular specimen.

material	ultimate strength (MPa)	yield strength (MPa)	elastic modulus (GPa)	elongation (%)
6061-T6	310 (262)	276 (241)	69	20
6061/Al$_2$O$_3$/10p	352 (324)	296 (262)	81	10
6061/Al$_2$O$_3$/20p	372 (345)	352 (317)	97	4

Table 1. Tensile properties (typical and minimum values) of extruded rods, from [Bill 2003; Lease 1994]. Minimum values based on a 99% confidence interval.

C_1 (MPa)	C_2 (MPa)	C_3 (MPa)	α_1	α_2	α_3
7841132	218948	17115	60172	2097	347

Table 2. Material constants used in the endochronic theory series expansion.

surface	hardening modulus ($\times 10^{-11}$)	yield stress (MPa)
1	0.381	150
2	0.476	175
3	1.150	225
4	1.307	237
5	1.515	275
6	4.167	330
7	5.556	315
8	16.667	325
9	111.111	340
10	222.222	350

Table 3. Discretization of the matrix uniaxial stress strain curve to ten surfaces.

Using the thin-wall assumption, the shear stress distribution in a tubular specimen was obtained in [Lease 1994; Wu et al. 1992] as

$$\tau = \frac{T}{2\pi r_m^2 t},$$
(29)

where r_m and t are the mean radius and wall thickness respectively. Equation (29) is applicable both to elastic and elastic-plastic material behavior in the outer region. The shear stress obtained in Equation (29) is normally considered to correspond to the strain at the mid-surface of the smooth tubular specimen. Consequently, the smaller the wall thickness of the specimen, the higher the accuracy of the results obtained. For the constitutive model verifications, if the smooth tubular specimen is subjected to an axial

load P, the stress distribution is uniform. It can be obtained from

$$\sigma = \frac{4P}{\pi (d_o - d_i)^2},$$ (30)

where σ is the uniform axial stress, and d_o and d_i (shown in Figure 1) are the outer and inner diameters of the tubular specimen in the gage section respectively. It should be noted that Equation (30) applies to both elastic and elastic-plastic material behavior.

A servo-hydraulic biaxial load frame [Instron 1992] was used to apply the loads. The frame can apply axial and/or torsional loads both monotonically and cyclically. It has an axial (P) and a torsional (T) load capacity of ± 250 kN and ± 2500 Nm respectively. Experimental tests were conducted using three loading paths: a biaxial proportional loading path (Figure 2) and two variable amplitude nonproportional loading paths (Figure 3).
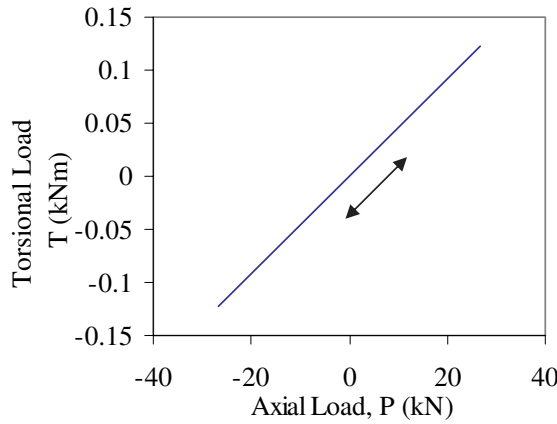
Figure 2. Cyclic proportional tension-torsion (p-t) loading path.
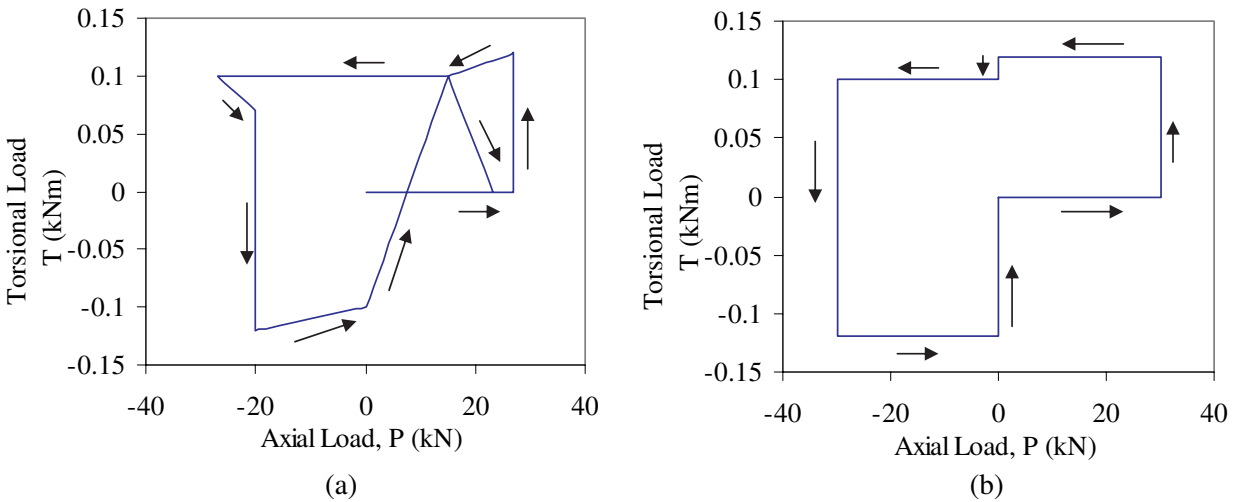
Figure 3. Variable amplitude nonproportional loading path: (a) path 1; (b) path 2.

A 3D image correlation technology system [Aramis 2003] was used to obtain both the axial and the shear strains on the exterior surface close to the middle section of the specimens gage length. The system has the capacity to measure surface strain fields with high resolution; the strain sensitivity is in the range of 50–100 microstrains. The equipment also has a measurement sensitivity of 1/30,000 field of view and thus provides extensive strain measurements at the gage length. To measure the 3D deformations and surface strains, a random or regular pattern is first applied to the area of the specimen under investigation. A typical pattern consists of a white dye penetrant developer, and black spray paint. The white dye is applied first, allowed to dry, then followed with very black spray paint. The pattern should exhibit a high contrast to the surface otherwise the matching of the captured images, from which the displacements and the surface strains are obtained, cannot be carried out correctly [Tyson et al. 2002]. As the loads are applied, the pattern deforms with the test specimen. An image of the deforming pattern is then captured either manually or automatically at desirable load or time intervals by a pair of high resolution digital cameras. The cameras enable the 3D image correlation system to register the 3D shape of the object. The initial image processing defines unique correlation areas known as macro-image facets, typically 5–20 pixels square across the entire imaging area. The center of each facet is a measurement point that can be thought of as an extensometer or a strain rosette. The system processes and visualizes the data gathered in order to obtain an impression of the distribution of strains in the object. It recognizes the surface of the specimen in digital images, and attributes coordinates to every pixel in the image. The system tracks the stochastic pattern applied to the measured surface with subpixel accuracy. Hence localized deformation can be tracked as long as the test specimen remains within the cameras field of view. Using photogrammetric principles [Aramis 2003] and image processing, the specimen's 3D coordinates, 3D displacements, and the surface strain field are automatically calculated using the associated software during the post-processing stage.

4. Results and discussion

The results for the two constitutive models are compared to the experimental results obtained from the tests conducted on the tubular specimens using the tension-torsion load paths in Figures 2 and 3. Note that all the relations presented in the previous sections are valid for cyclic nonproportional (constant or variable amplitude) loading. Either model can be employed knowing the material properties, and either the stress or strain history. Here, the models are demonstrated specifically for load-controlled simulations. In the numerical implementations, equations (29) and (30) are employed to obtain the composite experimental torsional and axial stresses respectively from the applied combined torsion (T) and Tension (P) loads. The elastic-plastic composite strains are subsequently obtained from the known stresses. The strain results obtained are compared with experimentally determined strains.

Figure 4 shows the predicted and experimental results for cyclically stable combined axial/torsional proportional loading (Figure 2) of the tubular specimens. The results of this proportional loading path show the ability of both models to predict the elastic-plastic hysteresis loops associated with cyclic loading. Most of the characteristics exhibited by the experimental results are reflected quite well by both models. However, the major disagreement that can be classified as quantitative is the difference in strain levels prescribed at high plastic strains. The results indicate the Mróz-based PMMCs constitutive model
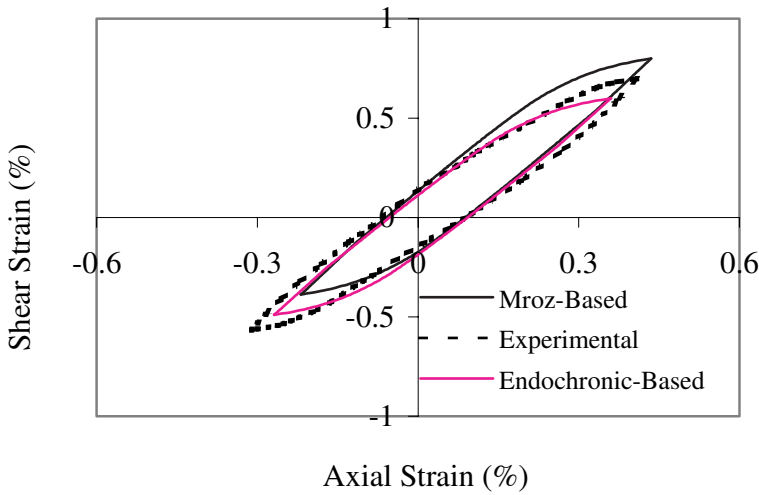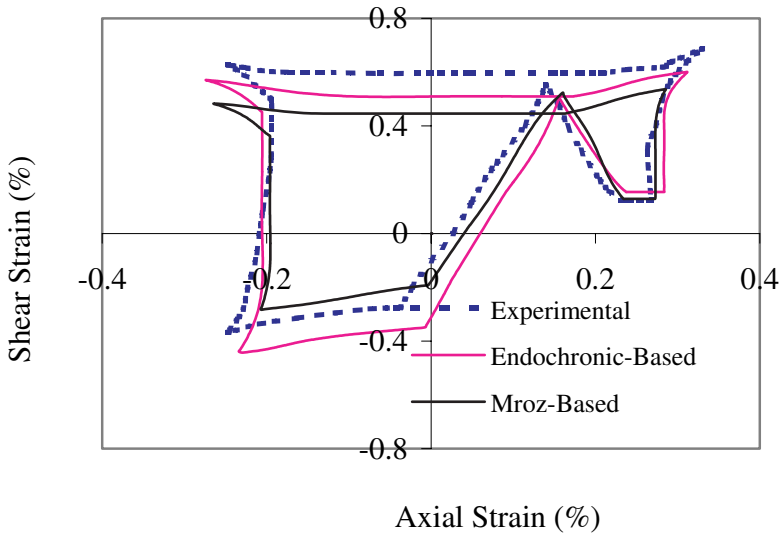
Figure 4. Experimental and simulated shear strains versus axial strains for hollow tube specimen under proportional cyclic load (10% volume fraction).

slightly over-predicts, while the endochronic theory-based PMMCs constitutive model slightly under-predicts the experimental shear strains. The difference between the predicted and experimental results for the endochronic theory-based PMMCs constitutive model may be due to the approximate method used to obtain the material constants. For the Mróz-based PMMCs constitutive model, the number of surfaces used in the multisurface model could have influenced the results. The number of surfaces used may have a significant effect on the direction of translation of the yield surfaces, and thus, affect the predicted results.

Figures 5 and 6 show the strain response of the tubular specimens predicted by the experimental and proposed models to the variable amplitude loading paths shown in Figure 3. Both models predict very similar strain responses for the loading paths and also give reasonable qualitative estimations of the measured strains. However, both models sometimes over-predict and at other times under-predict the measured strains. Generally, the endochronic theory-based PMMCs constitutive model predictions are closer to the experimental results than the Mróz-based PMMCs constitutive model predictions, particularly for the measured peaks and valleys that are essential for fatigue life prediction.

In the load paths considered, both models produce a reasonable qualitative and quantitative response of the composite behavior. The Mróz-based PMMCs constitutive model requires a large number of surfaces and a clearly defined yield point to give good results, while in the endochronic theory-based PMMCs constitutive model, determining the material constants necessary for its implementation is a very difficult task. The Mróz-based PMMCs constitutive model seems to be mathematically more complex than the endochronic theory-based PMMCs constitutive model. In general, the endochronic theory-based PMMCs constitutive model predictions are closer to the experimental results than the Mróz-based PMMCs constitutive model predictions for the load path tested. Thus, the endochronic theory-based PMMC constitutive model was used in [Owolabi and Singh 2006] to provide some of the relations that are necessary in defining notch-root stresses and strains in PMMC components with geometric discontinuities.

Figure 5. Experimental and simulated shear strains versus axial strains for hollow tube specimen under a variable amplitude load path (Figure 3a, 10% volume fraction).
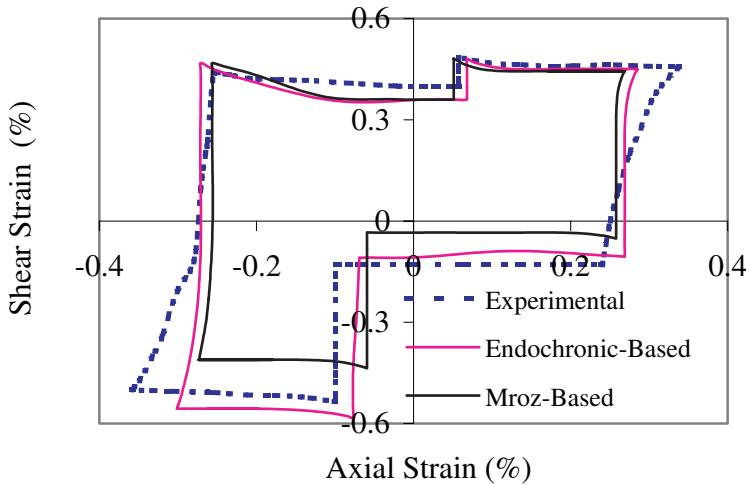
Figure 6. Experimental and simulated shear strains versus axial strains for hollow tube specimen under a variable amplitude load path (Figure 3b, 20% volume fraction).

The differences between the Mróz-based PMMCs constitutive model predictions and the experimental results may be due to the influence of the number of surfaces on the direction of translation of the backstress tensors of the yield surfaces. In addition, the number of load increments used may affect the predicted results. Theoretically, the Mróz-based PMMCs constitutive model can be used with large increments, however, as with other cyclic plasticity models, care must be taken in the specification of the input load increments. Since a quantitative relation between the number of surfaces, load increments,

and the predicted results is difficult to formulate, efforts were made in this research to use a combination of the number of yield surfaces and load increments that gave optimal and convergent results. Generally, for small load levels, the number of loading increments and/or yields surfaces used may not significantly affect the predicted results. However, for high load levels, the number of loading increments and/or yield surface may significantly affect the magnitudes of the predicted results. To address this limitation one can use the two-surface model based on the Mróz model and developed in [Dafalias and Popov 1975; McDowell 1985a; 1985b; Itoh et al. 2000].

5. Conclusions

In this paper, two elastic-plastic constitutive models were evaluated for their applicability to model the behavior of PMMCs under complex loading conditions. Details of the experimental and numerical results that demonstrate the basic qualitative and quantitative aspects of the cyclic plasticity models were presented. For most of the investigated loading paths, both models predict satisfactorily the amplitudes of the experimental strains and qualitatively predict reasonably the characteristics features of the experimental results. However, the endochronic theory-based constitutive model generally gives better qualitative and quantitative predictions of the measured strains. This is the first attempt to incorporate two cyclic plasticity routines into the development of elastic-plastic constitutive relations for PMMCs components particularly under multiaxial variable amplitude loading conditions. It is important to state that any plasticity model that incorporates path dependent material behavior may be used. However, the constitutive models used in this study provide a simple to implement explicit numerical algorithm valid for stress-controlled simulations. While the models are associated with some limitations and thus are not expected to be pertinent to all possible cyclic loading conditions, the results obtained, however, provide solid foundation for further and more systematic experimental and theoretical investigations.

Acknowledgments

References

[Aramis 2003] *Aramis user's manual: GOM measurements*, Version 5, GOM, Braunschweig, 2003.

[Armstrong and Frederick 1966] P. J. Armstrong and C. O. Frederick, "A mathematical representation of the multiaxial Bauschinger effect", Tech Report RD/B/N731, CEGB, 1966.

[Bill 2003] D. Bill, Personal correspondence, 2003.

[Chaboche 1986] J. L. Chaboche, "Time independent constitutive theories for cyclic plasticity", *Int. J. Plast.* **2**:2 (1986), 149–188.

[Chaboche et al. 1979] J. L. Chaboche, V. K. Dang, and G. Cordier, "Modelization of the strain memory effect on the cyclic hardening of 316 stainless steel", in *Transactions of the 5th International Conference on Structural Mechanics in Reactor Technology* (Berlin, 1979), North-Holland, Amsterdam, 1979. Paper L11/3.

[Chen et al. 2005] X. Chen, R. Jiao, and K. S. Kim, "On the Ohno–Wang kinematic hardening rules for multiaxial ratcheting modeling of medium carbon steel", *Int. J. Plast.* **21**:1 (2005), 161–184.

[Chiou and Yip 2003] Y. C. Chiou and M. C. Yip, "Effect of mean strain level on the cyclic stress-strain behavior of AISI 316 stainless steel", *Mater. Sci. Eng. A* **354**:1–2 (2003), 270–278.

[Dafalias and Popov 1975] Y. Dafalias and E. Popov, "A model of nonlinearly hardening materials for complex loading", *Acta Mech.* **21**:3 (1975), 173–192.

[Eshelby 1957] J. D. Eshelby, "The determination of the elastic field of an ellipsoidal inclusion, and related problems", *Proc. R. Soc. A* **241**:1226 (1957), 376–396.

[Fleming and Temis 2002] W. J. Fleming and J. M. Temis, "Numerical simulation of cyclic plasticity and damage of an aluminium metal matrix composite with particulate SiC inclusions", *Int. J. Fatigue* **24**:10 (2002), 1079–1088.

[Goodier 1933] J. N. Goodier, "Concentrations of stress around spherical and cylindrical inclusions and flaws", *J. Appl. Mech.* (*ASME*) **5** (1933), 39–44.

[Hashiguchi et al. 2005] K. Hashiguchi, T. Okayasu, and S. K., "Rate-dependent inelastic constitutive equation: the extension of elastoplasticity", *Int. J. Plast.* **21**:3 (2005), 463–491.

[Hershey 1954] A. V. Hershey, "The plasticity of an isotropic aggregate of anisotropic face-centered cubic crystals", *J. Appl. Mech.* (*ASME*) **21** (1954), 241–249.

[Hsu et al. 1991] S. Y. Hsu, S. K. Jain, and O. J. Griffin, Jr., "Verification of endochronic theory for non-proportional loading paths", *J. Eng. Mech.* (*ASCE*) **117** (1991), 110–131.

[Hutchison 1970] J. W. Hutchison, "Elastic-plastic behaviour of polycrystalline metals and composites", *Proc. R. Soc. A* **319** (1970), 247–272.

[Instron 1992] *Instron 8800 servohydraulic testing systems: operating instructions*, Instron Corporation, 1992.

[Itoh et al. 2000] T. Itoh, X. Chen, T. Nakagawa, and M. Sakane, "A simple model for stable cyclic stress-strain relationship of type 304 stainless steel under nonproportional loading", *J. Eng. Mater. Technol.* (*ASME*) **122**:1 (2000), 1–9.

[Ji and Wang 2003] B. Ji and T. Wang, "Plastic constitutive behavior of short-fibres/particles reinforced composites", *Int. J. Plast.* **19**:5 (2003), 565–581.

[Johnson and Mellor 1975] W. Johnson and P. B. Mellor, *Engineering plasticity*, Van Nostrand, 1975.

[Ju and Chen 1994] J. W. Ju and T. M. Chen, "A micromechanics and effective elastic-plastic behaviour of two phase metal matrix composites", *J. Eng. Mater. Technol.* (*ASME*) **116** (1994), 310–318.

[Kang et al. 2003] G. Z. Kang, N. Ohno, and Nebu., "Constitutive modeling of strain range dependent cyclic hardening", *Int. J. Plast.* **19**:10 (2003), 1801–1819.

[Khan and Wang 1988] A. S. Khan and X. Wang, "On non-proportional infinitesimal plastic deformation after finite plastic prestraining and partial unloading", *J. Mech. Phys. Solids* **36**:5 (1988), 519–535.

[Krieg 1975] R. D. Krieg, "A practical two-surface plasticity theory", *J. Appl. Mech.* (*ASME*) **47** (1975), 641–646.

[Kröner 1961] E. Kröner, "Zur plastischen Verformung des Vielkristalls", *Acta Metall.* **9**:2 (1961), 155–161.

[Lease 1994] K. B. Lease, *Deformation and fatigue of a particulate reinforced metal matrix composite*, Ph.D. thesis, University of Iowa, 1994.

[Lease et al. 1995] K. B. Lease, H. C. Wu, and P. Kurath, "Multiphase constitutive modeling of a particulate reinforced metal matrix composite", pp. 153–158 in *Micromechanics and constitutive modelling of composite materials*, vol. 202, 1995.

[Lease et al. 1996] K. B. Lease, R. I. Stephens, Y. Jiang, and P. Kurath, "Fatigue of a particulate reinforced aluminum metal matrix composite subjected to axial, torsional and combined axial-torsional loading conditions", *Fatigue Fract. Eng. Mater. Struct.* **19**:8 (1996), 1031–1043.

[Li and Chen 1990] Y. Y. Li and Y. Chen, "An incremental plastic analysis of multiphase materials", *J. Appl. Mech.* (*ASME*) **57** (1990), 562–568.

[McDowell 1985a] D. L. McDowell, "A two surface model for transient nonproportional cyclic plasticity, 1: Development of appropriate equations", *J. Appl. Mech.* (*ASME*) **52** (1985), 298–302.

[McDowell 1985b] D. L. McDowell, "A two surface model for transient nonproportional cyclic plasticity, 2: Comparison of theory with experiments", *J. Appl. Mech.* (*ASME*) **52** (1985), 303–308.

[Mori and Tanaka 1973] T. Mori and K. Tanaka, "Average stress in the matrix and average elastic energy of materials with misfitting inclusions", *Acta Metall.* **21**:5 (1973), 571–574.

[Mori and Wakashima 1990] T. Mori and K. Wakashima, "Successive iteration method in the evaluation of average fields in elastically inhomogeneous materials", pp. 269–282 in *Micromechanic and inhomogeneity: the Toshio Mura 65th anniversary volume*, Springer, New York, 1990.

[Mróz 1967] Z. Mróz, "On the description of anisotropic work hardening", *J. Mech. Phys. Solids* **15**:3 (1967), 163–175.

[Ogarevic 1992] V. V. Ogarevic, *Fatigue behavior and life predictions of particle reinforced metal matrix composites at room and elevated temperature*, Ph.D. thesis, University of Iowa, 1992.

[Owolabi and Singh 2003] G. M. Owolabi and M. N. K. Singh, "A comparison between two models that predict the elastic-plastic behavior of particulate metal matrix composites under multiaxial fatigue type loading", pp. 101–110 (Paper IMECE2003–42001) in *Proceedings of the 2003 International Mechanical Engineering Congress and Exposition* (Washington, DC), edited by R. Wetherhold, ASME MD **98**, ASME, New York, 2003.

[Owolabi and Singh 2006] G. M. Owolabi and M. N. K. Singh, "A comparison between two analytical models that approximate notch-root elastic-plastic strain-stress components in two-phase, particle-reinforced, metal matrix composites under multiaxial cyclic loading: theory", *Int. J. Fatigue* **28**:8 (2006), 910–917.

[Sadowsky and Sterberg 1952] M. A. Sadowsky and E. Sterberg, "On the axisymmetric problem of the theory of elasticity for an infinite region containing two spherical cavities", *J. Appl. Mech.* (*ASME*) **19** (1952), 19–27.

[Tandon and Weng 1988] G. P. Tandon and G. J. Weng, "A theory of particle reinforced plasticity", *J. Appl. Mech.* (*ASME*) **55** (1988), 126–145.

[Tong et al. 2004] J. Tong, Z. L. Zhan, and B. Vermeulen, "Modelling of cyclic plasticity and viscoplasticity of a nickel-based alloy using Chaboche constitutive equations", *Int. J. Fatigue* **26**:8 (2004), 829–837.

[Tyson et al. 2002] J. Tyson, T. Schmidt, and K. Galanulis, "Advanced photogrammetry for robust deformation and strain measurement", in *Proceedings of SEM 2002 Annual Conference* (Milwaukee, WI), 2002.

[Valanis 1971] K. C. Valanis, "A theory of viscoplasticity without a yield surface, I: General theory", *Arch. Mech.* **23** (1971), 517–533.

[Valanis 1980] K. C. Valanis, "Fundamental consequences of a new intrinsic time measure: plasticity as a limit of the endochronic theory", *Arch. Mech.* **32** (1980), 171–191.

[Vincent et al. 2004] L. Vincent, S. Calloch, and D. Marquis, "A general cyclic plasticity model taking into account yield surface distortion for multiaxial ratcheting", *Int. J. Plast.* **20**:10 (2004), 1817–1850.

[Watanabe and Atluri 1986] O. Watanabe and S. N. Atluri, "Internal time, general internal variable, and multi-yield-surface theories of plasticity and creep: a unification of concepts", *Int. J. Plast.* **2**:1 (1986), 37–57.

[Wu and Yang 1983] H. C. Wu and R. J. Yang, "Application of the improved endochronic theory of plasticity to loading with multiaxial strain-path", *Int. J. Non-Linear Mech.* **18**:5 (1983), 395–408.

[Wu et al. 1992] H. C. Wu, X. Zhiyou, and P. Wang, "The shear stress-strain curve determination from the tension test in the large strange range", *J. Test. Eval.* **20**:6 (1992), 396–402.

[Ziegler 1959] H. Ziegler, "A modification of Prager's hardening rule", *Q. Appl. Math.* **17**:1 (1959), 55–65. MR 21 #3160 Zbl 0086.18704

GBADEBO MOSES OWOLABI: owolabi@cc.umanitoba.ca
Department of Mechanical and Manufacturing Engineering, University of Manitoba, Winnipeg, Manitoba, R3T 5V6, Canada

MEERA NAND KAUR SINGH: singhmn@cc.umanitoba.ca
Department of Mechanical and Manufacturing Engineering, University of Manitoba, Winnipeg, Manitoba, R3T 5V6, Canada

BOUNDARY ELEMENT ANALYSIS OF THE STRESS FIELD AT THE SINGULARITY LINES IN THREE-DIMENSIONAL BONDED JOINTS UNDER THERMAL LOADING
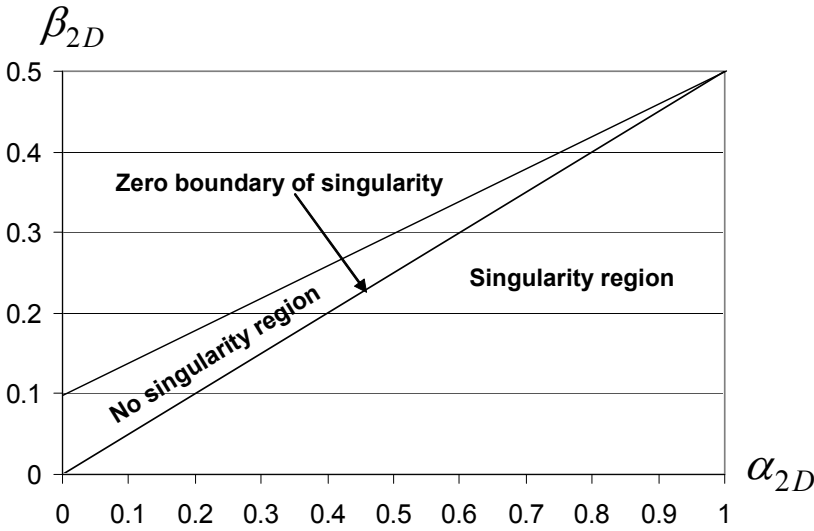
MONCHAI PRUKVILAILERT AND HIDEO KOGUCHI

The stress distribution near a point on the stress singularity line of dissimilar materials in three-dimensional joints under thermal loading are investigated using BEM based on Rongved's fundamental solutions. Stress distributions for the material combinations in the singularity region, in the no singularity region, and in the boundary between them on the Dundurs composite plane are investigated. The influences of thermal expansion coefficients, loading conditions and dimensions on the stress distribution in three-dimensional joints composed of two blocks are examined. The stress intensity factors in three-dimensional joints under a uniform change in temperature are proportional to the temperature variation, ΔT, and depend on the difference in the thermal expansion coefficients. Furthermore, the level of the stress distributions around the stress singularity lines also increases significantly as the length of one side in the parallel cross section to the interface decreases.

1. Introduction

Stress singularities at the interface in the bonded joints of dissimilar materials are induced by mechanical loading or thermal loading. Thermal stresses are caused by differences in elastic properties and thermal expansion coefficients in dissimilar materials joints. The stress singularities exist not only at the vertex in three-dimensional joints of dissimilar materials but also along the intersection of the interface with its free surfaces. The cross line has been referred to as the stress singularity line. Li et al. [1992] reported the results of stress analysis for dissimilar materials using three-dimensional BEM based on Kelvin's fundamental solutions. In the analysis, the interface must be divided using very fine meshes along the stress singularity lines, and hugely memory- and time-consuming procedures are required for accurate analysis. Then, Koguchi [1997] investigated the stress singularity in three-dimensional bonded joints using three-dimensional BEM based on Rongved's fundamental solutions. Rongved's fundamental solutions [Rongved 1955] satisfy boundary conditions at the interface. Therefore, the number of nodes and elements necessary for accurate analysis decreases, because the BEM based on Rongved's fundamental solutions does not require the interface area of dissimilar materials joints to be divided into elements. Koguchi et al. [2003] also used the fundamental solution for two-phase transversely isotropic materials to investigate the stress singularity fields in three-dimensional bonded joints using three-dimensional BEM. Furthermore, Prukvilailert and Koguchi [2005] reported on stress singularity analysis around a point on the stress singularity line in three-dimensional bonded joints using three-dimensional BEM based on Rongved's fundamental solutions. However, this previous research focused only on the stress

Figure 1. The Dundurs composite plane.

singularity distributions in three-dimensional bonded joints under mechanical loading. The distributions of the stress fields near the point on the stress singularity line in three-dimensional joints of dissimilar materials under thermal loading have not been made clear so far.

In recent years, there has been much research on thermal stresses at the interface in two-dimensional bonded joints. Munz and Yang [1992], Munz and Yang [1994] and Yang and Munz [1995] investigated the stress singularities and stress intensity factors near the free edge of a junction between dissimilar materials subjected to mechanical or thermal loading using the eigenfunction expansion method. Madenci et al. [1998] and Barut et al. [2001] developed global (special) elements in a finite element analysis to investigate the thermo-mechanical stress field in a junction between dissimilar materials. It is well-known that three-dimensional BEM is useful to efficiently analyze the stress fields in three-dimensional joints, since only surfaces are divided into meshes for analysis. Cruse et al. [1977] and Rizzo and Shippy [1977] determined the boundary integral equation for three-dimensional thermoelasticity. The thermoelastic integral equation was also derived using the body force analogy [Karami and Kuhn 1992; Cheng et al. 2001].

In this paper, we investigate the stress singularity fields near the singular point on the stress singularity line in three-dimensional joints of dissimilar materials under thermal loading using BEM based on Rongved's fundamental solutions. The material combinations are mapped on the $\alpha_{2D} - \beta_{2D}$ Dundurs composite plane [1969] for the order of stress singularity in a form of power-law singularity, λ_a, in plane strain condition as shown in Figure 1. These parameters are defined as:

$$\alpha_{2D} = \frac{Km_{(2)} - m_{(1)}}{Km_{(2)} + m_{(1)}},$$
$$\beta_{2D} = \frac{K(m_{(2)} - 2) - (m_{(1)} - 2)}{Km_{(2)} + m_{(1)}},$$
(1)
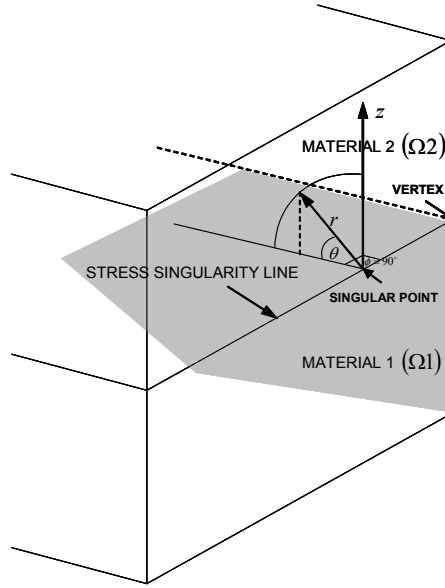
Figure 2. Stress singularity line in a three-dimensional joint of dissimilar materials and spherical coordinate system with the origin at the singular point.

where

$$K = \frac{G_{(1)}}{G_{(2)}}, \tag{2}$$

$$m_{(h)} = \begin{cases} 4(1 - v_{(h)}), & \text{for plane strain,} \\ \dfrac{4}{1 + v_{(h)}}, & \text{for plane stress,} \end{cases} \quad (h = 1, 2) \tag{3}$$

in which $G_{(h)}$ is the shear modulus and $v_{(h)}$ is the Poisson's ratio. The subscript h of these material properties represents the material region; subscript 1 refers to the region of material 1 and subscript 2 refers to the region of material 2. Prukvilailert and Koguchi [2005] investigated the eigenvalues for the point on the stress singularity line in three-dimensional bonded joints using the formulation of FEM eigen analysis developed by Yamada and Okumura [1981] and Pageau and Biggers [1995]. The eigen equation was derived using the principles of virtual work for deducing the root p (eigenvalue). We obtained quintuple roots ($p_l = 1$) of logarithmic singularity and a root p_a where $0 < p_a < 1$ of r^{λ_a} power-law singularity. We found that the order of stress singularity in a form of power-law singularity, $\lambda_a(\lambda_a = p_a - 1)$, at the point on the stress singularity line, is almost identical to that at the apex of two-dimensional bonded joints in plane strain condition, and the contour map of λ_a in the singular region of the Dundurs composite plane was plotted. The stress singularity field around the singular point on the stress singularity line according to the eigenvalues obtained by three-dimensional FEM eigen analysis can be expressed as follows:
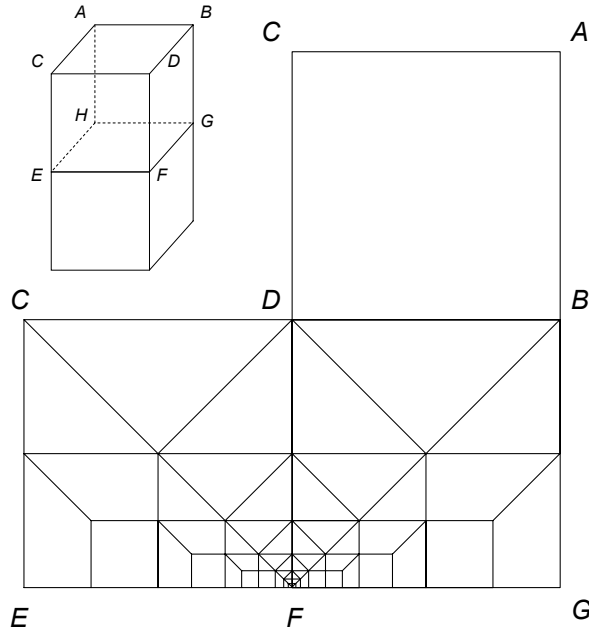
Figure 3. Mesh division of the model.

$$\sigma_{ij}(r,\theta,\phi) = L_{ij1}(\theta,\phi) + L_{ij2}(\theta,\phi)\ln(r/L) + L_{ij3}(\theta,\phi)(\ln(r/L))^2$$
$$+ L_{ij4}(\theta,\phi)(\ln(r/L))^3 + L_{ij5}(\theta,\phi)(\ln(r/L))^4 + (r/L)^{\lambda_a}K_{ija}(\theta,\phi,p_a), \quad (4)$$

where L is the characteristic length of the configuration. L_{ijm} is the stress intensity factor of the logarithmic singularity term ($m = 1, 2, \ldots, 5$), and K_{ija} is that of the $(r/L)^{\lambda_a}$ term. The subscripts i, j refer to r, θ and ϕ in a spherical coordinate system as shown in Figure 2.

2. BEM for thermoelasticity

The stress and displacement fields at a point in the joints with high stress are examined using BEM, which requires less memory than FEM, especially in the case of three-dimensional joints. Here, Rongved's fundamental solutions satisfying the boundary conditions at the interface in dissimilar materials are applied in our analysis. For thermoelasticity with a uniform temperature variation in dissimilar materials, the boundary integral equation is derived as follows:

$$C_{ij}u_j(P) = \int_S \big(t_j(Q)U_{ij}(P,Q) - T_{ij}(P,Q)u_j(Q)\big)dS(Q) + \int_S \big((n_jM\varphi)U_{ij}(P,Q)\big)dS(Q), \quad (5)$$

where S is the surface of the dissimilar materials model excluding the interface area, P and Q are points on the boundary, C_{ij} is the C-matrix derived from the configuration around a boundary point P, and U_{ij} and T_{ij} are Rongved's fundamental solutions for displacements and surface tractions. Parameter φ is a uniform temperature variation from the stress-free state. The term M varies according to the location of
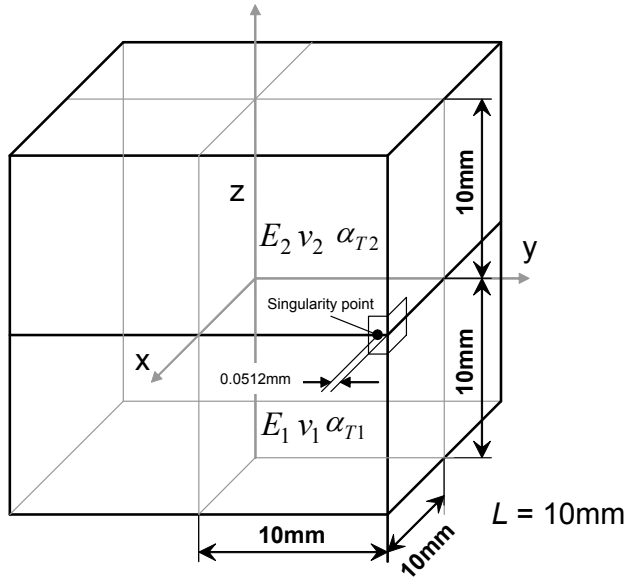
Figure 4. Model for analysis of a three-dimensional joint.

an element. We can define M as

$$
M = \begin{cases} \dfrac{2G_{(1)}\alpha_{T1}(1+v_{(1)})}{(1-2v_{(1)})}, & \text{in Material region 1,} \\[3mm] \dfrac{2G_{(2)}\alpha_{T2}(1+v_{(2)})}{(1-2v_{(2)})}, & \text{in Material region 2,} \end{cases} \tag{6}
$$

where α_{T1} and α_{T2} are the thermal expansion coefficients for material 1 and for material 2, respectively.

A very fine mesh division shown in Figure 3 is used to obtain an accurate stress distribution. The stress state at internal points can then be derived. First, the strain-displacement relation is written as

$$
\varepsilon_{ij} = \frac{1}{2}(u_{i,j} + u_{j,i}). \tag{7}
$$

The stress-strain relation for thermoelasticity is given by

$$
\sigma_{ij}^{(h)} = 2G_{(h)}\varepsilon_{ij} + N\delta_{ij}\varepsilon_{kk} - M\delta_{ij}\varphi, \tag{8}
$$

where

$$
N = \begin{cases} \dfrac{2G_{(1)}v_{(1)}}{(1-2v_{(1)})}, & \text{in material region 1,} \\[3mm] \dfrac{2G_{(2)}v_{(2)}}{(1-2v_{(2)})}, & \text{in material region 2.} \end{cases} \tag{9}
$$

Substitution of Equation (7) into Equation (8) then gives

$$
\sigma_{ij}^{(h)} = G_{(h)}(u_{i,j} + u_{j,i}) + N\delta_{ij}u_{k,k} - M\delta_{ij}\varphi. \tag{10}
$$
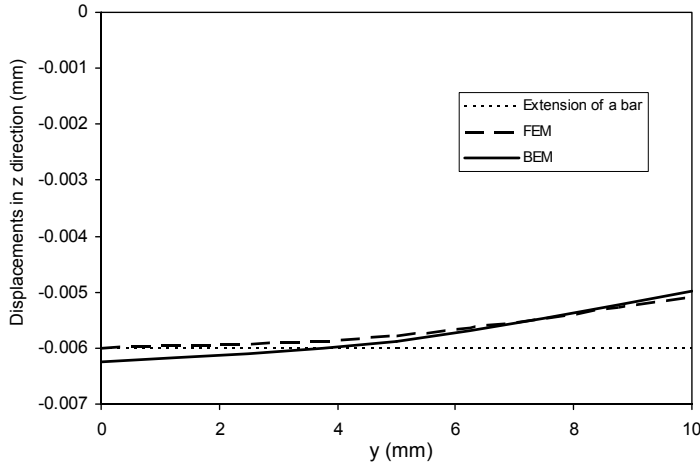
Figure 5. Displacements in the z-direction on the upper surface of the model along the
edge $x = 10$ mm for a uniform temperature variation ($\Delta T = -100$ K, cooling down.

Finally, the stress σ_{ij} at the internal point, ξ, can be obtained by differentiating Equation (5) and substituting into Equation (10) as follows:

$$\sigma_{ij}^{(h)}(\xi) = \int_S \Big(t_l(Q) D_{ijl}^{(h)}(\xi, Q) - V_{ijl}^{(h)}(\xi, Q) u_l(Q) \Big) dS(Q) + \int_S (n_l M\varphi) D_{ijl}^{(h)}(\xi, Q) dS(Q) - M\delta_{ij}\varphi, \quad (11)$$

where the third-order tensor components $D_{ijl}^{(h)}(\xi, Q)$ and $V_{ijl}^{(h)}(\xi, Q)$ are obtained by substituting Rongved's fundamental solutions $U_{ij}(\xi, Q)$ and $T_{ij}(\xi, Q)$, respectively, in the stress-displacement equations as follows:

$$D_{ijl}^{(h)}(\xi, Q) = G_{(h)}\big(U_{il,j}(\xi, Q) + U_{jl,i}(\xi, Q) \big) + N\delta_{ij} U_{kl,k}(\xi, Q)$$

$$V_{ijl}^{(h)}(\xi, Q) = G_{(h)}\big(T_{il,j}(\xi, Q) + T_{jl,i}(\xi, Q) \big) + N\delta_{ij} T_{kl,k}(\xi, Q), \quad (12)$$

where δ_{ij} is the Kronecker delta.

A typical model employed in our calculation is shown in Figure 4. The total number of nodes and elements are 3067 and 1370, respectively. A very fine mesh division is located around the singular point on the stress singularity line. For the boundary conditions, the displacements in the x-direction and the y-direction are free at all surfaces of the model. The displacement in the z-direction at the upper surface and side surfaces of the model is free, whereas that at the lower surface is fixed to zero.

3. Results and discussion

3.1. *Thermal loading.* In this section, thermal loading due to a uniform temperature variation ($\varphi = \Delta T$: constant) is applied to the three-dimensional joint model. The material combinations of the joint are chosen so as to lie in the singularity region, in the no-singularity region and at the boundary between the two; here "singularity" refers to the power-law singularity on the Dundurs composite plane in Figure 1. The

distance between the vertex of the joint and the singular point where the stress distribution is investigated is 0.0512 mm as shown in Figure 4. Material properties are first chosen as $E_{(1)} = 206$ GPa, $v_{(1)} = 0.3$, $E_{(2)} = 52.6742$ GPa, $v_{(2)} = 0.26316$. The corresponding Dundurs parameters ($\alpha_{2D} = 0.6$, $\beta_{2D} = 0.2$) are in the singularity region. The thermal expansion coefficient of material 1, α_{T1}, is $1.0 \times 10^{-6} K^{-1}$, and of material 2, α_{T2}, it is $5.0 \times 10^{-6} K^{-1}$. The uniform temperature variation ΔT is $-100 K$, which means that the temperature in the joint decreases from the stress-free state (ΔT is negative, indicating a cooling-down condition). The upper part of the model (material 2) allows more contraction than the lower part of the model (material 1, which has a lower value of the thermal expansion coefficient). A comparison of the displacements in the z-direction along the edge ($x = 10$ mm) on the upper surface of the model in the BEM analysis with those in the FEM and theoretical analysis is shown in Figure 5. The theoretical analysis based on the theory of thermoelasticity for the extension of a bar shows the average displacement over the upper surface of the model. As seen in Figure 5, the displacements for each of the three methods are close to each other. The results of the BEM and the FEM also show that the displacement varies over the upper surface of the model. The stress distribution of $\sigma_{\theta\theta}$ at the interface ($\theta = 0°$) near the singular point on the stress singularity line along the dimensionless distance r/L in the present BEM analysis for a uniform temperature variation ($\Delta T = -100 K$) is shown in Figure 6a. For comparison, we also provide the stress distributions of $\sigma_{\theta\theta}$ in two-dimensional bonded joints, computed using the formulation developed by Munz and Yang [1992] and the commercial FEM program (MARC) in plane strain condition. It can be seen that the stress distribution of $\sigma_{\theta\theta}$ for three-dimensional bonded joints is similar to that for two-dimensional bonded joints, but the magnitude is larger. The stress distributions of $\sigma_{\theta\theta}$ around the singular points located at 0.0392 mm and 0.0292 mm from the junction vertex are also investigated. To magnify the difference, Figure 6b shows the stress distributions of $\sigma_{\theta\theta}$ in a semilog scale for the three singular points. The level of the stress $\sigma_{\theta\theta}$ increases slightly as the singular point approaches the vertex point. Next, the stress distributions of $\sigma_{\theta\theta}$ for various uniform temperature variations are investigated and shown in Figure 7. The magnitude of the stress $\sigma_{\theta\theta}$ near the singular point is proportional to the value of a uniform temperature variation according to the Linear Theory of Elasticity. Figures 8a–8c show the distributions of several stress components $-\sigma_{ij}/\Delta T$ near the singular point in a log-log scale for various angles of θ. The stress level of $-\sigma_{\theta\theta}/\Delta T$ in Figure 8a increases as the angle θ approaches 0.

It is well-known that failure and cracks at the interface of joints usually occur due to the tensile stress of $\sigma_{\theta\theta}$. The stress distribution of $-\sigma_{\theta\theta}/\Delta T$ at $\theta = 0°$ in Figure 8a refers to the stress distribution of $\sigma_{\theta\theta}$ at the interface in Figure 6a divided by $\Delta T = -100 K$. Moreover, the stress level of $-\sigma_{r\theta}/\Delta T$ in Figure 8b decreases while the stress level of $-\sigma_{rr}/\Delta T$ in Figure 8c increases as the angle θ approaches the free surface of joints. The stress components computed at $\theta = -10°$, $-30°$ and $-60°$ are not reported in the corresponding figures since their values are negative. All plots obviously have negative slopes. Therefore, the occurrence of stress singularity in the form of $(r/L)^{\lambda_a}$ singularity (power-law singularity) is possible. However, the curves deviate from a straight line as the distance from the singular point increases. An attempt to estimate the stress distribution using a function of the 1st order logarithmic singularity term and the power-law singularity term for two-dimensional joints does not provide a good fit for the stress distribution of $-\sigma_{\theta\theta}/\Delta T$ at $\theta = -60°$ shown in Figure 8a. In the present study, three-dimensional FEM eigen analysis yields one root of power-law singularity, $p_a = 0.9073$, $\lambda_a = p_a - 1 = -0.0927$, and quintuple roots ($p_l = 1$) of logarithmic singularity. Then, a good fit for the profiles of the stress
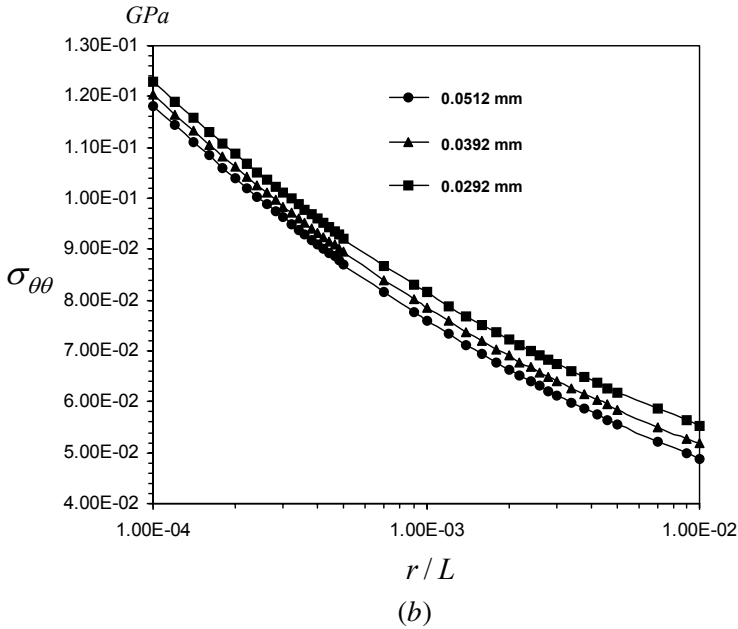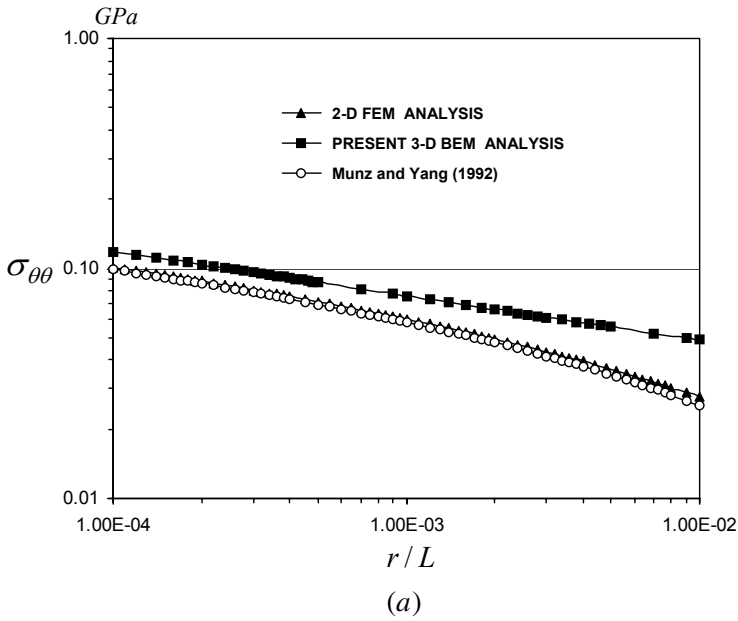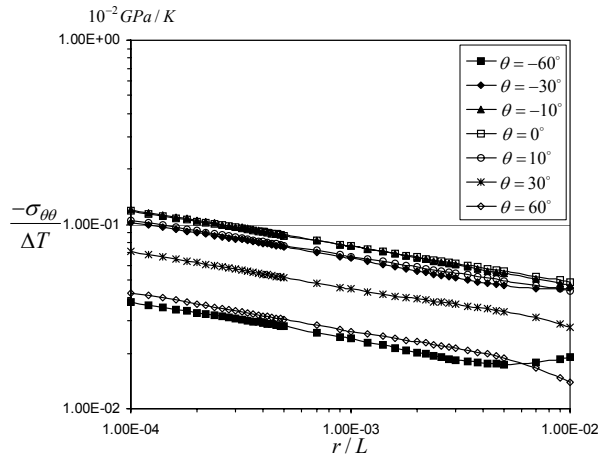
Figure 6. Stress distributions of $\sigma_{\theta\theta}$ at the interface near the singular point on the stress singularity line for a uniform temperature variation ($\Delta T = -100$ K).

distributions in the neighborhood of the singular point can be obtained using Equation (4) which is a combination of power-law singularity and 4th order logarithmic singularity distributions. Figure 9a shows the stress distributions of $-\sigma_{\theta\theta}/\Delta T$ at the interface ($\theta = 0°$) for various values of α_{T2} when α_{T1} is fixed to $1.0 \times 10^{-6} K^{-1}$. The stress level of $-\sigma_{\theta\theta}/\Delta T$ increases as the value of α_{T2} increases.
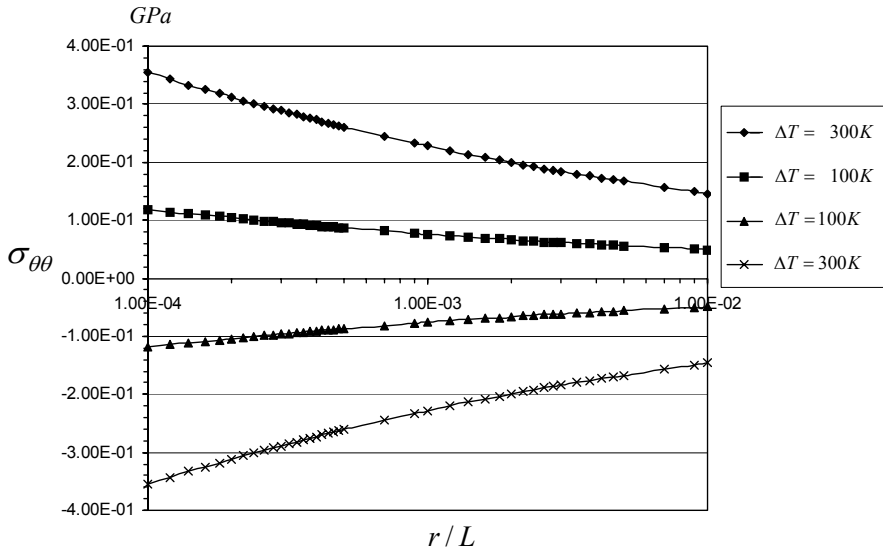
Figure 7. Stress distributions of $\sigma_{\theta\theta}$ at the interface for various uniform temperature variations in a semilog scale.

Furthermore, Figure 9b shows that the stress field is linear in the difference between the thermal expansion coefficients. Figures 10a–10c show the log-log plots of $-\sigma_{ij}/\Delta T$ for various angles of θ and the Dundurs parameters located at the zero boundary of singularity in plane strain condition ($\alpha_{2D} = 0.4$, $\beta_{2D} = 0.2$, $E_{(1)} = 206\,\text{GPa}$, $v_{(1)} = 0.3$, $E_{(2)} = 94.68124\,\text{GPa}$, $v_{(2)} = 0.15517$). The thermal expansion coefficients for two dissimilar materials are chosen as $\alpha_{T1} = 1.0 \times 10^{-6} K^{-1}$ and $\alpha_{T2} = 5.0 \times 10^{-6} K^{-1}$. From the three-dimensional FEM eigen value analysis, there are five roots of $p_l = 1$ and $\lambda_a = -0.000455$. We also used Equation (4) to approximate the curves of the stress distributions. Because of the very small order of stress singularity ($\lambda_a \to 0$), the $(r/L)^{\lambda_a}$ singularity term in Equation (4) is almost constant in the range $10^{-4} \leq r/L \leq 10^{-2}$. However, in Figure 10a, the plots of the stress $-\sigma_{\theta\theta}/\Delta T$ have significantly negative slopes. The plots for the stresses $-\sigma_{r\theta}/\Delta T$ and $-\sigma_{rr}/\Delta T$ in Figure 10b-10c also have negative slopes. This means that the existence of logarithmic singularity clearly influences the characteristics of the stress fields near the stress singularity line for material combinations at the zero boundary of singularity on the Dundurs composite plane. We also investigate the stress distributions of $-\sigma_{ij}/\Delta T$ for the Dundurs parameters located in the no-singularity region ($\alpha_{2D} = 0.3$, $\beta_{2D} = 0.2$, $E_{(1)} = 206\,\text{GPa}$, $v_{(1)} = 0.3$, $E_{(2)} = 121.2716\,\text{GPa}$, $v_{(2)} = 0.07143$, $\lambda_a = 0.02752 > 0$). It can be found that the characteristics of the stress distributions of $-\sigma_{ij}/\Delta T$ are similar to those at the zero boundary of singularity, because the Dundurs parameters in the two cases are not very different. The stress distributions of $-\sigma_{\theta\theta}/\Delta T$ at the interface for material combinations falling in the no-singularity region and at the zero boundary of singularity when the difference of the thermal coefficient is varied are shown in Figure 11. The stress distributions for material combinations in the singularity region, in the no-singularity region, and at the zero boundary of singularity show that the stress intensity factors in Equation (4) are proportional to the temperature variation ΔT and depend on the difference in the thermal expansion coefficients in
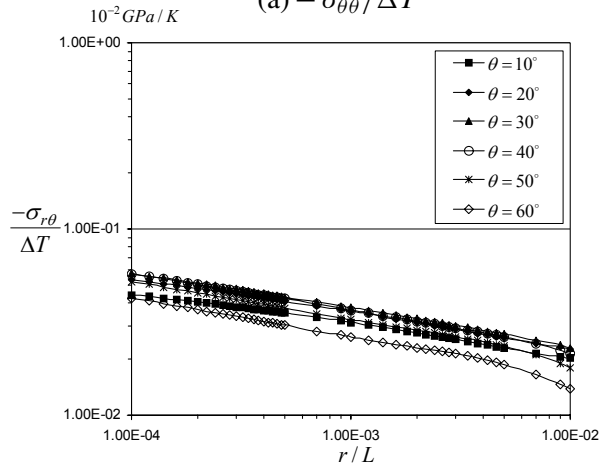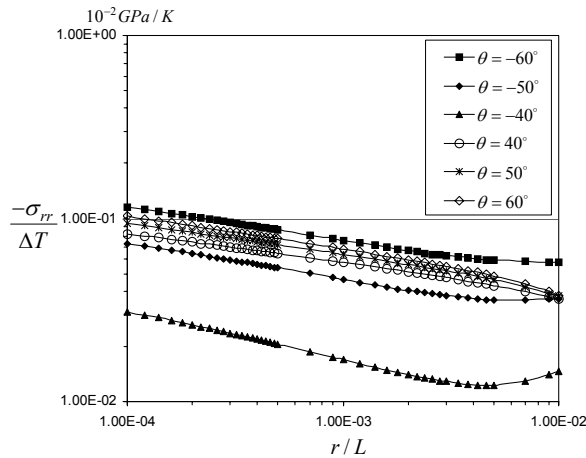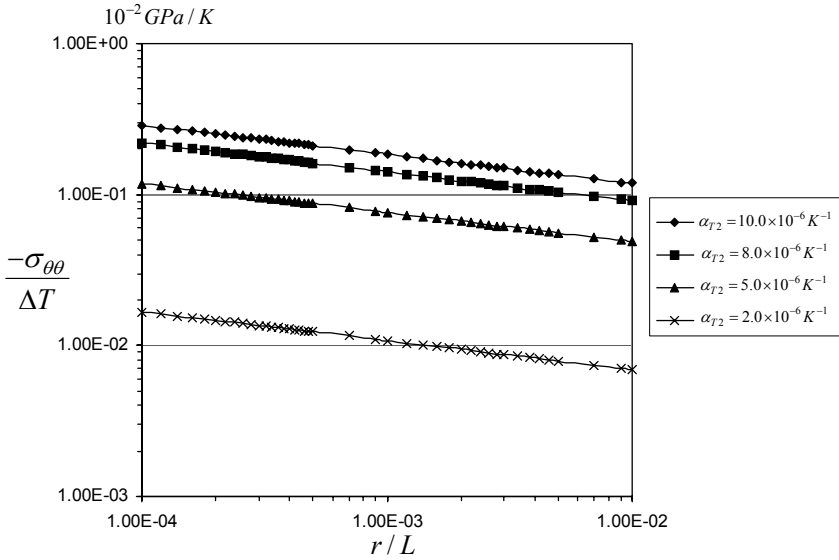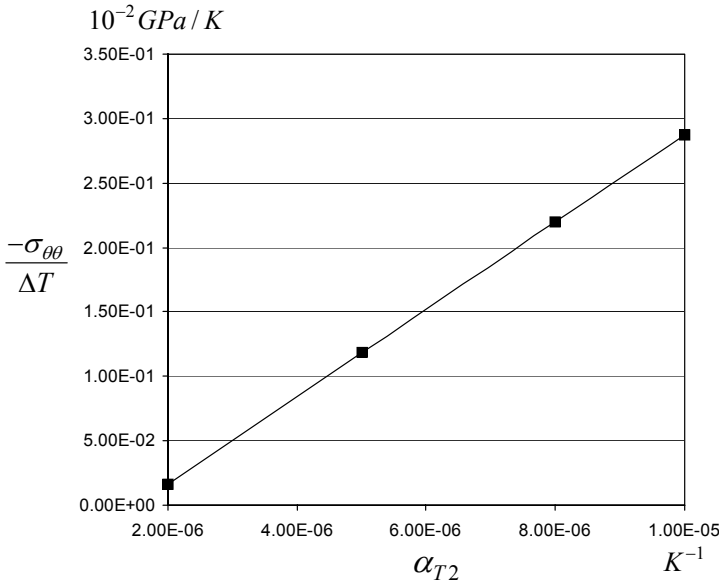
Figure 8. Stress distributions of $-\sigma_{ij}/\Delta T$ for various angles of θ ($\alpha_{2D} = 0.6$, $\beta_{2D} = 0.2$).
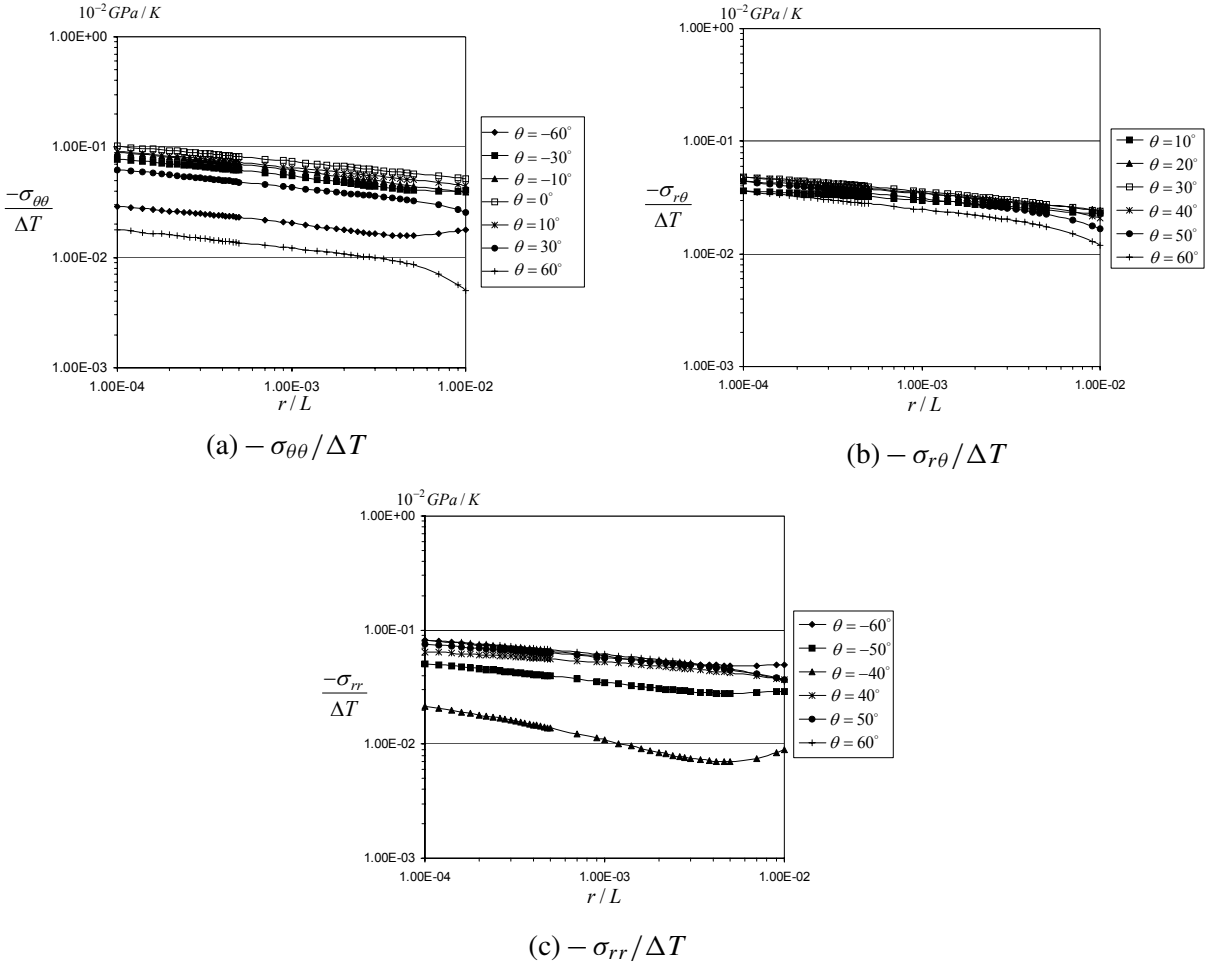
$10^{-2} GPa / K$

(a)

$10^{-2} GPa / K$

(b)

Figure 9. Stress distributions of $-\sigma_{\theta\theta}/\Delta T$ at the interface $\theta = 0°$ for various values of α_{T2} ($\alpha_{T1} = 1.0 x 10^{-6} K^{-1}$ and $\alpha_{2D} = 0.6$, $\beta_{2D} = 0.2$).

two-phase materials, that is,

$$L_{ijm} \qquad \text{and} \qquad K_{ija} \propto \Delta T. \tag{13}$$

The stress intensity factors for the stress $-\sigma_{\theta\theta}/\Delta T$ at the interface under a uniform temperature variation are shown in Table 1. The stress intensity factors $-L_{\theta\theta4}/\Delta T$ and $-L_{\theta\theta5}/\Delta T$ are relatively

(a) $-\sigma_{\theta\theta}/\Delta T$

(b) $-\sigma_{r\theta}/\Delta T$

(c) $-\sigma_{rr}/\Delta T$

Figure 10. Stress distributions of $-\sigma_{\theta\theta}/\Delta T$ for various angles of θ ($\alpha_{2D} = 0.4$, $\beta_{2D} = 0.2$).

	$-K_{\theta\theta a}/\Delta T$ 10^{-2} GPa/K	$-L_{\theta\theta 1}/\Delta T$ 10^{-2} GPa/K	$-L_{\theta\theta 2}/\Delta T$ 10^{-2} GPa/K	$-L_{\theta\theta 3}/\Delta T$ 10^{-2} GPa/K	$-L_{\theta\theta 4}/\Delta T$ 10^{-2} GPa/K	$-L_{\theta\theta 5}/\Delta T$ 10^{-2} GPa/K
$\alpha_{2D} = 0.6$, $\beta_{2D} = 0.2$ $\lambda = -0.0927$	4.233E-02	-5.381E-03	7.210E-03	1.072E-03	1.263E-06	8.683E-08
$\alpha_{2D} = 0.5$, $\beta_{2D} = 0.2$ $\lambda = -0.000455$	7.663E-02	-5.510E-02	-4.173E-03	4.575E-04	-1.015E-05	-6.968E-07
$\alpha_{2D} = 0.3$, $\beta_{2D} = 0.2$ $\lambda = -0.02752$	8.490E-02	-6.879E-02	-8.646E-03	1.069E-04	-1.382E-05	-9.482E-07

Table 1. Stress intensity factors for the stress $-\sigma_{\theta\theta}/\Delta T$ at the interface ($\theta = 0$) under a uniform temperature variation. Note: $\alpha_T 1 = 1.0 \times 10^{-6} K^{-1}$, $\alpha_{T2} = 5.0 \times 10^{-6} K^{-1}$.

$10^{-2} GPa/K$
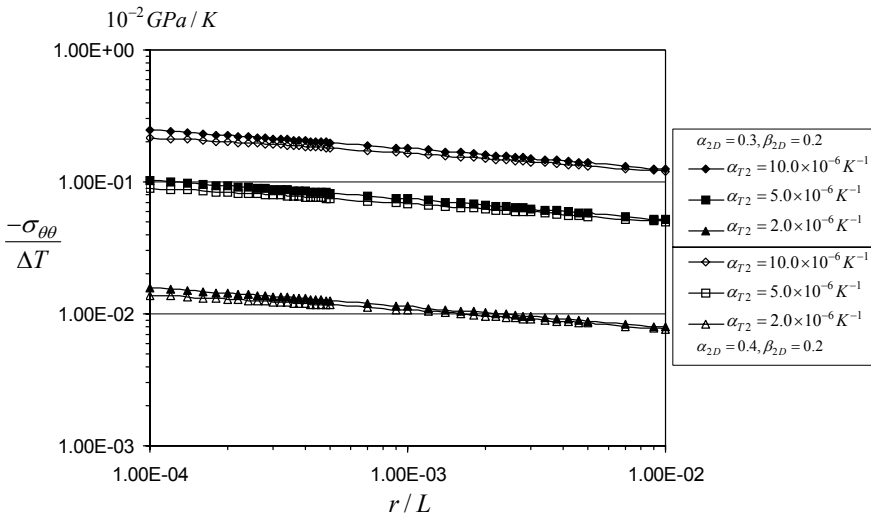
Figure 11. Effects of α_{T2} ($\alpha_{T1} 1.0 \times 10^{-6} K^{-1}$) on $\sigma_{\theta\theta}/\Delta T$ at the interface $\theta = 0$ for ($\alpha_{2D} = 0.4$, $\beta_{2D} = 0.2$) and ($\alpha_{2D} = 0.3$, $\beta_{2D} = 0.2$).

small compared with other stress intensity factors. For $\alpha_{2D} = 0.6$ and $\beta_{2D} = 0.2$ (singularity region), the stress intensity factor $-K_{\theta\theta a}/\Delta T$ of the $(r/L)^{\lambda_a}$ singularity term is obviously larger than that for
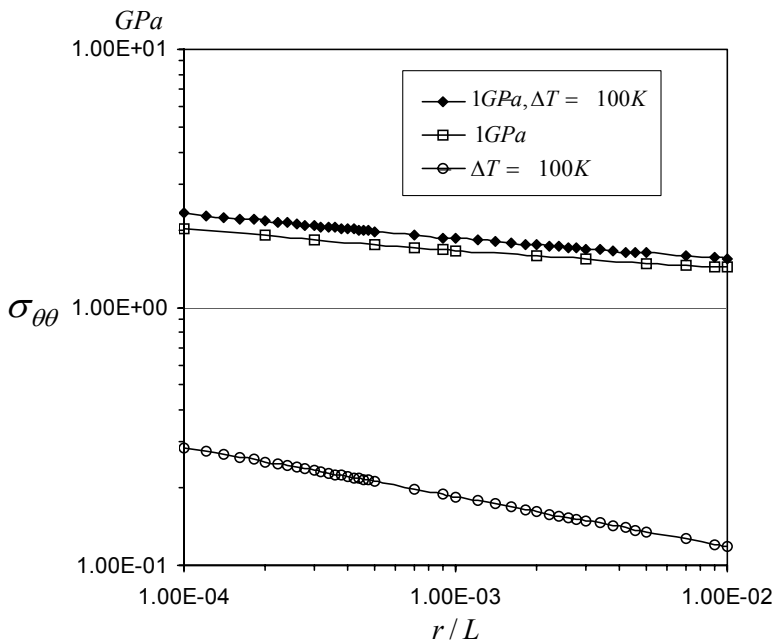
Figure 12. Stress distributions of $\sigma_{\theta\theta}$ at the interface near the singular point on the stress singularity line under various loading conditions.

each of the logarithmic singularity terms. For $(\alpha_{2D} = 0.4, \beta_{2D} = 0.2)$ and $(\alpha_{2D} = 0.3, \beta_{2D} = 0.2)$, it can be seen that the plots of the stress $-\sigma_{\theta\theta}/\Delta T$ against the dimensionless distance r/L in a log-log scale have significantly negative slopes due to the value of the stress intensity factors $-L_{\theta\theta 2}/\Delta T$ of the $\ln(r/L)$ term and $-L_{\theta\theta 3}/\Delta T$ of the $(\ln(r/L))^2$ term in Equation (4). In previous papers [Koguchi 1997; Prukvilailert and Koguchi 2005], it was found that the stress intensity factors (L_{ijm}, K_{ija}) under tensile loading are proportional to the magnitude of the applied tensile stress, P, on the upper surface of three-dimensional joints, that is,

$$L_{ijm} \qquad \text{and} \qquad K_{ija} \propto P. \tag{14}$$

For comparison, the stress distributions of $\sigma_{\theta\theta}$ under tensile loading ($P = 1\,\text{GPa}$) and under combined loading of tensile ($P = 1\,\text{GPa}$) and thermal loading ($\Delta T = -100K$) are also provided in Figure 12. It can be seen that the characteristic of the stress distribution of $\sigma_{\theta\theta}$ under a uniform temperature variation is different from that under tensile loading or combined loading. For combined loading, the stress level of $\sigma_{\theta\theta}$ increases with decreasing temperature from the stress-free state (cooling down).

3.2. Plate structure. Plate structures composed of dissimilar materials bonded together have many applications in solid mechanics. The stress distributions near the singular point on the stress singularity line of plate structures under thermal loading are investigated in this section. The geometry of the three-dimensional structure in Figure 4 is changed to a plate structure. Figure 13 shows the model for analysis. The width of the $y - z$ plane, $2w$, is varied. Two stress singularity lines exist for examination in this structure. One stress singularity line is located on the $y - z$ plane and another on the $x - z$ plane. The
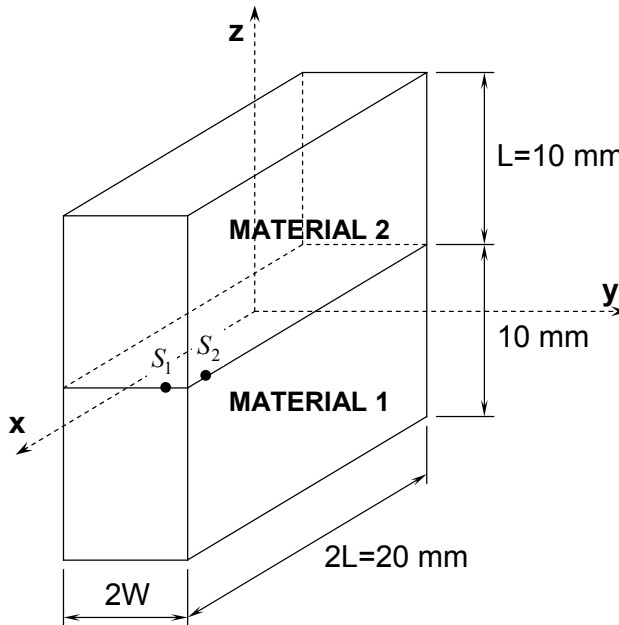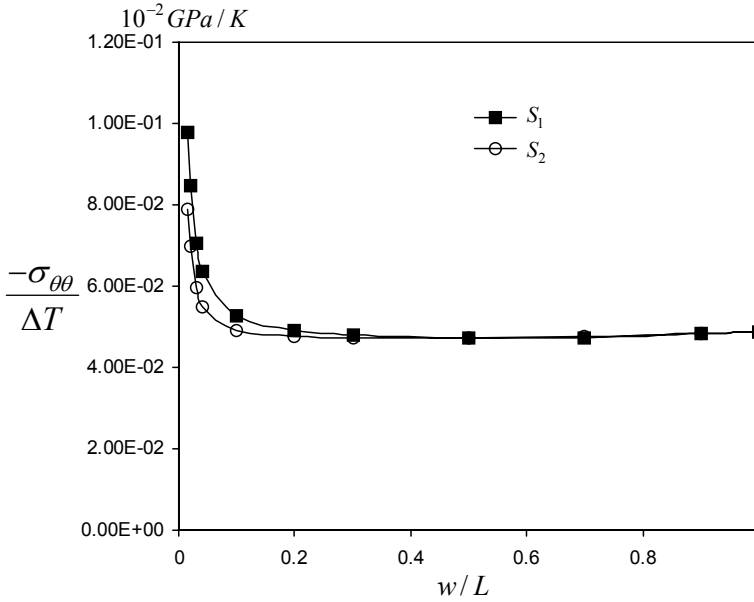

Figure 13. Model for analysis of a plate structure.
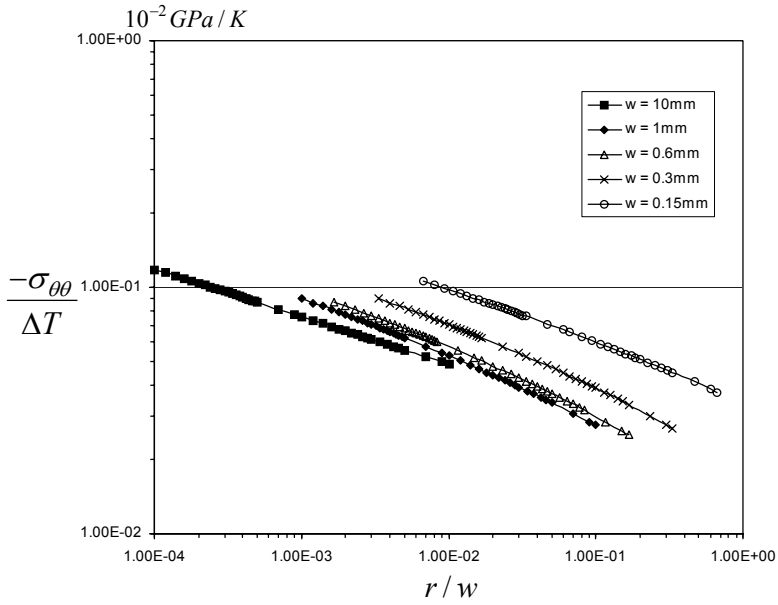
Figure 14. Stress distributions $-\sigma_{\theta\theta}/\Delta T$ around the singular point S_1 at the interface of plate structures.
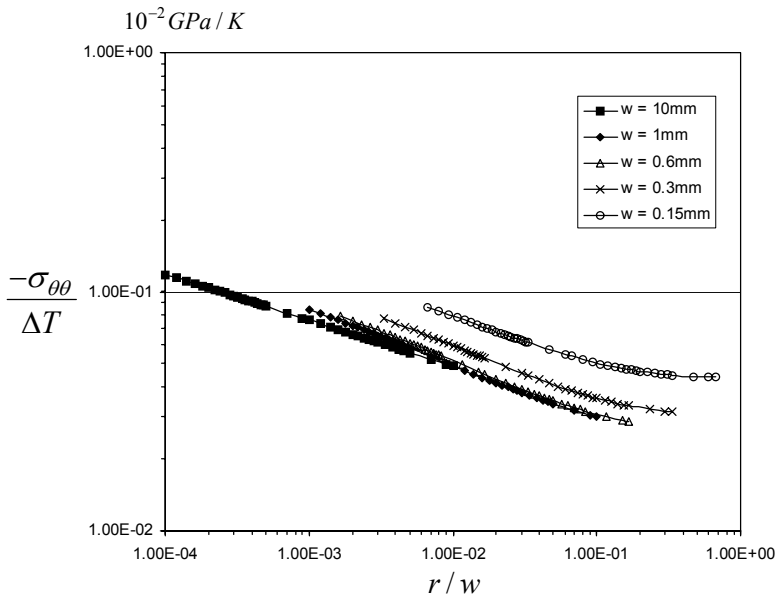
Figure 15. Stress distributions $-\sigma_{\theta\theta}/\Delta T$ around the singular point S_2 at the interface of plate structures.

Figure 16. Variation in the stress $-\sigma_{\theta\theta}/\Delta T$ at the interface against the dimensionless variable, w/L, in plate structures.

distance between the singular points (S_1 and S_2) and the vertex of the joint is 0.0512 mm. The material properties are chosen for material combinations corresponding to $\alpha_{2D} = 0.6$ and $\beta_{2D} = 0.2$ (singularity region). The thermal expansion coefficients are chosen as $\alpha_{T1} = 1.0 \times 10^{-6} K^{-1}$ and $\alpha_{T2} = 5.0 \times 10^{-6} K^{-1}$. The temperature variation is uniformly applied to the material regions. Figures 14 and 15 show the stress distributions of $-\sigma_{\theta\theta}/\Delta T$ at the interface around the singular points S_1 and S_2, respectively, against the dimensionless distance, r/w. The width, w, is varied from 10 mm to 0.15 mm. For the width w from 10 mm to 4 mm, we found that the plots are almost the same line. However, as the width w gets smaller (from 1 mm to 0.15 mm), the plots are clearly different from each other. Because the singular point S_1 is near the singular point S_2, the characteristics of the stress distributions of $-\sigma_{\theta\theta}/\Delta T$ around the two singular points at the interface are not very different from each other. It can be seen that the dimensionless distance, r/w, is an appropriate variable to determine the variations of the stress distributions around both singular points S_1 and S_2 in plate structures. Therefore, the characteristic length L in Equation (4) is replaced by the width w for the expression of the stress fields around the singular point on the stress singularity line in a plate structure.

Furthermore, the variations in the magnitude of the stress $-\sigma_{\theta\theta}/\Delta T$ for the two singular points (S_1 and S_2) at the interface against the dimensionless variable w/L for $r/w = 1.0 \times 10^{-2}$ are shown in Figure 16. For $1 \geq w/L \geq 0.4$, the width of the model is not much less than the length or the height. So, the model is a simple three-dimensional structure, and does not behave like a plate structure. Therefore, the variation of the width in the range $1 \geq w/L \geq 0.4$ has little influence on the stress distribution of $-\sigma_{\theta\theta}/\Delta T$ against the variable r/w around the two singular points. For $0.2 \geq w/L \geq 0.015$, the model obviously behaves like a plate structure. Then, the stress singularity lines get close enough to raise the

magnitude of the stress field around each line. Therefore, the level of the stress distributions of $-\sigma_{\theta\theta}/\Delta T$ around the singular points, S_1 and S_2, increases rapidly as the width w of a plate structure decreases.

4. Conclusion

In this paper, we created a three-dimensional BEM program for thermoelasticity based on Rongved's fundamental solution satisfying the boundary condition at the interface. As a result, accurate analysis using the present BEM program required less memory and was less time-consuming than BEM analysis based on Kelvin's fundamental solutions or FEM analysis. The distributions of stress singularity fields around the singular point on the stress singularity lines for dissimilar materials in three-dimensional bonded joints under thermal loading were presented and compared with the results in the previous research studies. For a uniform temperature variation applied to three-dimensional bonded joints, the stress intensity factors were proportional to the temperature variation, ΔT, and depended on the difference in the thermal expansion coefficients. Logarithmic singularity significantly influenced the characteristics of the stress distributions in three-dimensional bonded joints under thermal loading. For plate structures with very small thickness, the level of the stress distributions around the singular points on the stress singularity lines along the dimensionless distance, r/w, increased rapidly.

References

[Barut et al. 2001] A. Barut, I. Guven, and E. Madenci, "Analysis of singular stress fields at junctions of multiple dissimilar materials under mechanical and thermal loading", *Int. J. Solids Struct.* **38**:50–51 (2001), 9077–9109.

[Cheng et al. 2001] A. H.-D. Cheng, C. S. Chen, M. A. Golberg, and Y. F. Rashed, "BEM for thermoelasticity and elasticity with body force: a revisit", *Eng. Anal. Bound. Elem.* **25**:4–5 (2001), 377–387.

[Cruse et al. 1977] T. A. Cruse, D. W. Snow, and R. B. Wilson, "Numerical solution in axisymmetric elasticity", *Comput. Struct.* **7**:3 (1977), 445–451.

[Dundurs 1969] J. Dundurs, "Discussion of edge-bonded dissimilar orthogonal elastic wedges under normal and shear loading", *J. Appl. Mech. (ASME)* **36** (1969), 650–652.

[Karami and Kuhn 1992] G. Karami and G. Kuhn, "Implementation of thermoelastic forces in boundary element analysis of elastic contact and fracture mechanics problems", *Eng. Anal. Bound. Elem.* **10**:4 (1992), 313–322.

[Koguchi 1997] H. Koguchi, "Stress singularity analysis in three-dimensional bonded structure", *Int. J. Solids Struct.* **34**:4 (1997), 461–480.

[Koguchi et al. 2003] H. Koguchi, M. Yamaguchi, K. Minaki, and P. Monchai, "Analysis of stress singularity fields in three-dimensional joints by three-dimensional boundary element method using fundamental solution for two-phase transversely isotropic materials", *Trans. Jpn. Soc. Mech. Eng. A* **69**:679 (2003), 585–593. In Japanese.

[Li et al. 1992] Y. Li, H. Koguchi, and T. Yada, "Investigation of method of stress relaxation around the apex of ceramics-metal bonded structure (consideration of shape effect of apex in three dimensional dissimilar materials)", *Trans. Jpn. Soc. Mech. Eng.* **58** (1992), 1417–1423.

[Madenci et al. 1998] E. Madenci, S. Shkarayev, and B. Sergeev, "Thermo-mechanical stresses for a triple junction of dissimilar materials: global-local finite element analysis", *Theor. Appl. Fract. Mech.* **30**:2 (1998), 103–117.

[Munz and Yang 1992] D. Munz and Y. Y. Yang, "Stress singularities at the interface in bonded dissimilar materials under mechanical and thermal loading", *J. Appl. Mech. (ASME)* **59** (1992), 857–862.

[Munz and Yang 1994] D. Munz and Y. Y. Yang, "Stresses near the free edge of the interface in ceramic-to-metal joints", *J. Eur. Ceram. Soc.* **13**:5 (1994), 453–460.

[Pageau and Biggers 1995] S. S. Pageau and S. B. Biggers, Jr., "Finite element evaluation of free-edge singular stress fields in anisotropic materials", *Int. J. Numer. Methods Eng.* **38**:13 (1995), 2225–2239.

[Prukvilailert and Koguchi 2005] M. Prukvilailert and H. Koguchi, "Stress singularity analysis around the singular point on the stress singularity line in three-dimensional joints", *Int. J. Solids Struct.* **42**:11–12 (2005), 3059–3074.

[Rizzo and Shippy 1977] F. J. Rizzo and D. J. Shippy, "An advanced boundary integral equation method for three-dimensional thermoelasticity", *Int. J. Numer. Methods Eng.* **11**:11 (1977), 1753–1768.

[Rongved 1955] L. Rongved, "Force interior to one of two joined semi-infinite solids", pp. 1–13 in *Second Midwestern Conference on Solid Mechanics*, 1955.

[Yamada and Okumura 1981] Y. Yamada and H. Okumura, "Analysis of local stress in composite materials by the 3-D finite element", pp. 55–64 in *Proceedings of the Japan–U.S. Conference* (Tokyo), 1981.

[Yang and Munz 1995] Y. Y. Yang and D. Munz, "Stress intensity factor and stress distribution in a joint with an interface corner under thermal and mechanical loading", *Comput. Struct.* **57**:3 (1995), 467–476.

MONCHAI PRUKVILAILERT: monchai@stn.nagaokaut.ac.jp
Department of Mechanical Engineering, Nagaoka University of Technology, 1603-1 Kamitomioka, Nagaoka 940-2188, Japan

HIDEO KOGUCHI: koguchi@mech.nagaokaut.ac.jp
Department of Mechanical Engineering, Nagaoka University of Technology, 1603-1 Kamitomioka, Nagaoka 940-2188, Japan

SHEAR WAVES AT A CORRUGATED INTERFACE BETWEEN TWO DISSIMILAR FIBER-REINFORCED ELASTIC HALF-SPACES

SANASAM SARAT SINGH AND SUSHIL KUMAR TOMAR

A problem of reflection and transmission of shear waves (SH waves) at a corrugated interface between two distinct fiber-reinforced elastic half-spaces has been analyzed. Rayleigh's method of approximation is used to determine the reflection and transmission coefficients. We find that (i) these coefficients are functions of the angle of incidence and the elastic parameters of the media, (ii) the coefficients corresponding to irregularly reflected and transmitted waves are proportional to the amplitude of the corrugated interface, and (iii) reflection and transmission coefficients of the regularly reflected and transmitted waves are greater than those of irregularly reflected and transmitted waves. The energy ratios of reflected and transmitted waves are also presented. Numerical computations are performed and the results obtained are presented graphically. Some earlier results by other workers are recovered by our treatment.

1. Introduction

Problems of wave propagation in elastic media have applications in various fields, such as engineering, geophysics, and seismology. When elastic waves are transmitted through one medium to another medium of different characteristics, the phenomena of reflection and transmission take place. These phenomena depend not only upon the characteristics of the media but are also influenced by the shape of the interface between the two media. Thus, while investigating the problems of reflection and transmission of elastic waves from a corrugated interface, one must take into account the shape of the corrugated interface. Rayleigh [1893] was the first who attempted to solve a problem of wave scattering of sound waves and electromagnetic waves from a rough surface. He gave an approximate method of solving this problem for a sinusoidal surface with a small amplitude, restricting himself to the case of normal wave incidence. In his method, the amplitude and slope of the interface which is expressed in Fourier series are assumed to be very small. By using the boundary conditions of the problem, the unknown coefficients in the solutions are determined for any order of approximation. Rayleigh used this method, in his paper "On the dynamical theory of grating" [1907], and later, researchers in various fields applied his method to explain reflection and transmission phenomena of waves from irregular boundary surfaces. Using different techniques, many problems of reflection and refraction of elastic waves from irregular boundary surfaces have appeared in the open literature, such as [Abubakar 1962; Asano 1960; 1961; 1966; Dunkin and Eringen 1962; Tomar and Saini 1997; Okamoto and Takenaka 1999; Tomar et al. 2002; Gupta 1987; Kumar et al. 2003; Tomar and Kaur 2003; Kaur and Tomar 2004; Kaur et al. 2005].

Chattopadhyay and Choudhury [1990] studied propagation, reflection and transmission of magneto-elastic shear waves in a self-reinforced medium. Later, Chattopadhyay and Choudhury [1995] studied magnetoelastic shear waves in an infinite self-reinforced elastic plate. Sengupta and Nath [2001] investigated surface waves (Rayleigh, Love and Stoneley types) in anisotropic fiber-reinforced solid elastic media. Pradhan et al. [2003] studied the dispersion of Love waves in a self-reinforced layer over an elastic non-homogeneous half-space. Singh and Singh [2004] studied the propagation of plane waves in fiber-reinforced elastic media and showed that the phase velocities of quasi P and SV waves depended on the angle between direction of propagation and the direction of reinforcement. They also discussed the reflection of these elastic waves from the free surface of a fiber reinforced elastic half-space. In this paper, a problem of an SH wave striking obliquely at a corrugated interface between two dissimilar fiber-reinforced elastic half-spaces has been discussed. The amplitude and slope of the corrugated interface are assumed to be very small and Rayleigh's method of approximation has been used to explain the reflection and transmission coefficients for first and second order approximation of the corrugation. For a special type of interface, that is, where the corrugated interface is a simple harmonic interface given by $\zeta = d \cos npx$, we have obtained the formulae of reflection and transmission coefficients of regularly and irregularly reflected and transmitted waves in closed form for the first order approximation of the corrugation. Partitioning of energy due to reflected and refracted waves at the corrugated interface is also presented. Numerically, the effects of corrugation and frequency parameters on these coefficients are studied for a particular model and the results obtained are shown graphically. In the present work, if we neglect the reinforcement parameters, we reduce to the case of a problem in an isotropic medium. In this case, the problem of Asano [1960] can be recovered by setting $\alpha = \beta = 0$ and $\mu_L = \mu_T$. The expressions of energy ratios of regularly and irregularly reflected and transmitted waves are obtained and their variations are depicted graphically with respect to the angle of incidence.

2. Basic relations and equations

The constitutive relations for a fiber-reinforced linear elastic medium, as given in [Belfield et al. 1983], are

$$
\begin{aligned}
\tau_{ij} = \lambda e_{kk}\delta_{ij} + 2\mu_T e_{ij} &+ \alpha\big(a_k a_m e_{km}\delta_{ij} + e_{kk} a_i a_j\big) \\
&+ 2(\mu_L - \mu_T)\big(a_i a_k e_{kj} + a_j a_k e_{ki}\big) + \beta a_k a_m e_{km} a_i a_j, \quad (i, j, k, m = 1, 2, 3), \quad (1)
\end{aligned}
$$

where τ_{ij} is the stress tensor, e_{ij} is the strain tensor, μ_T and λ are elastic constants, α, β, and $(\mu_L - \mu_T)$ are fiber-reinforcement parameters having the dimensions of stress, and a_i are the components of a unit vector $\boldsymbol{a}$ that gives the direction of fiber-reinforcement. Spencer [1974] has shown that if the preferred direction of $\boldsymbol{a}$ is chosen along the x-axis then μ_T can be identified as the shear modulus in transverse shear across the preferred direction and μ_L as the shear modulus in longitudinal shear in the preferred direction. He also established some relations among the elastic constants and given their physical meaning. It can be seen that if $\alpha = \beta = 0$ and $\mu_L = \mu_T$, then (1) reduces to the generalized Hooke's law for an isotropic medium. The strain tensor e_{ij} in terms of displacement components u_i is given by

$$
e_{ij} = \frac{1}{2}\left(\frac{\partial u_i}{\partial x_j} + \frac{\partial u_j}{\partial x_i}\right). \tag{2}
$$

The equations of motion in a fiber-reinforced medium without body forces are

$$\frac{\partial \tau_{ij}}{\partial x_j} = \rho \frac{\partial^2 u_i}{\partial t^2}, \quad (i, j = 1, 2, 3), \tag{3}$$

where ρ is the density of the medium.

Let the direction of reinforcement be along the x-axis: $\boldsymbol{a} = (1, 0, 0)$. For an SH wave propagating in the $x_1 x_2$ plane and having displacement along x_3 axis, we have $\partial/\partial x_3 \equiv 0$. Using the notations $u_3 \equiv u$, $\partial/\partial x_1 \equiv \partial/\partial x$, and $\partial/\partial x_2 \equiv \partial/\partial y$, and substituting Equations (1) and (2) into (3), we obtain

$$\mu_L \frac{\partial^2 u}{\partial x^2} + \mu_T \frac{\partial^2 u}{\partial y^2} = \rho \frac{\partial^2 u}{\partial t^2}.$$

This is the equation of motion for SH wave propagation in a fiber-reinforced elastic medium.

3. Problem and boundary conditions

Let the x and z axes of a Cartesian coordinate system be on the horizontal plane and the y axis be pointing vertically downward. Let the equation of the corrugated interface separating the two different homogeneous fiber-reinforced elastic half-spaces, namely $L_1[-\infty < y \le \zeta(x)]$ and $L_2[\zeta(x) \le y < \infty]$, be given by $y = \zeta(x)$. The geometry of the problem is shown in Figure 1.
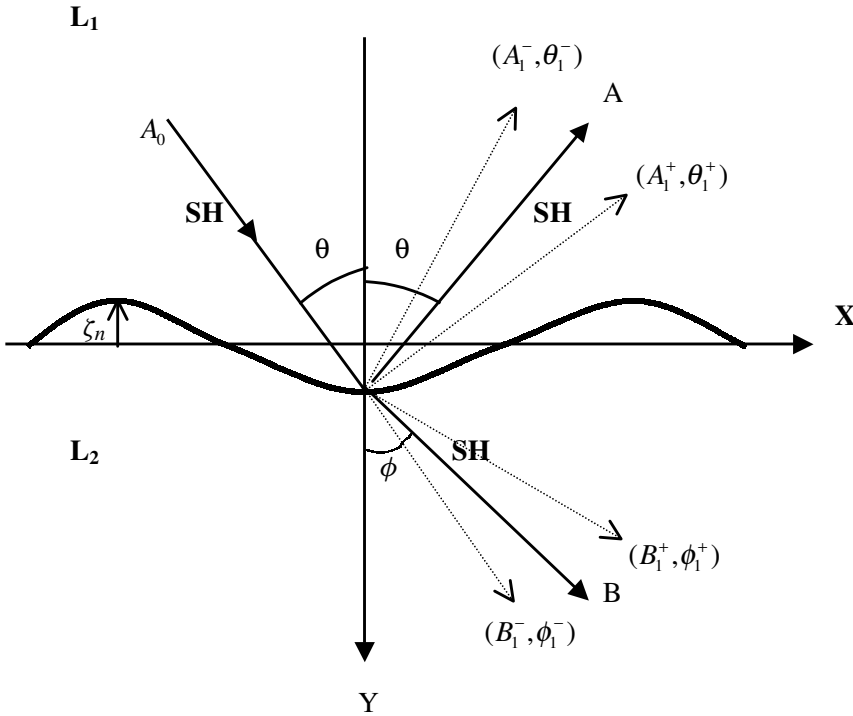
Figure 1. Geometry of the problem.

We shall take both the half-spaces as homogeneous such that the length scale of the reinforcement (that is, the cross section of the fiber, or the separation between fibers) is small compared to the wavelength. We denote the elastic parameters and density in the medium L_l ($l = 1, 2$) by the quantities μ_{L_l}, μ_{T_l}, and ρ_l, respectively. Fourier series representation of the function $\zeta(x)$ is given by

$$\zeta(x) = \sum_{n=1}^{\infty} \left(\zeta_n e^{inpx} + \zeta_{-n} e^{-inpx} \right), \tag{4}$$

where $\zeta(x)$ is a periodic function of x and independent of y whose mean value is zero, ζ_n and ζ_{-n} are Fourier series coefficients, p is the wave number, n is the series expansion order and $i = \sqrt{-1}$. Introducing the constants d, c_n and s_n such that $\zeta_1 = \zeta_{-1} = \frac{1}{2}d$, $\zeta_n = \frac{1}{2}(c_n - i s_n)$, $\zeta_{-n} = \frac{1}{2}(c_n + i s_n)$, and $n = 2, 3, 4, \ldots$ into (4), we obtain

$$\zeta = d \cos px + \sum_{n=2}^{\infty} \left[c_n \cos npx + s_n \sin npx \right].$$

If the coefficients $\zeta_n = \zeta_{-n}$ vanish for $n = 2, 3, 4, \ldots$ then the equation of the corrugated interface reduces to the simple harmonic interface $\zeta = d \cos px$, where d is the amplitude of the corrugation and $2\pi/p$ is the wavelength of corrugation.

The equation of motion for SH wave propagation in the fiber-reinforced elastic half-spaces L_l ($l = 1, 2$) are

$$\mu_{L_l} \frac{\partial^2 u_l}{\partial x^2} + \mu_{T_l} \frac{\partial^2 u_l}{\partial y^2} = \rho_l \frac{\partial^2 u_l}{\partial t^2}.$$

An incident plane SH wave at the corrugated interface, after propagating through the medium L_1, will give rise to regularly reflected and regularly transmitted waves as well as irregularly reflected and irregularly transmitted waves [Asano 1960]. The irregularly reflected and transmitted waves are due to the corrugation of the interface. Thus, the system of waves which arises due to corrugation on both sides of the regularly reflected waves are called *irregularly reflected waves*. Similarly, the system of waves which arises on both sides of regularly transmitted wave are called *irregularly transmitted waves*. These waves propagate with different amplitudes but with the same velocity as the regular waves. The n-th component of the spectrum form of an irregularly reflected wave is given by

$$u_1^{irr} = A_n^+ \exp\left(\frac{i\omega}{c_1} \left(c_1 t - x \sin \theta_n^+ + \eta_n^+ y \right) \right) + A_n^- \exp\left(\frac{i\omega}{c_1} \left(c_1 t - x \sin \theta_n^- + \eta_n^- y \right) \right),$$

where A_n^+ and A_n^- are the amplitude constants of the irregularly reflected SH waves propagating at angles of reflection θ_n^+ and θ_n^- respectively, and where

$$\eta_n^\pm = \sqrt{ \frac{\rho_1 c_1^2}{\mu_{T_1}} - \frac{\mu_{L_1}}{\mu_{T_1}} \sin^2 \theta_n^\pm }.$$

The total displacement u_1 in the medium L_1 will contain the displacements due to the incident wave, the regularly reflected wave, and all irregularly reflected SH waves:

$$u_1 = A_0 \exp\left(\frac{i\omega}{c_1}(c_1 t - x \sin\theta - \eta y)\right) + A \exp\left(\frac{i\omega}{c_1}(c_1 t - x \sin\theta + \eta y)\right)$$

$$+ \sum_{n=1}^{\infty}\left(A_n^+ \exp\left(\frac{i\omega}{c_1}(c_1 t - x \sin\theta_n^+ + \eta_n^+ y)\right) + A_n^- \exp\left(\frac{i\omega}{c_1}(c_1 t - x \sin\theta_n^- + \eta_n^- y)\right)\right), \quad (5)$$

where A_0 is the amplitude of the incident wave, θ is the angle of incidence, ω is the angular frequency, $c_1 = \sqrt{\mu_{L_1}/\rho_1}$ is the speed of SH wave along x-axis in medium L_1, A is the amplitude of the regularly reflected SH wave with the angle of reflection θ, and

$$\eta = \sqrt{\frac{\rho_1 c_1^2}{\mu_{T_1}} - \frac{\mu_{L_1}}{\mu_{T_1}}\sin^2\theta}.$$

Similarly, the n-th component of the spectrum form of the irregularly transmitted wave is given by

$$u_2^{irr} = B_n^+ \exp\left(\frac{i\omega}{c_2}(c_2 t - x \sin\phi_n^+ - \eta_{0n}^+ y)\right) + B_n^- \exp\left(\frac{i\omega}{c_2}(c_2 t - x \sin\phi_n^- - \eta_{0n}^- y)\right),$$

where B_n^+ and B_n^- are the amplitudes of the irregularly transmitted waves with transmitted angles ϕ_n^+ and ϕ_n^-, and

$$\eta_{0n}^{\pm} = \sqrt{\frac{\rho_2 c_2^2}{\mu_{T_2}} - \frac{\mu_{L_2}}{\mu_{T_2}}\sin^2\phi_n^{\pm}}.$$

Thus, the displacement u_2 in the medium L_2 will contain the displacements due to regularly transmitted waves and due to all irregularly transmitted SH waves as

$$u_2 = B \exp\left(\frac{i\omega}{c_2}(c_2 t - x \sin\phi - \eta_0 y)\right)$$

$$+ \sum_{n=1}^{\infty}\left(B_n^+ \exp\left(\frac{i\omega}{c_2}(c_2 t - x \sin\phi_n^+ - \eta_{0n}^+ y)\right) + B_n^- \exp\left(\frac{i\omega}{c_2}(c_2 t - x \sin\phi_n^- - \eta_{0n}^- y)\right)\right), \quad (6)$$

where $c_2 = \sqrt{\mu_{L_2}/\rho_2}$ is the speed of the SH wave along the x axis in medium L_2, B is the amplitude of the regularly transmitted wave, ϕ is the angle which the transmitted wave makes with the normal, and

$$\eta_0 = \sqrt{\frac{\rho_2 c_2^2}{\mu_{T_2}} - \frac{\mu_{L_2}}{\mu_{T_2}}\sin^2\phi}.$$

The angles of the regularly reflected and regularly transmitted waves are related by Snell's law:

$$\frac{\sin\theta}{c_1} = \frac{\sin\phi}{c_2} = \frac{1}{c}, \quad (7)$$

where c is the apparent velocity. The relation between the angles of the regular wave and the corresponding irregular waves is given by the Spectrum theorem [Abubakar 1962; Asano 1960]:

$$\sin\theta_n^{\pm} - \sin\theta = \pm\frac{npc_1}{\omega}, \qquad \sin\phi_n^{\pm} - \sin\phi = \pm\frac{npc_2}{\omega}, \quad (8)$$

where the $\pm$ signs on both sides of each equality are matched.

The appropriate boundary conditions are the continuity of displacements and traction at the corrugated interface. Mathematically, at $y = \zeta(x)$, these boundary conditions are

$$[u_1]_{L_1} = [u_2]_{L_2}, \tag{9}$$

$$[\tau_{32} - \zeta' \tau_{31}]_{L_1} = [\tau_{32} - \zeta' \tau_{31}]_{L_2}, \tag{10}$$

where

$$\zeta' = \sum_{n=1}^{\infty} (\zeta_n e^{inpx} - \zeta_{-n} e^{-inpx}) inp.$$

The boundary condition given in (10) can be expressed in terms of displacements as

$$\mu_{T_1} \frac{\partial u_1}{\partial y} - \zeta' \mu_{L_1} \frac{\partial u_1}{\partial x} = \mu_{T_2} \frac{\partial u_2}{\partial y} - \zeta' \mu_{L_2} \frac{\partial u_2}{\partial x}. \tag{11}$$

Substituting Equations (5)–(8) into the boundary conditions (9) and (11), we obtain

$$A_0 \exp\left(-i\eta \frac{\omega\zeta}{c_1}\right) + A \exp\left(i\eta \frac{\omega\zeta}{c_1}\right) + \sum_{n=1}^{\infty} \left(A_n^+ \exp\left(i\eta_n^+ \frac{\omega\zeta}{c_1}\right) e^{-inpx} + A_n^- \exp\left(i\eta_n^- \frac{\omega\zeta}{c_1}\right) e^{inpx} \right)$$

$$= B \exp\left(-i\eta_0 \frac{\omega\zeta}{c_2}\right) + \sum_{n=1}^{\infty} \left(B_n^+ \exp\left(-i\eta_{0n}^+ \frac{\omega\zeta}{c_2}\right) e^{-inpx} + B_n^- \exp\left(-i\eta_{0n}^- \frac{\omega\zeta}{c_2}\right) e^{inpx} \right) \tag{12}$$

and

$$-A_0 \mu_{T_1} \frac{\eta}{c_1} \exp\left(-i\eta \frac{\omega\zeta}{c_1}\right) + A\eta \frac{\mu_{T_1}}{c_1} \exp\left(i\eta \frac{\omega\zeta}{c_1}\right) \tag{13}$$

$$+ \sum_{n=1}^{\infty} \frac{\mu_{T_1}}{c_1} \left(A_n^+ \eta_n^+ \exp\left(i\eta_n^+ \frac{\omega\zeta}{c_1}\right) e^{-inpx} + A_n^- \eta_n^- \exp\left(i\eta_n^- \frac{\omega\zeta}{c_1}\right) e^{inpx} \right)$$

$$+ \zeta' \frac{\mu_{L_1}}{c_1} \left(\sin\theta \left(A_0 \exp\left(-i\eta \frac{\omega\zeta}{c_1}\right) + A \exp\left(i\eta \frac{\omega\zeta}{c_1}\right) \right) \right.$$

$$\left. + \sum_{n=1}^{\infty} \left(A_n^+ \left(\sin\theta + \frac{npc_1}{\omega}\right) \exp\left(i\eta_n^+ \frac{\omega\zeta}{c_1}\right) e^{-inpx} + A_n^- \left(\sin\theta - \frac{npc_1}{\omega}\right) \exp\left(i\eta_n^- \frac{\omega\zeta}{c_1}\right) e^{inpx} \right) \right)$$

$$= \frac{\mu_{T_2}}{c_2} \left(-B\eta_0 \exp\left(-i\eta_0 \frac{\omega\zeta}{c_2}\right) - \sum_{n=1}^{\infty} \left(B_n^+ \eta_{0n}^+ \exp\left(-i\eta_{0n}^+ \frac{\omega\zeta}{c_2}\right) e^{-inpx} + B_n^- \eta_{0n}^- \exp\left(-i\eta_{0n}^- \frac{\omega\zeta}{c_2}\right) e^{inpx} \right) \right)$$

$$+ \zeta' \frac{\mu_{L_2}}{c_2} \left(B \sin\phi \exp\left(-i\eta_0 \frac{\omega\zeta}{c_2}\right) \right.$$

$$\left. + \sum_{n=1}^{\infty} \left(B_n^+ \left(\sin\phi + \frac{npc_2}{\omega}\right) \exp\left(-i\eta_{0n}^+ \frac{\omega\zeta}{c_2}\right) e^{-inpx} + B_n^- \left(\sin\phi - \frac{npc_2}{\omega}\right) \exp\left(-i\eta_{0n}^- \frac{\omega\zeta}{c_2}\right) e^{inpx} \right) \right).$$

Equations (12) and (13) provide the reflection and transmission coefficients for any order of approximation of corrugation.

4. Solution for the first order approximation

Since we assume that the corrugation and slope of the interface are small, the first order approximation to the exponential term containing ζ can be written as

$$\exp\left(\pm i\eta \frac{\omega\zeta}{c_1}\right) = 1 \pm i\eta \frac{\omega\zeta}{c_1}, \quad \text{etc.} \tag{14}$$

Substituting Equations (4) and (14) into the boundary conditions (12) and (13), and comparing the term independent of x and ζ in both sides of the equations, we have

$$-\frac{A}{A_0} + \frac{B}{A_0} = 1, \qquad \mu_{T_1}\eta \frac{A}{A_0 c_1} + \mu_{T_2}\eta_0 \frac{B}{A_0 c_2} = \frac{\eta \mu_{T_1}}{c_1}. \tag{15}$$

Comparing the coefficients of e^{-inpx} for A_n^+ and B_n^+ on both sides of the equations, we get

$$\frac{A_n^+}{A_0} - \frac{B_n^+}{A_0} = i\zeta_{-n}\omega\left(\left(1 - \frac{A}{A_0}\right)\frac{\eta}{c_1} - \frac{B\eta_0}{c_2 A_0}\right), \tag{16}$$

$$\mu_{T_1}\eta_n^+ \frac{A_n^+}{A_0 c_1} + \mu_{T_2}\eta_{0n}^+ \frac{B_n^+}{A_0 c_2}$$
$$= i\zeta_{-n}\left(\mu_{L_1}np\frac{\sin\theta}{c_1} - \mu_{T_1}\omega\frac{\eta^2}{c_1^2} + \left(\mu_{L_1}np\frac{\sin\theta}{c_1} - \mu_{T_1}\omega\frac{\eta^2}{c_1^2}\right)\frac{A}{A_0} + \left(-\mu_{L_2}np\frac{\sin\theta}{c_1} + \mu_{T_2}\omega\frac{\eta_0^2}{c_2^2}\right)\frac{B}{A_0}\right). \tag{17}$$

Similarly, comparing the coefficients of e^{inpx} for A_n^- and B_n^-, we obtain

$$\frac{A_n^-}{A_0} - \frac{B_n^-}{A_0} = i\zeta_n\omega\left(\left(1 - \frac{A}{A_0}\right)\frac{\eta}{c_1} - \frac{B\eta_0}{c_2 A_0}\right), \tag{18}$$

$$\mu_{T_1}\eta_n^- \frac{A_n^-}{A_0 c_1} + \mu_{T_2}\eta_{0n}^- \frac{B_n^-}{A_0 c_2}$$
$$= i\zeta_n\left(-\mu_{L_1}np\frac{\sin\theta}{c_1} - \mu_{T_1}\omega\frac{\eta^2}{c_1^2} - \left(\mu_{L_1}np\frac{\sin\theta}{c_1} + \mu_{T_1}\omega\frac{\eta^2}{c_1^2}\right)\frac{A}{A_0} + \left(\mu_{L_2}np\frac{\sin\theta}{c_1} + \mu_{T_2}\omega\frac{\eta_0^2}{c_2^2}\right)\frac{B}{A_0}\right). \tag{19}$$

Solving the system of equations (15), we obtain the reflection and transmission coefficients of the regularly reflected and transmitted SH waves as

$$\frac{A}{A_0} = \frac{1-M}{1+M}, \qquad \frac{B}{A_0} = \frac{2}{1+M}, \tag{20}$$

where $M = (\mu_{T_2}\eta_0 c_1)/(\mu_{T_1}\eta c_2)$. These are the reflection and transmission coefficients of the SH wave at a plane interface between two different fiber-reinforced elastic half-spaces.

Solving the systems (16)–(17) and (18)–(19), we obtain

$$\frac{A_n^+}{A_0} = \frac{\Delta_{A_n^+}}{\Delta_n^+}, \qquad \frac{B_n^+}{A_0} = \frac{\Delta_{B_n^+}}{\Delta_n^+}, \qquad \frac{A_n^-}{A_0} = \frac{\Delta_{A_n^-}}{\Delta_n^-}, \qquad \frac{B_n^-}{A_0} = \frac{\Delta_{B_n^-}}{\Delta_n^-}, \tag{21}$$

where

$$\Delta_{A_n^+} = i\zeta_{-n}\left(\mu_{T_2}\omega\frac{\eta_{on}^+\eta}{c_1c_2} + \mu_{L_1}np\frac{\sin\theta}{c_1} - \mu_{T_1}\omega\frac{\eta^2}{c_1^2}\right.$$

$$+\left(\mu_{L_1}np\frac{\sin\theta}{c_1} - \mu_{T_1}\omega\frac{\eta^2}{c_1^2} - \omega\mu_{T_2}\frac{\eta_{on}^+\eta}{c_1c_2}\right)\frac{A}{A_0} + \left(-\mu_{L_2}np\frac{\sin\theta}{c_1} + \mu_{T_2}\omega\frac{\eta_0^2}{c_2^2} - \omega\mu_{T_2}\frac{\eta_{on}^+\eta_0}{c_2^2}\right)\frac{B}{A_0}\right),$$

$$\Delta_{B_n^+} = i\zeta_{-n}\left(\mu_{T_2}\omega\frac{\eta_{on}^+\eta}{c_1c_2} + \mu_{L_1}np\frac{\sin\theta}{c_1} - \mu_{T_1}\omega\frac{\eta^2}{c_1^2} - \mu_{T_1}\omega\frac{\eta\eta_n^+}{c_1^2} - \mu_{T_2}\omega\frac{\eta\eta_{0n}^+}{c_1c_2}\right.$$

$$+\left(\mu_{L_1}np\frac{\sin\theta}{c_1} - \mu_{T_1}\omega\frac{\eta^2}{c_1^2} - \omega\mu_{T_2}\frac{\eta_{on}^+\eta}{c_1c_2} + \omega\frac{\eta}{c_1}\left(\frac{\eta_n^+\mu_{T_1}}{c_1} + \frac{\eta_{0n}^+\mu_{T_2}}{c_2}\right)\right)\frac{A}{A_0}$$

$$+\left(-\mu_{L_2}np\frac{\sin\theta}{c_1} + \mu_{T_2}\omega\frac{\eta_0^2}{c_2^2} - \omega\mu_{T_2}\frac{\eta_{on}^+\eta_0}{c_2^2} + \omega\frac{\eta_0}{c_2}\left(\frac{\eta_n^+\mu_{T_1}}{c_1} + \frac{\eta_{0n}^+\mu_{T_2}}{c_2}\right)\right)\frac{B}{A_0}\right),$$

$$\Delta_{A_n^-} = i\zeta_n\left(\mu_{T_2}\omega\frac{\eta_{on}^-\eta}{c_1c_2} - \mu_{L_1}np\frac{\sin\theta}{c_1} - \mu_{T_1}\omega\frac{\eta^2}{c_1^2}\right.$$

$$-\left(\mu_{L_1}np\frac{\sin\theta}{c_1} + \mu_{T_1}\omega\frac{\eta^2}{c_1^2} + \omega\mu_{T_2}\frac{\eta_{on}^-\eta}{c_1c_2}\right)\frac{A}{A_0} + \left(\mu_{L_2}np\frac{\sin\theta}{c_1} + \mu_{T_2}\omega\frac{\eta_0^2}{c_2^2} - \omega\mu_{T_2}\frac{\eta_{on}^-\eta_0}{c_2^2}\right)\frac{B}{A_0}\right),$$

$$\Delta_{B_n^-} = i\zeta_n\left(\mu_{T_2}\omega\frac{\eta_{on}^-\eta}{c_1c_2} - \mu_{L_1}np\frac{\sin\theta}{c_1} - \mu_{T_1}\omega\frac{\eta^2}{c_1^2} - \mu_{T_1}\omega\frac{\eta\eta_n^-}{c_1^2} - \mu_{T_2}\omega\frac{\eta\eta_{0n}^-}{c_1c_2}\right.$$

$$-\left(\mu_{L_1}np\frac{\sin\theta}{c_1} + \mu_{T_1}\omega\frac{\eta^2}{c_1^2} + \omega\mu_{T_2}\frac{\eta_{on}^-\eta}{c_1c_2} + \omega\frac{\eta}{c_1}\left(\frac{\eta_n^-\mu_{T_1}}{c_1} + \frac{\eta_{0n}^-\mu_{T_2}}{c_2}\right)\right)\frac{A}{A_0}$$

$$+\left(\mu_{L_2}np\frac{\sin\theta}{c_1} + \mu_{T_2}\omega\frac{\eta_0^2}{c_2^2} - \omega\mu_{T_2}\frac{\eta_{on}^-\eta_0}{c_2^2} + \omega\frac{\eta_0}{c_2}\left(\frac{\eta_n^-\mu_{T_1}}{c_1} + \frac{\eta_{0n}^-\mu_{T_2}}{c_2}\right)\right)\frac{B}{A_0}\right),$$

$$\Delta_n^+ = \frac{\eta_n^+\mu_{T_1}}{c_1} + \frac{\eta_{0n}^+\mu_{T_2}}{c_2}, \qquad \Delta_n^- = \frac{\eta_n^-\mu_{T_1}}{c_1} + \frac{\eta_{0n}^-\mu_{T_2}}{c_2}.$$

The formulae in Equation (21) give reflection and transmission coefficients of irregularly reflected and transmitted waves for the first order approximations. Note that these coefficients depend on the elastic parameter of the medium, angle of incidence, corrugation parameter, and frequency of the incident wave.

5. Solution for second order approximation

For the second order approximation, we assume that the corrugation of the interface is so small that we can neglect the term containing the third and higher powers of ζ:

$$\exp\left(\pm i\eta\frac{\omega\zeta}{c_1}\right) = 1 \pm i\eta\frac{\omega\zeta}{c_1} - \left(\eta\frac{\omega\zeta}{c_1}\right)^2, \text{ etc.} \tag{22}$$

Substituting Equations (4) and (22) into the boundary conditions (12) and (13), and comparing the term independent of x, the coefficients of e^{-inpx}, and those of e^{inpx} separately on both sides of the resulting

equations, one obtains six equations in six unknowns (see Appendix). The reflection and transmission coefficients of the reflected and transmitted waves at the corrugated interfaces for the second order approximation can be obtained by solving these equations for any value of n.

6. The case of a simple harmonic interface

We now obtain the reflection and transmission coefficients of incident plane SH waves at an interface given by $\zeta = d \cos px$. This equation for the interface can be obtained by setting $\zeta_1 = \zeta_{-1} = \frac{1}{2}d$ and $\zeta_n = \zeta_{-n} = 0$ for $n = 2, 3, \ldots$ in Equation (4). In this case, $2\pi/p$ is the wavelength and d is the amplitude of corrugation. Thus, the reflection and transmission coefficients for the first order approximation of the corrugation can be obtained by setting $n = 1$ in Equation (21), and we obtain

$$\frac{A_1^+}{A_0} = \frac{\Delta_{A_1^+}}{\Delta_1^+}, \qquad \frac{B_1^+}{A_0} = \frac{\Delta_{B_1^+}}{\Delta_1^+}, \qquad \frac{A_1^-}{A_0} = \frac{\Delta_{A_1^-}}{\Delta_1^-}, \qquad \frac{B_1^-}{A_0} = \frac{\Delta_{B_1^-}}{\Delta_1^-}, \tag{23}$$

where

$$\Delta_{A_1^+} = \frac{id}{2}\left(\mu_{T_2}\omega\frac{\eta_{o1}^+\eta}{c_1 c_2} + \mu_{L_1}p\frac{\sin\theta}{c_1} - \mu_{T_1}\omega\frac{\eta^2}{c_1^2}\right.$$

$$+ \left(\mu_{L_1}p\frac{\sin\theta}{c_1} - \mu_{T_1}\omega\frac{\eta^2}{c_1^2} - \omega\mu_{T_2}\frac{\eta_{o1}^+\eta}{c_1 c_2}\right)\frac{A}{A_0} + \left.\left(-\mu_{L_2}p\frac{\sin\theta}{c_1} + \mu_{T_2}\omega\frac{\eta_0^2}{c_2^2} - \omega\mu_{T_2}\frac{\eta_{01}^+\eta_0}{c_2^2}\right)\frac{B}{A_0}\right),$$

$$\Delta_{B_1^+} = \frac{id}{2}\left(\mu_{T_2}\omega\frac{\eta_{o1}^+\eta}{c_1 c_2} + \mu_{L_1}p\frac{\sin\theta}{c_1} - \mu_{T_1}\omega\frac{\eta^2}{c_1^2} - \mu_{T_1}\omega\frac{\eta\eta_1^+}{c_1^2} - \mu_{T_2}\omega\frac{\eta\eta_{01}^+}{c_1 c_2}\right.$$

$$+ \left(\mu_{L_1}p\frac{\sin\theta}{c_1} - \mu_{T_1}\omega\frac{\eta^2}{c_1^2} - \omega\mu_{T_2}\frac{\eta_{o1}^+\eta}{c_1 c_2} + \omega\frac{\eta}{c_1}\left(\frac{\eta_1^+\mu_{T_1}}{c_1} + \frac{\eta_{01}^+\mu_{T_2}}{c_2}\right)\right)\frac{A}{A_0}$$

$$+ \left.\left(-\mu_{L_2}p\frac{\sin\theta}{c_1} + \mu_{T_2}\omega\frac{\eta_0^2}{c_2^2} - \omega\mu_{T_2}\frac{\eta_{o1}^+\eta_0}{c_2^2} + \omega\frac{\eta_0}{c_2}\left(\frac{\eta_1^+\mu_{T_1}}{c_1} + \frac{\eta_{01}^+\mu_{T_2}}{c_2}\right)\right)\frac{B}{A_0}\right),$$

$$\Delta_{A_1^-} = \frac{id}{2}\left(\mu_{T_2}\omega\frac{\eta_{o1}^-\eta}{c_1 c_2} - \mu_{L_1}p\frac{\sin\theta}{c_1} - \mu_{T_1}\omega\frac{\eta^2}{c_1^2}\right.$$

$$- \left(\mu_{L_1}p\frac{\sin\theta}{c_1} + \mu_{T_1}\omega\frac{\eta^2}{c_1^2} + \omega\mu_{T_2}\frac{\eta_{01}^-\eta}{c_1 c_2}\right)\frac{A}{A_0} + \left.\left(\mu_{L_2}p\frac{\sin\theta}{c_1} + \mu_{T_2}\omega\frac{\eta_0^2}{c_2^2} - \omega\mu_{T_2}\frac{\eta_{01}^-\eta_0}{c_2^2}\right)\frac{B}{A_0}\right),$$

$$\Delta_{B_1^-} = \frac{id}{2}\left(\mu_{T_2}\omega\frac{\eta_{01}^-\eta}{c_1 c_2} - \mu_{L_1}p\frac{\sin\theta}{c_1} - \mu_{T_1}\omega\frac{\eta^2}{c_1^2} - \mu_{T_1}\omega\frac{\eta\eta_1^-}{c_1^2} - \mu_{T_2}\omega\frac{\eta\eta_{01}^-}{c_1 c_2}\right.$$

$$- \left(\mu_{L_1}p\frac{\sin\theta}{c_1} + \mu_{T_1}\omega\frac{\eta^2}{c_1^2} + \omega\mu_{T_2}\frac{\eta_{o1}^-\eta}{c_1 c_2} + \omega\frac{\eta}{c_1}\left(\frac{\eta_1^-\mu_{T_1}}{c_1} + \frac{\eta_{01}^-\mu_{T_2}}{c_2}\right)\right)\frac{A}{A_0}$$

$$+ \left.\left(\mu_{L_2}p\frac{\sin\theta}{c_1} + \mu_{T_2}\omega\frac{\eta_0^2}{c_2^2} - \omega\mu_{T_2}\frac{\eta_{o1}^-\eta_0}{c_2^2} + \omega\frac{\eta_0}{c_2}\left(\frac{\eta_1^-\mu_{T_1}}{c_1} + \frac{\eta_{01}^-\mu_{T_2}}{c_2}\right)\right)\frac{B}{A_0}\right),$$

$$\Delta_1^+ = \frac{\eta_1^+\mu_{T_1}}{c_1} + \frac{\eta_{01}^+\mu_{T_2}}{c_2}, \qquad\qquad\qquad \Delta_1^- = \frac{\eta_1^-\mu_{T_1}}{c_1} + \frac{\eta_{01}^-\mu_{T_2}}{c_2}.$$

7. Energy equation

The expression of the energy flux for SH waves is obtained by multiplying the total energy per unit volume, which is twice the mean kinetic energy density, by the velocity of the propagation and the area of the wave front involved. The area of the wave front is proportional to the cosine of the angle between the wave normal and the vertical. The modulus of energy ratio of the regularly and irregularly reflected and transmitted SH waves are expressed as

$$
E_{\text{RF}} = \frac{|A|^2}{|A_0|^2}, \qquad E_{\text{RF}-n}^+ = \frac{|A_n^+|^2 \cos\theta_n^+}{|A_0|^2 \cos\theta}, \qquad E_{\text{RF}-n}^- = \frac{|A_n^-|^2 \cos\theta_n^-}{|A_0|^2 \cos\theta},
$$

$$
E_{\text{TR}} = \frac{|B|^2}{|A_0|^2} \frac{\rho_2 c_2^2 \tan\theta}{\rho_1 c_1^2 \tan\phi}, \qquad E_{\text{TR}-n}^+ = \frac{|B_n^+|^2}{|A_0|^2} \frac{\rho_2 c_2 \cos\phi_n^+}{\rho_1 c_1 \cos\theta},
$$

$$
E_{\text{TR}-n}^- = \frac{|B_n^-|^2}{|A_0|^2} \frac{\rho_2 c_2 \cos\phi_n^-}{\rho_1 c_1 \cos\theta},
$$

where E_{RF} is the ratio of the energy of regularly reflected wave to the energy of the incident wave, $E_{\text{RF}-n}^\pm$ are the ratios of the energy of an irregularly reflected wave for the n-th spectrum to the energy of an incident wave, E_{TR} is the ratio of the energy of a regularly transmitted wave to the energy of an incident wave, and $E_{\text{TR}-n}^\pm$ are ratios of the energy of an irregularly transmitted wave for n-th spectrum to the energy of an incident wave. Thus, the energy partitioning equation at the corrugated interface is given by

$$
\left|\frac{A}{A_0}\right|^2 + \sum_{n=1}^{\infty} \left(\frac{\cos\theta_n^+}{\cos\theta} \left|\frac{A_n^+}{A_0}\right|^2 + \frac{\cos\theta_n^-}{\cos\theta} \left|\frac{A_n^-}{A_0}\right|^2 \right) + \frac{\rho_2 c_2^2 \tan\theta}{\rho_1 c_1^2 \tan\phi} \left|\frac{B}{A_0}\right|^2
$$

$$
+ \sum_{n=1}^{\infty} \left(\frac{\rho_2 c_2 \cos\phi_n^+}{\rho_1 c_1 \cos\theta} \left|\frac{B_n^+}{A_0}\right|^2 + \frac{\rho_2 c_2 \cos\phi_n^-}{\rho_1 c_1 \cos\theta} \left|\frac{B_n^-}{A_0}\right|^2 \right) = 1. \quad (24)
$$

When $n = 1$, Equation (24) reduces to

$$
\left|\frac{A}{A_0}\right|^2 + \left|\frac{A_1^+}{A_0}\right|^2 \frac{\cos\theta_1^+}{\cos\theta} + \left|\frac{A_1^-}{A_0}\right|^2 \frac{\cos\theta_1^-}{\cos\theta} + \left|\frac{B}{A_0}\right|^2 \frac{\rho_2 c_2^2 \tan\theta}{\rho_1 c_1^2 \tan\phi} + \left|\frac{B_1^+}{A_0}\right|^2 \frac{\rho_2 c_2 \cos\phi_1^+}{\rho_1 c_1 \cos\theta} + \left|\frac{B_1^-}{A_0}\right|^2 \frac{\rho_2 c_2 \cos\phi_1^-}{\rho_1 c_1 \cos\theta} = 1.
$$

Thus, the sum of energy ratios of the reflected and transmitted waves at the interface $\zeta = d \cos px$ must be equal to unity.

8. Particular case

When the fiber-reinforced elastic half-spaces L_1 and L_2 are reduced to isotropic half-spaces, we have $\mu_{T_1} = \mu_{L_1} = \mu_1$, $c_1^2 = \mu_1/\rho_1$, $\mu_{T_2} = \mu_{L_2} = \mu_2$, $c_2^2 = \mu_2/\rho_2$, $\eta = \cos\theta$ and $\eta_0 = \cos\phi$. With these values, the reflection and transmission coefficients at the plane interface between two uniform elastic half-spaces can be obtained from Equation (20), with a modified value M given by $M = (\mu_2 c_1 \cos\phi)/(\mu_1 c_2 \cos\theta)$. This result perfectly matches those given in Achenbach [1976]. (For the relevant problem, refer to Equations (5.77) and (5.78) on page 184).

Moreover, in this case, the values of η_1^+, η_1^-, η_{01}^+ and η_{01}^- reduce to $\eta_1^+ = \cos\theta_1^+$, $\eta_1^- = \cos\theta_1^-$, $\eta_{01}^+ = \cos\phi_1^+$, $\eta_{01}^- = \cos\phi_1^-$. The reflection and transmission coefficients for the first-order approximation of corrugation are given by Equation (23), with the modified values

$$\Delta_{A_1^+} = \frac{id}{2}\left(\mu_2\omega\frac{\cos\phi_1^+\cos\theta}{c_1c_2} + \mu_1 p\frac{\sin\theta}{c_1} - \mu_1\omega\frac{\cos^2\theta}{c_1^2}\right.$$
$$+ \left(\mu_1 p\frac{\sin\theta}{c_1} - \mu_1\omega\frac{\cos^2\theta}{c_1^2} - \omega\mu_2\frac{\cos\phi_1^+\cos\theta}{c_1c_2}\right)\frac{A}{A_0}$$
$$\left. + \left(-\mu_2 p\frac{\sin\theta}{c_1} + \mu_2\omega\frac{\cos^2\phi}{c_2^2} - \omega\mu_2\frac{\cos\phi_1^+\cos\phi}{c_2^2}\right)\frac{B}{A_0}\right),$$

$$\Delta_{B_1^+} = \frac{id}{2}\left(\mu_2\omega\frac{\cos\phi_1^+\cos\theta}{c_1c_2} + \mu_1 p\frac{\sin\theta}{c_1} - \mu_1\omega\frac{\cos^2\theta}{c_1^2} - \mu_1\omega\frac{\cos\theta\cos\theta_1^+}{c_1^2} - \mu_2\omega\frac{\cos\theta\cos\phi_1^+}{c_1c_2}\right.$$
$$+ \left(\mu_1 p\frac{\sin\theta}{c_1} - \mu_1\omega\frac{\cos^2\theta}{c_1^2} - \omega\mu_2\frac{\cos\phi_1^+\cos\theta}{c_1c_2} + \omega\frac{\cos\theta}{c_1}\left(\frac{\cos\theta_1^+\mu_1}{c_1} + \frac{\cos\phi_1^+\mu_2}{c_2}\right)\right)\frac{A}{A_0}$$
$$\left. + \left(-\mu_2 p\frac{\sin\theta}{c_1} + \mu_2\omega\frac{\cos^2\phi}{c_2^2} - \omega\mu_2\frac{\cos\phi_1^+\cos\phi}{c_2^2} + \omega\frac{\cos\phi}{c_2}\left(\frac{\cos\theta_1^+\mu_1}{c_1} + \frac{\cos\phi_1^+\mu_2}{c_2}\right)\right)\frac{B}{A_0}\right),$$

$$\Delta_{A_1^-} = \frac{id}{2}\left(\mu_2\omega\frac{\cos\phi_1^-\cos\theta}{c_1c_2} - \mu_1 p\frac{\sin\theta}{c_1} - \mu_1\omega\frac{\cos^2\theta}{c_1^2}\right.$$
$$- \left(\mu_1 p\frac{\sin\theta}{c_1} + \mu_1\omega\frac{\cos^2\theta}{c_1^2} + \omega\mu_2\frac{\cos\phi_1^-\cos\theta}{c_1c_2}\right)\frac{A}{A_0}$$
$$\left. + \left(\mu_2 p\frac{\sin\theta}{c_1} + \mu_2\omega\frac{\cos^2\phi}{c_2^2} - \omega\mu_2\frac{\cos\phi_1^-\cos\phi}{c_2^2}\right)\frac{B}{A_0}\right),$$

$$\Delta_{B_1^-} = \frac{id}{2}\left(\mu_2\omega\frac{\cos\phi_1^-\cos\theta}{c_1c_2} - \mu_1 p\frac{\sin\theta}{c_1} - \mu_1\omega\frac{\cos^2\theta}{c_1^2} - \mu_1\omega\frac{\cos\theta\cos\theta_1^-}{c_1^2} - \mu_2\omega\frac{\cos\theta\cos\phi_1^-}{c_1c_2}\right.$$
$$- \left(\mu_1 p\frac{\sin\theta}{c_1} + \mu_1\omega\frac{\cos^2\theta}{c_1^2} + \omega\mu_2\frac{\cos\phi_1^-\cos\theta}{c_1c_2} + \omega\frac{\cos\theta}{c_1}\left(\frac{\cos\theta_1^-\mu_1}{c_1} + \frac{\cos\phi_1^-\mu_2}{c_2}\right)\right)\frac{A}{A_0}$$
$$\left. + \left(\mu_2 p\frac{\sin\theta}{c_1} + \mu_2\omega\frac{\cos^2\phi}{c_2^2} - \omega\mu_2\frac{\cos\phi_1^-\cos\phi}{c_2^2} + \omega\frac{\cos\phi}{c_2}\left(\frac{\cos\theta_1^-\mu_1}{c_1} + \frac{\cos\phi_1^-\mu_2}{c_2}\right)\right)\frac{B}{A_0}\right),$$

$$\Delta_1^+ = \frac{\cos\theta_1^+\mu_1}{c_1} + \frac{\cos\phi_1^+\mu_2}{c_2}, \qquad \Delta_1^- = \frac{\cos\theta_1^-\mu_1}{c_1} + \frac{\cos\phi_1^-\mu_2}{c_2}.$$

For the normal incidence, that is, when $\theta = \phi = 0$ and from spectrum theorem given by Equation (8), we have $\cos\theta_1^+ = \cos\theta_1^-$, $\cos\phi_1^+ = \cos\phi_1^-$. In this case of normal incidence, we see that $A_1^+/A_0 = A_1^-/A_0$ and $B_1^+/A_0 = B_1^-/A_0$. These are the same results as obtained by Asano [1960] for the relevant problem.

9. Numerical results and discussion

To study the effect of various parameters on reflection and transmission coefficients, we computed the latter for a specific model having a simple cosine law interface, $\zeta = d \cos px$. We used the following relevant elastic parameters in the fiber-reinforced media:

In medium L_1, $\mu_{L_1} = 4.4 \times 10^9 \, \text{N/m}^2$, $\mu_{T_1} = 1.89 \times 10^9 \, \text{N/m}^2$ and $\rho_1 = 5.60 \times 10^3 \, \text{kg/m}^3$. In medium L_2, $\mu_{L_2} = 5.66 \times 10^9 \, \text{N/m}^2$, $\mu_{T_2} = 2.46 \times 10^9 \, \text{N/m}^2$, and $\rho_2 = 7.80 \times 10^3 \, \text{kg/m}^3$. Unless otherwise specified, $\omega d/c_1 = 0.12$, $pd = 0.00155$ and $\theta = 25°$.

Figures 2 and 3 show the variation of the modulus of reflection and transmission coefficients and energy ratios of reflected and transmitted waves with angle of incidence θ. Figure 2, top, shows that the reflection coefficient A/A_0 decreases, while the transmission coefficient B/A_0 increases with increasing θ. It is also clear that the reflection and transmission coefficients at plane interface between two fiber-reinforced half-spaces possess reverse behavior with angle of incidence.

In Figure 2, bottom, the reflection coefficients A_1^+/A_0 and A_1^-/A_0 of irregularly reflected waves at angles θ_1^+ and θ_1^- start from a certain value which increases up to $\theta = 12°$, and thereafter decrease with increasing angle of incidence. The transmission coefficient B_1^+/A_0 of irregularly transmitted waves at angle ϕ_1^+ increases with increasing angle of incidence, while the transmission coefficient B_1^-/A_0 of irregularly transmitted waves at angle ϕ_1^- starts from a certain value which increases up to $\theta = 14°$ and thereafter decreases with angle of incidence. Figure 3 shows the variation of energy ratios with θ. Note that E_{RF} increases and E_{TR} decreases with the angle of incidence. However, the rate of increase or decrease is very slow up to $\theta = 60°$ but at a very fast rate thereafter. At normal incidence, E_{TR} has maximum value and E_{RF} has minimum value. The energy ratios E_{RF-1}^+ and E_{RF-1}^- of irregularly reflected waves at angles θ_1^+ and θ_1^-, respectively, start from a certain value, increase slightly up to $\theta = 13°$, and thereafter decrease with θ, achieving minimum values near grazing incidence. The energy ratio E_{TR-1}^+ increases with increase in the angle of incidence in an almost similar pattern as that of E_{RF} with θ. The energy ratio E_{TR-1}^- starts from a certain value at normal incidence and then increases until $\theta = 16°$. It then decreases to certain value and again starts increasing, achieving maximum value at $\theta = 83°$. Beyond this point, the energy ratio decreases with the angle of incidence. These figures show that for the incident energy, the maximum amount of energy is carried by regularly reflected and transmitted waves, and a very small amount by irregular waves. The sum of energy ratios is very close to unity, which shows that there is no dissipation during transmission.

Figures 4 and 5 show the variation of the modulus of reflection and transmission coefficients and energy ratios with the frequency parameter $(\omega d/c_1)$, when the SH wave is incident at $\theta = 25^0$. We see that the reflection and transmission coefficients of regular waves and their corresponding energy ratios are not influenced by the frequency parameter. The reflection coefficients A_1^+/A_0, and A_1^-/A_0, and the transmission coefficients B_1^+/A_0, and B_1^-/A_0 of the irregular waves increase linearly with the increase in the frequency parameter. Thus the reflection and transmission coefficients of irregular waves are influenced by the frequency parameter. Figure 5, bottom, shows that the energy ratios of irregular waves increase with increasing frequency parameter.

Figures 6 and 7 show the variation of the modulus of reflection and transmission coefficients and energy ratios with the corrugation parameter pd. The top part of Figures 6 and 7 show that reflection and transmission coefficients of regular waves and their corresponding energy ratios are not influenced by
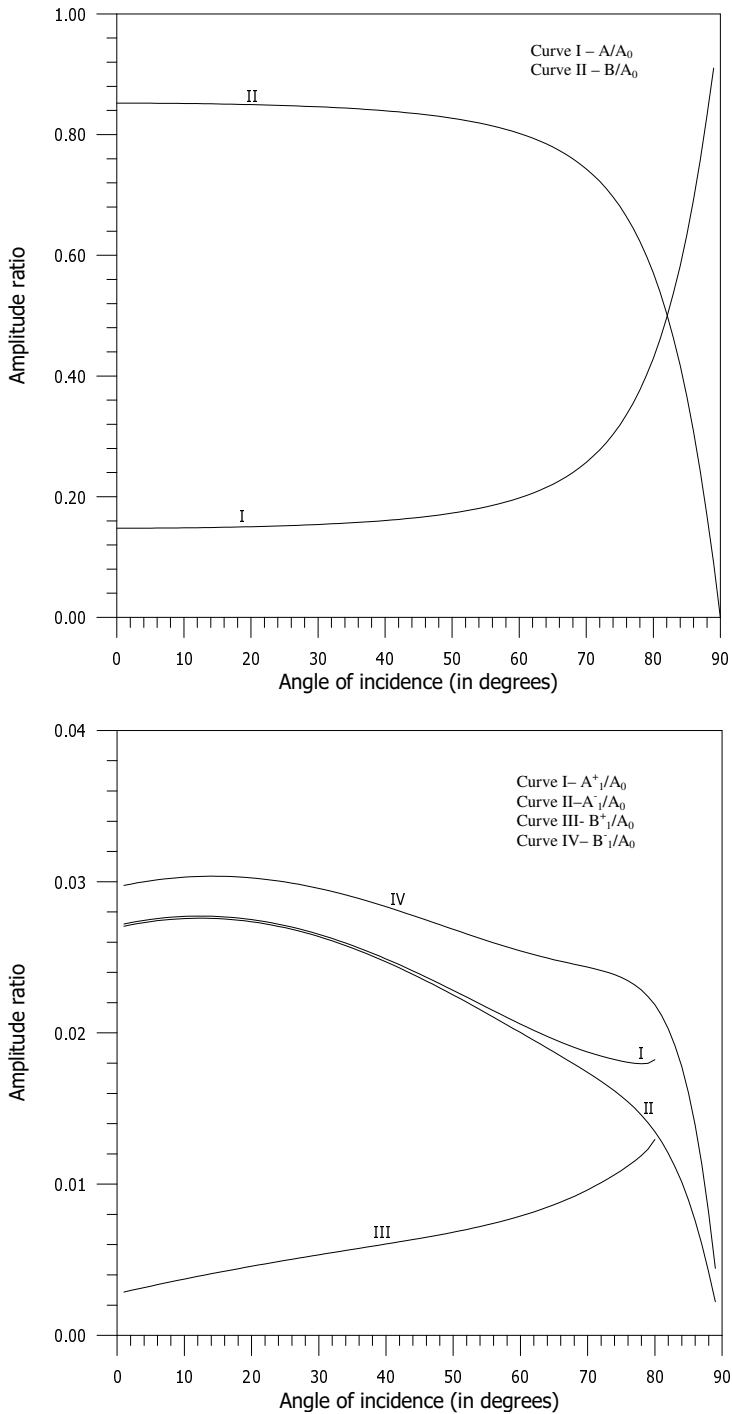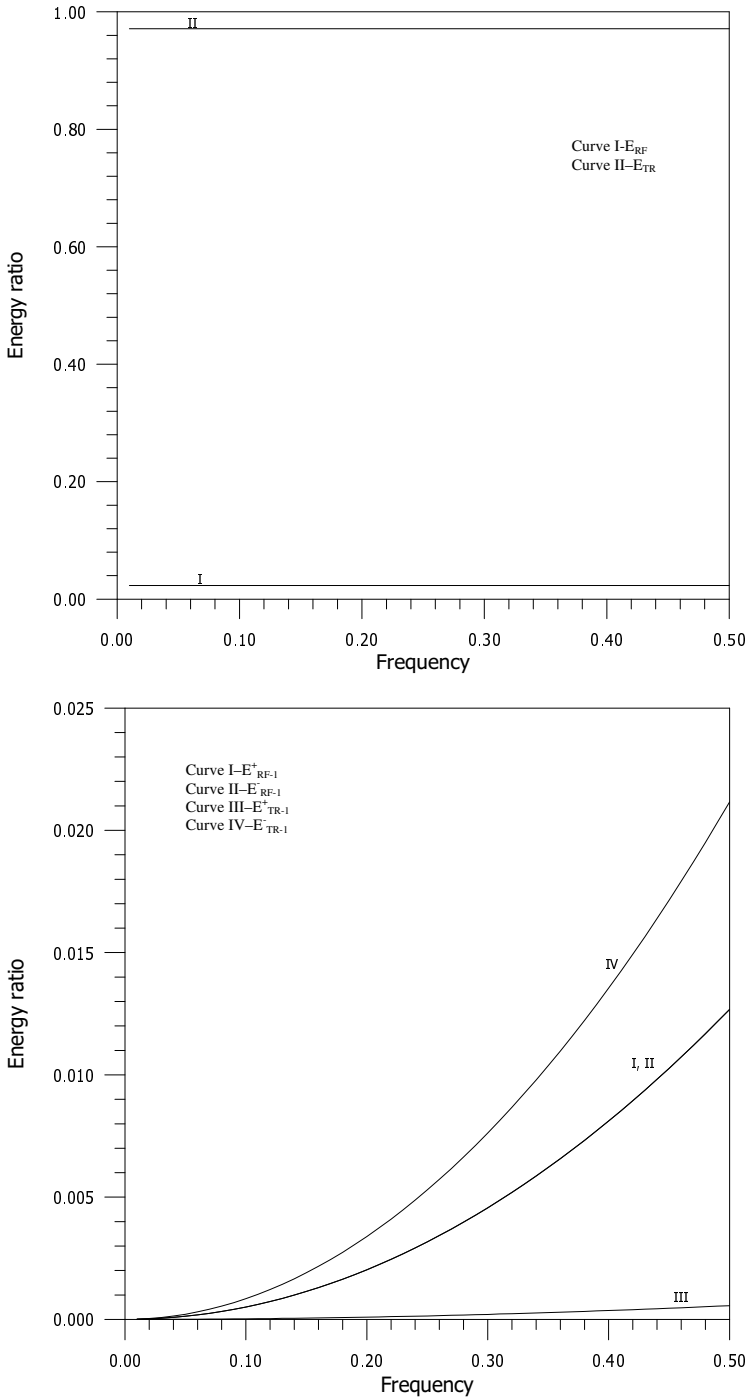
Figure 2. Variation of the modulus of reflection and transmission coefficients of regular (top) and irregular (top) waves with angle of incidence, when $pd = 1.55 \times 10^{-3}$ and $\omega d/c_1 = 0.12$.
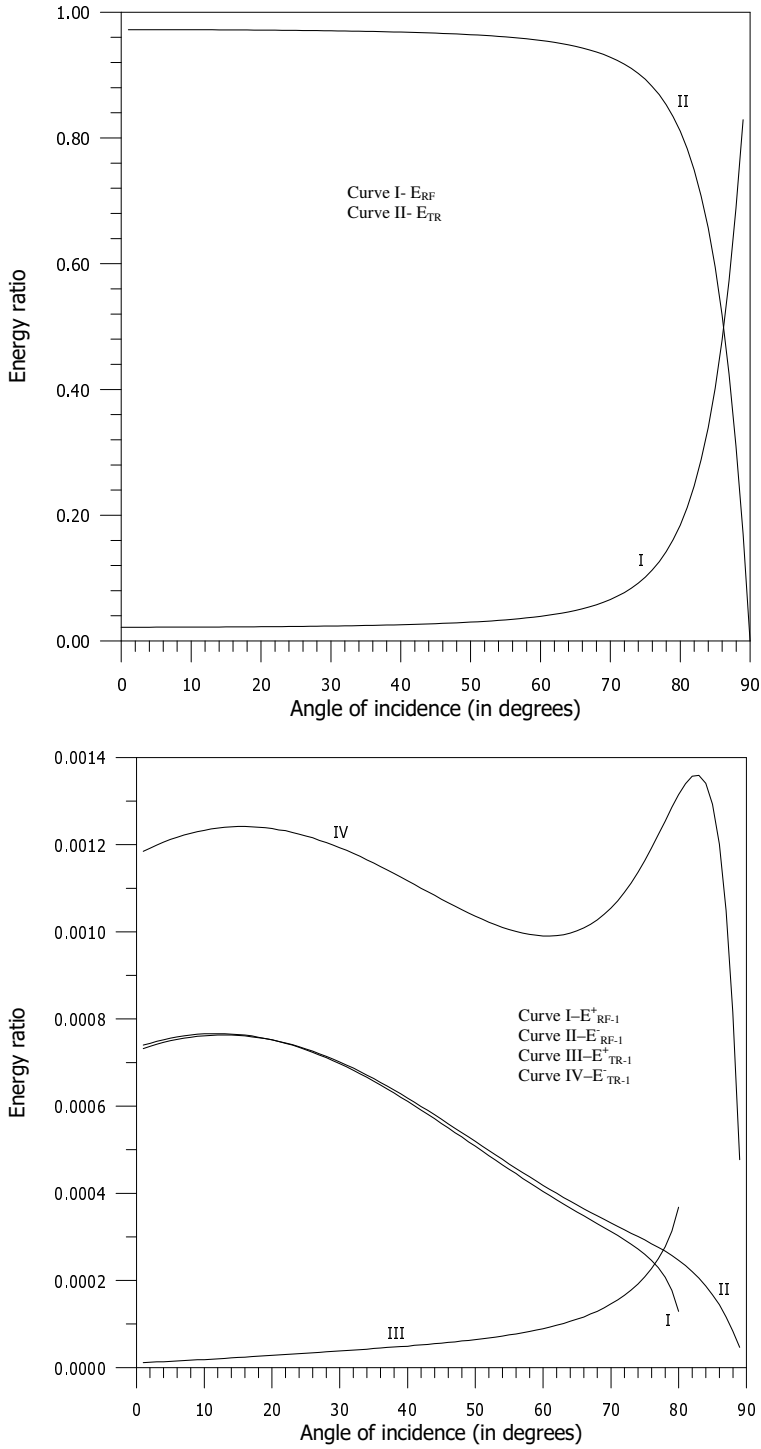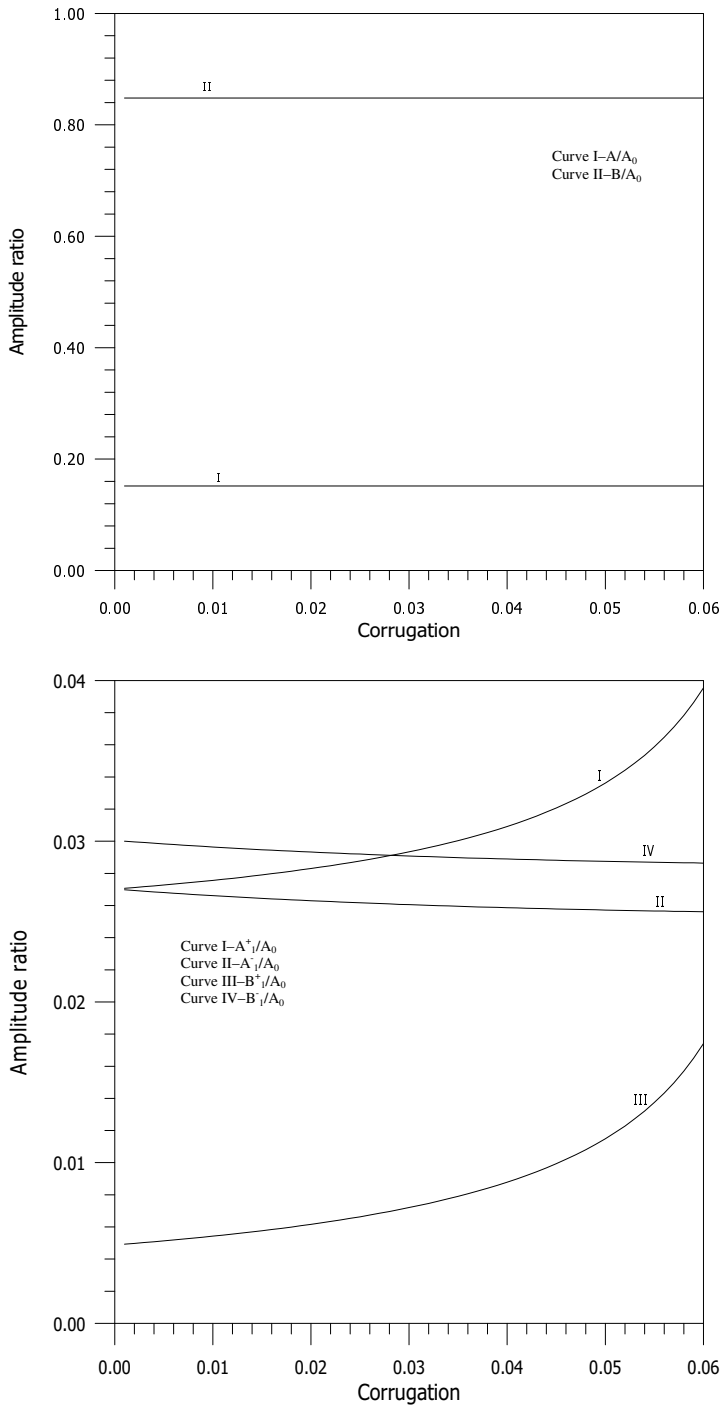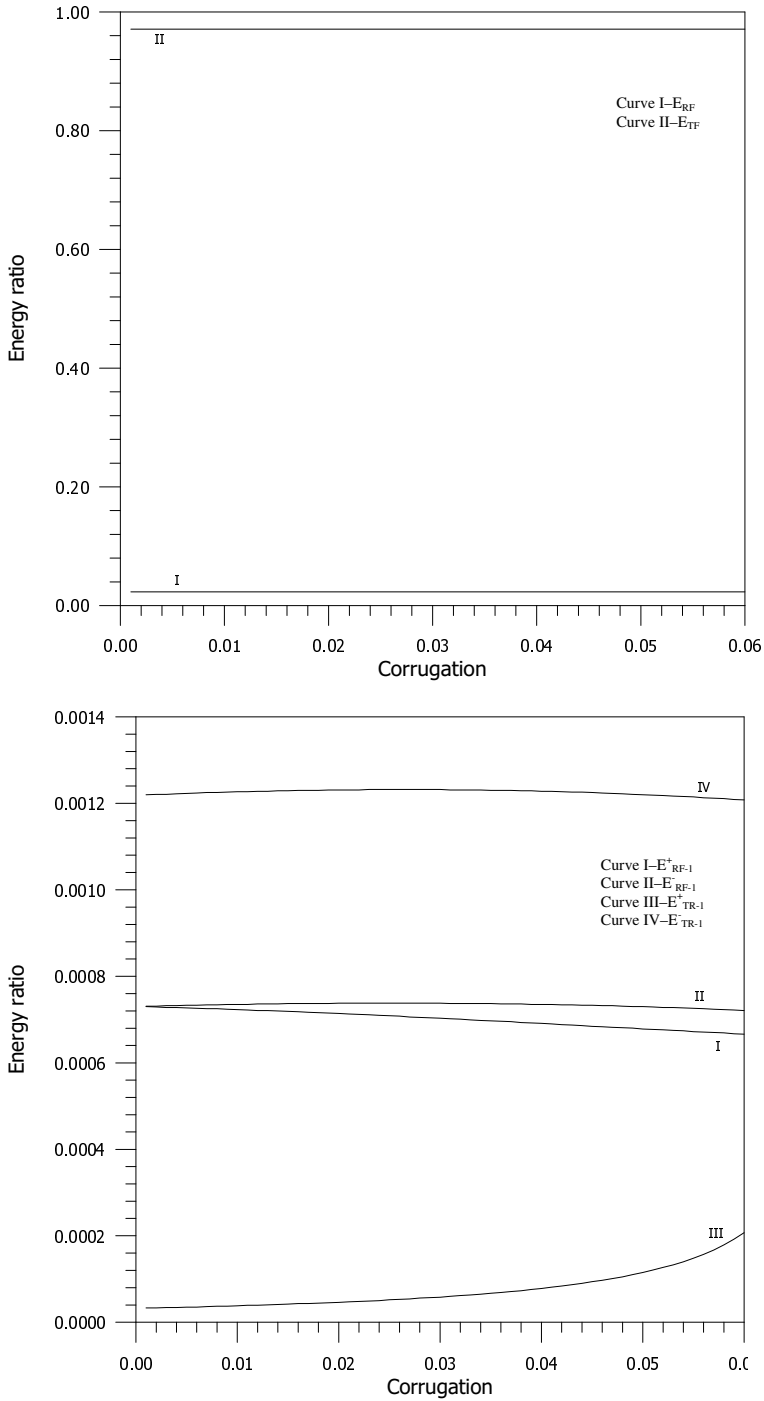
Figure 3. Variation of the modulus of the energy ratios of regularly (top) and irregularly (bottom) reflected and transmitted SH waves, when $pd = 1.55 \times 10^{-3}$ and $\omega d / c_1 = 0.12$.
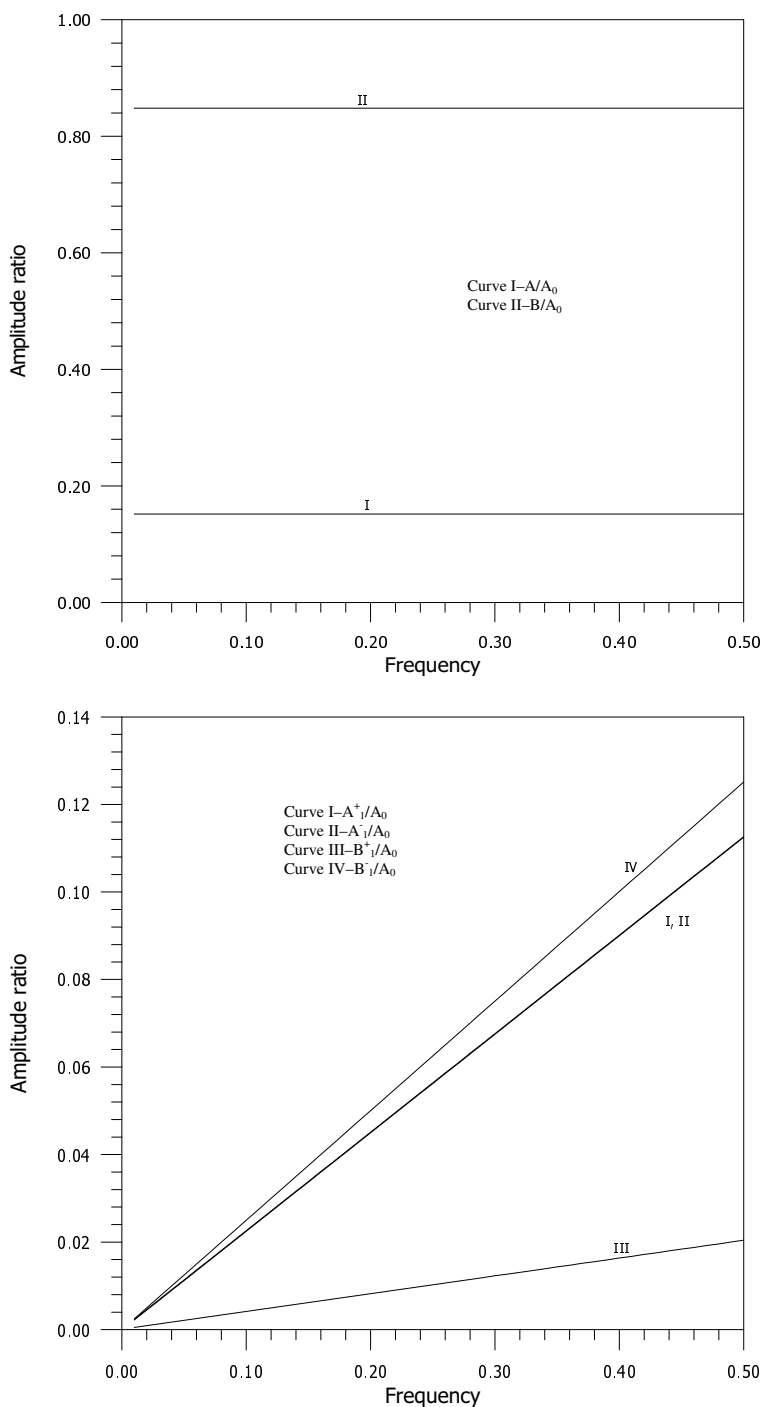
Figure 4. Variation of the modulus of reflection and transmission coefficients of regularly (top) and irregularly (bottom) reflected and transmitted SH waves with frequency $\omega d/c_1$, when $pd = 1.55 \times 10^{-3}$ and $\theta = 25°$.

Figure 5. Variation of modulus of energy ratios of regularly (top) and irregularly (bottom) reflected and transmitted SH waves with frequency $\omega d/c_1$, when $pd = 1.55 \times 10^{-3}$ and $\theta = 25°$.

Figure 6. Variation of the modulus of reflection and transmission coefficients of regularly (top) and irregularly (bottom) reflected and transmitted SH waves with corrugation parameter pd, when $\omega d/c_1 = 0.12$ and $\theta = 25°$.

Figure 7. Variation of the modulus of energy ratios of regularly (top) and irregularly (bottom) reflected and transmitted SH waves with corrugation parameter pd, when $\omega d / c_1 = 0.12$ and $\theta = 25°$.

the corrugation parameter, as was expected. Figure 6, bottom, shows that the reflection coefficient A_1^+/A_0 and the transmission coefficient B_1^+/A_0 increase as the corrugation parameter pd increases, while the reflection coefficient A_1^-/A_0 and the transmission coefficient B_1^-/A_0 decrease as pd increases. Hence, the coefficients corresponding to irregular waves are found to be influenced by the corrugation parameter pd. In Figure 7, bottom, we see that as the corrugation parameter pd increases, the energy ratios $E_{\mathrm{RF}-1}^+$ and $E_{\mathrm{RF}-1}^-$ decrease at a very small rate, the energy ratio $E_{\mathrm{TR}-1}^+$ increases, and the energy ratio $E_{\mathrm{TR}-1}^-$ decreases but at very small rate.

10. Conclusions

The reflection and transmission phenomena of an incident SH wave at a corrugated interface between two dissimilar elastic fiber-reinforced half-spaces are studied. It is assumed that amplitude and slope of the corrugated interface are small and the formulae for reflection and transmission coefficients for the first and second order approximations of corrugation are presented using Rayleigh's method of approximation. These coefficients are expressed in the closed form for the first order approximation of corrugation, and for a special type of interface. The energy partition equation at a corrugated interface is also obtained. Numerically, these coefficients and energy ratios are calculated for a specific model and the results obtained are shown graphically. We conclude that

  (i) The reflection and transmission coefficients are functions of elastic parameters and the angle of incidence. Moreover, the coefficients of irregularly reflected and transmitted waves, and hence the energy ratios, are functions of the corrugation parameters and frequency of the incident wave.

 (ii) The reflection and transmission coefficients of regularly reflected and transmitted SH waves are independent of the corrugation and frequency parameters. But there is a significant effect of corrugation and frequency on the reflection and transmission coefficients of irregularly reflected and transmitted waves. Reflection and transmission coefficients of irregularly reflected and transmitted waves increase as the normalized frequency $\omega d/c_1$ and corrugation parameter pd increase.

(iii) The reflection and transmission coefficients of regular waves are greater than those of irregular waves. It is also noted that the energy ratio of regular waves is greater than the energy ratios of irregular waves,

(iv) The coefficients and energy ratios of irregular waves increase with increasing frequency and corrugation parameter. The sum of the energy ratios of reflected and transmitted waves for first order approximation of corrugation is found to be very close to unity.

Acknowledgements

Appendix: Equations for the second-order approximation

$$\left(1 - 2\zeta_{-n}\zeta_n \frac{\omega^2\eta^2}{c_1^2}\right)(A_0 + A) + i\zeta_n\eta_n^+ \frac{\omega}{c_1}A_n^+ + i\zeta_{-n}\eta_n^- \frac{\omega}{c_1}A_n^-$$
$$= \left(1 - 2\zeta_{-n}\zeta_n \frac{\omega^2\eta_0^2}{c_2^2}\right)B - i\zeta_n\eta_{0n}^+ \frac{\omega}{c_2}B_n^+ - i\zeta_{-n}\eta_{0n}^- \frac{\omega}{c_2}B_n^-,$$

$$\mu_{T_1}\frac{\eta}{c_1}\left(1 - 2\zeta_{-n}\zeta_n \frac{\omega^2\eta^2}{c_1^2}\right)(A - A_0) + \mu_{T_2}\frac{\eta_0}{c_2}\left(1 - 2\zeta_{-n}\zeta_n \frac{\omega^2\eta_0^2}{c_2^2}\right)B$$
$$+ i\zeta_n\left(\mu_{T_1}(\eta_n^+)^2\frac{\omega}{c_1^2} + \mu_{L_1}np\frac{\sin\theta_n^+}{c_1}\right)A_n^+ + i\zeta_{-n}\left(\mu_{T_1}(\eta_n^-)^2\frac{\omega}{c_1^2} - \mu_{L_1}np\frac{\sin\theta_n^-}{c_1}\right)A_n^-$$
$$= i\zeta_n\left(\mu_{T_2}(\eta_{0n}^+)^2\frac{\omega}{c_2^2} + \mu_{L_2}np\frac{\sin\phi_n^+}{c_2}\right)B_n^+ + i\zeta_{-n}\left(\mu_{T_2}(\eta_{0n}^-)^2\frac{\omega}{c_2^2} - \mu_{L_2}np\frac{\sin\phi_n^-}{c_2}\right)B_n^-,$$

$$i\eta\zeta_{-n}\frac{\omega}{c_1}(A_0 + A) - \left(1 - 2\zeta_{-n}\zeta_n \frac{(\omega\eta_n^+)^2}{c_1^2}\right)A_n^+ + \zeta_{-n}^2\frac{(\omega\eta_n^-)^2}{c_1^2}A_n^-$$
$$= i\zeta_{-n}\eta_0\frac{\omega B}{c_2} - \left(1 - 2\zeta_{-n}\zeta_n \frac{(\omega\eta_{0n}^+)^2}{c_2^2}\right)B_n^+ + \zeta_{-n}^2\frac{(\omega\eta_{0n}^-)^2}{c_2^2}B_n^-,$$

$$i\zeta_{-n}\left(\mu_{T_1}\eta^2\frac{\omega}{c_1^2} - \mu_{L_1}np\frac{\sin\theta}{c_1}\right)(A_0 + A) - i\zeta_{-n}\left(\mu_{T_2}\frac{\omega\eta_0^2}{c_2^2} - \mu_{L_2}np\frac{\sin\theta}{c_1}\right)B$$
$$+ \mu_{T_1}\frac{\eta_n^+}{c_1}\left(1 - 2(\eta_n^+)^2\zeta_n\zeta_{-n}\frac{\omega^2}{c_1^2}\right)A_n^+ + \zeta_{-n}^2\left(\mu_{T_1}(\eta_n^-)^3\frac{\omega^2}{c_1^3} - \mu_{L_1}np\eta_n^-\frac{\sin\theta_n^-}{c_1^2}\right)A_n^-$$
$$= -\mu_{T_2}\frac{\eta_{0n}^+}{c_2}\left(1 - 2\zeta_{-n}\zeta_n\frac{(\omega\eta_{0n}^+)^2}{c_2^2}\right)B_n^+ + \zeta_{-n}^2\frac{\omega\eta_{0n}^-}{c_2^2}\left(\mu_{T_2}(\eta_{0n}^-)^2\frac{\omega}{c_2} - \mu_{L_2}np\sin\phi_n^-\right)B_n^-,$$

$$i\eta\zeta_n\frac{\omega}{c_1}(A_0 + A) + \zeta_n^2\frac{(\omega\eta_n^+)^2}{c_1^2}A_n^+ - \left(1 - 2\zeta_{-n}\zeta_n\frac{(\omega\eta_n^-)^2}{c_1^2}\right)A_n^-$$
$$= i\zeta_n\eta_0\frac{\omega B}{c_2} + \zeta_n^2\frac{(\omega\eta_{0n}^+)^2}{c_2^2}B_n^+ - \left(1 - 2\zeta_{-n}\zeta_n\frac{(\omega\eta_{0n}^-)^2}{c_2^2}\right)B_n^-,$$

$$i\zeta_n\left(\mu_{T_1}\frac{\omega\eta^2}{c_1^2} + \mu_{L_1}np\frac{\sin\theta}{c_1}\right)(A_0 + A) - i\zeta_n\left(\mu_{T_2}\frac{\omega\eta_0^2}{c_2^2} + \mu_{L_2}np\frac{\sin\theta}{c_1}\right)B$$
$$- \frac{\omega\zeta_n^2}{c_1^2}\eta_n^+\left(\mu_{T_1}\frac{\omega(\eta_n^+)^2}{c_1} + \mu_{L_1}np\sin\theta_n^+\right)A_n^+ + \mu_{T_1}\frac{\eta_n^-}{c_1}\left(1 - 2(\eta_n^-)^2\zeta_n\zeta_{-n}\frac{\omega^2}{c_1^2}\right)A_n^-$$
$$= \zeta_n^2\left(\mu_{T_2}\frac{\omega^2(\eta_{0n}^+)^3}{c_2^3} + \mu_{L_2}\eta_{0n}^+np\frac{\omega\sin\phi_n^+}{c_2^2}\right)B_n^+ - \mu_{T_2}\frac{\eta_{0n}^-}{c_2}\left(1 - 2\zeta_{-n}\zeta_n\frac{(\omega\eta_{0n}^-)^2}{c_2^2}\right)B_n^-.$$

References

[Abubakar 1962] I. Abubakar, "Scattering of plane elastic waves at rough surfaces, I", *P. Camb. Philos. Soc.* **58a** (1962), 136–157.

[Achenbach 1976] J. D. Achenbach, *Wave propagation in elastic solids*, North-Holland, Amsterdam, 1976.

[Asano 1960] S. Asano, "Reflection and refraction of elastic waves at a corrugated boundary surface, I: The case of incidence of SH wave", *B. Earthq. Res. I. Tokyo* **38**:2 (1960), 177–197.

[Asano 1961] S. Asano, "Reflection and refraction of elastic waves at a corrugated boundary surface, II", *B. Earthq. Res. I. Tokyo* **39**:3 (1961), 367–466.

[Asano 1966] S. Asano, "Reflection and refraction of elastic waves at a corrugated interface", *B. Seismol. Soc. Am.* **56**:1 (1966), 201–221.

[Belfield et al. 1983] A. J. Belfield, T. G. Rogers, and A. J. M. Spencer, "Stress in elastic plates reinforced by fibers lying in concentric circles", *J. Mech. Phys. Solids* **31**:1 (1983), 25–54.

[Chattopadhyay and Choudhury 1990] A. Chattopadhyay and S. Choudhury, "Propagation, reflection and transmission of magnetoelastic shear waves in a self-reinforced medium", *Int. J. Eng. Sci.* **28**:6 (1990), 485–495.

[Chattopadhyay and Choudhury 1995] A. Chattopadhyay and S. Choudhury, "Magnetoelastic shear waves in an infinite self-reinforced plate", *Int. J. Numer. Anal. Methods Geomech.* **19**:4 (1995), 289–304.

[Dunkin and Eringen 1962] J. W. Dunkin and A. C. Eringen, "Reflection of elastic waves from the wavy boundary of a half-space", pp. 143–160 in *Proceedings of the 4th U.S. National Congress of Applied Mechanics* (Berkeley, 1962), edited by R. M. Rosenberg, ASME, New York, 1962.

[Gupta 1987] S. Gupta, "Reflection and transmission of SH waves in a laterally and vertically heterogeneous media at an irregular boundary", *Geophys. Trans.* **33**:2 (1987), 89–111.

[Kaur and Tomar 2004] J. Kaur and S. K. Tomar, "Reflection and refraction of SH waves at a corrugated interface between two monoclinic elastic half-spaces", *Int. J. Numer. Anal. Methods Geomech.* **28**:15 (2004), 1543–1575.

[Kaur et al. 2005] J. Kaur, S. K. Tomar, and V. P. Kaushik, "Reflection and refraction of SH-waves at a corrugated interface between two laterally and vertically heterogeneous viscoelastic solid half-spaces", *Int. J. Solids Struct.* **42**:13 (2005), 3621–3643.

[Kumar et al. 2003] R. Kumar, S. K. Tomar, and A. Chopra, "Reflection/refraction of SH-waves at a corrugated interface between two different anisotropic and vertically heterogeneous elastic solid half-spaces", *ANZIAM J.* **44**:3 (2003), 447–460.

[Okamoto and Takenaka 1999] T. Okamoto and H. Takenaka, "A reflection/transmission matrix formulation for seismoacoustic scattering by an irregular fluid-solid interface", *Geophys. J. Int.* **139**:2 (1999), 531–546.

[Pradhan et al. 2003] A. Pradhan, S. K. Samal, and N. C. Mahanti, "Influence of anisotropy on the Love waves in a self reinforced medium", *Tamkang J. Sci. Eng.* **6**:3 (2003), 173–178.

[Rayleigh 1893] L. Rayleigh, "On the reflection of sound or light from a corrugated surface", *Rep. Brit. Assoc. Adv. Sci.* (1893), 690–691.

[Rayleigh 1907] L. Rayleigh, "On the dynamical theory of gratings", *Proc. R. Soc. A* **79**:532 (1907), 399–416.

[Sengupta and Nath 2001] P. R. Sengupta and S. Nath, "Surface waves in fibre-reinforced anisotropic elastic media", *Sadhana* **26**:4 (2001), 363–370.

[Singh and Singh 2004] B. Singh and S. J. Singh, "Reflection of plane waves at the free surface of a fibre-reinforced elastic half-space", *Sadhana* **29**:3 (2004), 249–257.

[Spencer 1974] A. J. M. Spencer, "Boundary layers in highly anisotropic plane elasticity", *Int. J. Solids Struct.* **10**:10 (1974), 1103–1123.

[Tomar and Kaur 2003] S. K. Tomar and J. Kaur, "Reflection and transmission of SH waves at a corrugated interface between two laterally and vertically heterogeneous anisotropic elastic solid half-spaces", *Earth, Planets, Space* **55** (2003), 531–547.

[Tomar and Saini 1997] S. K. Tomar and S. L. Saini, "Reflection and refraction of SH waves at a corrugated interface between two-dimensional transversely isotropic half spaces", *J. Phys. Earth* **45** (1997), 347–362.

[Tomar et al. 2002] S. K. Tomar, R. Kumar, and A. Chopra, "Reflection and refraction of SH waves at a corrugated interface between transversely isotropic and visco-elastic solid half spaces", *Acta Geophys. Pol.* **50**:2 (2002), 231–249.

SANASAM SARAT SINGH: saratcha32@yahoo.co.uk
Department of Mathematics, Panjab University, Chandigarh 160 014, India

SUSHIL KUMAR TOMAR: sktomar@yahoo.com
Department of Mathematics, Panjab University, Chandigarh 160 014, India

ON TORSIONAL VIBRATIONS OF INFINITE HOLLOW POROELASTIC CYLINDERS

M. Tajuddin and S. Ahmed Shah

Employing Biot's theory of wave propagation in liquid saturated poroelastic media, the propagation of torsional vibrations in an infinite homogeneous, isotropic hollow poroelastic circular cylinder is investigated. Considering the boundaries to be stress free, the frequency equation of torsional vibrations is obtained in presence of dissipation. The frequency equation is discussed for the first two modes in the cases of a poroelastic thin shell, a poroelastic thick shell and a poroelastic solid cylinder. Phase velocity, group velocity and attenuation are determined and computed for the first mode of vibration for two different poroelastic materials as a function of frequency. These values are displayed graphically and then discussed.

1. Introduction

An understanding of the free vibrations of any beam is a prerequisite to the understanding of its response in forced vibrations. Propagation of elastic waves and vibrations in circular rods of uniform cross-section has been extensively studied [Love 1944; Kolsky 1963]. Armenàkas [1965] studied the torsional waves in composite infinite circular solid rods of two different materials. A study of inhomogeneous anisotropic hollow cylinders was presented by Stanisic and Osburn [1967].

The study of torsional vibrations of an elastic solid is important in several fields, for example, soil mechanics, transmission of power through shafts with flanges at the ends as integral parts of the shafts. It is now recognized that virtually no high-speed equipment can be properly designed without obtaining solution to what are essentially lateral or torsional vibration problems. Examples of torsional vibrations are vibrations in gear train and motor-pump shafts. Thus, from engineering point of view the study of torsional vibrations has great interest. Such vibrations, for example, are used in delay lines. Further, based on reflections and refractions during the propagation of a pulse, imperfections can be identified. The other use of torsional vibrations is the measurement of the shear modulus of a crystal.

The dynamic equations of a poroelastic solid are given in Biot [1956]. Biot's model consists of an elastic matrix permeated by a network of interconnected spaces called pores, saturated with liquid. Following Biot's theory of wave propagation, Tajuddin and Sarma [1980] studied torsional vibrations of poroelastic cylinders. Coussy et al. [1998] presented two different approaches for dealing with the mechanics of a deformable porous medium. Dynamic poroelasticity of thinly layered structures was studied by Gelinsky et al. [1998]. Degrande et al. [1998] studied the wave propagation in layered dry, saturated and unsaturated poroelastic media. Malla Reddy and Tajuddin [2000] studied the plane-strain vibrations of thick-walled hollow poroelastic cylinders. Wisse et al. [2002] presented the experimental

results of guided wave modes in porous cylinders. The edge waves of poroelastic plates under plane-stress conditions were studied by Malla Reddy and Tajuddin [2003]. Chao et al. [2004] studied the shock-induced borehole waves in porous formations. Tajuddin and Ahmed Shah [2006] studied the circumferential waves of infinite hollow poroelastic cylinders in the presence of dissipation.

In the present analysis, the frequency equation of torsional vibrations of a homogeneous and isotropic poroelastic hollow circular cylinder of infinite extent is derived in the presence of dissipation and then discussed. Let the boundaries of the hollow poroelastic cylinder be free from stress. The frequency equation is discussed for the first mode in the case of a poroelastic thin shell, a poroelastic thick shell and a poroelastic solid cylinder. This progression is intended to describe the transition from the case of a plate — regarded as the limit of a curved thin shell as the thickness tends to zero — to the case of a poroelastic solid cylinder. Two values are considered for the ratio h/r_1 of wall thickness h to inner radius r_1. As this ratio tends to zero, the modes of an infinite poroelastic plate of thickness equivalent to wall thickness are obtained. All the modes of the thick-walled hollow poroelastic cylinder asymptotically approach the analogous modes for a poroelastic solid cylinder of radius h as the ratio r_1/h tends to zero. The expressions for nondimensional phase velocity, group velocity and attenuation are presented and then computed for the first mode as a function of nondimensional frequency for two types of poroelastic materials and then discussed.

2. Solution of the problem

Let (r, θ, z) be the cylindrical polar coordinates. Consider a homogeneous, isotropic hollow infinite poroelastic circular cylinder with inner and outer radii r_1 and r_2, respectively, whose axis is in the direction of z-axis. Then the thickness of the hollow poroelastic cylinder is $h[= (r_2 - r_1)] > 0$. Let the boundaries of the isotropic poroelastic cylinder be free from stress. The only nonzero displacement components of solid and liquid media are $\boldsymbol{u}(0, v, 0)$ and $\boldsymbol{U}(0, V, 0)$, respectively. These displacements are functions of r, z and time, t. Then the equations of motion [Biot 1956] reduce to

$$
\begin{cases}
N\left(\nabla^2 - \dfrac{1}{r^2}\right)v = \dfrac{\partial^2}{\partial t^2}(\rho_{11}v + \rho_{12}V) + b\dfrac{\partial}{\partial t}(v - V), \\[2mm]
\qquad\quad 0 = \dfrac{\partial^2}{\partial t^2}(\rho_{12}v + \rho_{22}V) - b\dfrac{\partial}{\partial t}(v - V),
\end{cases}
\tag{1}
$$

where ρ_{11}, ρ_{12}, ρ_{22} are mass coefficients following Biot [1956], N is the shear modulus, b is the dissipation coefficient and ∇^2 is the well-known Laplacian operator. Let the propagation mode shapes of solid and liquid v and V be

$$
v = f(r)e^{i(kz+\omega t)}, \qquad V = F(r)e^{i(kz+\omega t)},
\tag{2}
$$

where k is the wavenumber, ω is the frequency of wave and i is complex unity or $i^2 = -1$. Substitution of Equation (2) in (1) results in

$$
\begin{cases}
N\Delta f = -\omega^2(K_{11}f + K_{12}F), \\[1mm]
\quad\; 0 = -\omega^2(K_{12}f + K_{22}F),
\end{cases}
\tag{3}
$$

where

$$\Delta = \frac{d^2}{dr^2} + \frac{1}{r}\frac{d}{dr} - \frac{1}{r^2} - k^2,$$

$$K_{11} = \rho_{11} - \frac{ib}{\omega},$$

$$K_{12} = \rho_{12} + \frac{ib}{\omega},$$

$$K_{22} = \rho_{22} - \frac{ib}{\omega}.$$

The second equation in (3) gives

$$F = -\frac{K_{12}}{K_{22}} f. \tag{4}$$

Substituting Equation (4) into the first equation of (3), we obtain

$$\left(\frac{d^2}{dr^2} + \frac{1}{r}\frac{d}{dr} - \frac{1}{r^2} + \alpha_3^2\right) f = 0, \tag{5}$$

where V_3 is the shear wave velocity [Biot 1956] and α_3^2 is

$$\alpha_3^2 = \xi_3^2 - k^2, \qquad \xi_3^2 = \frac{\omega^2(K_{11}K_{22} - K_{12}^2)}{NK_{22}}, \qquad V_3^2 = \frac{NK_{22}}{K_{11}K_{22} - K_{12}^2}. \tag{6}$$

A solution of Equation (5) is

$$f(r) = C_1 J_1(\alpha_3 r) + C_2 Y_1(\alpha_3 r).$$

Thus the displacement of the solid is

$$v = (C_1 J_1(\alpha_3 r) + C_2 Y_1(\alpha_3 r)]e^{i(kz+\omega t)}, \quad (\alpha_3 \neq 0). \tag{7}$$

When $\alpha_3 = 0$, Equation (5) reduces to the form

$$\left(\frac{d^2}{dr^2} + \frac{1}{r}\frac{d}{dr} - \frac{1}{r^2}\right) f = 0, \tag{8}$$

and thus its bounded solution is

$$f(r) = C_1 r.$$

Therefore the propagation mode shapes are given by the displacement solutions

$$v = \begin{cases} (C_1 J_1(\alpha_3 r) + C_2 Y_1(\alpha_3 r))e^{i(kz+\omega t)} & \alpha_3 \neq 0 \\ C_1 r & \alpha_3 = 0 \end{cases}. \tag{9}$$

Here C_1 and C_2 are constants.

From Equation (2), it can be seen that the normal strains e_{rr}, $e_{\theta\theta}$ and e_{zz} are all zero. Therefore the dilatations of solid and liquid media are both zero. Hence the liquid pressure s following Biot [1956] is identically zero. Accordingly for torsional vibrations no distinction between a pervious and an impervious surface is made. Considering the boundary to be stress free, the frequency equation obtained

for torsional vibrations is the same for both pervious and impervious surfaces. Then the only nonzero computed stress, $\sigma_{r\theta}$ (see [Biot 1956]), is

$$\sigma_{r\theta} = -N\big(C_1 J_2(\alpha_3 r) + C_2 Y_2(\alpha_3 r)\big)e^{i(kz+\omega t)}. \tag{10}$$

3. Frequency equation

The stress-free boundary conditions for torsional vibrations at the inner and outer surfaces of the hollow poroelastic cylinder are at $r = r_1$ and $r = r_2$,

$$\sigma_{r\theta} = 0, \qquad s = 0, \qquad \frac{\partial s}{\partial r} = 0. \tag{11}$$

First two equations of (11) are to be satisfied for a pervious surface, while the first and third equations of (11) are to be satisfied for an impervious surface. Since the considered vibrations are shear vibrations, the dilatations of solid and liquid media are both zero, thus liquid pressure s developed in solid-liquid aggregate will be identically zero and no distinction between pervious and impervious surface is made. Thus the second and third equations of (11) are satisfied identically. Equations (11) together with Equation (10) yield a system of two homogeneous equations in two constants C_1 and C_2. By eliminating these constants, one can obtain

$$J_2(\alpha_3 r_1)Y_2(\alpha_3 r_2) - J_2(\alpha_3 r_2)Y_2(\alpha_3 r_1) = 0. \tag{12}$$

Equation (12) is the frequency equation of torsional vibrations of an infinite hollow poroelastic cylinder whether the surface is pervious or impervious. By eliminating liquid effects from (12), the results for a purely elastic solid [Gazis 1959, Equation (43)] are obtained as a special case. The roots will increase with increasing r_1 tending to infinity as r_1 tends to r_2. Two cases of special interest for limiting values of ratio of thickness to inner radius h/r_1 when these values are too small and too large are considered:

3.1. *For thin poroelastic cylindrical shell.* When $h/r_1 \ll 1$, under the verifiable assumption of nonzero $\alpha_3 h$ it is seen that $\alpha_3 r_1 \gg 1$ and $\alpha_3 r_2 \gg 1$. By using Hankel–Kirchhoff asymptotic approximations for Bessel functions [Abramowitz 1964]

$$\begin{cases} J_2(x) \approx -\sqrt{\dfrac{2}{\pi x}}\Big[\cos\Big(x - \dfrac{\pi}{4}\Big) - \dfrac{15}{8x}\sin\Big(x - \dfrac{\pi}{4}\Big)\Big], \\[2ex] Y_2(x) \approx -\sqrt{\dfrac{2}{\pi x}}\Big[\sin\Big(x - \dfrac{\pi}{4}\Big) + \dfrac{15}{8x}\cos\Big(x - \dfrac{\pi}{4}\Big)\Big], \end{cases}$$

the frequency equation of torsional vibrations, that is, Equation (12), reduces to

$$\sin \alpha_3 h - \frac{15\alpha_3 h}{8\alpha_3^2 r_1 r_2}\cos \alpha_3 h = 0. \tag{13}$$

Equation (13) is the frequency equation of vibrations of a thin poroelastic cylindrical shell. In the limiting case, when $\alpha_3 r_1 \to \infty$, $\alpha_3 r_2 \to \infty$, (13) simplifies to

$$\sin \alpha_3 h = 0, \tag{14}$$

and hence

$$\alpha_3 h = \pi q, \quad q = 1, 2, 3, \ldots$$

so that

$$\omega = V_3 \left(\frac{q^2 \pi^2}{h^2} + k^2 \right)^{\frac{1}{2}}, \quad q = 1, 2, 3, \ldots \tag{15}$$

which are the frequencies of poroelastic plate of thickness h. Moreover near the origin $h/r_1 = 0$, and substituting

$$\alpha_3 h = q\pi + \epsilon^*, \quad \epsilon^* \ll 1, \tag{16}$$

into the frequency equation of torsional vibrations of a thin poroelastic cylindrical shell, Equation (13), gives

$$\epsilon^* = \frac{15}{8(q\pi)} \left(\frac{h}{r_1} \right)^2, \quad q = 1, 2, 3, \ldots \tag{17}$$

Substituting Equation (17) into (16) gives the frequency values obtained from (15) in the form

$$\omega = \frac{V_3}{h} \left(q^2 \pi^2 \left[1 + \frac{15}{8(q\pi)^2} \left(\frac{h}{r_1} \right)^2 \right]^2 + k^2 h^2 \right)^{\frac{1}{2}}, \quad q = 1, 2, 3, \ldots . \tag{18}$$

These are the frequencies of torsional vibrations of a poroelastic plate of thickness h near the origin.

3.2. For poroelastic solid cylinder. When $h/r_1 \gg 1$, the frequency equation, (12), tends asymptotically to

$$J_2(\alpha_3 h) = 0, \tag{19}$$

which is the frequency equation of torsional vibrations of a poroelastic solid cylinder of radius h discussed in Tajuddin and Sarma [1980]. The limiting cases $hr_1^{-1} \ll 1$ and $hr_1^{-1} \gg 1$ cover the torsional vibrations of thick-walled poroelastic hollow cylinders in the entire range from 0 to ∞. Thus we are modeling the transition from plate (hence shell) vibrations to the vibrations of a poroelastic solid cylinder.

If the wave number k is zero, the problem reduces to the special case of axially symmetric shear vibrations studied in Malla Reddy and Tajuddin [2000, Sections 5.1.1 and 5.1.2], where a thin poroelastic cylindrical shell and a solid poroelastic cylinder are discussed in detail. Accordingly the case $k \neq 0$ is of special interest, and that is what we discuss below.

To analyze further the frequency equation, it is convenient to introduce the following nondimensional variables:

$$m_{11} = \rho_{11}\rho^{-1}, \qquad m_{12} = \rho_{12}\rho^{-1}, \qquad m_{22} = \rho_{22}\rho^{-1}, \qquad b_1 = bh(c_0\rho)^{-1},$$
$$\Omega = \omega h c_0^{-1}, \qquad g = r_2 r_1^{-1}, \tag{20}$$

so that $hr_1^{-1} = g - 1$, where b_1, Ω are nondimensional dissipation and frequency, and

$$\rho = \rho_{11} + 2\rho_{12} + \rho_{22}, \qquad c_0^2 = N\rho^{-1}.$$

Let

$$R_n^{\,2} = \alpha_3^2 h^2,$$

where α_3^2 is given in Equation (6). From these equations, we can write

$$\frac{N(R_n^2 + k^2 h^2)}{\rho \omega^2 h^2} = E_r - i E_i, \tag{21}$$

where E_r and E_i are

$$E_r = \frac{\Omega^2 m_{22}(m_{11} m_{22} - m_{12}^2) + b_1^2}{\Omega^2 m_{22}^2 + b_1^2}, \qquad E_i = \frac{b_1 \Omega (m_{12} + m_{22})^2}{\Omega^2 m_{22}^2 + b_1^2}. \tag{22}$$

To investigate the values of R_n, the frequency equation (12) in nondimensional form is

$$J_2\left(\frac{R_n}{g-1}\right) Y_2\left(\frac{R_n g}{g-1}\right) - J_2\left(\frac{R_n g}{g-1}\right) Y_2\left(\frac{R_n}{g-1}\right) = 0. \tag{23}$$

In (23) g is the ratio of outer to inner radius.

Three cases of physical interest have been considered, varying the g value: 1.034, 3, and infinity. These three cases represent a thin poroelastic shell, thick poroelastic shell and poroelastic solid cylinder, respectively. The phase and group velocities and attenuation can be determined for the first two modes, which have been computed from the frequency equation (23) for $\omega > |k V_3|$. The values for the said cases are 3.1423, 6.2835; 3.736, 6.6477; and 5.1356, 8.4172.

4. Phase velocity, group velocity and attenuation

Due to the dissipative nature of the medium, the wave number k is complex. The waves generated obey a diffusion process, and therefore get attenuated. Let $k = k_r + i k_i$; then the phase velocity c_p, group velocity c_g and attenuation x_h, respectively, are

$$c_p = \text{Real part } (\omega k^{-1}) = \frac{\omega}{|k_r|}, \qquad c_g = \frac{d\omega}{dk} \qquad \text{and} \qquad x_h = \frac{1}{|k_i|},$$

which in turn reduces to nondimensional form as

$$c_p c_0^{-1} = \sqrt{2} \Omega (B_1 + B_2)^{-\frac{1}{2}}, \tag{24}$$

$$c_g c_0^{-1} = 2\sqrt{2} B_3^{-1} (B_1 + B_2)^{\frac{1}{2}}, \tag{25}$$

and

$$x_h h^{-1} = \sqrt{2} (B_1 - B_2)^{-\frac{1}{2}}. \tag{26}$$

In Equations (24)–(26), B_1, B_2 and B_3 are

$$\begin{cases} B_1 = \left(\Omega^4 (E_r^2 + E_i^2) - 2\Omega^2 E_r R_n^2 + R_n^4\right)^{\frac{1}{2}}, \\ B_2 = (\Omega^2 E_r - R_n^2), \\ B_3 = \Omega^2 G_1 (1 + \Omega^2 E_r B_1^{-1} - R_n^2 B_1^{-1}) \\ \quad + 2\Omega E_r (1 - R_n^2 B_1^{-1}) \\ \quad + \Omega^3 B_1^{-1} \left(\Omega E_i G_2 + 2(E_r^2 + E_i^2)\right), \end{cases} \tag{27}$$

Material Parameter	m_{11}	m_{12}	m_{22}
Material I	0.901	-0.001	0.101
Material II	0.877	0	0.123

Table 1. Properties of materials I and II.

where Ω is nondimensional frequency and R_n denotes modes of vibration, E_r and E_i are given in (22) while G_1 and G_2 are

$$G_1 = \frac{2b_1^2(E_r - 1)}{\Omega\,(\Omega^2 m_{22}^2 + b_1^2)}, \qquad G_2 = \frac{(b_1^2 - \Omega^2 m_{22}^2)E_i}{\Omega\,(\Omega^2 m_{22}^2 + b_1^2)}. \qquad (28)$$

The nondimensional phase velocity, group velocity and attenuation equations of a poroelastic plate are similar to (24)–(26), respectively, wherein R_n is to be replaced by $q\pi$ ($q = 1, 2, 3, \ldots$). Different values of q represent different modes of vibration. It is interesting to note that the first two modes of a poroelastic plate tally with the first two modes of a thin poroelastic shell.

5. Results and discussion

Two types of poroelastic materials are considered to carry out the computational work: sandstone saturated with kerosene, which we call Material I [Fatt 1959], and sandstone saturated with water, called Material II [Yew and Jogi 1976]. Their physical parameters are defined in Table 1.

For a given material, the nondimensional phase velocity, group velocity and attenuation are determined as a function of nondimensional frequency (Ω). The different dissipation parameters (b_1) chosen are 0.01, 0.1 and 1.

The phase velocity as a function of frequency is presented for first mode for the two materials in Figure 1 (top) for different dissipations in the case of a thin shell. The phase velocity has nearly the same shape when $b_1 = 0.01$ and 0.1 in material I. This is also true for material II. For $b_1 = 1$, the phase velocity is almost identical in both materials. The group velocity with respect to frequency is presented in Figure 1 (middle) for the first mode in case of a thin poroelastic shell. The results are true for all three dissipations considered, and are almost same as the phase velocity for both materials. The attenuation is presented in Figure 1 (bottom) for the first mode. When $b_1 = 0.01$, the attenuation is almost the same for both materials, and for $b_1 = 0.1$ and 1 it is virtually the same for both materials. Besides, it is clear that as b_1 increases from 0.01 to 1 the attenuation is decreasing. The nondimensional phase velocity and group velocity as a function of frequency is presented in Figure 2 for the two materials, for a thick poroelastic shell.

From Figure 2 (top) it is clear that for the first mode, the phase velocity is increasing in $0 < \Omega < 5$, and then decreasing in $5 \le \Omega < 10$, and when $\Omega \ge 10$ it is constant for both the referred materials and for different dissipations. The phase velocity decreases as the dissipation b_1 increases, and it is less for material I than for material II. The same figure also shows that when $b_1 = 1$, the phase velocity is same for both materials. In Figure 2 (middle), the group velocity as a function of frequency is presented for first mode. It is clear that for $b_1 = 0.1$ and 1, both materials have the same group velocity, while when
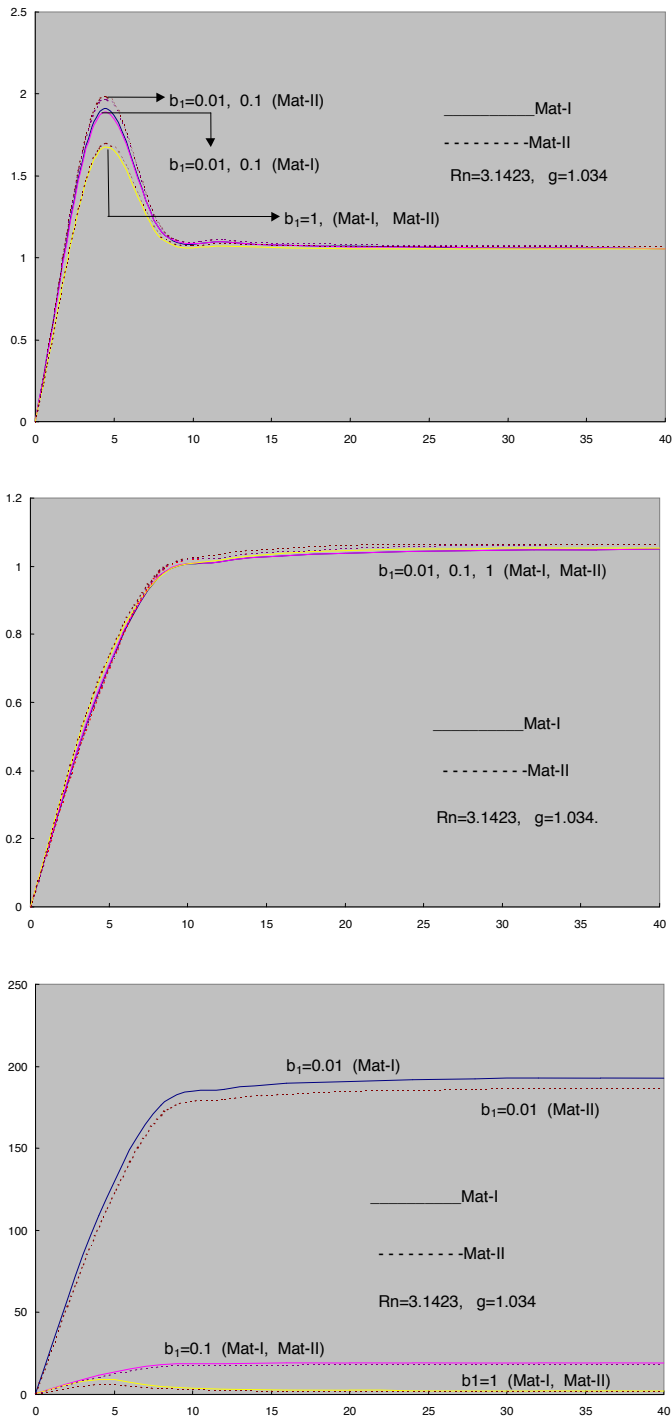
Figure 1. Torsional vibrations of hollow poroelastic cylinder, thin shell. The graphs show the phase velocity (top), group velocity (middle) and attenuation (bottom) as functions of frequency for the first mode, using reduced (nondimensional) variables.
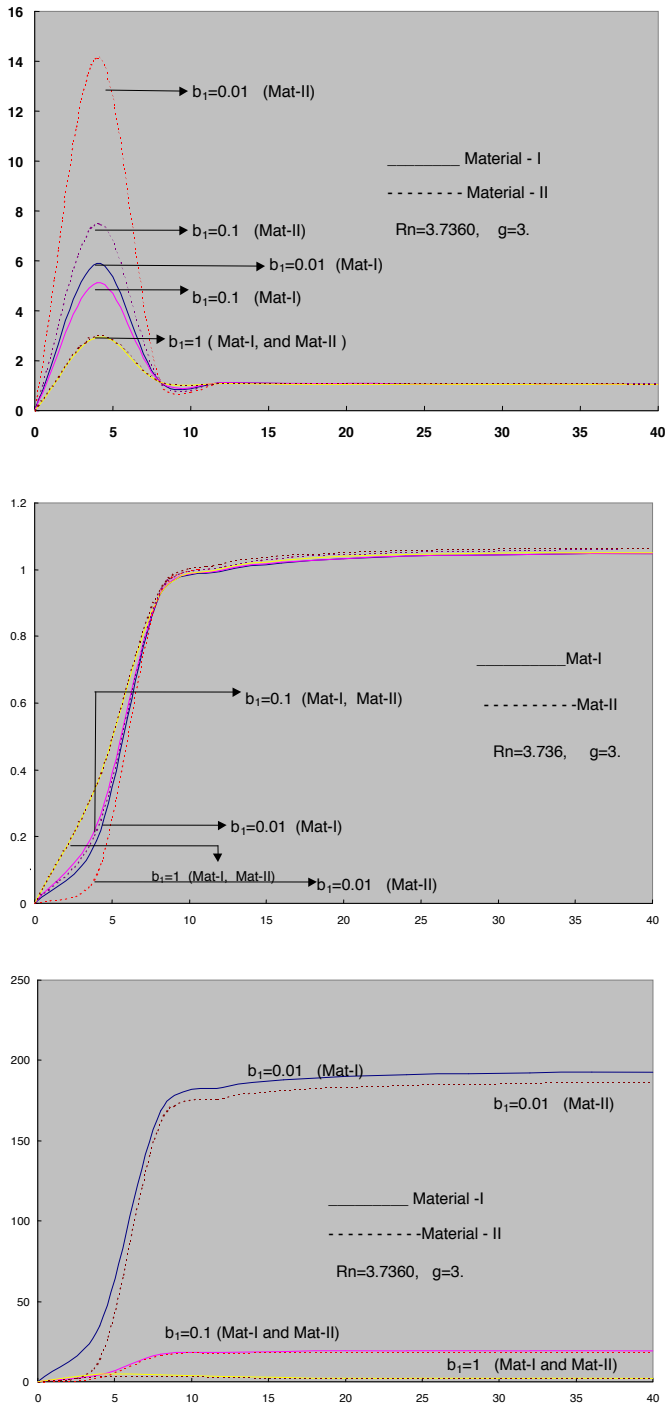
Figure 2. Torsional vibrations of hollow poroelastic cylinder, thick shell. The graphs show the phase velocity (top), group velocity (middle) and attenuation (bottom) as functions of frequency for the first mode, using reduced (nondimensional) variables.
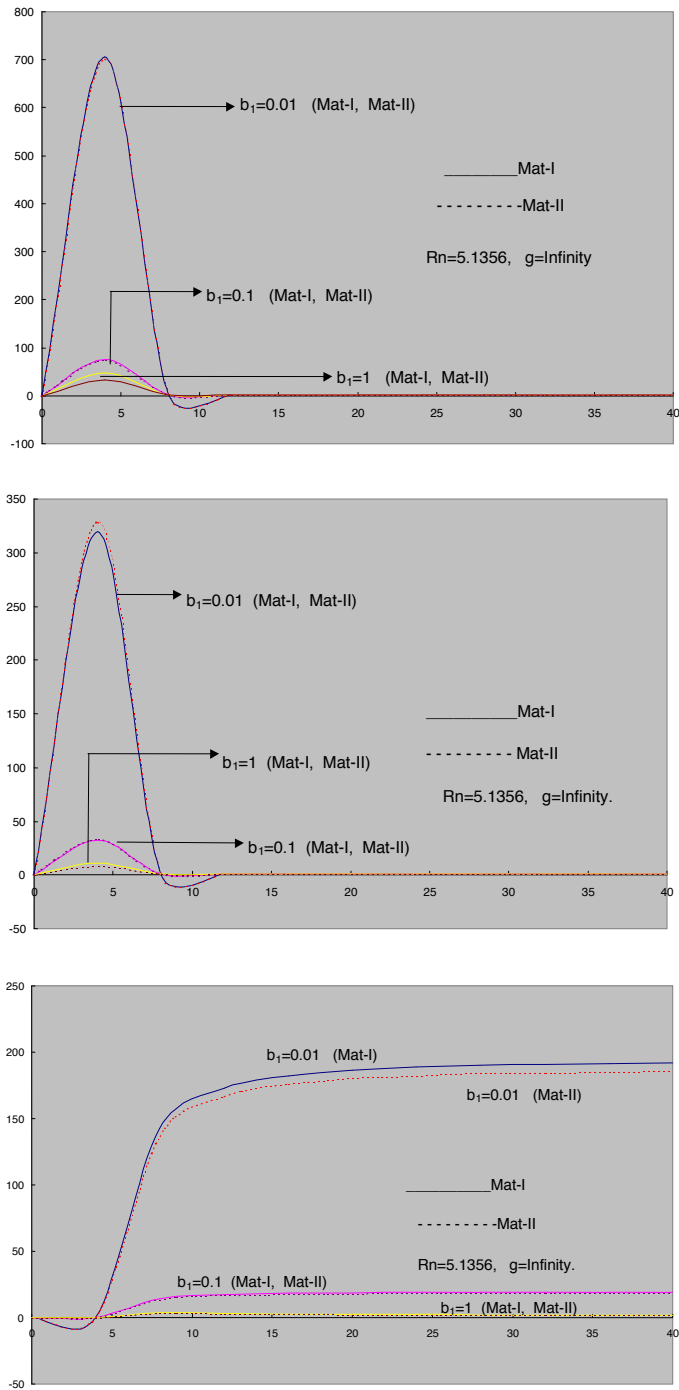
Figure 3. Torsional vibrations of solid poroelastic cylinder. The graphs show the phase velocity (top), group velocity (middle) and attenuation (bottom) as functions of frequency for the first mode, using reduced (nondimensional) variables.

$b_1 = 0.01$ the group velocity in material II is less than that of material I for $0 < \Omega < 5$. When $\Omega \geq 5$ the group velocity in materials I and II is almost the same for all dissipations. The attenuation is presented in Figure 2 (bottom) for a thick poroelastic shell in the case of the first mode. Its variation is similar to that of a thin shell.

The phase velocity of a poroelastic solid cylinder for the first mode is shown in Figure 3 (top). The phase velocity takes the same path for both materials when $b_1 = 0.01, 0.1$ and 1, but it decreases as dissipation increases. The group velocity for a poroelastic solid cylinder for the first mode is shown in Figure 3 (middle). Its variation is similar to that of the phase velocity (top figure). The group velocity of a poroelastic solid cylinder is seen to be less than the phase velocity for both materials. The attenuation of a poroelastic solid cylinder for the first mode is presented in Figure 3 (bottom). The attenuation in both materials is the same when $b_1 = 0.01, 0.1$ and 1; the figure also shows that the attenuation is higher for $b_1 = 0.01$ than for $b_1 = 0.1$ and 1.

6. Concluding remarks

The investigation of torsional vibrations of hollow poroelastic cylinders for different dissipations in the cases of a thin poroelastic shell, a thick poroelastic shell and a poroelastic solid cylinder has lead to the following conclusion:

 (i) The phase velocity increases as we progress from a hollow poroelastic cylinder through thin and thick poroelastic shells to a poroelastic solid cylinder.

 (ii) In general, the group velocity is less than the phase velocity.

(iii) The presence of a coupling parameter reduces the phase and group velocities.

(iv) It is observed that the increasing of the mass of a solid reduces both phase and group velocities.

 (v) An increase in dissipation reduces the phase and group velocities as well as the attenuation for both materials.

(vi) There is no significant variation in attenuation between a thin poroelastic shell, a thick shell and a poroelastic solid cylinder.

(vii) The phase and group velocities for the second mode are in general higher than the corresponding values for the first mode, in all cases.

Acknowledgements

References

[Abramowitz 1964] A. Abramowitz and I. A. Stegun (editors), *Handbook of mathematical functions with formulas, graphs, and mathematical tables*, edited by A. Abramowitz and I. A. Stegun, National Bureau of Standards Applied Mathematics Series **55**, U.S. Government Printing Office, Washington, DC, 1964. MR 29 #4914 Zbl 0171.38503

[Armenàkas 1965] A. E. Armenàkas, "Torsional waves in composite rods", *J. Acoust. Soc. Am.* **38**:3 (1965), 439–446.

[Biot 1956] M. A. Biot, "Theory of propagation of elastic waves in a fluid-saturated porous solid, I: low-frequency range", *J. Acoust. Soc. Am.* **28**:2 (1956), 168–178.

[Chao et al. 2004] G. Chao, D. M. J. Smeulders, and M. E. H. van Dongen, "Shock-induced borehole waves in porous forma-
tions: theory and experiments", *J. Acoust. Soc. Am.* **116**:2 (2004), 693–702.

[Coussy et al. 1998] O. Coussy, L. Dormieux, and E. Detournay, "From mixture theory to Biot's approach for porous media",
Int. J. Solids Struct. **35**:34–35 (1998), 4619–4635.

[Degrande et al. 1998] G. Degrande, G. De Roeck, P. Van Den Broeck, and D. Smeulders, "Wave propagation in layered dry,
saturated and unsaturated poroelastic media", *Int. J. Solids Struct.* **35**:34–35 (1998), 4753–4778.

[Fatt 1959] I. Fatt, "The Biot–Willis elastic coefficients for a sandstone", *J. Appl. Mech.* (*ASME*) **26** (1959), 296–297.

[Gazis 1959] D. C. Gazis, "Three-dimensional investigation of the propagation of waves in hollow circular cylinders, I: Ana-
lytical foundation", *J. Acoust. Soc. Am.* **31**:5 (1959), 568–573.

[Gelinsky et al. 1998] S. Gelinsky, S. A. Shapiro, T. Muller, and B. Gurevich, "Dynamic poroelasticity of thinly layered
structures", *Int. J. Solids Struct.* **35**:34–35 (1998), 4739–4751.

[Kolsky 1963] H. Kolsky, *Stress waves in solids*, Dover, New York, 1963.

[Love 1944] A. E. H. Love, *A treatise on the mathematical theory of elasticity*, Dover, New York, 1944.

[Malla Reddy and Tajuddin 2000] P. Malla Reddy and M. Tajuddin, "Exact analysis of the plane-strain vibrations of thick-
walled hollow poroelastic cylinders", *Int. J. Solids Struct.* **37**:25 (2000), 3439–3456.

[Malla Reddy and Tajuddin 2003] P. Malla Reddy and M. Tajuddin, "Edge waves in poroelastic plate under plane-stress condi-
tions", *J. Acoust. Soc. Am.* **114**:1 (2003), 185–193.

[Stanisic and Osburn 1967] M. M. Stanisic and C. M. Osburn, "On torsional vibrations of inhomogeneous anisotropic hollow
cylinder", *Z. Angew. Math. Mech.* **47** (1967), 465–466.

[Tajuddin and Ahmed Shah 2006] M. Tajuddin and S. Ahmed Shah, "Circumferential waves of infinite hollow poroelastic
cylinders", *J. Appl. Mech.* (*ASME*) **73**:4 (2006), 705–708.

[Tajuddin and Sarma 1980] M. Tajuddin and K. S. Sarma, "Torsional vibrations of poroelastic cylinders", *J. Appl. Mech.*
(*ASME*) **47** (1980), 214–216.

[Wisse et al. 2002] C. J. Wisse, D. M. J. Smeulders, M. E. H. van Dongen, and G. Chao, "Guided wave modes in porous
cylinders: experimental results", *J. Acoust. Soc. Am.* **112**:3 (2002), 890–895.

[Yew and Jogi 1976] C. H. Yew and P. N. Jogi, "Study of wave motions in fluid-saturated porous rocks", *J. Acoust. Soc. Am.*
60:1 (1976), 2–8.

M. TAJUDDIN: taj_osmania@yahoo.co.in
Department of Mathematics, Osmania University, Hyderabad 500 007, India

S. AHMED SHAH: ahmed_shah67@yahoo.com
Department of Mathematics, Osmania University, Hyderabad 500 007, India

SUBMISSION GUIDELINES

ORIGINALITY

Authors may submit manuscripts in PDF format on-line. Submission of a manuscript acknowledges that the manuscript is *original and has neither previously, nor simultaneously, in whole or in part, been submitted elsewhere.* Information regarding the preparation of manuscripts is provided below. Correspondence by email is requested for convenience and speed. For further information, write to:

<div align="center">

Marie-Louise Steele
Division of Mechanics and Computation
Durand Building, Room 262
Stanford University
Stanford CA 94305

</div>

LANGUAGE

Manuscripts must be in English. A brief abstract of about 150 words or less must be included. The abstract should be self-contained and not make any reference to the bibliography. Also required are keywords and subject classification for the article, and, for each author, postal address, affiliation (if appropriate), and email address if available. A home-page URL is optional.

FORMAT

Authors are encouraged to use LaTeX and the standard article class, but submissions in other varieties of TeX, and, exceptionally in other formats, are acceptable. Electronic submissions are strongly encouraged in PDF format only; after the refereeing process we will ask you to submit all source material.

REFERENCES

Bibliographical references should be listed alphabetically at the end of the paper and include the title of the article. All references in the bibliography should be cited in the text. The use of BibTeX is preferred but not required. Tags will be converted to the house format (see a current issue for examples), however, in the manuscript, the citation should be by first author's last name and year of publication, e.g. "as shown by Kramer, et al. (1994)". Links will be provided to all literature with known web locations and authors are encoraged to provide their own links on top of the ones provided by the editorial process.

FIGURES

Figures prepared electronically should be submitted in Encapsulated PostScript (EPS) or in a form that can be converted to EPS, such as GnuPlot, Maple, or Mathematica. Many drawing tools such as Adobe Illustrator and Aldus FreeHand can produce EPS output. Figures containing bitmaps should be generated at the highest possible resolution. If there is doubt whether a particular figure is in an acceptable format, the authors should check with production by sending an email to:

<div align="center">

production@mathscipub.org

</div>

Each figure should be captioned and numbered so that it can float. Small figures occupying no more than three lines of vertical space can be kept in the text ("the curve looks like this:"). It is acceptable to submit a manuscript with all figures at the end, if their placement is specified in the text by means of comments such as "Place Figure 1 here". The same considerations apply to tables.

WHITE SPACE

Forced line breaks or page breaks should not be inserted in the document. There is no point in your trying to optimize line and page breaks in the original manuscript. The manuscript will be reformatted to use the journal's preferred fonts and layout.

PROOFS

Page proofs will be made available to authors (or to the designated corresponding author) at a web site in PDF format. Failure to acknowledge the receipt of proofs or to return corrections within the requested deadline may cause publication to be postponed.